Inaugural dissertation

for

obtaining the doctoral degree

of the

Combined Faculty of Mathematics, Engineering and Natural Sciences

of the

Ruprecht - Karls - University

Heidelberg

Presented by

M. Sc. Sara Kathrin Götz

born in: Weingarten, Germany

Oral examination: 14.02.2022

Quantitative and Structural Description of Molecular Crowding Using In-Cell Cryo-Electron Tomography

Referees:
Prof. Dr. Michael Knop
Dr. Judith Zaugg

This project was conducted in the Structural and Computational Biology (SCB) unit at the European Molecular Biology Laboratory (EMBL) Heidelberg from October 2017 to November 2021 supervised by Dr. Julia Mahamid.

Contents

Summary

Living cells are densely populated with macromolecules (Fulton 1982). To understand how proteins and nucleic acids dynamically inhabit and function in cellular volumes, knowledge of molecular crowding is critical to appreciate their modes of interactions and their spatio-temporal distributions. However, none of the existing approaches to measure molecular crowding allow for label-free and spatially-resolved analyses at the molecular scale. In this thesis, I quantitatively and structurally described molecular crowding inside cells utilizing recent advances in cryo-electron tomography (cryo-ET) (Koning et al. 2018, Schaffer et al. 2017, Turk and Baumeister 2020). Specifically, I investigated intracellular crowding in yeast cells under varying nutritional conditions. As their cytosol undergoes a dramatic transition from a liquid- to a solid-like state upon starvation (Joyner et al. 2016, Munder et al. 2016), I mapped changes in local molecular concentrations of ribosomes and fatty acid synthase (FAS) complexes, as well as structural rearrangements of these macromolecules, and other meso-scale protein assemblies. For this purpose, I co-developed methods for automated, high-throughput cryo-sample preparations, in particular cryo-focused ion beam (FIB) milling, and automated data mining utilizing deep-learning algorithms. These workflows allow for the analysis of large datasets which take stochastic cell-to-cell variations into account and are also applicable to other cell types. The automated methods will increase throughput and enable exploration of new biological questions in the long term.

In this thesis, I showed that energy-depletion leads to large-scale reorganization of the wild-type yeast cytosol, including variations in particle distributions, conformational changes of specific macromolecular species and the formation of various higher-order assemblies. Determination of their structures provided novel insights into local alterations of macromolecules within the cellular context under different physiologically-relevant conditions. In particular, for both ribosomes and FAS distinct structural conformations were observed upon energy depletion which hint at stationary states, possibly protecting these molecular machines during stress. Future structural analysis of all visualized macromolecular assemblies in combination with coarse-grain and molecular dynamics modeling, will ultimately enable a more holistic understanding of cytosolic phase transitions at a molecular level.

Zusammenfassung

Lebende Zellen sind dicht mit Makromolekülen gepackt (Fulton 1982). Um zu verstehen, wie Proteine und Nukleinsäuren dynamisch zelluläre Räume einnehmen und dort funktionieren, ist die Kenntnis der molekularen Verdrängung, auch molekulares 'Crowding' genannt, entscheidend. Dies trägt zudem zum Verständnis über die Art ihrer Interaktionen und über ihre räumlich-zeitliche Verteilung bei. Keiner der bestehenden Ansätze zur Bestimmung von molekularem Crowding ermöglicht jedoch räumlich aufgelöste Analysen auf molekularer Ebene ohne die Markierung von bestimmten Makromolekülen. In der vorliegenden Arbeit habe ich das molekulare Crowding innerhalb von Zellen quantitativ und strukturell beschrieben und dabei die neuesten Fortschritte in der Kryo-Elektronentomographie genutzt (Koning et al. 2018, Schaffer et al. 2017, Turk und Baumeister 2020). Konkret untersuchte ich das intrazelluläre Crowding in Hefezellen unter verschiedenen Nährstoffbedingungen. Da ihr Zytosol unter Hungerbedinungen eine drastische Transformation von einem flüssigen in einen feststoffähnlichen Zustand erfährt (Joyner et al. 2016, Munder et al. 2016), bestimmte ich die lokalen Molekülkonzentrationen von Ribosomen und Fettsäure-Synthasen (FAS) sowie die strukturelle Neuordnung dieser Makromoleküle und anderer Proteinansammlungen. Zu diesem Zweck habe ich Methoden für die automatisierte Kryoprobenbereitung mit hohem Durchsatz mitentwickelt, insbesondere die mikrotechnische Bearbeitung von Zellen mit einem fokussierten Ionenstrahl, sowie die automatisierte Datenprozessierung, die Deep-Learning-Algorithmen verwendet. Diese Arbeitsabläufe ermöglichen die Analyse großer Datensätze unter Berücksichtigung stochastischer Variationen zwischen individuellen Zellen und sind auch auf andere Zelltypen anwendbar. Die automatisierten Methoden werden die Verarbeitungsmenge erhöhen und langfristig die Erforschung neuer biologischer Fragen, die über den Rahmen der vorliegenden Arbeit hinausgehen, ermöglichen.

In dieser Arbeit habe ich gezeigt, dass Energieentzug zu einer groß angelegten Reorganisation des Zytosols wildtypischer Hefen führt. Dies umfasst Variationen in der Partikelverteilung, Konformationsänderungen spezifischer makromolekularer Spezies und der Bildung verschiedener Proteinzusammenlagerungen von höherer Ordnung. Die Charakterisierung ihrer Strukturen ermöglichte neue Einblicke in lokale Veränderungen von Makromolekülen im zellulären Kontext unter verschiedenen physiologisch relevanten Bedingungen. Insbesondere wurden sowohl für Ribosomen als

auch für FAS unterschiedliche strukturelle Konformationen bei Energieentzug beobachtet, die auf stationäre Zustände hindeuten, um diese molekularen Maschinen möglicherweise bei Stress zu schützen. Zukünftige Strukturanalysen aller visualisierten makromolekularen Ansammlungen in Kombination mit Grobkornmodellierung und der Verwendung von Molekulardynamikmodellen werden letztlich zu einem ganzheitlicheren Verständnis der Phasenübergänge im Zytosol auf molekularer Ebene beitragen.

Publications and manuscripts

Concepts and ideas about biomolecular condensation and the underlying molecular structures introduced in chapter 1 were discussed in-depth and published in the following review article:

Visualizing Molecular Architectures of Cellular Condensates: Hints of Complex Coacervation Scenarios

Sara K. Goetz and Julia Mahamid; Developmental Cell (2020).

The results described in chapter 5.1.2 are part of the following manuscript which is published on bioRxiv and currently under peer-revision:

A Modular Platform for Streamlining Automated Cryo-FIB Workflows

Sven Klumpe*, Herman K. H. Fung*, Sara K. Goetz*, Ievgeniia Zagoriy, Bernhard Hampoelz, Xiaojie Zhang, Philipp S. Erdmann, Janina Baumbach, Christoph W. Müller, Martin Beck, Jürgen M. Plitzko, Julia Mahamid; bioRxiv (2021).

* These authors contributed equally

The results described in chapter 5.1.4 are part of the following manuscript which is currently in preparation:

Convolutional networks for supervised mining of intracellular molecular landscapes

Irene de Teresa*, Sara K. Goetz*, Alexander Mattausch, Christian Zimmerli, Mauricio Toro-Nahuelpan, Dorothy W.C. Cheng, Fergus Tollervey, Constantin Pape, Martin Beck, Anna Kreshuk, Julia Mahamid and Judith Zaugg.

* These authors contributed equally

In addition, I contributed to the following manuscript that is not part of this thesis:

Nuclear pores dilate and constrict *in-cellulo*

Christian E. Zimmerli*, Matteo Allegretti*, Vasileios Rantos, Sara K. Goetz, Agnieszka Obarska-Kosinska, Ievgeniia Zagoriy, Aliaksandr Halavatyi, Julia Mahamid, Jan Kosinski and Martin Beck; Science (2021).

* These authors contributed equally

Throughout this thesis, results, figures and methods which were jointly produced or generated by someone else are marked appropriately.

1 Introduction

1.1 Cellular organization

The basic unit of life is a cell (Mazzarello 1999). The essential characteristic of this entity is its physical separation from the environment by a membrane that confines biomolecules in a dedicated space. Consequently, a cell concentrates molecules and establishes intricate conditions for biochemical reactions. However, the ubiquitously crowded interior of cells is much more complex than a random turmoil of molecules. In order to fulfill a plethora of functions the molecules of life: proteins, nucleic acids, metabolites and lipids, are highly organized in space and time. This self-organization establishes coherent macromolecular architectures within whole cells (Figure 1 A). The complex cellular interior is built up by smaller units or compartments which are ubiquitous. They are established on the micron scale of membrane-bound or membrane-less organelles, meso-scale assemblies such as cytoskeletal filaments or even on the nanometer scale of protein complexes such as the proteasome with specialized reaction chambers (Erdmann et al. 2018, Harold 2005). These unique cellular structures are highly modular to enable dynamic processes from very basic reactions to complex pathways. The resulting intricate, local environments are required for replication and growth and thus make the innumerable forms of life possible.

The organizational concept of modularity which has been described in many scientific fields (Callebaut 2005), is already apparent at the level of proteins. They are constituted by domains, interact with different factors and substrates, and assemble into larger multi-enzyme complexes or polymers. However, protein functions arise not only from their structures and the connected enzymatic activities but are also determined by their localization in the cell and the interactions with neighboring biomolecules (Gavin et al. 2006, Huh et al. 2003). Proteins indeed have large interaction networks that cover transient or more persistent encounters. The underlying interactions are determined by the protein's surface characteristics and are either functional, often via high affinity binding, or compete with promiscuous non-specific protein-protein interactions (Levy et al. 2012). This "molecular sociology" (Beck and Baumeister 2016) of either intentional or random encounters depends on both

protein abundance and distribution. For example, a single yeast cell is predicted to have around 5,000 protein-coding genes with a total of around 5-6 * 10^7 protein molecules per cell (Carpy et al. 2014, Futcher et al. 1999, Marguerat et al. 2012). The levels of the expressed, individual proteins vary between 1.1 * 10^6 to less than 100 copies per cell (Carpy et al. 2014, Ho et al. 2018, Marguerat et al. 2012). In general, protein concentrations are regulated to meet the functional demands and usually change during the cell cycle, but not during growth, which indicates that protein abundances are scaled with growing cell sizes (Campbell et al. 2020, Marguerat et al. 2012). The question on how individual proteins meet and how protein interaction networks are orchestrated on a whole cell level is highly dependent on protein localization (Levy et al. 2014). Molecular crowding describes these variations in local macromolecule concentrations and how they affect their surrounding cellular environment. A quantitative and structural understanding of this phenomenon will thus provide a more holistic view of cellular organization.

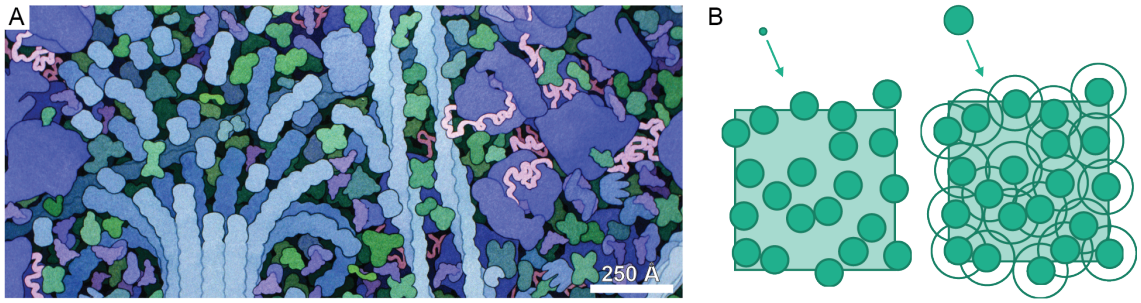

Figure 1: The interior of living cells is ubiquitously crowded. A) Macromolecules with varying sizes and shapes such as dynamic microtubules (bright blue, fountain-like filament), ribosomes (dark blue) which actively translate nascent peptide chains (pink), actin filaments (bright blue filaments with a twist) and many other macromolecules (green) occupy cytosolic space. Illustration by David S. Goodsell (Goodsell 2005). B) Depending on the size, molecules exclude a certain amount of volume. Small particles can freely diffuse while larger molecules are limited due to steric repulsion.

1.2 Molecular crowding

Molecular crowding describes the phenomenon that macromolecules occupy and thus exclude a significant fraction (5-40 %) of the cellular volume (Ellis and Minton 2003, Fulton 1982). In fact, the total weight per volume concentrations of all proteins and

RNA molecules inside a cell range from 80 g/L to over 400 g/L (Fulton 1982, McGuffee and Elcock 2010, Sharp 2015, Zimmerman and Trach 1991). In extreme cases, such as yeast spores, the cellular mass density can reach 1 kg/L (Jiang et al. 2010). Thereby, different numbers, sizes and shapes of macromolecules encounter each other and generate varying local crowding, contributing to unique environments for biochemical processes. Variations in local crowding can affect many physicochemical equilibria and protein properties such as diffusion, viscosity, conformational states, association, protein folding, (self-) oligomerization and aggregation, as well as the efficiency of molecular chaperones and enzymes (Boersma et al. 2015, Ellis 2001, Garenne et al. 2020, Kuznetsova et al. 2014, Kuznetsova et al. 2015, Levy et al. 2012, McGuffee and Elcock 2010, Mourao et al. 2014). These alterations can be caused by non-specific steric repulsion between macromolecules competing for physical space, which is further influenced by cellular compartmentalization, and leads to an entropic effect of volume exclusion. As a consequence, less solvent is accessible to macromolecules which can in turn favor non-specific or weak interactions and change their effective concentrations (Figure 1 B). In addition, altered protein hydration shells can have severe effects on structure, conformation, stability and activity (Ebbinghaus et al. 2007, Pocker 2000). The solubility is further affected by salt and metabolite concentrations which also add to local crowding (Madeira et al. 2012, Sharp 2015, Theilet et al. 2017, Theillet et al. 2014).

In vitro studies of individual proteins in solution are not ideal to investigate molecular crowding, as they do not represent accurately the crowded intracellular milieu. Therefore, *in vivo* experimental systems have been developed to analyze the behavior of tracer molecules inside living cells or measure intracellular mass density (Abuhattum et al. 2018, Boersma et al. 2015, Joyner et al. 2016, Miyagi et al. 2021, Munder et al. 2016, Smith et al. 2016). However, studying the effects of crowding with a single, labeled protein species can potentially perturb cellular functions, or produce diffusion rates that are relevant only for the specific size of the analyzed particle. These methods also have limited spatial resolution and thus do not describe in detail the heterogeneous distribution of molecules in a cell.

Thus, *in silico* computational modelling has been employed to gain insights on molecular crowding. Molecular dynamics simulations of atomistic models representing the cytosol with macromolecules, metabolites, ions and water, have been

conducted to connect molecular with cellular behavior (Feig et al. 2017, Yu et al. 2016). However, they are still limited by a lack of experimental data, especially in the case of eukaryotic cells, to describe the cellular heterogeneity and complexity in molecular detail. Thus, the ultimate goal is to generate realistic cell models by integrating data across scales from different imaging modalities in order to understand how subcellular organization creates various crowded environments with particular functions.

1.3 Sub-cellular organization into membrane-less compartments

As described above, cells need to organize and compartmentalize their interior in order to control or regulate biochemical reactions in the crowded cellular environment. Complementing the classical view of cellular organization into membrane-bound organelles and deterministic assembly of molecules into structured complexes, a new concept of membrane-less compartments has emerged in the last decade (Banani et al. 2017, Hyman et al. 2014, Shin and Brangwynne 2017, Walter and Brooks 1995). The formation of these biomolecular condensates is suggested to be driven by the regulated process termed liquid-liquid phase separation (LLPS), a well-known concept from the field of physical chemistry. When macromolecules reach their solubility limit, they can phase separate into a dense phase, co-existing with the more dilute cytosol (Hyman et al. 2014, Shin and Brangwynne 2017). Phase separation thus organizes molecules in space and time in a dynamic and concentration-dependent manner without the need of sealed compartments which require dedicated transporters for exchange with the surrounding environment.

1.4 Factors driving cellular phase separation

Phase-separated compartments are constituted by many components. The fine interplay of their constituents influences their assembly and biophysical state (Banani et al. 2016, Guillen-Boixet et al. 2020). Molecular characteristics driving LLPS are intrinsically disordered protein domains (IDRs), low-complexity sequences and interactions between multivalent, globular domains (Banani et al. 2017). Factors affecting condensation include local macromolecular concentrations, pH, salt, osmolytes and metabolites, and post-translational modifications (PTMs). These have mainly been investigated by *in vitro* studies or modeled computationally while some factors have also been shown to drive phase separation *in vivo* (Franzmann et al.

2018, Hofweber and Dormann 2019, Nott et al. 2015, Von Bulow et al. 2019). Especially, crowding can increase local molecular concentrations, which may favor the formation of weak, multivalent interactions between molecules, ultimately driving phase separation (Alberti 2017, Hyman et al. 2014, Woodruff et al. 2017). The growing awareness of subcellular organization in non-membrane-bound compartments and the considerable influence of molecular crowding on their formation by phase separation demonstrated *in vitro* (Banani et al. 2017, Hyman et al. 2014, Walter and Brooks 1995) highlight the relevance to quantitatively characterize this fundamental cellular phenomenon.

1.5 The physical phases of cellular condensates

Inside cells, biomolecular condensates constituting various physical states have been described on the micron scale (Alberti and Dormann 2019). Their biophysical properties vary from true liquid, liquid-, gel-, or glass-like, and even solid states. A *bona fide* liquid phase is defined by fast dynamics of freely diffusing, soluble molecules with weak and transient interactions and no memory of the previous configuration. Phase transitions towards more rigid states show decreasing mobility of their components and increasing strength of the interaction networks. This process can be highly dynamic and functional in order to meet cellular demands. For example, the pericentriolar matrix (PCM) seems to change its physical phase during cell cycle. It first forms liquid-like assemblies that grow at the onset of mitosis and transition into a gel-like scaffold which can counteract microtubule pulling forces in metaphase. A subsequent brittle state during anaphase has been observed which is followed by disassembly of the PCM (Mittasch et al. 2020, Raff 2019, Woodruff et al. 2017).

Other cellular phases are purely solid with positional order and long-range interactions. In a functional form they represent for example highly structured, *in-vivo* grown protein crystals. *D. punctate* embryos contain a crystalline compartment constituted by glycosylated milk proteins that bind lipids. Thereby, nutrients are stored in a more concentrated way than it would be possible in a liquid phase (Banerjee et al. 2016, Mudogo et al. 2020). However, when phase separation is not regulated tightly, it can lead to thermodynamically stable, solid states in the form of aggregates or amyloid structures which are often connected to neurodegenerative diseases (Alberti and Dormann 2019, Guo et al. 2018, Patel et al. 2015). This irreversible

phase transition is driven by hydrophobic interactions of unfolded proteins or IDRs and can be enhanced by mutations or specific PTMs. For some proteins, *in vitro* experiments have shown that liquid droplets can age and solidify over time (Franzmann et al. 2018, Murakami et al. 2015, Patel et al. 2015). In order to prevent aberrant phase transitions *in vivo*, adenosine tri-phosphate (ATP)-dependent chaperones are employed to preserve the liquid state. Their mode of action involves the stabilization of proteins in an unfolded but refolding-competent state, as they are otherwise prone to misfolding and aggregation. For instance, HSP70, HSP27 and HSPB8 chaperone phase-separating proteins, such as TDP-43 and FUS (Boczek et al 2021, Mateju et al 2017, Yu et al 2021). Physical phases thus need to be actively controlled inside cells, where energy is consumed to preserve the metastable, liquid state of biomolecular condensates (Alberti 2017, Alberti et al. 2019, Brangwynne et al. 2015).

1.6 Investigating molecular architectures of cellular condensates

On the structural level, the variety of molecular architectures constituting cellular condensates is remarkable. As these assemblies are highly sensitive to their physicochemical environment, in-cell methods, in particular cryo-electron tomography (cryo-ET) and cross-linking mass spectrometry (CL-MS), are required to probe their protein interaction networks and molecular architectures, as well as potential formation mechanisms (Zhang and Mahamid 2020). In combination with light microscopy experiments, these methods have revealed that liquid cellular condensates show a spectrum of structural organization. From highly ordered, liquid crystals to structured complexes with disordered linkers, such as the Rubisco complex in the *C. reinhardtii* pyrenoid, and even functional amorphous condensates like the Ede1-containing autophagy compartments in yeast (Rosenzweig et al. 2017, Tarafder et al. 2020, Wilfling et al. 2020). This wide range of un-/structured constituents of cellular phases also hints at complex assembly scenarios (Goetz and Mahamid 2020). In the material sciences the classical concept of crystal growth via monomer addition has been challenged by observations of crystal formation via amorphous, metastable phases observed for biological mineralization (Addadi et al. 2003, De Yoreo et al. 2015). Multiple pathways are therefore also conceivable for the phase separation processes of cellular condensates, especially the ones displaying structured organization. Folded globular proteins can condense into clusters and form

colloid solutions while they can also oligomerize in a repetitive manner to establish biological polymers, such as cytoskeletal filaments. In addition, the specific (physiological) conditions and cellular cues that induce the transition from one physical state to another remain to be exlored. For example, environmental stresses such as nutrient scarcity can cause biomolecular condensation and change the overall biophysical properties of a cell. Such strains can interfere with the underlying, delicate cellular architectures leading to rearrangements of meso-scale macromolecular assemblies and conformational changes of the sub-nanometer protein structures.

1.7 Yeast as a model organism to study nutrient stress

Yeast is a well-established model system for molecular biology and the investigation of conserved protein machineries in eukaryotes. It has been employed to study LLPS by light microscopy in the context of many cellular processes *in vivo* (Franzmann et al. 2018, Fuller et al. 2020, Noda et al. 2020, Oshidari et al. 2020, Wheeler et al. 2016). Yeast is easy to manipulate, has short reproduction times, and, due to its small size, it can provide information on the level of individual cells and whole populations by light microscopy techniques. The two yeast species *Saccharomyces cerevisiae* (*S. cerevisiae*, budding yeast) and *Schizosaccharomyces pombe* (*S. pombe*, fission yeast) separated around 1.1 million years ago and, like other biological systems, have evolved to dynamically cope with and adapt on many levels to environmental fluctuations, harsh conditions and perturbations in order to survive (De Virgilio 2012, Lennon and Jones 2011, Toone and Jones 2004). Yeast cells can adjust their metabolism, growth rates and change their morphologies upon external strains such as heat shock (De Virgilio et al. 1990, Meaden et al. 1999), osmotic and oxidative stresses (Hohmann 2002, Jamieson 1998). Moreover, they transition into dormancy upon nutrient scarcity. This dormant state is reversible and characterized by low metabolic activity upon starvation conditions. The starved state depends on the type of nutrient limitation (Klosinska et al. 2011, Winderickx et al. 2003). For instance, the whole proteome can change tremendously upon challenging nutrient conditions in both *S. pombe* and *S. cerevisiae* (Marguerat et al. 2012, Murphy et al. 2015).

In particular, in *S. cerevisiae* glucose depletion induces a reduction in transcription and mRNA degradation (Jona et al. 2000), inhibition of translation (Ashe

et al. 2000, Castelli et al. 2011) as well as alteration of autophagy (Lang et al. 2014, Mejlvang et al. 2018, Weber et al. 2020). Metabolites, including ATP, are rapidly depleted within 1 h of glucose starvation (Weber et al. 2020). In this low energy state, endogenous components are subjected to vacuolar hydrolysis and beta-oxidation in order to provide energy for a minimal set of metabolic actions required for survival. Thereby plasma membranes are internalized to catabolize membrane proteins and lipids. In addition, lipases hydrolyze triacyl glycerides (TAGs) in lipid droplets (LDs) to free fatty acids for beta-oxidation at the inner mitochondrial membrane (Weber et al. 2020). This can also be observed on a structural level at the LD's periphery where crystalline layers of sterol esters form upon glucose restriction (Rogers et al. 2021).

Nutrient scarcity also changes organelle morphologies in yeast. Mitochondria fission into smaller, spherical compartments upon glucose starvation in *S. pombe* and *S. cerevisiae* (Bagamery et al. 2020, Liu et al. 2019, Zheng et al. 2019). Furthermore, *S. cerevisiae* vacuoles fuse and swell upon glucose depletion similarly to what has been observed under hypo-osmotic stress (Li and Kane 2009). *S. pombe* vacuoles are small and spherical under ideal growth conditions. Upon hypo-osmotic stress they rapidly fuse occupying more space to keep the cytosol isotonic (Bone et al. 1998).

1.8 Solidification of the yeast cytosol upon energy depletion

One strategy of unicellular organisms to promote survival of unfavorable conditions is the adjustment of the physical properties of the cytosol, for example in the form of spores or seeds (Lennon and Jones 2011). A particularly striking example of phase transition inside cells is the solidification of the yeast cytosol induced by energy depletion (ED) (Joyner et al. 2016, Munder et al. 2016). Under experimental conditions, ED is achieved through inhibition of glycolysis with the glucose analog 2-Deoxyglucose (2-DG) and suppression of ATP production in the respiratory chain with Antimycin A. This leads to a reduction of cellular ATP levels below 1 % (Serrano 1977, Takaine et al. 2019). Yeast cells likely encounter similarly challenging environments in their natural habitats (De Virgilio 2012). Energy depletion affects yeast cells in several ways. It leads to cytosolic acidification measured by endogenously expressed, pH-sensitive, fluorescent proteins (Joyner et al. 2016, Munder et al. 2016). ED also induces a reduction in cell volume of around 7 % and decreases

the mobility of organelles, endogenous macromolecules and foreign tracers probed by single particle tracking of fluorescent fusion proteins (Joyner et al. 2016, Munder et al. 2016) (Figure 2). In addition, the formation of supramolecular protein assemblies was observed upon ED and visualized using fluorescence light microscopy and room temperature electron tomography (Munder et al. 2016, Marini et al. 2020). The reduced particle dynamics suggested a transition from a liquid to a solid-like state with increased mechanical stability. This was further investigated by spheroblasting experiments, which revealed no deformation of energy-depleted cells upon enzymatic cell wall removal. In comparison, this treatment relaxes cells into spherical shapes under control conditions. Atomic force microscopy measurements of spheroblasted cells also confirmed increased stiffness (Joyner et al. 2016, Munder et al. 2016).

The question on how the previously described solidification is established upon ED remains elusive. The gain in mechanical stability was suggested to be caused by either a general increase in molecular crowding or to be constituted by the self-assembly of proteins into dense compartments that collectively establish solid-like physical properties (Joyner et al. 2016). For *S. pombe* an overall increase in mass density has been observed by optical diffraction tomography upon lowering intracellular pH, which was employed to mimic energy depletion conditions (Abuhattum et al. 2018). Upon ATP depletion increased cytosolic viscosity was described by fluorescence recovery after photobleaching (FRAP) experiments and suggested to be caused by glycogen and trehalose production which adds to cellular crowding (Persson et al. 2020). Furthermore, metabolomics experiments revealed that within 1 h of glucose depletion, proteasomal degradation does not play a role in ATP generation and that autophagy processes only start to contribute cellular ATP after several hours of nutritional stress (Weber et al. 2020, Adachi et al. 2017). This suggests that within 1 h of ED, protein abundances stay the same but a spatial reorganization of the proteome is taking place. These observations together with the described energy depletion-induced reduction in cell size, suggest a general increase in molecular crowding which potentially drives the liquid-to-solid phase transition. It may also influence local phase-separation behavior and likely influences biomolecular condensation.

Aside from the influence of molecular crowding on the cytosolic properties, the decrease in ATP levels upon ED might also contribute to solidification by driving

self-assembly of proteins into condensed phases. It has been shows that ATP functions not only as a provider of energy, but it also acts at millimolar concentrations as a biological hydrotrop (Patel et al. 2017, Traut 1994). Under normal nutrient conditions the cellular concentration of ATP is around 2 mM (Koc et al. 2004), keeping protein solutions soluble, while a decrease in ATP levels reduces their solubility.

Furthermore, the cytosolic pH of around 7.4 in normal nutrient conditions (Joyner et al. 2016) is rapidly and reversibly regulated by the glucose metabolism, in particular by the vacuolar ATPase. This proton pump requires energy to maintain the acidic milieu inside vacuoles (Dechant et al 2010). Thus, cytosolic acidification, which was documented to accompany energy depletion in yeast (Joyner et al. 2016, Munder et al. 2016), is likely caused by the inactivity of the vacuolar ATPase. The observed drop in cytosolic pH can change protein surface charges and thereby might also be a driver of biomolecular condensation or oligomerization in concert with increased local molecular crowding (Munder et al 2016, Petrovska et al 2014).

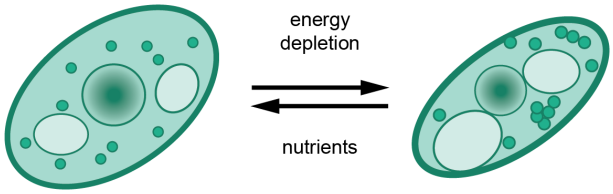

Figure 2: Adaptation of yeast cells to nutrient conditions. The schematic illustrates how energy depletion induces a decrease in cell volume, changes in organelle morphologies and condensation of smaller particles. This cytosolic reorganization is reversible once nutrients are supplied. Figure inspired by Marini et al. 2020.

1.9 Nutrient-dependent condensation of metabolic enzymes

In yeast, a surprising number of proteins involved in metabolism and stress response form cytosolic foci displaying assembly and dissolution based on nutrient-specific availability (Franzmann et al. 2018, Narayanaswamy et al. 2009, Noree et al. 2019a, Noree et al. 2010b, Park and Horton 2019, Prouteau and Loewith 2018, Stoddard et al. 2020). Indeed, protein sequences have evolved very close to protein self-assembly in *E. coli*. This was shown by single point mutations that can lead to polymerization *in vivo* via heterologous expression in yeast (Garcia-Seisdedos et al. 2017). Thus, it is not surprising that upon unpredictable environmental conditions such as nutrient stress, several metabolic enzymes also have been shown to form highly-ordered filaments with varying molecular organization (Park and Horton 2019, Prouteau and Loewith 2018). For instance, upon nutrient scarcity in *S. cerevisiae* the asparagine synthetase paralogs Asn1p and Asn2p co-assemble into a common filament (Noree et al. 2010a, Noree et al. 2019b) and the acetyl-CoA carboxylase forms large self-assemblies (Shen et al. 2016). Other yeast proteins that polymerize upon nutritional stress are septins in *S. pombe* (Heimlicher et al. 2019, Liu et al. 2019) and the eukaryotic translation initiation factor 2B (eIF2B) in *S. cerevisiae* which forms filaments upon energy depletion, protecting it from degradation and indirectly inhibiting translation (Marini et al. 2020). Upon cytosolic acidification, which is inducible via glucose starvation, proteins such as the glutaminase 1 (Gln1 (Petrovska et al. 2014)) form filaments. In comparison, enzyme filamentation can also be induced by metabolites. In *S. cerevisiae* the actin-fold protein glucokinase 1 (Glk1) polymerizes at high cellular concentrations upon glucose addition. In the formed filaments, Glk1 gets trapped in a closed, ligand-bound conformation which is not active and prevents ATP-dependent sugar phosphorylation. Here, filament formation is a regulatory mechanism which counteracts a toxic imbalance between the early steps of glycolysis which consume ATP and the subsequent steps which produce it (Stoddard et al. 2020).

In all these cases, oligomerization is reversible upon stress relieve. Filamentation is suggested to be a general mechanism in order to control enzyme activity and cellular homeostasis upon environmental strains. Polymerization of folded, inactive proteins protects and stores them in their functional conformations and allows rapid re-entry into an active state once stress is relieved. However, the described filaments have

so far mainly been studied in labeled or mutated, over-expressed systems and their structures determined in isolation. It remains to be explored whether they also polymerize under more native conditions and what the underlying filament formation processes are. Future in-cell structural biology studies may decipher whether they entail classical growth by monomer addition, liquid demixing, a transition via intermediate physical phases such as an amorphous state, or other types of coacervation (Goetz and Mahamid 2020).

1.10 The role of type I fungal fatty acid synthase in yeast lipid metabolism

Lipid biosynthesis is essential for the metabolic state of a cell. The fungal type I fatty acid synthase (FAS) is a crucial protein complex in the lipid metabolism of yeast. It catalyzes the formation of long-chain fatty acids which are important building blocks for membranes, energy storage in the form of TAGs in LDs or precursors of second messenger molecules (Johansson et al. 2009). Due to its particular structural signature and thermal stability, FAS has been employed early for structural studies using negative-staining EM and X-ray crystallography (Lynen 1980, Oesterhelt et al. 1969, Stoops et al. 1992). This 2.6 megadalton multienzyme complex exhibits a D_3-symmetric barrel-shaped architecture with two half domes and a central alpha helical wheel (Figure 3). Both alpha wheel and half dome are comprised of each six FAS1/β and FAS2/α subunits. One half dome contains six catalytic sites between which substrate and intermediates are shuttled by the dynamic acyl carrier protein (ACP). Three ACPs are confined to each half dome, establishing close local proximity between the catalytic sites and this substrate shuttling domain to facilitate efficient catalysis of fatty acid elongation. Upon activation of the ACP via attachment of a phosphopantetheine moiety via the phosphopantetheine transferase (PPT), fatty acid synthesis is initialized by transferring the acetyl group of the substrate acetyl-CoA on to the ACP. For the production of C_{16}-C_{18} saturated fatty acids, the primed ACP then moves the substrate in the following sequence to the malonyl/palmitoyl transferase (MPT), the ketoacyl synthase (KS), the ketoacyl reductase (KR), the dehydratase (DH), and the enoyl reductase (ENR) (Johansson et al. 2009, Makarova et al. 2020).

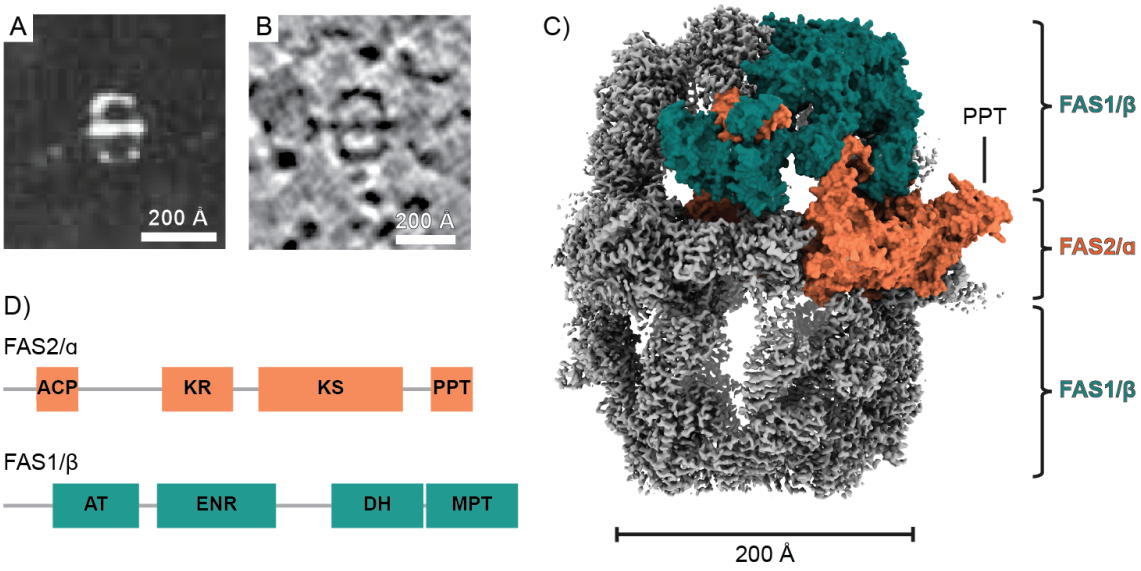

Figure 3: The yeast fatty acid synthase complex. A) Electron micrograph of negatively stained FAS (Lynen 1980). B) 2D slice through a cryo-electron tomogram of the *S. pombe* cytosol, acquired for the present work, depicting the barrel-shaped FAS in its native cellular environment. C) Single-particle cryo-EM reconstruction of *S. cerevisiae* FAS (Joppe et al. 2020) with two individual FAS1/β and FAS2/α subunits represented as molecular surfaces in petrol and orange, respectively. D) Domain organization of the two FAS subunits adapted from (Johansson et al. 2009, Johansson et al. 2008).

The localization of the ACPs is suggested to be linked to the activity of the whole multi-enzyme complex and to be species-dependent. Lack of electron density for the ACP in an X-ray crystal structure has been explained by its dynamics (Jenni et al. 2007), specific localizations have been connected to stalled states where substrate was missing in the sample preparations (Leibundgut et al. 2007) or the inhibitor cerulenin was added (Gipson et al. 2010). Recently, the γ subunit was discovered and revealed varying ACP localizations and two distinct rotational states of FAS in dependence of NADPH concentrations (Singh et al. 2020). Also, species-dependent differences in ACP localization have been observed. For example, in *C. thermophilium* (Kastritis et al. 2017) it is in close vicinity to the catalytic ENR domain or in *T. lanuginosus* the ACP was not observed and thus was suggested to be disordered (Jenni et al. 2007).

Under normal nutrient conditions FAS is evenly distributed within the yeast cytosol but has been shown to condense into distinct foci upon four days of glucose starvation

in *S. cerevisiae* (Suresh et al. 2015). The complex has been confirmed to be still functional but its activity state, as well as structural integrity and arrangement within the condensates, remained elusive. As the polymerization of several metabolic enzymes has been connected to specific functions, in addition to their storage and protection, FAS foci might also display an additional stress-induced purpose.

1.11 Nutritional stress affects translation and ribosome conformations

Ribosomal translation is a crucial step in eukaryotic protein biosynthesis. The ribosome, a large RNA-protein complex decodes mRNA coupled to peptide bond formation. It is constituted by two subunits: the small 40S and the large 60S subunit (Figure 4). Yeast cells are highly crowded with ribosomes that occupy around 20 % of the cytosolic volume and thereby affect the effective concentrations of other biomolecules in a size-dependent manner. In order to estimate nutrient-dependent changes in crowding on a molecular level, cytosolic ribosome concentrations can be used as an approximation (Delarue et al. 2018). Furthermore, ribosomes consume large amounts of resources to produce proteins for cellular homeostasis, proliferation and growth. Several ribosomes can assemble on and translate the same mRNA and thereby organize into higher-order structures, called polysomes (Figure 4 D, (Afonina et al. 2014, Afonina et al. 2015, Zhou et al. 2020)). The intricate interplay between ribosomal RNA (rRNA), ribosomal proteins, mRNA and tRNAs, as well as auxiliary translation factors, tightly regulates each step of the translation cycle which is the most energy consuming cellular process (Lindqvist et al. 2018). Protein synthesis requires energy in form of ATP for initiation and elongation (around 20 % of cellular levels (Buttgereit and Brand 1995)), and GTP for termination (Leibovitch and Topisirovic 2018). It is therefore tightly connected to the metabolic state of a cell, where nutrient limitation can lead to reversible translation shutdown. Upon glucose starvation, polysomes have been shown to disassemble and translation was reduced in *S. cerevisiae* (Ashe et al. 2000, Brengues et al. 2005). However, partial recovery has been observed after 60 min of glucose withdrawal suggesting an upregulated translation of proteins crucial for starvation adaptation (Arribere et al. 2011). Polysome profiling experiments have also revealed polysome disassembly and downregulation of translation within 10 min of energy depletion (Nuske et al. 2020). Translation termination under normal growth conditions results in subunit dissociation by the termination factor Dom34, Hsp70 subfamily B suppressor

1 (Hbs1) and the ATP-dependent factor RNase L inhibitor 1 (Rli 1, corresponding to human ABCE1 (Heuer et al. 2017, Van den Elzen et al. 2014)). However, the ribosomal subunits can also associate in a hibernating state in a nutrient-limiting environment. In this stationary state, fully assembled *S. cerevisiae* 80S ribosomes have a vacant peptidyl transferase center (PTC) lacking tRNAs. It can be protected by different factors such as Stm1 and Lso2 (Van den Elzen et al. 2014, Wells et al. 2020). The latter is suggested to promote a recycling-competent state for rapid translation re-activation upon nutrient supply.

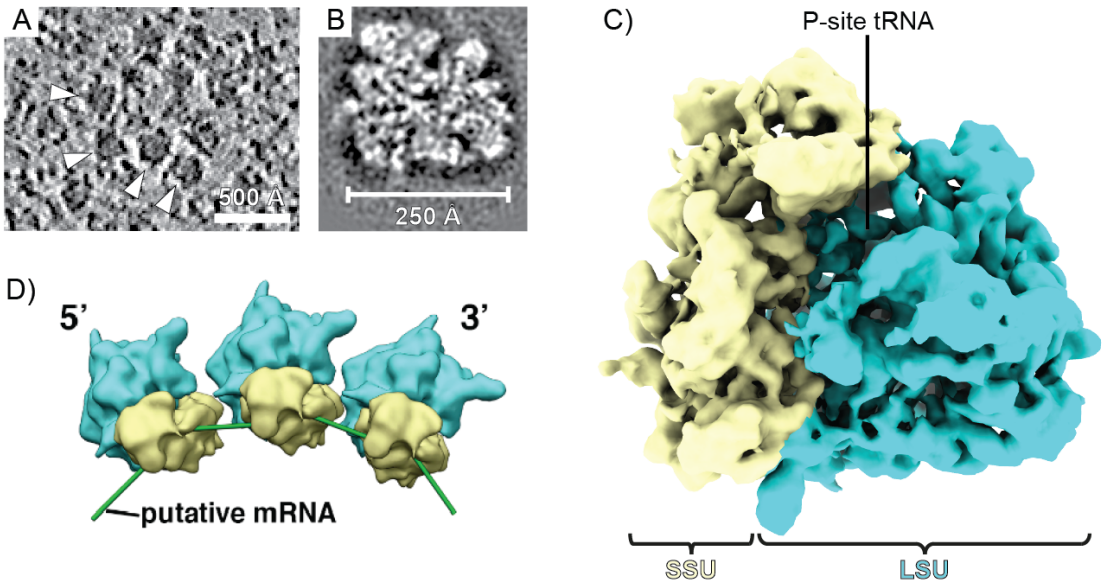

Figure 4: The *S. cerevisiae* ribososome. A) 2D slice through a cryo-electron tomogram of the *S. cerevisiae* cytosol. Dark globular structures are ribosomes (some highlighted by white arrowheads). B) 2D slice through the published ribosome subtomogram average of *S. cerevisiae* (EMDB 4372 (Delarue et al. 2018)). C) 3D visualization of the *S. cerevisiae* ribosome depicted in B. The peptidyl transferase center (PTC) between the small subunit (SSU, yellow) and the large subunit (LSU, cyan) contains a P-site tRNA. D) Polysome arrangement of HeLa cell ribosomes on a single mRNA (green) adapted from Mahamid et al. 2016.

Structural studies can thus provide valuable information on the functional state of ribosomes under stress conditions in the context of this thesis. The *S. cerevisiae* 80S ribosome has been heavily studied by various structural biology techniques. Furthermore, a cryo-ET study has revealed an in-cell ribosome subtomogram average, giving insights on structural configurations in the functional, cellular context of normal nutrient state *S. cerevisiae* (Delarue et al. 2018). To date, there is no

S. pombe 80S ribosome structure available. The nutrient-dependent structures of *S. cerevisiae* and *S. pombe* ribosomes thus still need to be explored, especially in their native environments.

1.12 Visualizing cellular landscapes by cryo-electron tomography

Cryo-electron tomography (cryo-ET) unravels crowded molecular landscapes inside cells (Danev et al. 2014, Pfeffer and Mahamid 2018). The power of such in-cell studies is that they image cellular volumes with the structures preserved in a close-to-native, vitrified state. Thus, cryo-ET provides snapshots of not only specific but all nanoscale macromolecular assemblies in their micron scale pleomorphic habitats (Beck and Baumeister 2016, Mahamid et al. 2016). Unlike other structural biology methods, molecules are not studied in isolation but they are imaged in their functional context capturing even weak or transient interactions and thus providing a more holistic view of the cellular interior. Cryo-ET is a label-free method and can be applied to a large variety of cells, both prokaryotes and eukaryotes. Pioneering cryo-ET studies have visualize liquid-like condensates starting to give unprecedented insights on their underlying architectures exhibiting molecular organization on a spectrum from disordered, amorphous states to highly structured component and even crystalline arrangements (Albert et al. 2020, Bauerlein et al. 2017, Dahlberg et al. 2020, Gruber et al. 2018, Lasker et al. 2020, Rosenzweig et al. 2017, Tarafder et al. 2020, Wilfling et al. 2020, Yasuda et al. 2020, Yu et al. 2021). Recent advances in cryo-ET enable the 3D reconstruction of highly abundant macromolecules at sub-nanometer resolution, while at the same time obtaining information about their local distribution and interaction partners inside a cell (O'Reilly et al. 2020, Tegunov et al. 2021). Cryo-ET can thus provide quantitative structural and spatial details on molecular crowding of large complexes with unique structural signatures inside cells (Delarue et al. 2018).

1.13 The cryo-electron tomography workflow: advances and challenges

In order to visualize macromolecules by in-cell cryo-ET, samples have to be vitrified to preserve their delicate cellular structures, cryo-light microscopy performed for targeted specimen preparations or imaging, and samples thinned via cryo-focused ion beam (FIB) milling to render them electron-transparent. The generated cellular slices, called lamellae, are subsequently imaged in a transmission electron microscope

(TEM) operated at cryo-temperature, in particular at liquid nitrogen temperatures of -196 °C (Figure 5). In the following chapters I will describe the state-of-the-art cryo-ET workflow and point out current challenges that need to be overcome to achieve higher throughput for quantitative studies.

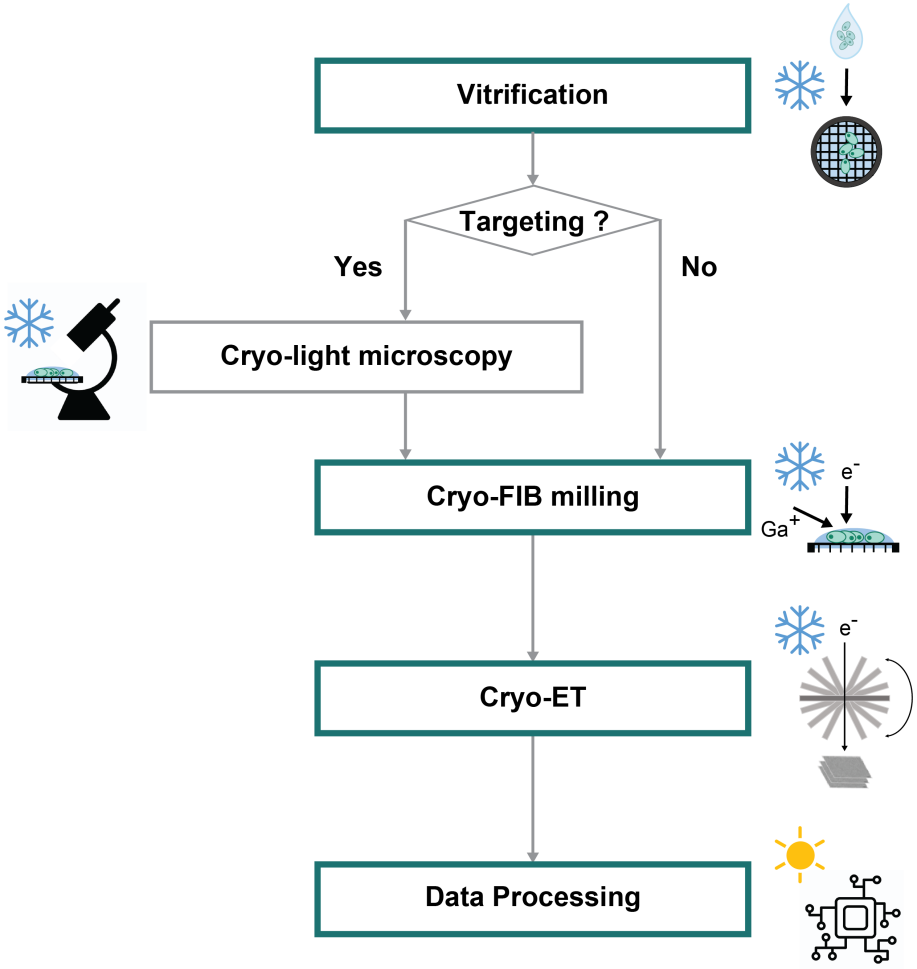

Figure 5: Cryo-ET workflow. Main sample preparation steps are displayed and highlighted in boxes. Optional targeting using fluorescently labeled structures of interest is feasible via cryo-light microscopy (grey box). Figure inspired by Erdmann et al. 2018.

1.13.1 Cryo-sample preparation

Imaging biological samples by cryo-electron tomography requires the preservation of cellular structures and their fine details in a frozen-hydrated state, that is also electron-transparent at a thickness below approximately 300 nm when imaged in a

cryo-TEM. This can be achieved by trapping water molecules, and thus the cells, in a glass-like, termed vitreous, state by either plunge freezing (Dubochet et al. 1988, Dubochet and Mcdowall 1981) or for volumes and samples larger than 5 µm, such as whole organisms or tissues, via high pressure freezing (Dubochet 1995). Both methods prevent the formation of crystalline ice which would destroy the delicate cellular structures. In the case of plunge freezing, cells are applied to a TEM-grid, typically made of metal (e. g., Cu with a mesh of 200 openings per inch) and a holey support foil with a specific mesh size (e. g., R2/1 with circular holes of 2 µm diameter at a spacing of 1 µm). This supports the sample but allows excess liquid to be blotted away from the back (Figure 6). Adherent cells can be guided by micropatterning to grow in the center of grid squares which are easier to access by subsequent TEM imaging or cryo-FIB lamella preparation (Toro-Nahuelpan et al. 2020). Immediately after blotting, cells are vitrified by rapidly plunging the grid in liquid ethane at around -185 °C, cooled with liquid nitrogen, right above its melting point. Henceforth, samples are kept in cryo-conditions, i.e. stored, handled, manipulated and imaged in vacuum at liquid nitrogen temperatures (-196 °C).

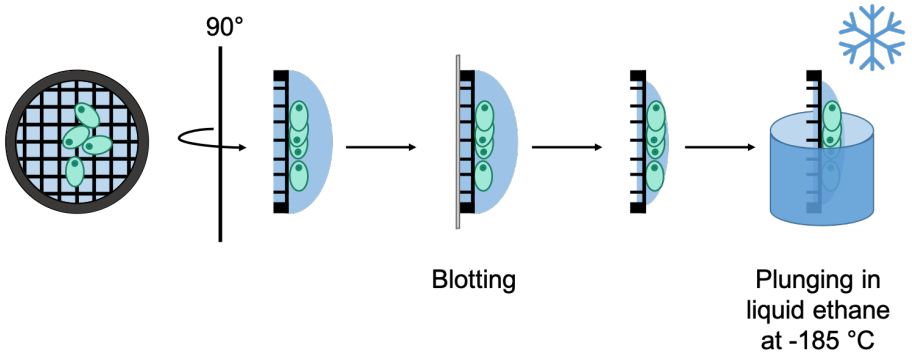

Figure 6: Plunge-freezing cells to preserve their interior structures for cryo-ET. Adherent cells are either grown on grids or cell suspensions are applied right before blotting. Access liquid is removed from the back of the grid and the sample is then immediately plunged into liquid ethane at -185 °C, cooled with liquid nitrogen.

1.13.2 Cryo-correlative light microscopy

In order to visualize and track a specific molecule or event across different scales, cryo-correlative light and electron microscopy (cryo-CLEM) can be employed (Jun et al. 2019, Plitzko et al. 2009, Schorb et al. 2017). Low-abundant or dynamic subcellular structures are fluorescently tagged or stained to achieve precise, site-specific targeting in subsequent sample thinning approaches (Arnold et al. 2016). Fluorescent fiducials, such as microbeads, are externally applied and act as markers for the correlation between different imaging modalities. Several fluorescent dyes and labels can be used at cryo-temperatures as their behaviors have been characterized in detail under these conditions (Tuijtel et al. 2019). The sample is then imaged in a cryo-wide field or confocal fluorescence light microscope (FLM). The resolution limit is determined by the diffraction of light, a trade-off between the objective's numeric aperture, the so-far limited availability and compatibility of cryo-immersion liquids (Faoro et al. 2018), and the working distance which for current state-of-the-art instruments restricts cryo-CLEM to features of interest of a size larger than approximately 400 nm (Arnold et al. 2016, Van Driel et al. 2009). To overcome this limitation, correlative super resolution cryo-CLEM methods are being developed to advance the resolvable feature size closer to the sub-nanometer scale of TEM imaging (Moser et al. 2019, Tuijtel et al. 2019).

Moreover, light microscopy imaging prior to cryo-fixation, which has been implemented in a microfluidic chip, allows time-dependent freezing of a specific event (Fuest et al. 2019). This also minimizes sample transfers as the grid does not have to be moved from the plunger to the cryo-FLM. Transferring vitrified specimen bears the risks of sample damage, de-vitrification and introduction of contaminants such as ice crystals that obscure TEM imaging, which all increase with the number of different instruments and therefore transfers. Built-in solutions for cryo-FLM and cryo-FIB microscopes and hardware improvements for sample loading stations try to prevent such contaminations and handling-induced sample loss (Bieber et al. 2021, Tacke et al. 2021).

For common applications, 3D FLM stacks are collected which are subsequently deconvolved to remove delocalized signal such as out-of-focus noise (Shaw 2006). The z-stacks can then be resliced and are transformed (including scaling, rotation

and translation) based on the matching of fiducials between imaging modalities (Arnold et al. 2016). For example, the signal can be projected on FIB images for site-specific sample thinning and followingly registered with a low magnification map of the lamella recorded in a TEM to guide tomography acquisition (Klein et al. 2021).

1.13.3 Cryo-FIB milling

Whole cells are too thick to be imaged by TEM. Thus, the next step of cellular cryo-ET sample preparation is the step-wise ablation of the vitrified samples to access the underlying ultrastructures. The mean free path, meaning the maximal distance that electrons can traverse through a sample with the least amount of interference, in a 300 kV TEM is around 400 nm (Russo and Passmore 2016a). Thus, samples need to be thinner in order to retrieve the contained information at a sufficient signal-to-noise ratio (SNR) that is otherwise hampered by inelastic scattering events. Serial-sectioning of vitrified samples is feasible with a cryo-microtome, but has the drawback of potential sample deformations (Al-Amoudi et al. 2005). Thus, non-compressing ablation of biological material with a focused ion beam (FIB) of gallium ions (Ga^+) has become the state-of-the-art method (Rigort et al. 2012, Rigort and Plitzko 2015, Schaffer et al. 2015, Schaffer et al. 2017, Villa et al. 2013). In a step-wise manner with decreasing ion beam currents, a thin cellular slice is created with a thickness of around 200 nm, supported by the remaining cellular material (Figure 7). The entire process is monitored and guided by imaging with a built-in scanning electron microscope (SEM). Larger samples are also amenable to cryo-FIB milling. Lamella lift-out techniques allow retrieval of a slab from a high pressure-frozen sample with a micromanipulator, and subsequent thinning to electron transparency (Mahamid et al. 2015, Schaffer et al. 2019). In addition, the waffle method enables lamella preparation from large, high-pressure frozen volumes containing many cells, resolving preferred sample orientations induced by adherence and blotting (Kelley et al. 2021).

One current limitation of cryo-FIB milling is the slow ablation rate of Ga^+ ions which has led to the development of fast-ablating plasma FIB instruments. However, these still need to be adjusted to cryo-workflows (Burnett et al. 2016). Moreover, cryo-FIB milling requires a high level of expertise. To make the technique more accessible,

automation procedures have been established, which require less user supervision and additionally ensure a high degree of reproducibility (Buckley et al. 2020, Kuba et al. 2020, Zachs et al. 2020). However, these software are limited to standard on-grid lamella preparations. More advanced cryo-FIB approaches, such as cryo-FIB SEM volume imaging, cryo-CLEM, lamella lift-out or other future workflows, require more modular solutions (Figure 7). A platform that combines several modules for such cryo-FIB approaches has been co-developed within the scope of this thesis and is presented in chapter 5.1.2 (Klumpe, Fung and Goetz et al. 2021).

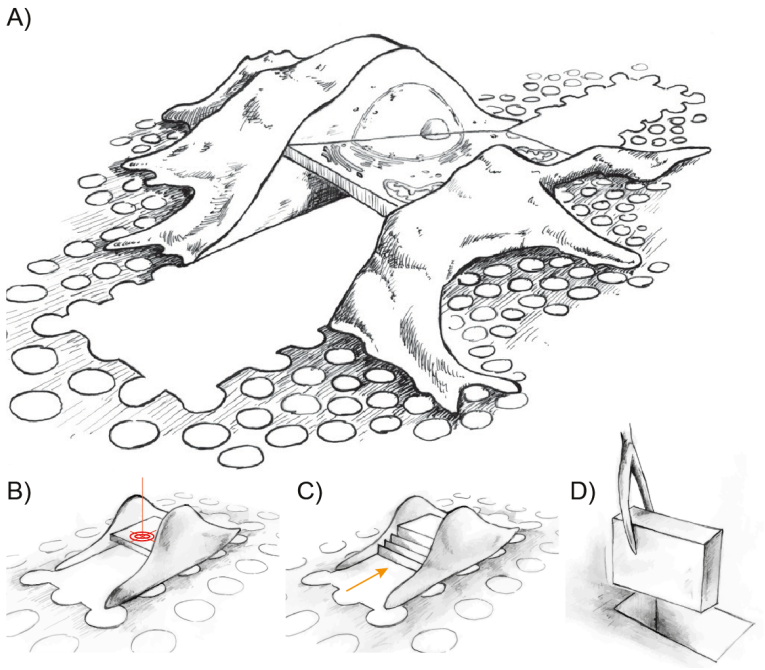

Figure 7: Cryo-FIB milling of vitrified cellular samples. Standard on-grid lamella preparation of a single, eukaryotic cell. B) Site-specific, cryo-light microscopy-guided FIB milling. Targeting a particular cellular position is indicated in red. C) Cryo-FIB SEM volume imaging: serial slice removal by the FIB (yellow arrow) and imaging with the SEM from the top. D) Lamella lift-out approach: a micromanipulator removes a slab from bulk cellular material. Drawings kindly provided by Jürgen Plitzko and figure adapted from Villa et al. 2013 and Klumpe, Fung and Goetz et al. 2021.

Another important consideration for cryo-FIB milling is sample stability. Vitrified samples demand gentle handling as the thin layer of ice and the support can easily fracture, rendering the frozen cellular sample instable. Also, vitrification can cause internal stresses and differential compression due to varying heat expansion coeffi-

cients of grid and support materials (Naydenova et al. 2020, Russo and Passmore 2016b, Thorne 2020). The tension can be released upon milling leading to lamella bending or even breakage. Micro-expansion joints cut into the peripheral parts of a vitrified cell prior to lamella preparation relieve stress from the sample (Wolff et al. 2019).

First generation commercial cryo-FIB microscopes struggle with imperfect vacuum and do not contain a cryo-trap to prevent condensation of amorphous ice from the remaining partial water vapor on the vitrified sample. This currently limits microscope time after the last milling step has been completed to around 1 h (for condensation rates of 50 nm/h) and thus affects the number of lamellae that can be prepared on a single grid during one session. It also hampers more advanced workflows which would benefit from automated overnight operations. Hardware improvements will likely resolve these issues in the future (Tacke et al. 2021).

1.13.4 Image formation in transmission electron microscopy

In transmission electron microscopy, electrons traverse through a specimen and are subsequently captured on a detector. The thinner a sample, the more incident electrons are transmitted and do not interact with the biological material, while a fraction of electrons is scattered by the Coulomb potential of the underlying atoms. Scattering can be elastic (without energy loss) or inelastic, in which case energy is transferred to the specimen. TEM images are thereby formed via amplitude and phase contrast (Orlova and Saibil 2011). Amplitude contrast is caused by electrons that are absorbed by the sample or deflected by the objective aperture located at the back-focal plane of the microscope's objective lens. This modulates the intensity of the incident beam. As vitrified, biological specimen are composed of light atoms (C, H, N, O, S and P) and therefore hardly absorb any electrons, amplitude contrast contributes very little (around 7 % (Penczek 2010)) to the image formation process. These sample types can be approximated as weak phase objects (Glaeser 2013) that elastically scatter a fraction of the electrons which interfere at the image plane with the unscattered electron beam resulting in phase contrast. The induced phase shift of the electron wave is close to zero when the sample is imaged in focus, causing low image contrast. Changing the focus of the objective lens induces a phase shift that results in improved image contrast. The modulation of contrast is described

by the contrast transfer function (CTF). This equation models several factors of image formation, including defocus, phase shift and optical aberrations. The CTF can be fitted to the radial average of a TEM image's Fourier spectrum and thus its modulations, such as defocus values, are determined and the image can subsequently be corrected.

1.13.5 Cryo-ET acquisition and tomogram reconstruction

In cryo-electron microscopy, 2D projection images of (biological) samples are collected. For cryo-electron tomography (cryo-ET) the specimen, such as a cryo-FIB milled lamella, is physically tilted and projections are collected at varying, incremental angles relative to the electron beam in order to sample a 3D cellular volume at multiple orientations. This creates an inherent limitation of cryo-ET as it suffers from missing information in form of a wedge in Fourier space at the angles below and above around $\pm$ 60° which cannot be reached due to increased sample thickness and the finite tilt range of the grid holder on the microscope stage.

As frozen-hydrated, biological specimens are highly radiation sensitive, cryo-ET is usually performed with low electron doses, distributed over several tilts via different acquisition schemes (Hagen et al. 2017). In general, cryo-EM is operated in so-called "low dose mode" which results in a low SNR but prevents electrons from damaging the sample early-on. This preserves the high-frequency information, in particular fine structural details, which are required for high-resolution structural analysis. Therefore, dose-symmetric tilt schemes are employed in cryo-ET that start from 0° of the sample, perpendicular to the electron beam, resulting in the shortest mean free path for electrons to traverse through the sample. Consequently, the least scattering events happen, which improves the SNR and sustains high-resolution features as the sample has not yet suffered from radiation damage. Subsequent projections are collected at increasing tilts with accumulating electron doses.

Recent technological developments have further advanced cryo-ET and significantly improved SNR, contrast, and resolution in cryo-electron tomograms. Direct electron detectors record movies for each tilt and subsequent computational alignment of individual movie frames account for beam-induced movement and stage drift which otherwise blur the images (Brilot et al. 2012, Li et al. 2013). In addition, energy

filters reduce noise as they remove unwanted, inelastically scattered electrons based on their wavelength before they can hit the detector (Fukuda et al. 2015). Furthermore, phase plates have been developed to improve image contrast. In particular, the Volta potential phase plate (VPP) has been proven to be practical in identifying structural features and visual segmentations (Danev et al. 2014, Danev et al. 2017, Mahamid et al. 2016). The VPP is located at the back-focal plane and conditioned by the electron beam to generate an electrostatic potential that ideally leads to a 90° phase shift of the scattered electron wave which results in improved contrast when it is recombined with the unscattered electrons at the image plane (Orlova and Saibil 2011). However, it has been observed that VPPs hamper high-resolution signal and are prone to unwanted charging effects and electron scattering (Buijsse et al. 2020, Turonova et al. 2020). Further promising developments of laser phase plates will likely enable stable and tunable phase shifts for reliable enhancement of image contrast in cryo-ET (Schwartz et al. 2019).

Another challenge for cryo-ET is inconsistent vitrification of the sample. Areas that are not properly vitrified often stem from too thick samples or cellular features such as nuclei in eukaryotic cells. Devitrification can occur during transfers between microscopes when samples are not sufficiently cooled. Here, also ice contaminations on top of the sample can get introduced, leading to ice reflections and obscuring areas to be imaged. They also limit the information that can be retrieved from the biological sample. The collection of tomograms on FIB-milled lamellae can be further constricted by the remaining cellular material that is holding the cellular slice (cf. Figure 7); if the lamella is not perfectly aligned with the TEM's tilt axis, these areas come into the field of view at higher tilts and thus do not allow data collection in their vicinity.

Another challenge in cryo-ET is the small sample size. A tomogram usually represents less than 1 % of the volume of a whole cell and thus high throughput is required to achieve datasets for quantitative analysis. Advanced, batch acquisition schemes are being developed and faster and better performing cameras employed to overcome this obstacle and gain more output from traditionally low-throughput cryo-ET (Mastronarde 2005, Mastronarde 2018, Myasnikov et al. 2018).

New software developments allow bundled pre-processing of the collected data including estimation of the contrast transfer function (CTF) to inform on data quality and the theoretical resolution limit (Tegunov and Cramer 2019). Batch applications align frames and movie sums of each tilt and generate a 3D reconstruction of the imaged cellular volume utilizing different algorithms, such as weighted back-projection (WBP) or the simultaneous iterations reconstruction technique (SIRT) (Mastronarde and Held 2017).

1.13.6 Data mining

Reconstructed tomograms are grey-scale intensity matrices representing the 3D Coulomb potential of the imaged cellular material. In order to retrieve and interpret the convoluted biological information contained in this voxel-based intensity distribution, image analysis pipelines are required to segment cellular structures and localize particles. The identification and localization of macromolecules in the inherently low contrast tomograms is a major bottleneck of cryo-ET. Thus, software solutions often need to be tailored to specific structures. In many cases, manual inspection and voxel-based classification, called segmentation, are used, at least as a starting point. This visual pattern recognition task is very time-consuming and requires a high level of expertise. The result is influenced by the complexity of the imaged cellular interior and biased by the analyst. Thus, automated solutions need to be developed to capture the quantitative structural and spatial information convoluted in cryo-electron tomograms in a more objective manner.

As a first step in data mining, image contrast can be enhanced by filtering or denoising (Bepler et al. 2020, Buchholz et al. 2019, Tegunov and Cramer 2019). New methods utilize machine learning to generate missing information (Liu et al. 2021, Moebel and Kervrann 2020). Software to identify and trace cellular structures such as membranes or cytoskeletal filaments exist but do not yet provide satisfactory segmentations (Chen et al. 2017, Martinez-Sanchez et al. 2014, Martinez-Sanchez et al. 2020, Stalling et al. 2005).

For determining the coordinates of a protein complex of interest, called particle picking, the traditionally used method is template matching (TM) which is a computationally expensive and time-consuming 3D cross correlation search with an *a*

priori reference structure (Bohm et al. 2000, Hrabe et al. 2012). However, it is limited to easily detectable, large structures such as ribosomes. The advent of deep-learning methods has revolutionized and automated the localization of single particles in cryo-EM (Sanchez-Garcia et al. 2018, Tegunov and Cramer 2019, Wagner et al. 2019). It is now starting to also advance pattern recognition in cryo-electron tomograms (Chen et al. 2017, Moebel et al. 2021). Here, a great challenge is the limited publicly available ground truth data with expert annotations, which is required for supervised training of convolutional neural networks (CNNs). In addition, libraries of ready-to-use CNNs which are already available for single particle cryo-EM are still not provided for data mining in cryo-electron tomograms. Unsupervised networks are also emerging and harbor the potential of determining the coordinates of all structured macromolecules contained in the reconstructed cellular volume (Gubins et al. 2019, Martinez-Sanchez et al. 2020, Zeng et al. 2021).

1.13.7 Subtomogram averaging

In order to retrieve structural information of the localized macromolecules, subtomograms are either extracted from tomograms or reconstructed individually. They are subsequently 3D-aligned and averaged to generate 3D density maps of the underlying structures (Bharat and Scheres 2016, Briggs 2013, Castano-Diez 2017, Galaz-Montoya et al. 2015, Hrabe et al. 2012, Zivanov et al. 2018). Subtomogram averaging thus improves the signal-to-noise ratio of individual particles and reveals overall structural configurations. 3D classifications can further provide details on heterogeneous particle populations inside cells. The achievable resolution depends on the data quality, the particle number and the flexibility of the analyzed structure, the latter of which contributes to the noise of subtomogram averages (Rosenthal and Henderson 2003). Improved per-particle tilt series alignments taking local sample deformations such as doming effects into account (Fernandez et al. 2018, Himes and Zhang 2018, Tegunov et al. 2021) and per-particle 3D CTF estimation and correction (Turonova et al. 2017) have advanced subtomogram averaging. This has led to the recent achievement of sub-nanometer resolution ribosome subtomogram averages with in-cell cryo-electron tomography (Tegunov et al. 2021). Other methods employ different data acquisition and processing schemes which utilize 2D projections. They are developed to improve 3D reconstructions further in order to retrieve high-resolution information together with the functional context provided

by cryo-ET (Faelber et al. 2019, Lucas et al. 2021).

Published high-resolution structures obtained by the myriad of structural biology methods can be docked or modeled into the resulting maps. Depending on the resolution, even atomic models can be built based on the cryo-ET density and the underlying complexes unambiguously identified (O'Reilly et al. 2020, Tegunov et al. 2021). The large number of available structures and maps deposited in public databases, as well as AlphaFold2 models (Jumper et al. 2021) that provide a solution to the long-standing problem of protein prediction, open the possibility to register potentially all protein complexes inside cryo-electron tomograms. This visual proteomics approach combined with automated segmentations of organelles will facilitate our understanding of how macromolecules inhabit cellular landscapes, "socialize" and thereby give rise to specific functions (Bauerlein and Baumeister 2021, Beck and Baumeister 2016). Consequently, higher throughput cryo-ET sample preparation and data mining pipelines will allow to quantify cell-to-cell and subcellular structural variations, as well as the effect of perturbations on local particle distributions.

2 Aim of this work

Cryo-ET is a label-free method that visualizes the internal organization of cells and thereby reveals local distribution of macromolecular complexes in a holistic manner. This enables the development of new approaches to measure molecular crowding in terms of quantitative, spatial and structural information on the variations in crowding at a molecular level in the context of an unperturbed cell. In order to generalize observations from the tomographic scale to whole cell models, cryo-ET has to become a higher-throughput method. To achieve this, I have set the following aims:

1) Establishment of high-throughput cryo-sample preparations and processing pipelines

2) Characterization of nutrient-dependent cytosolic reorganization in unlabeled, wild-type yeast

3) Quantification of molecular crowding in cryo-electron tomograms

4) Structural analysis of macromolecules to assess local variations and nutrient-dependent conformational changes

5) Combining cryo-ET results with light microscopy experiments in live cells to investigate condensation dynamics

In order to test the feasibility of this approach, I analyzed the structural properties of normal and energy-depleted yeast cells. As outlined above, recent studies have shown that during starvation, the biophysical properties of the yeast cytosol are dramatically altered. Thus, the transition of the cytoplasm from a liquid- to a solid-like state in energy-depleted yeast cells represents an appropriate biological model to investigate molecular crowding with cryo-ET. For calculating molecular concentrations that inform on changes in local crowding, the distributions of large reference macromolecules of known structures that pose great effects on local crowding, such as ribosomes, have been mapped and structurally analyzed. Dynamics of fatty acid synthases by light microscopy inform further on the biophysical state of energy depletion-induced structural assemblies into condensates. Changes in protein conformations and distributions together with particle dynamics provide functional insights. Integrating these data in the future to generate whole cell models will

enable a more holistic understanding of the cytosolic organization and the influence of perturbations (Earnest et al. 2017).

3 Materials

3.1 Strains

S. pombe

ID	Background	Genotype	Source
fjm1	K972	Sp h-	Häring lab, EMBL (originally from Paul Nurse)
fjm9	K972	Sp h- FAS2-mCherry: :Nat	Mahamid lab, EMBL, generated by Ievgeniia Zagoriy

S. cerevisiae

ID	Background	Genotype	Source
yjm1	W303	MATα, ade2-1, trp1-1, can1-100, leu2-3,112,his3-11,15, ura3, GAL, psi+	Häring lab, EMBL (originally from Paul Nurse)
yjm6	BY4742	MATα his3Δ1;leu2Δ0;lys2Δ0;ura3Δ0 Fas1-mcherry: :kanMX6	Bukau and Mogk lab, university of Heidelberg (Suresh et al. 2015)

Strains of HeLa, Sum159, *E. huxleyi* and *C. reinhardtii* cells used for automated lamella milling with SerialFIB are described in detail in Klumpe, Fung and Goetz et al. 2021.

3.2 Compounds, buffers and media

Medium	Source
Normal nutrient (NN), full medium for *S. pombe*	YES broth (Formedium)
NN, full medium agar for growing *S. pombe* on plates	YES agar (Formedium)
Glucose control medium for *S. pombe*	EMM Broth without dextrose (Formedium), 20 mM D-Glucose
ED medium for *S. pombe*	EMM Broth without dextrose (Formedium), 20 mM 2-Deoxy-Glucose, 10 µM Antimycin A
Glucose depletion medium for *S. pombe*	EMM Broth without dextrose (Formedium)
Sorbitol medium for *S. pombe*	EMM Broth without dextrose (Formedium), 20 mM D-Glucose, 1.2 M sorbitol
NN, full medium for *S. cerevisiae*	YPD medium (Formedium)
NN, full medium agar for growing *S. cerevisiae* on plates	YPD agar (Formedium)
Glucose control medium for *S. cerevisiae*	Complete supplement mixture (CSM, Formedium), Yeast nitrogen base without aminoacids (Formedium), 20 mM D-Glucose
ED medium for *S. cerevisiae*	Complete supplement mixture (CSM, Formedium), Yeast nitrogen base without aminoacids (Formedium), 20 mM 2-Deoxy-Glucose, 10 µM Antimycin A

Chemical or buffer	Description
D(+)-Glucose monohydrate (Merck)	Dissolved in deionized water at a concentration of 20 %(w/v), sterile filtered (0.2 µm) and stored at +8 °C
2-Deoxy-D-Glucose (Sigma Aldrich)	Stored at +8 °C
Antimycin A from Streptomyces sp. (Sigma Aldrich)	Dissolved in methanol at 1 mM (1000x stock) and stored at -20 °C
D-Sorbitol (Sigma Aldrich)	Stored at room temperature
Concanavalin A (Sigma Aldrich)	Dissolved in PBS at 1 mg/ml and stored at -20 °C
5(6)-Carboxy-2',7'-dichlorofluorescein diacetate (CDCFDA) (Sigma Aldrich)	10 mM stock solution, stored at -20 °C
FM4-64 (invitrogen)	1 mg/mL in DMSO, stored at -20 °C
PBS (Sigma Aldrich)	1x stock prepared by the media kitchen at EMBL, Heidelberg
BSA (Sigma Aldrich)	Stored at -20 °C
Ampicillin (Sigma Aldrich)	Dissolved in deionized water at a concentration of 100 mg/mL and stored at -20 °C

3.3 Equipment

Item	Description
Pelco Easy glow	Glow discharger
Quantifoil R1/2, Cu 200 mesh, holey carbon or SiO_2 film; R1.2/20 Ti 200 mesh SiO_2; R1/4, Au 200 mesh SiO_2	TEM grids
Ultraspec 2100 pro (Amersham Biosciences)	Photometer to measure optical densities (ODs) at 600 nm
Cuvettes, semi-micro PS (ratiobal)	Cuvettes for photometer
Minisart syringe filters 0.2 µm (sartorius)	Filters for sterile filtering solutions
Eppendorf centrifuge 5424R	Centrifuge for up to 2 mL reaction tubes
Megafuge 16 (Thermo Fisher Scientific)	Centrifuge for up to 50 mL falcons
NCU-Shaker mini (Benchmark)	Shaker for liquid cell cultures
MyTemp mini digital incubator (Benschmark Scientific)	Incubator used for yeast agar plates
Thermomixer compact (Eppendorf)	Table top shaker
Whatman filter paper circles diameter 55 mm (GE Healthcare Life Sciences)	Filter paper for plunger
Leica EM GP or GP2	Plunger for vitrification
Titan Krios (Thermo Fisher Scientific)	Cryo-electron microscope
Volta potential phase plate (VPP, Thermo Fisher Scientific, (Danev et al. 2017))	Phase plate for cryo-EM
Quantum post column energy filter (Gatan)	Energy filter for cryo-EM
K2 Summit direct detection or K3 (Gatan)	Camera for cryo-EM
Aquilos Dual beam microscope (ThermoFisher Scientific)	Cryo-FIB SEM microscope
LSM 780 or 880 (Zeiss)	Confocal light microscopes for fluorescence imaging

3.4 Software and databases

Software and databases	Description
Serial EM (Mastronarde 2005, Mastronarde 2018)	Cryo-EM and tomography acquisition
Warp (Tegunov and Cramer 2019)	Cryo-EM data pre-processing
M (Tegunov et al. 2021)	Multi-particle cryo-EM refinement
Amira (version 2020.2, Thermo Fisher Scientific)	Segmentation of EM data
Pytom, tom toolbox (Hrabe et al. 2012)	Python-based toolbox for localization of macromolecules
ImageJ/Fiji (Schindelin et al. 2012)	Platform for biological image analysis
UCSF Chimera (Pettersen et al. 2004), UCSF ChimeraX (Pettersen et al. 2021)	3D structure visualization tools
MATLAB (version 2016b, Matworks)	Programming language and environment
Python (Van Rossum 2020, Van Rossum and Drake 2011)	Programming language and environment
Snakemake (Mölder et al. 2021)	Python-based data analysis workflow tool
Relion 3 (Zivanov et al. 2018)	Cryo-EM structure determination software
MAPS (Thermo Fisher Scientific)	Navigation software for Aquilos Dual beam microscopes
ZEN (black edition, Zeiss)	Software for confocal Zeiss microscopes
Ilastik (version 1.3.3 (Berg et al. 2019, Haubold et al. 2016))	Machine-learning-based image analysis
R (version 3.6.3 (R Core Team 2013)) and Rstudio (version 1.2.5033 (Allaire 2012))	Programming language and environment for statistical computing
EMDB (`https://www.ebi.ac.uk/emdb/`)	Electron microscopy databank
PDB (`https://www.rcsb.org`)	Protein databank

3.5 Code availability

Software	Description	Version date
SerialFIB	https://github.com/sklumpe/SerialFIB/	17.05.2021
3DCT	https://github.com/hermankhfung/3dct https://github.com/hermankhfung/tools3dct	27.05.2021
DeePiCt 2D CNN for compartment segmentations	https://git.embl.de/mattausc/tomo-organelle-detection	15.05.2020
DeePiCt 3D CNN for particle localization, membrane and cytoskeleton segmentations	https://git.embl.de/trueba/3d-unet	28.04.2021
FRAPAnalyser_2.1.0	https://github.com/ssgpers/FRAPAnalyser	28.10.2016
Microscopy Pipeline Constructor (MyPiC)	https://git.embl.de/grp-ellenberg/mypic/-/wikis/home	28.10.2018

4 Methods

4.1 Yeast cell culture

S. pombe and *S. cerevisiae* were recovered from frozen stocks and streaked onto YES or YPAD agar plates, respectively. After incubation at 30 °C for 1-3 days or at room temperature for three days, cells were streaked on fresh agar plates containing respective media. For liquid cultures, single colonies were picked and inoculated in full media or glucose control media with equivalent osmolarity compared to energy depletion media. Initial liquid culture volumes varied between 5-20 mL and were incubated in Erlenmeyer glass flasks with a size fitting 10 times the volume of the culture, shaking at 180-200 rpm and 30 °C overnight (NCU-Shaker mini, Benchmark). Cell densities were measured the next day, if necessary diluted and incubated again, to use yeast cells in their exponential growth phase at $OD_{600} = 0.2\text{-}0.6$.

4.2 Nutritional and osmotic stress of yeast cells

Cell cultures of *S. pombe* and *S. cerevisiae* were nutritionally stressed via medium exchange. For energy depletion, respective media containing 10 µM Antimycin A and 20 mM 2-DG were used. For glucose depletion, respective synthetic media lacking glucose were utilized. Osmotic stress was induced with synthetic medium containing 1.2 M sorbitol and 20 mM D-Glucose. First, 3-5 mL liquid culture in glucose control media were centrifuged at 4000 rpm for 3 min (Megafuge 16, Thermo Fisher Scientific). The supernatant was discarded, the cell pellet was resuspended in 1 mL of energy depletion media and transferred into 1.5 mL Eppendorf tubes. This wash step was repeated three times with centrifugation at 4000 rpm for 3 min (Eppendorf 5424R centrifuge). After final resuspension, the solution was added to the respective depletion medium in order to obtain the desired experimental cell density in an Erlenmeyer glass flask with a size fitting 10 times the volume of the culture. This was selected as the zero-time point. Cultures were then incubated at 30 °C while shaking at 165-200 rpm, for varying times depending on the experiment.

4.3 Plunge freezing cells for cryo-ET

Yeast cells were vitrified with a Leica EM GP (Leica Microsystems) at liquid nitrogen temperatures. The cell suspension was diluted to an OD_{600} of around 0.3 in respective medium or, following a prior wash step, in PBS containing 5 % or 10 %

BSA as cryo-protectant. TEM grids (Quantifoil R1/2, Cu 200 mesh, holey carbon or SiO_2 film) were glow discharged on both sides for 45 s at 0.26 mbar and 15 mA (Pelco Easy glow) immediately before usage. Within the plunger chamber, 4 µl of the cell solution was directly applied to the grids and excess liquid removed via blotting from the back side of the support for 1-2 s at 22 °C and 99 % humidity. Cells were plunge frozen in liquid ethane ($\sim$ -185 °C) and stored in grid boxes until further usage.

Cryo-samples of HeLa and Sum159 cells were provided by Ievgeniia Zagoriy and Wioleta Dudka, *E. huxleyi* by Zohar Eyal and *C. reinhardtii* by Sven Klumpe and are described in detail in Klumpe, Fung and Goetz et al. 2021.

4.4 Cryo-FIB milling of cellular samples

Sample transfer and subsequent cryo-focused ion beam (cryo-FIB) milling were performed at liquid nitrogen temperatures. Vitrified TEM grids were fixed in autogrids with a cut-out to enable micromachining at shallow angles. Grids were transferred on a shuttle into an Aquilos Dual beam microscope (ThermoFisher Scientific). Cells were sputtered with platinum for 10-20 s (1 kV, 10 mA, 10 Pa). Subsequently, a layer of organometallic platinum was applied by opening the gas injection system (GIS, reservoir at 28 °C) for 8-11 s at a stage height of 10.6-11.6 mm. Lamellae were prepared at a milling angle of 15°-20°. Single cells (HeLa or Sum159) or agglomerations of several cells (*S. cerevisiae*, *S. pombe*, *E. huxleyi*) were thinned either manually or by utilizing the developed automation software SerialFIB (Klumpe, Fung and Goetz et al. 2021) in three steps of rough milling to thicknesses of 5 µm, 3 µm and 1 µm with a constant ion beam voltage of 30 kV and 1 nA, 0.5 nA and 0.3 nA currents, respectively. The scanning electron microscope beam (SEM, 10 kV, 50 pA) was utilized to visually inspect the milling progress between each milling step. Lamellae were fine-milled to a target thickness of around 200 nm by either manual operation at 50 pA or using SerialFIB and the parameters specified in Supplementary Table S1. Milling parameters were optimized empirically. For cryo-TEM imaging, cellular slices were sputtered with platinum for 3-5 s (1 kV, 10 mA, 10 Pa) to render them conductive. The grid was transferred into a dedicated box and stored in a Dewar filled with liquid nitrogen.

Table S1: Optimized milling parameters for lamella generation using SerialFIB. Automation parameters for *S. pombe* micro-expansion joint and fine milling did not provide optimal results and require further optimization (grey). Table adapted from Klumpe, Fung and Goetz et al. 2021.

Sample	**Micro-expansion joints milling**				**Rough milling**				**Optimized fine milling parameters**			
	distance from lamella [µm]	width [µm]	current [nA]	time [sec]	step	nominal lamella thick-ness [µm]	current [nA]	time [sec]	step	nominal lamella thick-ness [nm]	current [pA]	time [sec]
Sum 159	4	0.3	1	30	1	5	1	480	1	400	100	210
					2	3	0.5	210	2	300	50	150
					3	1	0.3	210				
HeLa	4	0.3	1	30	1	5	1	540	1	300	50	360
					2	3	0.5	300				
					3	1	0.3	270				
E. huxleyi	4	0.3	1	120	1	5	1	600	1	800	100	240
					2	3	0.5	480	2	600	50	240
					3	1	0.3	480	3	300	30	240
C. reinhardtii	5	0.5	0.3	60	1	5	0.3	210	1	800	50	90
					2	3	0.3	120	2	800	50	90
					3	1	0.1	120	3	600	50	90
S. cerevisiae	5	0.5	0.3	60	1	5	0.3	210	1	800	50	90
					2	3	0.3	120	2	600	50	90
					3	1	0.1	120	3	400	50	60
S. pombe	4	0.5	1	15	1	5	1	150	1	300	50	140
					2	3	0.5	100				
					3	1	0.3	100				

4.5 Cryo-CLEM workflow for targeted FIB milling

Cryo-CLEM samples were prepared and imaged by Ievgeniia Zagoriy and Wioleta Dudka on a prototype Leica cryo-confocal microscope based on the Leica TCS SP8 system, equipped with a cryo-stage, 50x objective, NA 0.90 and two HyD detectors. As described in Klumpe, Fung and Goetz et al. 2021, z-stacks were collected of HeLa cells on clipped Au SiO_2 or Ti SiO_2 grids. Prior to plunge freezing, cells were stained with MitoTracker Green FM (Thermo Fisher Scientific), BODIPY 558/568 (Thermo Fisher Scientific) and Crimson Microspheres applied (1.0 µm diameter, Thermo Fisher Scientific). Laser excitation at 488 nm was used to detect BODIPY at 500-545 nm, excitation at 552 nm to detect MitoTracker at 561-630 nm and microbeads at 673-731 nm. Grids were transferred to the cryo-FIB SEM microscope (Aquilos, ThermoFisher Scientific) and SEM and fluorescence overview images were matched in 2D using the software MAPS (Thermo Fisher Scientific). Grid positions with individual cells located in the center of grid squares that also encompass evenly distributed fiducials on the grid squares were chosen for 3D correlation of microbeads in 3D FLM volumes and SEM images using 3DCT (Arnold et al. 2016). The calculated transformations were rotated to match the FIB view and adjusted to optimize the correlation. Lipid droplets were then selected and projected onto FIB images. FIB images and corresponding 3DCT outputs were imported into SerialFIB and targeted lamellae were prepared via rough and fine milling as described above. Post-milling correlations were performed in 3DCT utilizing new features developed by Herman Fung including masking of the FLM volume to the size of the SEM lamella and generation of individual FLM slices (along the FIB y-axis) with a thickness of 300 nm. Their maximum intensities were projected onto SEM images and TEM overviews of the prepared lamellae in Fiji using BigWarp (Bogovic et al. 2016, Schindelin et al. 2012) to guide tomography acquisition and compare the fluorescence signal of lipid droplets and beads with the structural signatures in the TEM projections. Deformations of the specimens in the FIB, such as warping or doming effects, were analyzed by Herman Fung using bUnwarpJ (Sorzano et al. 2005). Elastic registration of FIB images of the same grid positions before and after milling were performed and broken squares or ice contaminations were masked out.

4.6 Cryo-FIB SEM volume imaging

Cryo-samples of Sum159 and HeLa cells were subjected to cryo-FIB SEM volume imaging. Cellular slices were ablated in 100 nm steps with "rectangular cross-section" patterns using the FIB operating at 30 kV, 0.5 nA for 10-20 s. SEM data were collected at 5 kV, 50 pA, a dwell time of 1 µs, and line integration of 16, which resulted in a dose of 0.464 $e^-/\mathring{A}^2$ per image (Goggin et al. 2020). Images were acquired with dimensions of 3072 x 2048 on an Everhart-Thornley detector (ETD) and a pixel size of 10.377 nm and 19.271 nm for Sum159 and HeLa cells, respectively. In total, a volume of 14.3 µm x 2.0 µm x > 13.0 µm of Sum159 and 25.9 µm x 6.2 µm x > 16.0 µm of HeLa cells was ablated and imaged.

SEM image stacks were postprocessed using a python-based script which is available on the SerialFIB GitHub repository (s. code availability 3.5). The following steps were performed: cropping to the FIB-milled area using Fiji (Schindelin et al. 2012), removal of curtaining artifacts with pywt (Spehner et al. 2020) by wavelet decomposition and Gaussian blurring of the vertical component (sigma = 6), charge compensation by masking with a Gaussian-blurred, two times eroded image, and local contrast enhancement by limited adaptive histogram equalization with a slope of three in Fiji (CLAHE, (Zuiderveld 1994)). With the SIFT algorithm (Fiji, (Schindelin et al. 2012)) images were aligned and stretched in y by 1/sin (52°) to compensate for image distortion by the angle between FIB and SEM beams. Lipid droplets and the nucleus in Sum159 cells, as well as lipid droplets and fiducial microbeads in HeLa cells were manually segmented in cryo-FIB SEM volumes using Amira 2020.2 (Thermo Fisher Scientific).

For the Hela cell sample, the cryo-FIB SEM volume was registered to the cryo-FLM volumes by Herman Fung in the following steps: centroids of lipid droplet and fiducial bead segmentations were extracted by connected-component labeling in Matlab (Mathworks) and iteratively fitted to 1D and 2D Gaussian curves in 3DCT (Arnold et al. 2016). Points (n = 133) within cryo-FLM volumes of lipid droplets and fiducial beads were fitted to 2D projections of the cryo-FIB SEM segmentations in 3DCT. An affine transform between the extracted cryo-FIB SEM and cryo-FLM points was calculated in OpenCV using three different approaches (RANSAC, L-BFGS-B-based local minimization starting from the TEASER algorithm (Heng et al. 2020), basin-

hopping coupled to L-BFGS-B-based local minimization). A python-based script to perform the registration is available on the SerialFIB github repository (s. code availability 3.5).

4.7 Cryo-ET data acquisition

Autogrid-clipped grids containing lamellae were loaded under liquid nitrogen into a cassette and transferred via a capsule into a Titan Krios microscope (Thermo Fisher Scientific). During loading, grids were orientated in a way that the lamellae were aligned with the milling direction perpendicular to the tilt axis of the microscope. The transmission electron microscope equipped with a Quantum post-column imaging energy filter was operated at 300kV in EFTEM, in zero-energy loss and dose-fractionation mode. The different yeast datasets were collected with varying cryo-ET acquisition parameters (Supplementary Table S2). Depending on the direct electron detector, tomograms were collected at 42,000x or 26,000x magnification and a resulting calibrated pixel size of 3.3702 Å or 3.425 Å for K2 Summit and K3 (both Gatan), respectively. Tilt series were collected using automation scripts in SerialEM, at 2-4 µm underfocus (Mastronarde 2018, Weis and Hagen 2020). Starting from the lamella pre-tilt, movies were collected at each tilt in 2-3° increments for up to ± 64° in a dose-symmetric fashion (Hagen et al. 2017) with a constant dose per image resulting in a maximal total dose of 147 $e^-/\mathring{A}^2$. Defocus-only (DEF) tomograms were collected with a 70 µm objective aperture. A Volta potential phase plate (VPP, Thermo Fisher Scientific, (Danev et al. 2017)) was used after conditioning for around 5 min.

Table S2: Cryo-ET data acquisition of yeast cells under different nutritional conditions and cryo-samples utilized for benchmarking SerialFIB on-grid lamella preparation. Data collection parameters including the number of sessions (#), tomograms (tomo) and usage of a Volta potential phase plate (VPP) are summarized. For all tilt series, a dose-symmetric tilt scheme was used (Hagen et al. 2017). Defocus-only data for *S. cerevisiae* NN was provided by Matteo Allegretti (Allegretti et al. 2020) indicated by (1).

Sample	**#**	**VPP**	**pixel size [Å]**	**tilt range [°]**	**starting tilt [°]**	**tilt step [°]**	**total dose [e-/Å²]**	**thick-ness [nm]**	**under-focus [µm]**	**Tomo**
S. pombe NN	1	N/Y	3.3702	50 to -50	0	2	120	80-390	2 to 4 in steps of 0.5	36
	2	Y	3.3702	50 to -50	0	2	108	110-300	2 to 4 in steps of 0.5	23
	3	Y	3.3702	58 to -42	8	2	104	200-400	2 to 4 in steps of 0.5	39
	4	Y	3.3702	50 to -50	0	2	102	220-390	2 to 4 in steps of 0.5	7
	5	N	3.425	64 to -50	10	2	121	130-470	2 to 4 in steps of 0.5	7
	6	Y	3.3702	60 to -44	8	2	116	150-430	2 to 4 in steps of 0.5	26
S. pombe 1 h ED	1	N	3.3702	48 to -62	-12	2	116	95-485	3 to 4 in steps of 0.25	45
	2	Y	3.3702	60 to -44	8	2	111	175-400	2 to 4 in steps of 0.5	32
	3	Y	3.3702	54 to -62	-10	2	120	120-270	3 to 4 in steps of 0.25	21
	4	Y	3.3702	48 to -60	-12	2	125	135-430	2 to 4 in steps of 0.5	19
S. pombe 3.5 h ED	1	N	3.425	62 to -48	12	2	116	190-520	2 to 4 in steps of 0.25	35
	2	N	3.425	62 to -48	12	2	117	260-520	2 to 4 in steps of 0.25	41
S. pombe 17 h ED	1	N	3.3702	60 to -48	12	2	117	215-485	3 to 4 in steps of 0.25	34
S. pombe 4 d glucose depletion	1	N	3.425	48 to -58	-12	2	111	205-410	2 to 4 in steps of 0.25	31
S. cerevisiae NN	1	N (1)	3.3702	50 to -64	-13	3	147	170-350	2.5 to 4 in steps of 0.25	10
	2	Y	3.3702	60 to -50	8	2	111	190-340	2 to 4 in steps of 0.5	30
	3	Y	3.3702	50 to -62	-10	2	124	160-310	2.5	24
S. cerevisiae 1 h ED	1	N	3.3702	48 to -62	-12	2	120	130-295	3 to 4 in steps of 0.25	29
	2	Y	3.3702	48 to -60	-8	2	121	160-400	2 to 4 in steps of 0.5	33
S. cerevisiae 6 h ED	1	N	3.425	48 to -62	-12	2	112	190-480	2 to 4 in steps of 0.25	47
	2	N	3.425	62 to -48	12	2	116	190-370	2 to 4 in steps of 0.25	9
HeLa	1	Y	3.3702	50 to -48	0	2	107	100-450	2.5 to 4.5 steps of 0.5	37
Sum159	1	Y	3.3702	52 to -64	-12	2	134	70-410	2 to 4 in steps of 0.25	25
E. huxleyi	1	N	2.129	62 to -50	12	2	133	175-470	2.5 to 4.5 in steps of 0.25	28

4.8 Tomogram reconstruction

Tilt movie frames were aligned using a SerialEM plug-in (Mastronarde 2018). Tomograms were initially reconstructed in etomo (IMOD/4.9.4 software package (Mastronarde and Held 2017)) for visual inspection and particle picking. For this purpose, four times binned tilt series were filtered by Fourier cropping according to the accumulated dose utilizing the mtffilter function (IMOD/BETA4.10.12 (Mastronarde and Held 2017)). Dose-symmetric tilt stacks were sorted by tilt angle using a python script. Tilts (movie sums) were then aligned using patch tracking or via platinum fiducials which were deposited on top of the lamella during sputtering after FIB milling. Tomograms were reconstructed using weighted back-projection. Tomogram visualization and thickness measurements were performed in 3dmod (IMOD, (Mastronarde and Held 2017), cf. Supplementary Table S2).

4.9 Tomogram segmentation

Ground truth annotations of cellular features and compartments including organelles, cytosol, membranes, ED filaments and ED FAS condensates were performed in Amira on four times binned tomograms (version 2020.2, Thermo Fisher Scientific). Approximately every 5^{th}-15^{th} slice was annotated and 3D segmentations calculated via interpolation and subsequent manual cleaning.

DeePiCt 2D CNNs for organelles and cytosol were based on the U-net architecture (Ronneberger et al. 2015) with a depth of $D = 5$ and initial features $IF = 16$. Input tomograms were four times binned and preprocessed via amplitude spectrum matching to the tomogram depicted in Figure 18 A with a low-pass cut-off at 350 voxel and smoothening of the sigmoid curve at a cut-off of 20 voxel in Fourier space. Prediction parameters included a patch size of 288 x 288 voxel cropped by 40 voxel to avoid 2D tile stitching artifacts and a z-cut-off of 200 to only predict 100 slices above and below the z center of the tomogram. Predictions were post-processed via assembly of 2D tiles into 3D volumes, filtering with a 1D Gaussian along the z-axis ($\text{sigma} = 5$) to remove false positives and thresholding at 0.7 for the CNN's output score applied.

Calculation of physical 3D volumes was performed in MATLAB (Matworks) by integrating all classified voxel in binary matrixes of the respective cytosol segmentations. Voxel-based volumes were multiplied by pixel sizes and binning factors to calculate

physical sizes of the cellular volume occupied by the segmented compartments.

4.10 Ribosome localization in yeast cryo-electron tomograms

Ribosomes were localized in four times binned tomograms (13.48 Å and 13.70 Å pixel sizes for K2 and K3 data, respectively). Template matching (TM) using the pyTOM toolbox (Hrabe et al. 2012) was performed with the large subunit (60S) of the published *S. cerevisiae* ribosome (EMDB 3228). This reference was scaled to the corresponding pixel size in a box of 128 voxel and a sphere mask with a 100-voxel diameter (smoothed by a Gaussian, sigma = 5) was applied. Using the EMBL high performance cluster, a 3D cross-correlation search over 1,944 Euler angle combinations was performed. In MATLAB (version 2016 b, Matworks), the resulting scoring matrix was multiplied with a lamella mask to remove false positives on top and below the cellular volume in the tomogram. The coordinates corresponding to the top 2,000-3,000 scores with a radius of 10 voxel, contained inside the tomogram with an edge of 20 voxel to the tomogram's boundaries, were extracted. Subsequent visual inspection was performed in four times binned, filtered tomograms (Gaussian, sigma = 3) using tom_chooser (pyTOM toolbox (Hrabe et al. 2012)).

For ground truth generation of ribosomes in each of the 10 VPP and DEF *S. pombe* NN tomograms, utilized to develop DeePiCt, the TM coordinates served as initial input for three rounds of 3D CNN training. The output was inspected in tom_chooser as described above. Remaining, undetected ribosomes were manually picked in up to three rounds in four times binned, filtered (Gaussian, sigma = 3) tomograms using e2spt_boxer.py in EMAN2 (Tang 2019).

Ground truth generation in other datasets (*S. pombe* 1 h ED, *S. cerevisiae* NN and 1 h ED) was performed via TM, manual inspection in tom_chooser (pyTOM toolbox (Hrabe et al. 2012)) and picking with e2spt_boxer.py in EMAN2 (Tang 2019) for up to three rounds as described above.

A 3D CNN for ribosome detection trained in 10 VPP *S. pombe* NN tomograms based on the U-net architecture (Ronneberger et al. 2015) constituted by a depth of D = 2, initial features IF = 4 and batch normalization BN was used to predict ribosomes in all remaining datasets (s. Supplementary Tables S6-S13). Input tomograms were

preprocessed via amplitude spectrum matching (s. above). Predictions were performed with a box size of 64 voxel and post-processed via thresholding at 0.5 for the CNN's output score. Ribosome coordinates were calculated from centroids of clusters with a minimal size of 100 voxel and further intersected with predicted cytosol masks at a contact size of 10 voxel in order to remove false positives in organelles and the extracellular area or within 25 nm distance to specific organelle segmentations (for endoplasmic reticulum (ER) and mitochondria-associated ribosome analysis). Performance analysis via precision and recall was conducted to compare DeePiCt predictions with ground truth annotations and a 10-voxel tolerance radius to identify corresponding particles was used.

4.11 FAS localization in yeast cryo-electron tomograms

FAS particles were picked manually in four times binned, Gaussian-filtered (sigma = 3) tomograms using e2spt_boxer.py in EMAN2 (Tang 2019) because TM with the *S. cerevisiae* FAS map (EMDB 1623) as reference was not successful. For the DeePiCT ground truth dataset (*S. pombe* NN), the coordinates were utilized to train 3D CNNs to localize undetected FAS. The new particles were visually revised with e2spt_boxer.py in EMAN2 and additional FAS manually detected. For all other datasets only manually detected FAS complexes were utilized (cf. Supplementary Tables S6, S9 and S11).

FAS predictions by DeePiCT utilized a 3D CNN based on the U-net architecture with a depth of D = 2, initial features of IF = 16 and batch normalization BN, which was trained on the VPP ground truth dataset for *S. pombe* NN. Predictions were performed with a box size of 64 voxel and post-processed via thresholding at 0.5 for the CNN's output score. FAS coordinates were calculated from centroids of clusters with a minimal size of 500 voxel and further intersected with predicted cytosol masks at a contact size of 10 voxel in order to remove false positives in organelles and the extracellular area. Performance analysis via precision and recall was performed to compare DeePiCt predictions with ground truth annotations and used a 10-voxel tolerance radius to identify corresponding particles.

4.12 Calculation of cytosolic concentrations and volume occupancies

For particle concentrations, the numbers of detected ribosome or FAS particles (localizations described above) were divided by the physical cytosolic or ED volumes that they occupied per tomogram. For cytosolic volume occupancy of filaments in ED tomograms, their respective segmented volumes were converted into physical units of μm^3 (as described above) and divided by the cytosolic volume plus the volume that they occupied.

4.13 Subtomogram analysis

4.13.1 Data pre-processing and subtomogram reconstruction

Raw tomography data were pre-processed in Warp (Tegunov and Cramer 2019) starting from either the frames, utilizing built-in movie alignments to compensate for beam-induced motion, or from movie sums generated via the above described SerialEM plug-in (Mastronarde 2018). Following CTF estimation and tilt stack sorting, tilt series alignments from etomo were imported. Particle coordinates were utilized to reconstruct subtomograms and corresponding CTF models in Warp with unbinned pixel sizes (cf. Supplementary Table S2), and box sizes of 140 x 140 x 140 voxel and a diameter of 350 Å for volume normalization of ribosomes, or 160 x 160 x 160 voxel and a diameter of 400 Å for FAS.

4.13.2 Subtomogram 3D alignments and classifications of ribosomes

Subtomograms were 3D-aligned, averaged and 3D-classified in RELION (version 3.0.7 (Zivanov et al. 2018)). An initial average was generated via 3D classification into a single class with the published *S. cerevisiae* structure (EMDB 3228) as reference, which was scaled to the corresponding unbinned pixel size (cf. Supplementary Table S2), a box size of 140 x 140 x 140 voxel and low-pass filtered at 60 Å. Subsequent 3D refinements utilized this single class average as a reference and resulted in an initial map of all particles per dataset. In the case of DEF data, per-particle tilt series alignments and CTF models of this initial average were refined in M (Tegunov et al. 2021) with three sub-iterations and the usage of 60 % of the available resolution in the first sub-iteration. Geometries were refined for particle poses. Image warping was performed with a grid of 3 x 3 tiles, volume warping with a grid of 3 x 3 x 2 tiles and 10 frames utilized in order to model non-linear

deformations. Optimized particles and CTF models were reconstructed and subsequent hierarchical 3D classifications into two classes with 25 iterations per job were performed in RELION. For VPP data, the initial RELION-refined alignments were used for hierarchical 3D classifications with the same parameters as for DEF data. Focused classifications with binary masks indicated in the respective figures (Figure 30 for densities close to the head of the 40S subunit and Figure 31 for exit tunnel densities) did not employ image alignments.

Finally, well-aligned classes were further refined in M using the same geometry settings but utilizing CTF refinements of defocus values in case that the averages achieved resolutions better than 10 Å. Resolutions indicated in the corresponding figures were either calculated in RELION (post-processing step) or in M via Fourier shell correlations (FSCs) between two half-maps. The averages were then filtered to their respective resolutions (FSC cut-off criterion 0.143 (Rosenthal and Henderson 2003)) and visualized using Chimera (Pettersen et al. 2004) or ChimeraX (Pettersen et al. 2021). These software were further utilized to fit publicly available maps into the reconstructed densities and to calculate a cross-correlation (CC) score.

4.13.3 Subtomogram 3D alignments and classifications of FAS

FAS particles were 3D-aligned in RELION using the 3D classification task and the published *S. cerevisiae* structure as a starting reference (EMDB 1623 (Gipson et al. 2010)), rescaled to the corresponding unbinned pixel size (cf. Supplementary Table S2) and a box of 160 x 160 x 160 voxel, as well as low-pass filtered at 60 Å. The resulting single class subtomogram average was used as a reference for subsequent 3D refinements with applied D_3 symmetry. For DEF data, this average was further optimized in M with applied D_3 symmetry using either the ribosome-refined image and volume models or refining the FAS alignments for the same geometries as for ribosomes (s. above). Optimized particles and corresponding CTF models were reconstructed in M and hierarchical 3D classifications performed in RELION with each 25 iterations and clustering into two classes. For VPP data, the RELION-refined average was used for hierarchical 3D classifications.

Well-aligned classes were post-processed in RELION. FSCs were calculated as described above for ribosomes and the averages were filtered to their respective reso-

lutions. FAS subtomogram averages were visualized using Chimera (Pettersen et al. 2004) or ChimeraX (Pettersen et al. 2021).

4.14 Confocal light microscopy

Confocal light microscopy experiments were performed with Willram Scholz and supported by Ievgeniia Zagoriy. Fluorescence images of tagged or stained yeast cells were acquired at 30 °C on an LSM 880 (Zeiss) confocal light microscope and a Plan-Apochromat 63x/1.4 Oil DIC M27 objective, unless stated otherwise. The C-terminally tagged FAS-mCherry was excited at a wavelength of 561 nm and detected at 578-696 nm, in order to investigate stress-dependent cellular distribution of FAS over time. Changes in pH were observed with the compound CDCFDA, which stains acidic environments once it is activated by hydrolyzation via intracellular esterases (Richards et al. 2012). It was excited at 488 nm and detected at 499-562 nm. The lipophilic styryl compound FM4-64 which stains membranes was utilized to observe organelle morphology changes and endocytosis. This dye was excited with a wavelength of 561 nm and detection at 571-695 nm. Microscopy slides (µ-slide 8 well, Ibidi) were incubated for 10 min at room temperature with 200 µL of Concavalin A (at 1 mg/mL concentration) and then washed two times with deionized water. Wells were dried and then 300 µL of cells were applied in different media depending on the experiment. For all light microscopy experiments, data was visualized in Fiji (Schindelin et al. 2012).

4.14.1 Time-lapse experiments of FAS-mCherry in energy-depleted and osmotically stressed yeast cells

S. pombe (fjm9) and *S. cerevisiae* (yjm6) expressing C-terminally tagged FAS-mCherry were grown in liquid cultures to exponential growth phase ($OD_{600} \sim 0.2$-0.6) and washed three times with respective energy depletion, glucose control and osmotic stress media as described above. If required, cell cultures were diluted with the same medium to achieve an OD_{600} of $\sim$ 0.2-0.4 prior to application of 300 µL in an imaging well. Z-stacks were collected at three positions per yeast strain and condition, covering more than 40 individual cells, with a z-spacing of 644 nm, a total number of 20 z-slices with image dimensions of 688 x 688 pixels and a pixel size of 98.1 nm.

For energy depletion time lapse experiments, the Microscopy Pipeline Constructor (MyPiC) was utilized to recall positions and collect z-stacks at intervals of 1 h for a total of 12 time points. For osmotic stress conditions, z-stacks were manually collected at 15 min, 30 min, 55 min and 3 h after treatment.

FLM data was quantified in terms of number of foci per cell over time of energy depletion. An automated analysis pipeline was empoyed which was developed by Willram Scholz and uses Fiji (Schindelin et al. 2012) to detect foci within the full field of view containing several cells, ilastik (version 1.3.3 (Berg et al. 2019, Haubold et al. 2016)) to segment individual cells and R (version 3.6.3 (R Core Team 2013) and RStudio version 1.2.5033 (Allaire 2012)) to integrate the data and calculate foci numbers per cell. First, the central image z-slice was automatically selected in Fiji by detection of the slice with the highest standard deviation of fluorescence intensity. The position was refined within a range of two slices above and below the initial estimation using the lowest integrated intensity in the bright field channel processed with an IsoData threshold algorithm (Ridler and Calvard 1978). Within an area of four slices above and below the central z-slice, the 3D object counter (Bolte and Cordelières 2006) was utilized with a minimal voxel size of nine and an empirically determined threshold intensity of 132 plus the average FAS-mCherry intensity.

To segment individual cells in ilastik, maximum intensity z-projections of the central slice, as well as one slice above and below, in the bright filed channel were subjected to pixel classification. Cell wall and background (including out-of-focus cells) were manually labeled to train a network with the selected features of Gaussian smoothing, Laplacian of Gaussian, Gaussian gradient magnitude, difference of Gaussians, structure tensor eigenvalues and Hessian of Gaussian eigenvalues. The resulting probability maps served as input for subsequent boundary-based cell segmentations. Employing a watershed algorithm with empirically determined thresholds of 0.2 to 0.3 and a pre-smoothing of 1.0 to 2.0. Initial minimum boundary and superpixel sizes were set to 0, clustered seed labeling and thin structure preservation were employed to train a network that classified segmentation edges that could iteratively be selected or excluded. The final multicut segmentation was then performed with the Nifty_FMGreedy solver (implemented in ilastik) and a bias parameter of 0.4. In order to generate individual cell segmentations, object classification was performed with the multicut segmentation and bright field z-projections as input. The ilastik

output was a binary mask that was multiplied with the multicut segmentations in R to generate a mask with 0 intensity values for all background (including out-of-focus cells) and individual integers for each cell. Finally, this result was integrated with the foci counts from the 3D object counter to evaluate foci numbers per cell over the imaged ED periods.

Automatically detected central z-slices of FAS-mCherry FLM volumes were further utilized to calculate mean, maximum and minimum intensities per field of view in both yeast strains upon ED. Intensity values were min-max normalized, three replicates were averaged and the resulting values are displayed in Supplementary Table S3 and plotted in Supplementary Figure S1.

Table S3: Averaged and normalized mean intensities of FAS-mCherry in glucose control and ED time lapse microscopy experiments. Mean intensities were measured in Fiji for central z-slices, which were automatically selected based on the image analysis pipeline desribed above. Intensities of three replicates were min-max normalized and averaged. Minimal values are displayed for the ED times.

Time [min]	***S. pombe* FAS-mCherry intensity**		***S. cerevisiae* FAS-mCherry intensity**	
	Glucose control	**ED**	**Glucose control**	**ED**
50	0.57	0.28	0.00	0.62
110	1.00	1.00	0.34	1.00
170	0.73	0.85	0.56	0.55
230	0.60	0.55	0.88	0.24
290	0.41	0.47	0.96	0.23
350	0.22	0.55	0.96	0.15
410	0.14	0.14	0.95	0.19
470	0.18	0.32	0.97	0.15
530	0.01	0.27	0.92	0.14
590	0.04	0.22	0.82	0.10
650	0.05	0.21	0.87	0.01
980	0.00	0.00	0.29	0.21

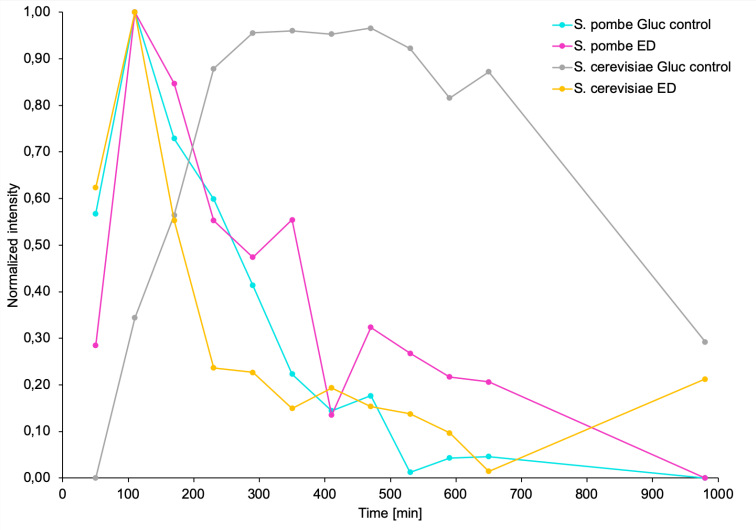

Figure S1: Averaged and normalized mean intensities of yeast FAS-mCherry treated with glucose control or ED media. Intensities detected by light microscopy (cf. Supplementary Table S3) are plotted against the time of treatment. Intensities initially increased in all conditions either due to foci formation (ED) or cell growth and division (control). At later time points fluorescence intensities decreased which could be caused by dissolution of FAS assemblies (ED), protein degradation (ED and control) or false z-slice detection in overgrown wells (control).

4.14.2 Distribution of FAS-mCherry and acidification in glucose-depleted yeast cells

The distribution of FAS-mCherry expressed in *S. pombe* (fjm9) and *S. cerevisiae* (yjm6), as well as the acidification of cellular compartments stained by CDCFDA, were investigated upon up to 7 days of glucose depletion. As described above, exponentially growing yeast cells were washed three times with respective synthetic media lacking glucose and diluted to an OD_{600} of around 0.03 in a total volume of 20 mL in a glass flask. In addition, Ampicillin was added to a final concentration of 100 µg/mL to prevent bacteria contamination during prolonged incubations. Cultures were kept shaking at 200 rpm and 30 °C. Around 1 h after treatment, cells were imaged which equals day 0. At an interval of 1 d for a total of seven days, 400 µL of cell suspension were retrieved from the culture and 0.4 µL CDCFDA added to a final concentration of 10 µM. 300 µL were transferred into a well of an imaging slide. Three positions were selected covering at least ten individual cells and z-stacks of mCherry and CDCFDA fluorescence signals were collected with a spacing of 640 nm, a total of 18 z-slices and with an image size of 792 x 792 pixel at a pixel size of 85.2 nm.

4.14.3 Acidification and membrane morphologies in yeast cells upon nutrient stress

Glucose and energy depletion were applied to *S. pombe* (fjm1) and *S. cerevisiae* (yjm1) wild-type strains and acidification was monitored via CDCFDA staining, as well as membrane morphologies were observed with FM4-64. Exponentially growing cells were collected and washed three times as described above. The samples were diluted to achieve an OD_{600} of around 0.2 in a volume of 1 mL. CDCFDA was added in a 1:1000 dilution resulting in a concentration of 10 µM. A volume of 300 µL was then transferred into the imaging well. Finally, 0.6 µL of FM4-64 were added directly to the well to achieve a final concentration of 2 µg/mL. The samples were imaged with the same parameters as for the prolonged glucose depletion experiments described above (cf. 4.14.2). The only exception was the total number of 19 slices per z-stack. Images were collected at an interval of 10 min and a total of 14 images collected starting from around 1 h after treatment with either glucose or energy depletion media.

4.15 FRAP measurements of FAS-mCherry in yeast cells upon energy depletion

In order to analyze the mobility of FAS upon energy depletion, fluorescence recovery after photobleaching was measured at different time points after treatment. FAS-mCherry expressing *S. pombe* (fjm9) and *S. cerevisiae* (yjm6) were imaged at an OD_{600} of around 0.1 on an LSM 880 (Zeiss) confocal light microscope.

For *S. pombe* FAS-mCherry (fjm9), a C-Apochromat 40x/1.2 W Korr FCS M27 water objective was utilized to collect single z-slices of 140 x 120 pixel with a pixel size of 117 nm fitting individual cells. Imaging was performed with 2 % laser power (DPSS laser), 2.46 µs pixel dwell time and 0.1 s frame time. A series of 500 images was collected at an interval of 1 s to record fluorescence mCherry signal. A rectangular area (44 x 16 pixel) covering parts of a single cell including cytosol and FAS assemblies in energy depletion conditions (cf. Figure 53 C) was bleached once after image 40 with 100 % laser power (DPSS laser) and a pixel dwell time of 7.49 µs. Five replicates (corresponding to five different positions and cells) were performed for each condition (glucose control, ED for > 10 min, > 180 min, > 470 min).

For *S. cerevisiae* FAS-mCherry (fjm6), FRAP was measured with a Plan-Apochromat 63x/1.4 Oil DIC M27 oil objective. A total of 300 individual z-slices with a dimension of 132 x 132 pixel and a pixel size of 85.2 nm were collected. Imaging was performed with a time interval of 0.10 s, a laser intensity of 15 %, 1.65 µs pixel dwell time and a frame time of 0.07 s. A rectangular area (63 x 16 pixel) covering parts of the cytosol including ED foci (cf. Figure 53 C) was bleached after image 20 employing 40 % laser power (DPSS laser) and a pixel dwell time of 3.30 µs. 21 replicates (corresponding to 21 different positions and cells) were measured for each glucose control and energy depletion for > 300 min.

FRAP data were analyzed with the FRAPAnalyser (version 2.1.0, cf. code availability 3.5). Data was double-normalized against the background and a reference region. In the case of *S. pombe* a whole cell reference was employed which was generated by segmentation using the above described pipeline in Fiji and ilastik. For *S. cerevisiae* a rectangular area of the same size as the bleach area was used which covered parts of a neighboring, unbleached cell. For normalization, the following

equation was employed (Halavatyi and Terjung 2017):

$$I_{norm}(t) = \frac{I_{frap}(t) - I_{back}(t)}{\langle I_{frap}(t)\rangle_{pre} - \langle I_{back}(t)\rangle_{pre}} \cdot \frac{\langle I_{ref}(t)\rangle_{pre} - \langle I_{back}(t)\rangle_{pre}}{I_{ref}(t) - I_{back}(t)} \quad (1)$$

The normalized intensity values (I_{norm}(t)) were calculated with the intensity values of the bleached region (I_{frap}(t)), the reference region (I_{ref}(t)) and the background region (I_{back}(t)), as well as the averaged values prior to bleaching $\langle ... \rangle_{pre}$ over time (t).

After normalization, replicates were averaged and fitted using the Levenberg-Marquardt (gradient) method utilizing a single (glucose control) or double exponential model (ED) with the following equations (Halavatyi and Terjung 2017):

$$FRAP(t) = I_0 + I_1 \cdot \left(1 - e^{\frac{t - t_{bleach}}{\tau}}\right) \quad (2)$$

$$FRAP(t) = I_0 + I_1 \cdot \left(1 - e^{\frac{t - t_{bleach}}{\tau_1}}\right) + I_2 \cdot \left(1 - e^{\frac{t - t_{bleach}}{\tau_2}}\right) \quad (3)$$

From these equations recovery half-times were calculated with $t_{1/2} = \tau \cdot \ln 2$. The immobile fractions were calculated for each condition with (1-I_0-I_1)/(1-I_0) (cf. Table 5).

5 Results

5.1 Methods towards high-throughput in-cell cryo-ET

The exploration of molecular crowding inside yeast cells required first the generation of a large cryo-electron tomography dataset in order to sample multiple cells and various nutritional conditions. Subsequently, data processing pipelines were developed to retrieve quantitative and structural information from the imaged molecular landscapes to gain biological insights.

Rendering cryo-ET a high-throughput method to investigate molecular crowding inside cells under varying nutritional conditions required:

1) Cryo-sample optimization
2) Automation of cryo-FIB milling to streamline lamella preparations
3) Automated tilt series acquisition
4) High-throughput data processing pipelines to mine and localize particles and segment organelles inside cryo-electron tomograms

In the following, I will illustrate the obtained results for each step of the pipeline and the developed tools that enabled me to prepare and analyze a large yeast cryo-ET dataset.

5.1.1 Cryo-sample optimization

First, cryo-preservation of yeast cells by plunge-freezing was optimized to facilitate subsequent cryo-FIB milling. Initial trials with a Vitrobot (Thermo Fisher Scientific) resulted in a gradient of cell concentrations over the whole grid (Figure 8 A). In this instrument the blotting paper is applied in an angle to achieve a gradient distribution of ice thicknesses over the whole grid which is desirable for protein solutions to increase the chance of obtaining optimal grid squares for single-particle cryo-EM. However, for cells, the generated gradient is unwanted. Thus blotting in a parallel manner, meaning that the blotting paper is aligned parallel to the grid, is preferred to get even distributions of cells (cf. Figure 6). Such a parallel set-up is feasible in a Leica plunger and was therefore used to evenly distribute cells on a grid (Figure

8 B). In addition, cell concentrations and blotting times were optimized. Yeast cell densities were adjusted to $OD_{600} = 0.2\text{-}0.3$ (optical density/absorbance at 600 nm, unitless) and resulted together with a blotting time of 1 s in optimal grids. The agglomerations of several cells in the center of many grid squares were ideal for targeting with the FIB (Figure 8 C-E).

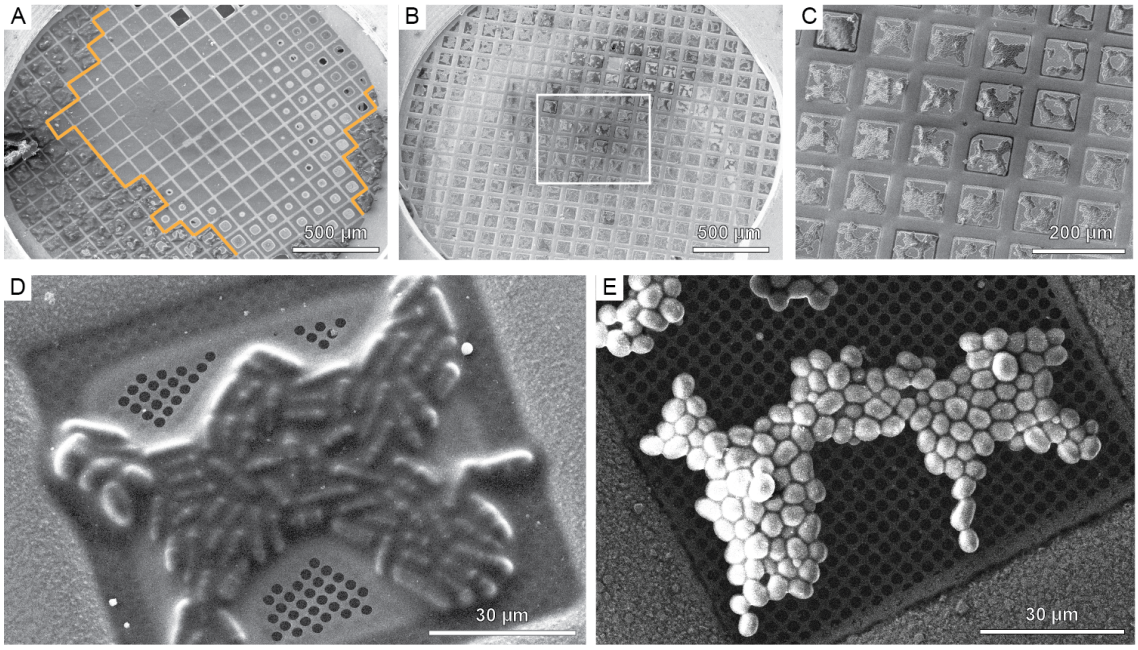

Figure 8: SEM images of yeast cells plunge-frozen on TEM grids under various conditions. A) Gradient of *S. pombe* cells plunge-frozen at OD_{600} 0.6 with a Vitrobot on a TEM grid. Empty grid squares framed in orange. B) *S. pombe* plunge-frozen at OD_{600} 0.3 with a Leica plunger. C) Zoom into the grid in B) (boxed area) reveals optimal ice thickness and homogenous distribution of cells on many grid squares. Individual grid squares show optimal agglomerations of D) *S. pombe* and E) *S. cerevisiae* cells that were targeted for FIB-milling.

5.1.2 Automation of focused-ion beam milling for multi-modal cryo-electron tomography applications

Sampling a variety of intracellular landscapes under varying conditions requires high throughput of cryo-FIB milling to produce lamellae of sufficient quality for cryo-ET. Automation of this process facilitates the otherwise laborious task and renders it more reproducible as manual operation entails a high level of expertise.

In collaboration with Sven Klumpe and Herman Fung, I developed a modular open-source software tool with a graphical user interface (GUI) to automate cryo-FIB milling procedures and streamline standard, as well as more advanced, workflows. In this section I will illustrate the results jointly produced with Sven Klumpe and Herman Fung (Klumpe, Fung and Goetz et al. 2021).

5.1.2.1 SerialFIB software design

The automation software, termed SerialFIB, was developed to facilitate cryo-FIB milling for a broad set of cryo-sample preparations. It enables a) automated on-grid lamella milling, b) targeted lamella milling utilizing prior localization by 3D correlative light microscopy, c) cryo-FIB SEM volume imaging and d) custom milling procedures, e. g. for lamella lift-out workflows (Mahamid et al. 2015, Schaffer et al. 2019). SerialFIB is python-based and encompasses a driver script that connects the graphical user interface (GUI, Figure 9) with specific functions and the microscope's application programming interface (API) to perform customizable tasks. It also includes a scripting interface (Script Editor) that allows the user to tailor milling procedures to their needs by directly implementing python scripts. In addition, Lamella Designer, Pattern Designer and Volume Designer further allow the user to customize their own protocols and adjust milling parameters to their demands without the need for scripting.

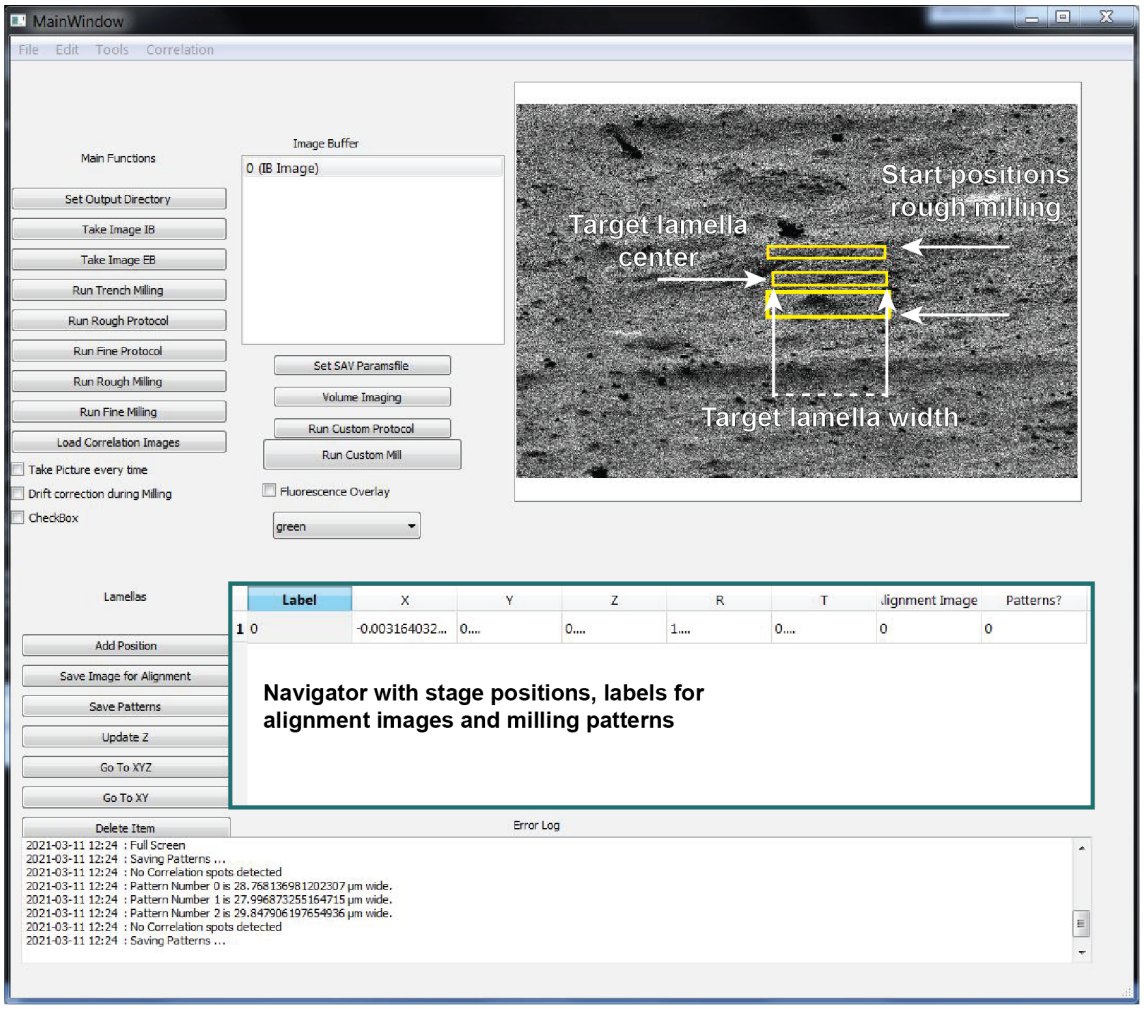

Figure 9: Graphical user interface (GUI) of SerialFIB. Main functions such as taking images or starting an automated milling protocol can be chosen from the top left buttons panel. A list of acquired reference images is stored in the image buffer. Additional buttons for volume imaging, custom milling tasks or to load fluorescence images for correlation are selectable below. Stage positions are stored in the coordinate navigator (middle) and connected to their respective reference images and milling patterns via the buttons panel on the left hand side. A log file is created and displayed to inform the user about each step and selected parameters. Lamella, Pattern and Volume Designers, as well as the Script Editor, are available via the tools tab on the top panel. Figure adapted from (Klumpe, Fung and Goetz et al. 2021) and produced jointly with Sven Klumpe and Herman Fung.

5.1.2.2 SerialFIB workflow

Similar to manual procedures (Schaffer et al. 2015, Schaffer et al. 2017, Villa et al. 2013), positions of interest on the sample are selected and the coincidence height between ion and electron beams is determined by the user on the microscope PC. The corresponding stage parameters are then stored in the GUI's navigator (Figure 9). A reference ion beam image and user-defined target sites as well as milling patterns relative to each position, are connected to each item. The milling patterns define extreme points at the top and bottom of the targeted lamella site (along the FIB y-axis) at which ablation of biological material will start. Setting up site-specific patterns individually for each target site prevents milling of obstacles such as ice crystals or grid bars. The software then automatically moves the sample to each saved stage position, takes an ion beam image at low currents (10 pA) and realigns to the previously saved reference image in order to accurately recall the target site (Figure 10). The alignment is based on image cross correlation (Guizar-Sicairos et al. 2008) and calculated offsets are applied by either stage movements (above 10 µm) or image shifts (below 10 µm) to compensate for stage drift or sample movements. When changing between ion beam currents, another image-based alignment step is performed, which utilizes image shifts only and accounts for misalignments between currents.

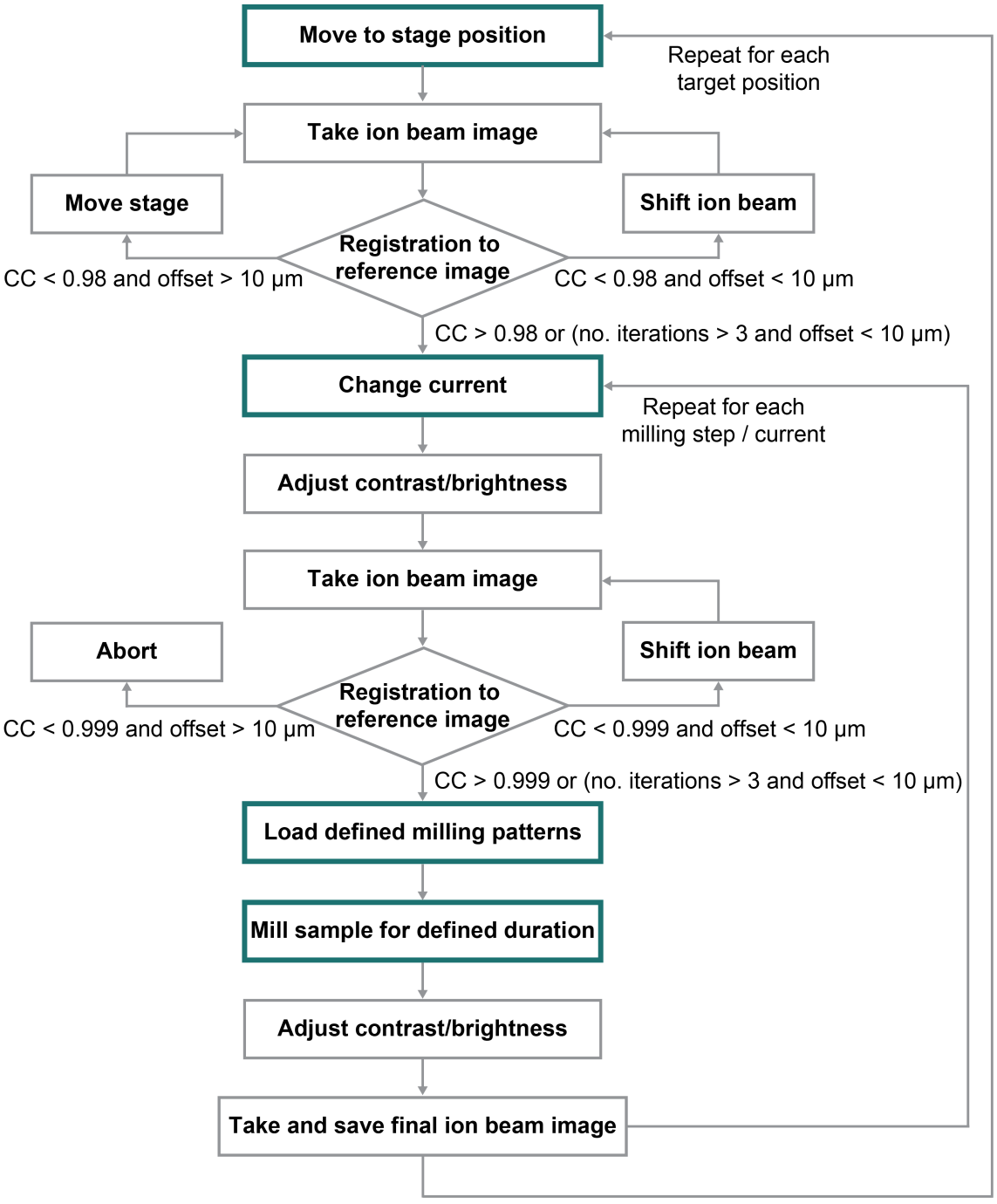

Figure 10: Automated cryo-FIB milling workflow implemented in SerialFIB. In general, for each target site, the following series of steps is performed: the stage is moved to the respective position, the ion beam current changed and the milling process is started using prior defined milling patterns (main tasks highlighted in dark green). Reference, first (pre-milling) and final (post-milling) images are taken at 10 pA. Depending on the quality of the image alignments subsequent steps after registration are triggered (diamond-shaped boxes). Figure adapted from Klumpe, Fung and Goetz et al. 2021 and produced jointly with Sven Klumpe and Herman Fung.

5.1.2.3 Automated on-grid lamella milling

Similar to manual procedures, automated lamella preparation from cryo-fixed cells on grids can be split into two main tasks of rough and fine milling. An initial step of cutting micro-expansion joints in order to relieve tension in the sample (Wolff et al. 2019) is also feasible and implemented in SerialFIB. During rough milling, cells are thinned in three consecutive steps to target thicknesses of 5 µm, 3 µm and finally 1 µm with ion beam currents of 1 nA, 0.5 nA and 0.3 nA, respectively. Samples are fine-milled with an ion beam current of 50 pA to a final thickness of around 200 nm, at which the frozen specimens are electron-transparent for subsequent TEM imaging.

For example, I employed automated rough milling using SerialFIB to micromachine both energy-depleted (ED) *S. pombe* and *S. cerevisiae* cells on different supports (Cu 200 R2/1 SiO_2 or Carbon). Milling of micro-expansion joints was only feasible on grids with SiO_2 support as Carbon got immediately torn and damaged. As grids were rather dry and did not have a continuous layer of amorphous buffer, SerialFIB was utilized only for rough milling, aiming at a target thickness of 1 µm. The final lamella thickness of around 200 nm was reached by manual micromachining to account for lamella bending (Figure 11). Subsequent tomogram acquisition enabled lamella thickness estimation and visually confirmed similar quality in comparison to manual lamella preparations.

Milling parameters, such as the number of steps and milling times, were benchmarked and successfully applied to six different cellular samples, namely Sum159, HeLa, *E. huxleyi*, *C. reinhardtii*, *S. cerevisiae* and *S. pombe*. A total of 145 sites were targeted with success rates of 91.5 % and 83.1 % for rough and fine milling, respectively (Table 1). The causes of automation failure were either sample instability (i. e., lamella bending or breaking of the support) or non-optimal milling parameters during initial stages of parameter optimization for each cell type. While expert users likely achieve success rates of up to 100 %, as milling can simply be stopped manually to prevent sample damage, unexperienced users should benefit from the successful generation of high-quality lamellae using SerialFIB. All users will further save time as the automation software does not require manual intervention during FIB milling.

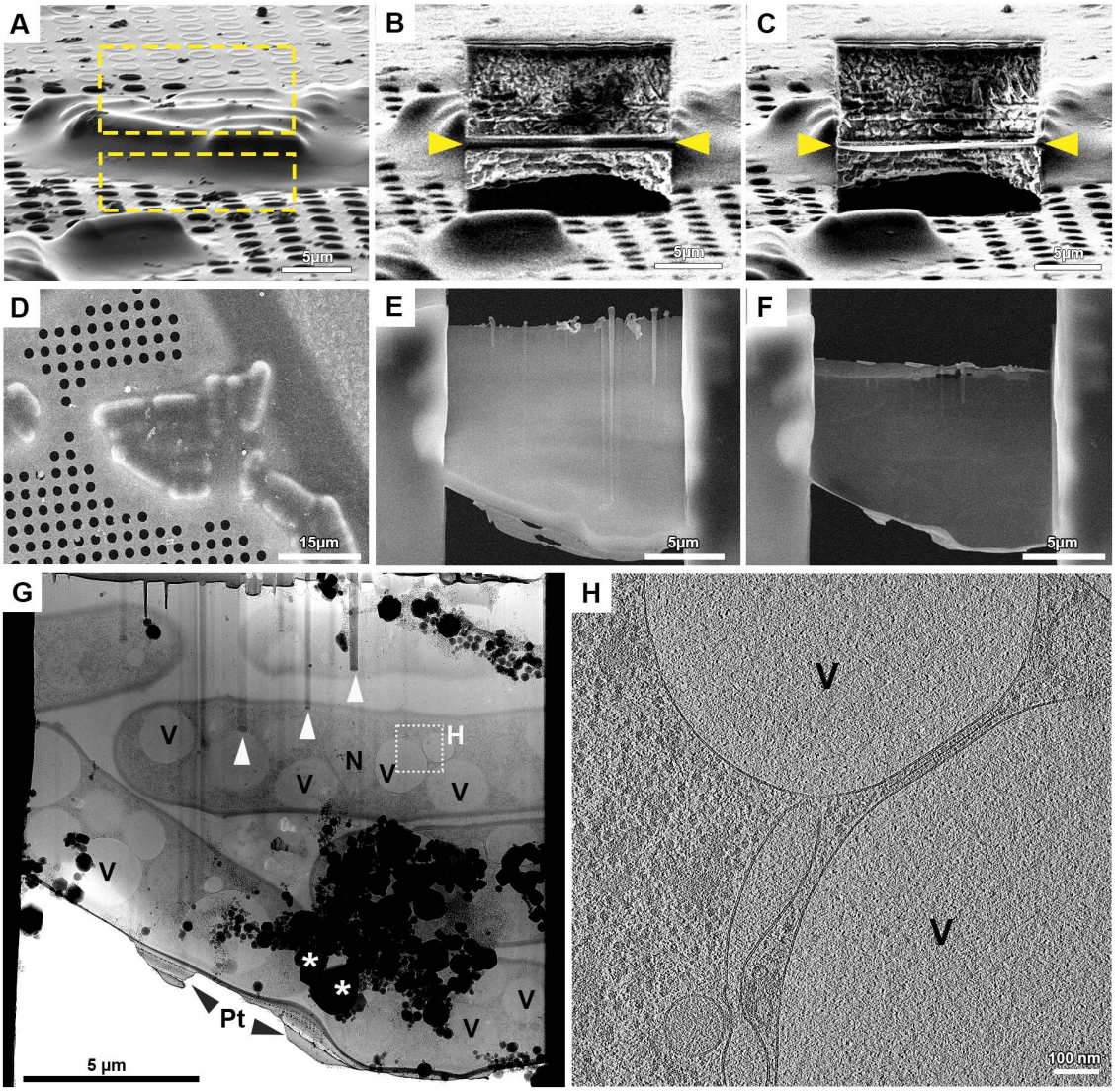

Figure 11: Automated lamella milling of *S. pombe* after 17 h ED. FIB (A-C) and SEM (D-F) views of targeted cells (A, B), rough milling to 1 µm target thickness (B, E, rough milling patterns indicated in A by yellow dashed boxes), and manual fine-milling to around 200 nm of an agglomeration of cryo-preserved *S. pombe*. G) TEM overview of the lamella in C (indicated by yellow arrowheads) and F displays individual cells with nuclei (N) and vacuoles (V). Curtaining artifacts from milling lipid droplets (white arrowheads), ice crystals (asterisks) and the protective platinum layer (Pt) at the lamella front are observable. H) Tomographic slice of the highlighted area in G reveals the cellular interior of an *S. pombe* cell after 17 h ED.

Table 1: Statistics of automated cryo-FIB milling with SerialFIB. For Sum159 and HeLa cells, two lamellae each were subjected to cryo-FIB SEM volume imaging and therefore only fine-milled in SerialFIB (*). Energy depletion (ED) samples were manually fine-milled due to lamella bending (cf. Figure 11 C). Data produced jointly with Sven Klumpe and Herman Fung (Klumpe, Fung and Goetz et al. 2021).

Sample	**# Target sites**	**# Rough-milled lamellae**	**# Fine-milled lamellae**	**Lamella thickness [nm]**
Sum159	22	18*	19	70-410
HeLa	22	19*	18	100-450
E. huxleyi	9	9	9	175-470
C. reinhardtii	16	16	10	140-350
S. cerevisiae	8	8	8	190-300
S. cerevisiae ED	29	22	N/A	180-400
S. pombe ED	39	37	N/A	200-490
Total	145	92	64	
Success rate [%]		91.5	83.1	

Each sample type required empirical optimization of milling protocols (Supplementary Table S1). This accounts for the fact that the cellular content depends on cell type. For example, lipid droplets in *S. pombe* are very dense and thus require longer ablation times by the FIB (Figure 11). Similarly, the breast cancer cell line Sum159 exhibits a large amount of lipid droplets which lead to curtaining effects (Figure 12 B). Such artifacts are also caused by other cellular high-density objects such as calcium carbonate crystals, which are formed by the single-cell algae coccolithophore *E. huxleyi*. Extended milling times were therefore employed in SerialFIB to remove curtaining artifacts, which are observable in the direction of milling (Figure 12).

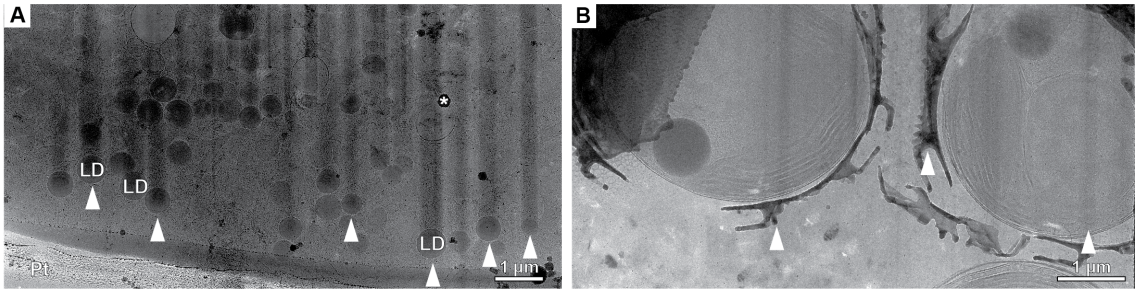

Figure 12: Automated lamella preparation of Sum159 and *E. huxleyi* with milling artifacts caused by dense features. A) TEM lamella overview of a Sum159 cell containing many lipid droplets (examples labeled LD) which result in curtaining artifacts (white arrowheads) along the FIB milling direction. B) *E. huxleyi* cells with intra- and extracellular $CaCO_3$ crystals which require longer ablation times by the FIB and thus impair even removal of biological material (curtains highlighted with white arrowheads). Cryo-samples of Sum159 cells provided by Ievgeniia Zagoriy and *E. huxleyi* cells by Zohar Eyal.

5.1.2.4 Cryo-CLEM workflow for targeted lamella preparations

Creating a lamella at a specific site within a cellular sample for subsequent cryo-ET acquisition requires cryo-correlative light and electron microscopy (cryo-CLEM) workflows. In order to correlate fluorescence light microscopy (FLM) data with SEM or FIB images, features need to be identified in both imaging modalities. Fluorescent fiducials which are visible in SEM and FIB images allow the transformation (scaling, rotation and translation) and projection of a cryo-FLM volume onto corresponding 2D SEM and FIB images (Arnold et al. 2016). Thus, a lamella can be created at the correlated site of a fluorescently labeled cellular feature. To demonstrate the feasibility of using SerialFIB for such CLEM procedures, fluorescently stained lipid droplets (diameter of around 200-500 nm) were targeted in HeLa cells (Figure 13).

Correlations were calculated with the software tool 3DCT (Arnold et al. 2016). In a first step, fiducials were selected on FLM maximum intensity projections and manually assigned to their corresponding signatures on an SEM image. Knowledge of the geometric relationship between SEM and FIB views enabled in a next step the application of the correlation transformations to the FIB view, by detecting fiducials in a semi-automated manner. These fiducial transformations can be extrapolated to the whole cryo-fixed sample allowing the projection of cellular fluorescence signals onto the FIB image for targeted lamella preparation (Figure 13 A-B). The FIB images of a target lamella site can then be imported into the SerialFIB GUI together with the correlated positions calculated in 3DCT. This enables site-specific lamella and milling pattern generation for subsequent automatic rough and fine milling (Figure 13 C).

In four FIB sessions corresponding to four grids, a total of 15 sites were correlated to target lipid droplets in HeLa cells using SerialFIB. During optimization of milling parameters, one lamella was lost resulting in 14 fine-milled lamellae. In all cases, the final lamella height (along y in the FIB view) did not coincide with the target position prior to milling. This is likely due to sample deformations over time, which can already be observed on grid squares that do not even contain cells (Figure 14). As fiducials are selected on grid bars evenly surrounding the target cell, displacement of the grid square support in y likely lead to a mismatch between FLM and FIB view in this area.

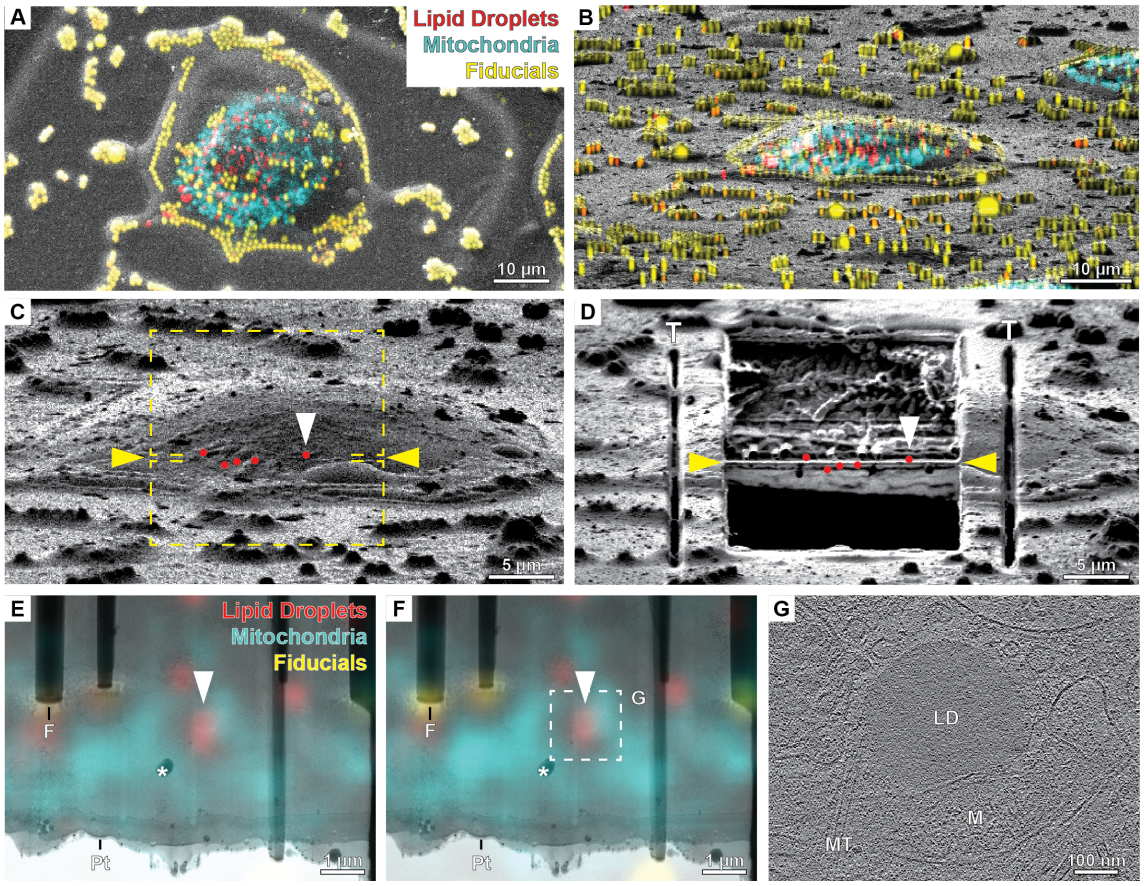

Figure 13: CLEM workflow using SerialFIB for targeted lamella creation of lipid droplets inside a HeLa cell. A) Maximum intensity projection (MIP) of fluorescence volumes of lipid droplets (red), mitochondria (cyan) and microbeads used as fiducials (yellow) for correlation and transformation onto the SEM view of a HeLa cell in the center of a grid square. B) MIP of the same fluorescence signals as in A projected onto the FIB view via semi-automated transformation. C) FIB view with marked correlated lipid droplet positions including the target position (white arrowhead) for which lamella and milling patterns (yellow arrowheads and dashed box) were created in SerialFIB. D) FIB view after trench (T), rough and fine milling resulted in a lamella (yellow arrowheads) 169 nm below the target lipid droplet (white arrowhead). E) Overlay of TEM lamella map with MIP of a 300 nm fluorescence slice at the lamella height displayed in D shows misplaced fluorescence signal for the target lipid droplet (red, white arrowhead). Curtaining artifacts are caused by internalized fiducials (F). Ice crystals (*) occupy parts of the lamella. At the lamella front, a continuous platinum layer (Pt) is visible. F) Overlay of TEM lamella map with MIP of a 300 nm fluorescence slice at the target lipid droplet site which fits best with the structural signatures in the TEM map (white arrowhead). G) Cryo-electron tomogram depicting the target lipid droplet highlighted in F (dashed box) in close proximity to a mitochondrion (M) and a microtubule (MT). Data produced jointly with Herman Fung, adapted from Klumpe, Fung and Goetz et al. 2021.

In order to assess successful retention of the target lipid droplet independent of sample deformations, TEM maps were acquired of each lamella. The observed intracellular features were then compared to the fluorescence signal of different y-slices (in the FIB view) retrieved from the transformed FLM volume prior to FIB-milling using a new 3DCT feature (s. code availability 3.5). This enabled the calculation of relative distances from the best fitting fluorescence y-plane determined by visual comparison, to the original target height and to the post-milling lamella position. The targeted lipid droplet could be identified in seven out of 10 lamellae created on three $TiSiO_2$ grids whereas none of the four lamellae created on one $AuSiO_2$ support contained the aimed feature. In the cases where the target LD was preserved in the final cellular slice, distances between the best fitting fluorescence y-plane and the target height ranged between +337 nm to -506 nm. The offset between the best fitting fluorescence y-plane and the post-milling lamella height was -337 nm to -1518 nm. Thus, all final lamellae were located below the best fitting plane indicating overall sinking of the sample.

Collection of cryo-electron tomograms from successfully correlated, FIB-milled lamellae, visualized the specific lipid droplets in their cellular environments (Figure 13). This confirms the usability of SerialFIB for cryo-CLEM workflows. Consequently, the software can be used to target other features of interest, such as biomolecular condensates in yeast cells, in future studies.

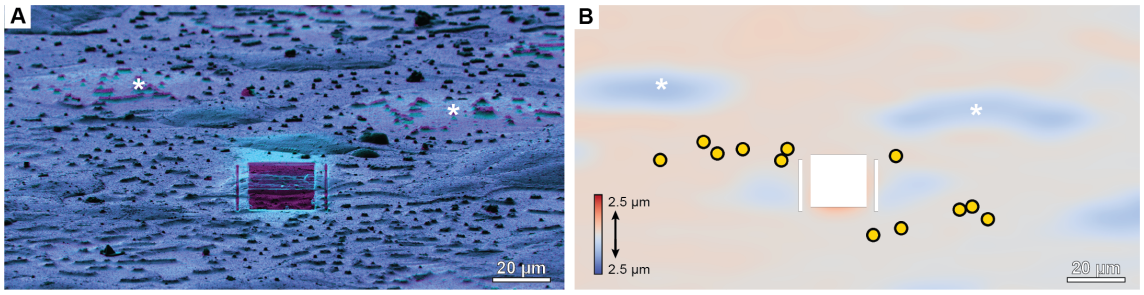

Figure 14: FIB images before and after milling of a HeLa cell show sample deformations within the whole field of view. A) Overlay of FIB views before (magenta) and after (cyan) FIB milling of an example HeLa cell. Deformations are also visible on grid squares without cells (*). B) Displacement in y across the field of view with the area of lamella creation masked. Fiducials used for correlation between FLM and FIB view are highlighted in yellow. Data produced jointly with Herman Fung, adapted from Klumpe, Fung and Goetz et al. 2021.

5.1.2.5 Cryo-FIB SEM volume imaging

Another application implemented in SerialFIB is cryo-FIB SEM volume imaging. This module enables the collection of an SEM image series of a defined cellular volume with valuable nano-scale information of organelle sizes, localizations and distributions. Applying this workflow in a consistent and streamlined manner requires automated approaches, such as the implementation in SerialFIB. The observed cellular features may also guide the user to find a suitable position for subsequent lamella preparation in SerialFIB, potentially mitigating the adverse effects of local specimen deformation in 3D CLEM described in the previous section. Cellular slices of Sum159 cells were iteratively ablated with the FIB in 100 nm steps and the remaining cross-sections imaged with the SEM. Imaging parameters were empirically adjusted to generate sufficient signal-to-noise ratios in the unstained sample (e.g., via dwell time and line integration), but also to minimize acquisition times and exposure doses. Image post-processing, including contrast enhancement and removal of milling artifacts such as curtaining from lipid droplets readily visualized the cellular organelle organization and facilitated manual segmentation of lipid droplets and the nucleus (Figure 15).

After collection of a serial FIB-SEM volume containing the nucleus and its periphery, a lamella was prepared roughly 100 nm below the last exposed surface imaged by the SEM. On this lamella, cryo-electron tomograms were collected that are of similar quality as conventionally prepared on-grid lamellae (Figure 15).

The feasibility of multimodal imaging to correlate cryo-FIB SEM volumes with cryo-FLM data was tested for HeLa cells with fluorescent signals for lipid droplets, mitochondria and fiducial microbeads. After correlation in 3DCT, an area between two cells was subjected to serial cryo-FIB SEM imaging. The resulting SEM slices were post-processed as described above to enhance contrast and remove curtaining artifacts. Subsequently, beads and lipid droplets were manually segmented. Centroids of fluorescence signals from beads and lipid droplets were affine transformed and registered to centroids calculated from the cryo-FIB SEM volume annotations. Although outliers were observed, the overall fitting accuracy with a root-mean-square residual of 386 nm lies within the current resolution limits of cryo-FLM (around 400 nm (Arnold et al. 2016, Van Driel et al. 2009)) and is thus adequate for 3D-

targeted lamella preparations. This confirmed the possibility to combine multiple cryo-imaging modalities and may facilitate targeted lamella preparations using cryo-FLM signals in larger cellular volumes in the future.

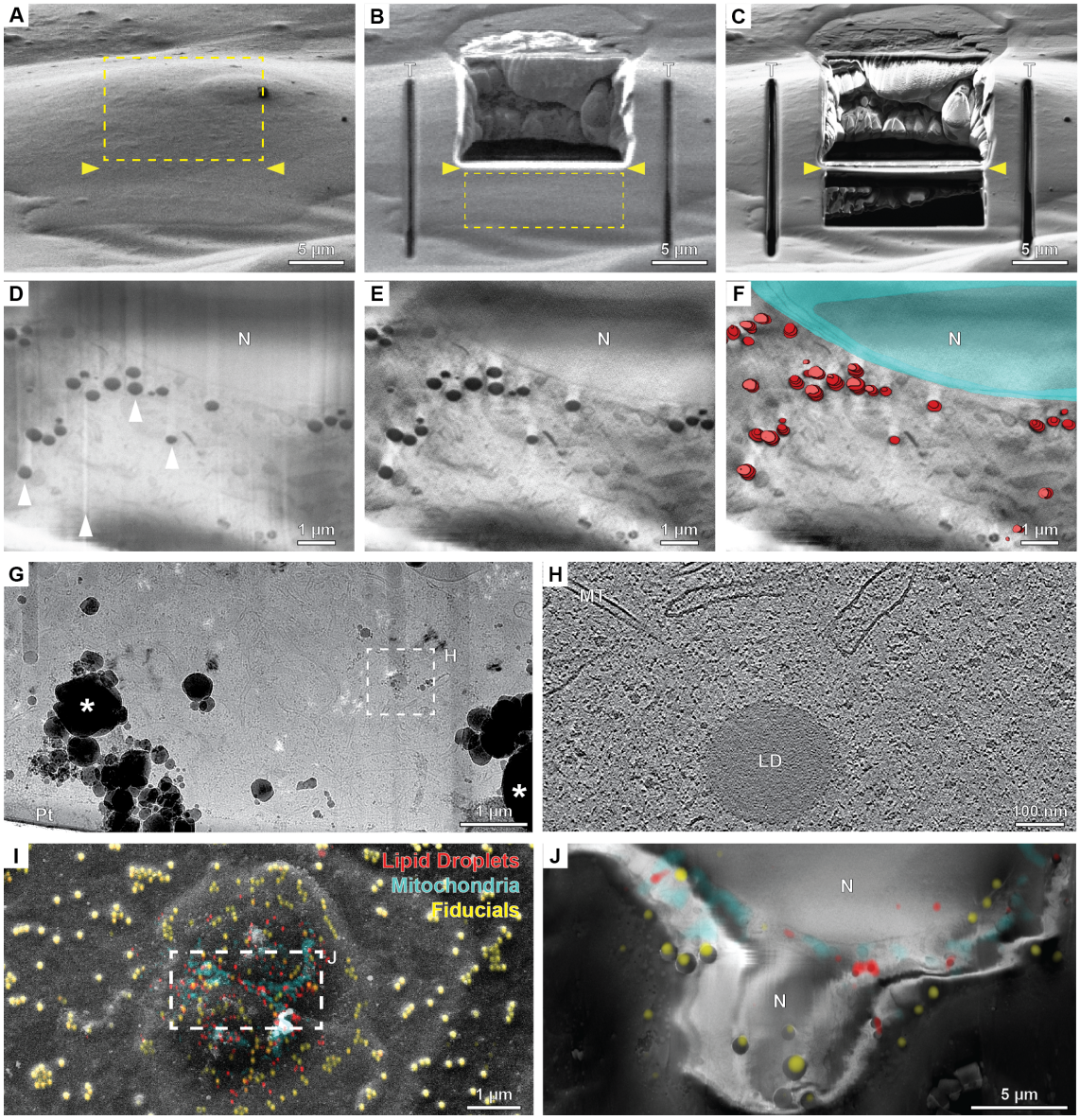

Figure 15: Multimodal cryo-FIB SEM volume imaging using SerialFIB. A) FIB view of a Sum159 cell which was targeted for cryo-FIB SEM volume imaging (yellow dashed box) and subsequent lamella milling (yellow arrowheads). B) The same cell as in A after trench milling and cryo-FIB SEM volume imaging. C) The final lamella (yellow arrowheads) from the Sum159 cell in A and B at a target thickness of 200 nm. D) Raw serial FIB-SEM image of the cellular interior showing the nuclear periphery with curtains caused by lipid droplets (white arrowheads) along the direction of FIB milling. E) SEM slice in D) after image processing including wavelet decomposition to remove milling artifacts and contrast enhancement. F) Overlay of E with manual segmentations of lipid droplets (red) and the nucleus (N, cyan). G) TEM lamella overview of the lamella created in C below the area where the FIB-SEM volume was ablated. Ice contaminations (*) and the platinum (Pt) layer at the front of the lamella are visible. H) 2D slice of a reconstructed cryo-electron tomogram depicting a lipid droplet (LD) and a microtubule (MT) highlighted in G (dashed box). I) Overlay of an SEM view of two HeLa cells with maximum intensity projections of correlated and transformed fluorescence volumes of lipid droplets (red), mitochondria (cyan) and fiducial microbeads (yellow). The highlighted area (dashed box) is enlarged in J after serial sectioning with the FIB visualizing the two nuclei (N) and the cytosol of the two cells. J) The cellular features overlay nicely with their respective fluorescence signals (root-mean-square residual of 386 nm). Data produced jointly with Herman Fung, adapted from Klumpe, Fung and Goetz et al. 2021.

5.1.3 Automated cryo-electron tomography acquisition

High-throughput lamella preparation using SerialFIB generated a large number of cellular slices for cryo-electron tomography. Automation of this imaging technique reduces microscope time, minimizes supervision and intervention by the user, and thus streamlines large scale data generation for quantitative analysis.

In order to investigate molecular crowding inside yeast cells, optimized cryo-specimen preparations, and the subsequent manual and automated FIB-lamella milling, resulted in over 25 TEM-grids (with 5-6 lamellae per grid) and more than 140 lamellae in total. Each of these slices contained sections through several yeast cells representing cellular areas spanning tens of micrometers. To image the full spectrum of cellular compartments, the acquisition of around 10 tilt series on one lamella by cryo-electron tomography was automated with the help of Wim Hagen and Felix Weis using SerialEM (Figure 16, (Mastronarde 2005, Mastronarde 2018, Weis and Hagen 2020)). Stage positions are linked to reference images at intermediate and high magnifications and saved in the software's navigator panel (6,500x resulting in pixel sizes of 22.84 Å or 28.04 Å, and 42,000x or 26,000x which correspond to pixel sizes at the specimen of 3.37 Å and 3.43 Å, depending on the camera type, K2 or K3, respectively). Running batch tilt series acquisition, the sample is sequentially moved to the saved coordinates and image alignments performed to recall the original position on the lamella. A single tomogram covered a field of view of around 1.3 or 1.4 µm x 1.3 or 2.0 µm depending on the camera type (K2 or K3, respectively). Followingly, tilt series were collected with user-defined parameters (e.g., defocus values, exposure time and dose, maximal tilt angles and tilt increments, cf. Supplementary Table S2). Thereby, a single cryo-ET session can potentially provide over 50 tomograms of cellular landscapes (assuming one TEM grid with five lamellae). In total, I acquired over 560 tomograms of yeast cells under different cellular conditions (detailed in chapter 5.2) in more than 20 sessions with thickness ranges of 95-520 nm.

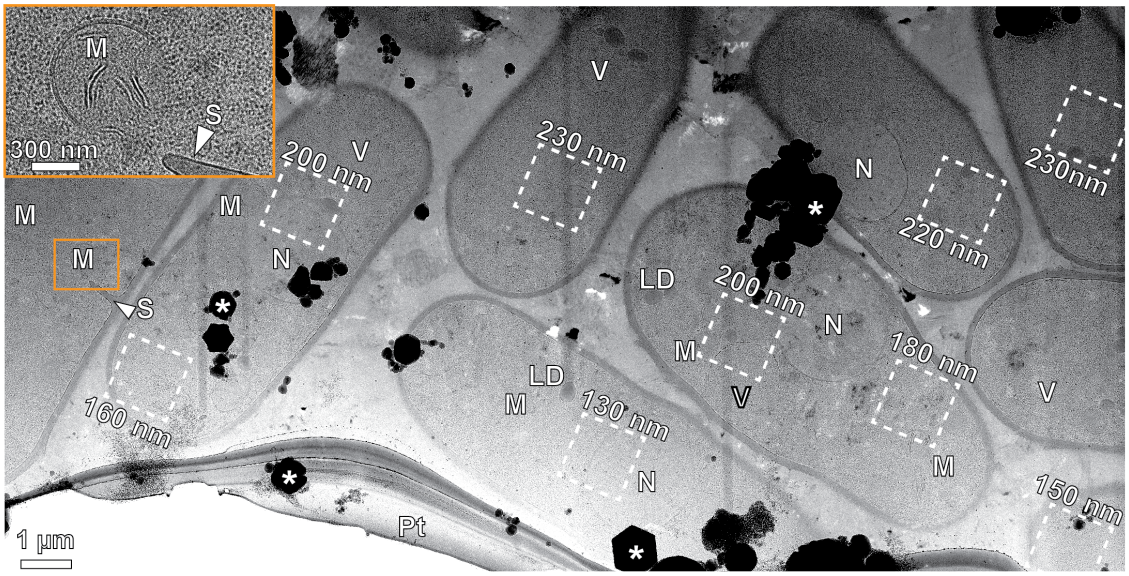

Figure 16: TEM overview of a lamella created from an agglomerate of *S. pombe* cells after 1 h energy depletion. On the lamella map, cellular areas of nine individual *S. pombe* cells surrounded by a dense cell wall are observable, containing nuclei (N), mitochondria (M, highlighted orange area is enlarged in inset), vacuoles (V), lipid droplets (LD), and for the very left cell a fission septum (S). 10 tomogram positions were selected for automated cryo-ET acquisition (dashed boxes, one tomogram position covered by orange inset). Tomogram thicknesses (along z) were determined from 3D reconstructions, and increased along the direction of milling (bottom to top). Tomogram reconstruction was not possible for the top left target position as tracking during acquisition failed after the third tilt. Ice contaminations (*) obscure areas of the lamella that cannot be imaged. The lamella front is covered by platinum (Pt).

5.1.4 CNN-based data mining enables objective and fast organelle segmentation and particle localization

In order to obtain quantitative biological and structural information from the large number (> 500) of cryo-electron tomograms generated with the methods described above, cellular structures need to be segmented and particle coordinates determined. Traditional pattern recognition techniques detect and segment cellular features. They often need to be tailored to the specific structures of interest as they otherwise do not provide satisfactory results. Due to the inherently low signal-to-noise ratio, imaging artifacts within cryo-electron tomograms and the crowded nature of the native cytosol, they further require a high level of expertise and are laborious. To overcome these limitations, we developed a supervised deep-learning based software, termed DeePiCt (Deep Picker in Context), to automatically detect cellular structures and macromolecules in cryo-electron tomograms. Due to the lack of annotated experimental (real) cryo-ET data, the implementation of DeePiCt first required expert-supervised segmentations of organelles, cytosol, membranes, as well as determination of ribosome and fatty acid synthase (FAS) coordinates in yeast cryo-electron tomograms. The comprehensively annotated data set then enabled training and testing of 2D and 3D convolutional neural networks (CNNs) for cellular compartment segmentation and particle picking procedures, respectively. The software thus provides information on macromolecules in their native cellular context. In addition, it not only facilitates analysis of the data acquired for yeast cells under varying nutritional conditions, but also allows transfer to other organisms, and thus biological questions. The method and results illustrated below were developed and jointly produced with Irene de Teresa and Alexander Mattausch (De Teresa and Goetz et al., 2021, joint manuscript in preparation).

5.1.4.1 Ground truth data set construction

The training and validation data set for developing DeePiCt consisted of 20 selected high-quality cryo-electron tomograms visualizing intracellular landscapes of wild-type *S. pombe* grown in normal nutrient conditions (full medium). For this purpose, I FIB-milled lamellae from cryo-preserved cells and acquired cryo-ET data with varying defocus values (2 µm to 4 µm). For 10 of the tomograms, a Volta potential phase plate (VPP) was used to enhance phase contrast which facilitates

the detection of cellular structures. The other 10 tomograms were acquired only with varying defocus values (DEF), as with this data type higher resolution subtomogram averages can be achieved (Turonova et al. 2020). In the reconstructed VPP and DEF tomograms, organelles, cytosol, and membranes were segmented (Figure 18). Organelle and cytosol volumes were annotated manually on every 10^{th}-15^{th} slice, followed by interpolation in Amira (Thermo Fisher Scientific). Membranes were first continuously segmented in five tomograms. These annotations were converted into binary volumes and used to train a CNN to predict in the remaining tomograms. Membrane predictions were further manually optimized and completed.

For the CNN-based localization of macromolecules, I determined the coordinates of ribosomes in three steps: first, template matching (TM, (Hrabe et al. 2012)) using the large subunit (LSU, 60S) of a published *S. cerevisiae* 80S ribosome map (EMDB 3228) as a reference and subsequent visual review of the top 2,000-3,000 cross-correlation hits in each tomogram. Next, in three iterative rounds, CNNs were trained first with the cleaned TM results and then with the newly detected particles from the previous CNN round. In the case of DEF ground truth generation, the first CNN was trained on DEF TM results, whereas the following CNN rounds utilized CNNs trained in the VPP data. After each round, predictions were manually inspected and cleaned. Finally, all remaining, yet undetected particles, were picked manually inside cryo-electron tomograms. The complete ribosome ground truth is constituted on average by initial 30 % TM, additional 32 % by DeePiCt predictions and ultimately 38 % manual annotations (Figure 17). Finally, particle lists were cleaned by calculating the elliptic distance between the coordinates to remove particles that were picked twice (Supplementary Table S4).

For FAS ground truth annotations, TM with the published *S. cerevisiae* FAS (EMDB 1623) as reference failed. Therefore, I localized particles in a first step by manual picking. The determined coordinates were used to train a CNN, of which predictions were obtained and manually revised. In a third step, additional FAS were detected manually and the complete annotations (on average 29 % DeePiCt, 71 % manual, Figure 17) cleaned to remove any duplicates (Supplementary Table S5).

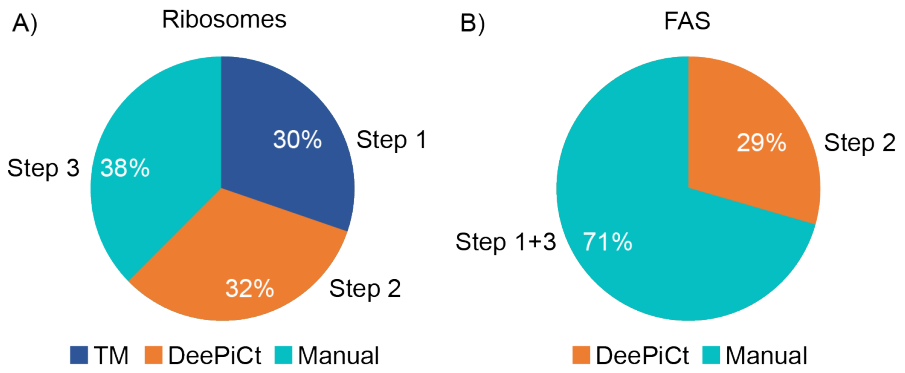

Figure 17: Ribosome and FAS ground truth construction in 20 *S. pombe* tomograms. A) Ribosomes were initially localized by TM (30 %). In a second step, over three iterative rounds DeePiCt detected additional particles (32 %) and finally remaining undetected ribosomes were manually picked (38 %). B) FAS particles were initially manually picked as TM failed. These annotations were utilized by DeePiCt detecting additional particles (29 %). The ground truth annotation was completed by a final manual step, adding on average 71 % of the complete ground truth. Data produced jointly with Irene De Teresa.

Figure 18 depicts an example VPP tomogram and its comprehensive annotations for membranes, organelles, ribosomes and fatty acid synthases. It visualizes up to around 0.18 µm^3 of an average cellular volume, accounting for less than 1 % percent of an *S. pombe* cell (approximately up to 150 µm^3 total volume (Nurse 1975, Wu and Pollard 2005)). It is one of the above described 20 fully annotated tomograms (10 VPP and 10 DEF). On average, 2,561 ± 1,089 ribosomes and 53 ± 29 FAS particles were picked per tomogram. This, of course, depends on the imaged cytosolic volume. In general, similar ribosome numbers were picked in VPP and DEF tomograms (2,532 ± 948 and 2,591 ± 1,267, for VPP and DEF, respectively). The fraction of ribosomes that was only detected by DeePiCt (new true positives) resembles the subtomogram averages of all ground truth ribosomes (cf. Figure 18 F). However, more FAS particles were detected in VPP tomograms (69 ± 25 and 37 ± 23, for VPP and defocus, respectively), likely due to the more optimal contrast necessary to localize this rather hollow structure.

Taken together, the mined data is considered “ground truth”. However, it has to be taken into account that it may not be complete or still contains false annotations due to the limitations of each particle picking approach, manual segmentations and revisions, as well as the complexity of cellular cryo-ET data. Nevertheless, subtomogram averages of all cytosolic ribosome and FAS particles confirm their structural

identity in both VPP and defocus-only data (Figure 18 F, G). This is further underpinned by hierarchical 3D classifications in RELION (Figures 19-21). For both ribosomes and FAS, a well-aligned class was identified. In the case of 3D classifications of ribosomes, more than half of DEF particles did not cluster in well-aligned averages, whereas all VPP classes appear defined (Figures 19-20). In addition, a class that only contained the 60S large subunit (LSU) was detected in VPP, but not recovered in DEF, although both datasets were acquired on the same sample. This observation is likely due to the improved signal-to-noise ratio in raw VPP tomograms which appeared to facilitate 3D classifications.

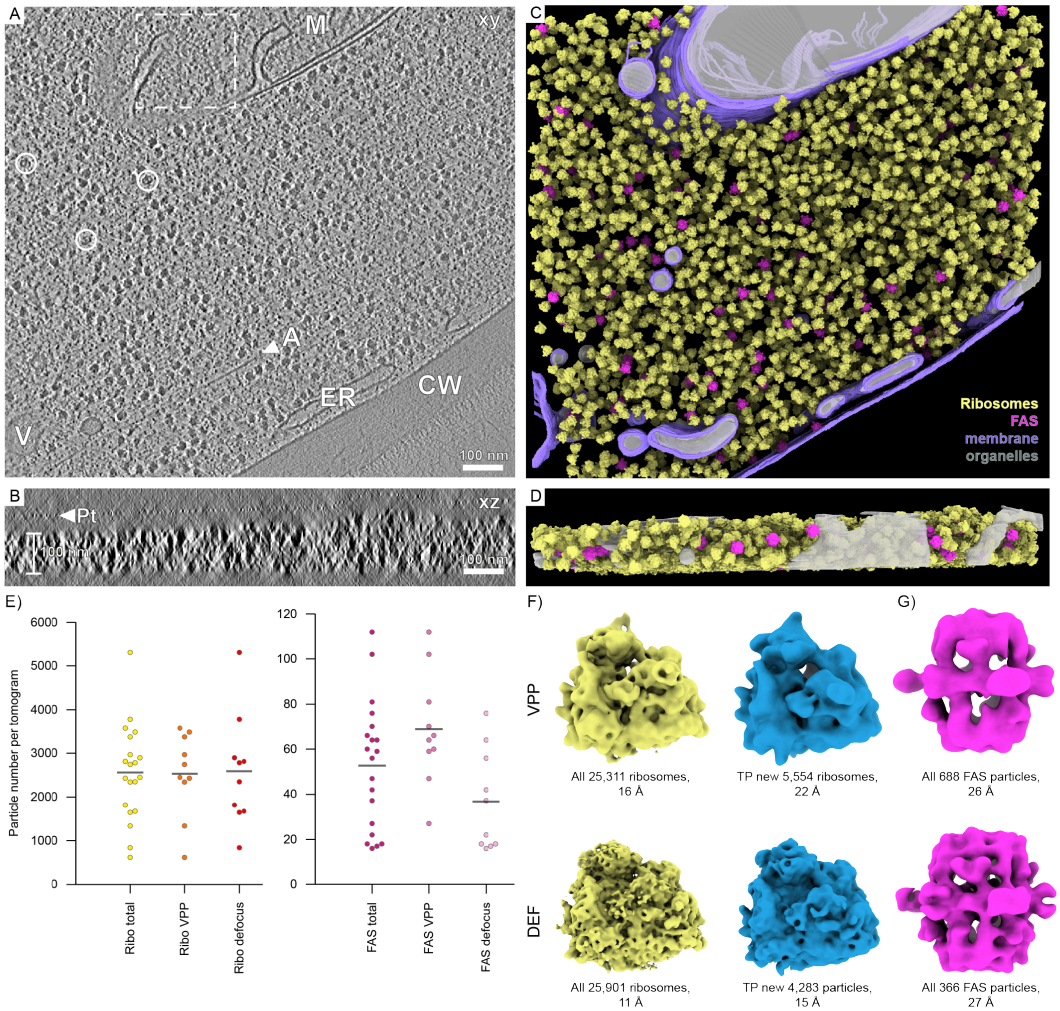

Figure 18: Ground truth annotations of cellular structures and macromolecules in *S. pombe* cryo-electron tomograms. A) 2D slice (xy view) of an example VPP tomogram from the ground truth dataset. Cellular features enclosed by the cell wall (CW) such as ribosomes (abundant dark objects in the cytosol), fatty acid synthases (FAS, white circles), a mitochondrion (M) with ATP synthases decorating cristae (white dashed box), actin filament (A), vesicle (V) and the endoplasmic reticulum (ER) are readily identifiable by eye. B) Rotation of the tomogram in A by -90° around x allows the estimation of tomogram thickness. The thinnest point at the lamella front (left) is 100 nm. A gap between cellular volume and Pt layer at the top reveals a layer of condensed water. C) 3D representation of ground truth annotations for organelles (grey), membranes (purple), ribosomes (yellow) and FAS (pink). D) XZ view of the segmentation volume in C without membranes. E) Particle numbers per tomogram. On average 2561 ± 1089 cytosolic ribosomes (left plot) were detected with 2532 ± 948 and 2591 ± 1267 for VPP and defocus data, respectively. In total, 53 ± 29 FAS particles were picked per tomogram (right plot). Overall, more FAS particles were detected in VPP data (69 ± 25) than in defocus-only tomograms (37 ± 23 FAS). The mean of each dataset is marked by a grey horizontal line. F) Subtomogram averages of all cytosolic ribosomes (yellow) and true positives (TP) newly detected by DeePiCt (blue). Particles were localized in VPP (top) and defocus tomograms (bottom). G) FAS subtomogram averages detected in VPP (top) and defocus (bottom) tomograms. Data produced jointly with Irene De Teresa.

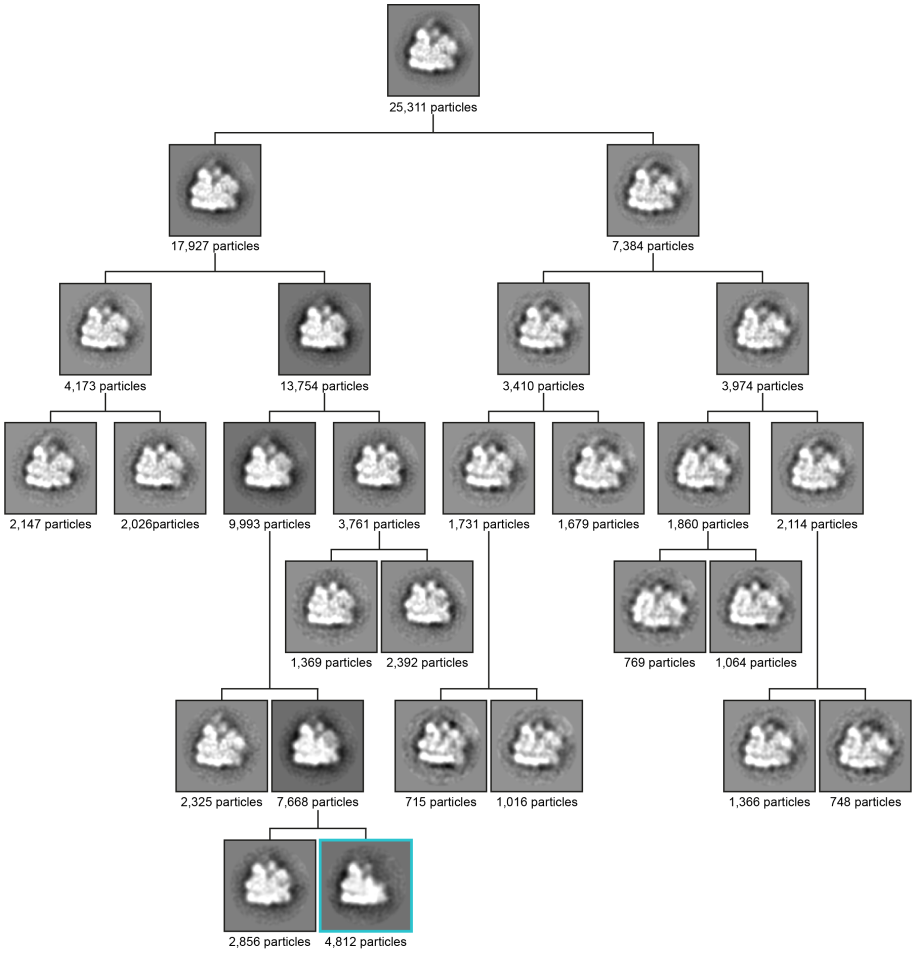

Figure 19: Cytosolic VPP ground truth ribosomes hierarchically 3D-classified starting from initial alignments. 25,311 roughly aligned particles were stepwise clustered into two classes per step (indicated by branching points). This process dissected a fraction that only contained the 60S large ribosomal subunit (highlighted in cyan). For each class, 3D averages of iteration 25 are displayed as 2D slices. Figure adapted from De Teresa and Goetz et al., 2021, joint manuscript.

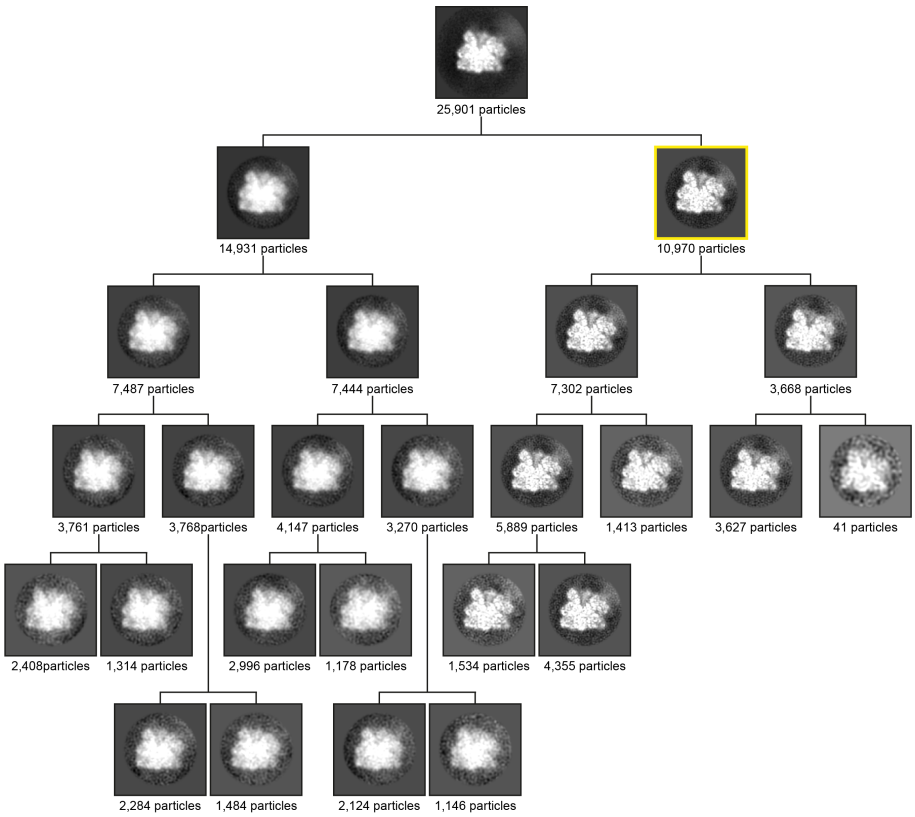

Figure 20: Cytosolic defocus ground truth ribosomes hierarchically 3D-classified. Starting from 25,901 M-refined particles, ribosomes were clustered into two classes at each step (indicated by branching points). A well-aligned class was extracted (yellow box) which could be refined to a resolution of 9.3 Å in M (Tegunov et al. 2021). More than half of the particles ended up in poorly defined classes (left branch). For each class, 3D averages of iteration 25 are displayed as 2D slices. Figure adapted from De Teresa and Goetz et al., 2021, joint manuscript.

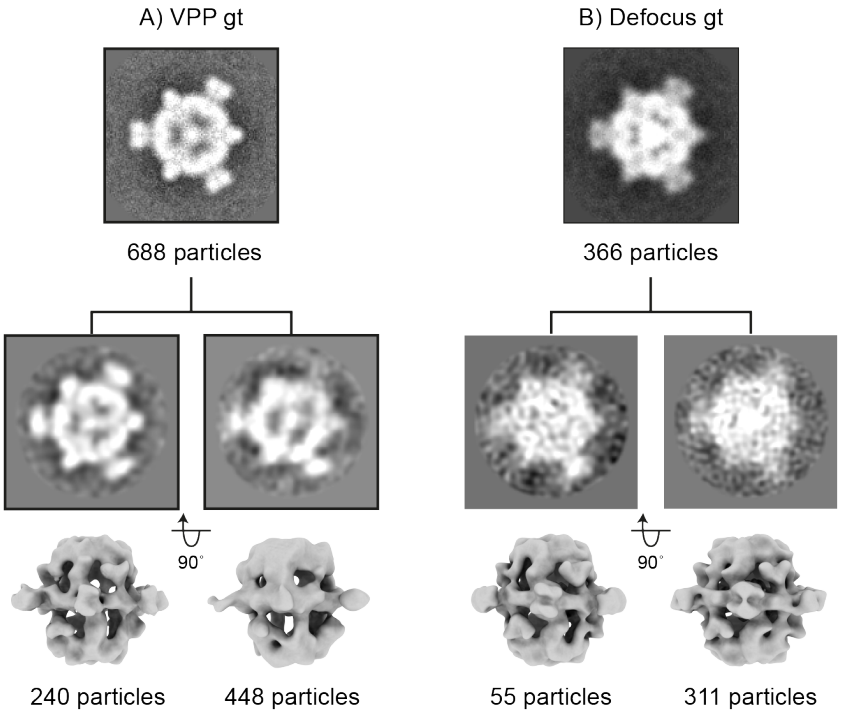

Figure 21: VPP and defocus ground truth FAS 3D classifications. FAS annotated in A) VPP and B) defocus ground truth (gt) datasets and 3D-refined with applied D_3 symmetry. For both, two 3D classes were separated (without specified symmetry and indicated by branching points) of which one was better aligned than the other. The resulting classes were 3D refined in RELION with applied D_3 symmetry and for defocus data also in M (Danev et al. 2017). For each class, 3D averages of iteration 25 are displayed as 2D slices or post-processed averages (bottom). Figure adapted from De Teresa and Goetz et al., 2021, joint manuscript.

5.1.4.2 DeePiCt workflow design

The established ground truth annotations in *S. pombe* cryo-ET data enabled training and testing of supervised deep-learning networks. The DeePiCt workflow is python-based and consists of two CNNs implemented as independent Snakemake procedures (Mölder et al. 2021): A 2D CNN segments cellular compartments, such as organelles and cytosol, and a 3D CNN localizes particles (macromolecules such as ribosomes) and predicts cellular features (such as membranes, nuclear pore complexes (NPCs) and cytoskeletal elements). The combination of both networks has two advantages: compartment segmentations can optimize particle localizations (e. g., cytosol masking reduces false positive hits in other organelles) and provide cellular context to macromolecules, such as direct organelle interactions.

The CNNs were designed on the basis of the U-Net architecture (Figure 22) (Ronneberger et al. 2015), which uses a data augmentation strategy to overcome limitations by small training data sets such as the 10 ground truth VPP tomograms. The input is either 2D or 3D tomography data with binary masks of ground truth annotations of the cellular features to be learned. Raw tomograms exhibit different signal-to-noise ratios due to varying sample thicknesses and acquisition parameters, especially defocus values and the usage of the VPP. To account for these differences, the user can employ an initial pre-processing step which adjusts the tomogram's amplitude spectrum to match that of a tomogram with high image contrast (Figure 22 top). For example, the amplitude spectrum of a VPP tomogram acquired on a lamella of around 110 nm thickness was used as reference (cf. Figure 18 A).

The cellular compartment segmentation task was implemented in 2D as this is faster and less computationally expensive. 2D operations were feasible for organelles and cytosol as they are large and easy to be recognized on a tomographic slice. Data was augmented by random flipping and rotation in 90° steps of input tiles. Particle picking was performed in 3D since macromolecular complexes are much smaller than organelles and have finer structural details. Thus, they require more dimensional sampling and per-particle adjustable model parameters to facilitate localization in cryo-electron tomograms. 3D input data was extended by adding noise (salt-and-pepper or Gaussian), and applying random translations, stretching and compression (elastic deformations), and rotations.

The network architecture for both 2D and 3D networks consists of two symmetric paths, one for down and one for up sampling (Figure 22 middle). The CNN's depth (D) is defined by the number of max pooling operations along the spatial axes to contract the data. Successive up-sampling from the deepest point by concatenation with maps from the down-sampling path or padding with zeros, returns the output at the original resolution. On each level, convolutional layers that basically involve application of filters and a rectified linear unit (ReLU) to the input data, result in feature maps. The network adjusts these filters over time of the training process. The down and up sampling paths are therefore also called encoder and decoder. In the DeePiCt implementation, the number of feature maps on the first level of the encoder path, called initial features (IF), is variable and can be adjusted per target structure to be learned. On each subsequent layer, a defined number of two filters are applied. In addition, hyperparameters of batch normalization (BN) and optional dropout are implemented on each layer. BN normalizes the output of the previous layer and thereby standardizes the input of the current layer. Dropout is a method for regularization that randomly drops nodes of the CNN. Both BN and dropout are used to avoid overfitting of the model and to accelerate the training by reducing the number of epochs required for the network to converge (Ioffe and Szegedy 2015, Srivastava et al. 2014).

The 2D CNN for compartment segmentation consists of five layers ($D = 5$) and 16 initial features ($IF = 16$). The 3D CNN architecture depends on the cellular feature to be learned and therefore D, IF and dropout parameters can be adjusted by the user. This accounts for the structural complexity, abundance, size of specific macromolecules and the amount and quality of training data. For FAS $IF = 16$ was found to be optimal whereas $IF = 4$ was sufficient for ribosome and membrane networks. A depth of two was employed for the three 3D networks.

During CNN training, the output is compared to the input after each run through the network. An error is calculated using Adam optimizer and the dice loss function. Over time and depending on the number of epochs (repetitions of learning cycles) the loss function should drop off to a minimal error, which indicates that the training has converged.

Trained CNNs can readily be applied to unseen tomograms. In the case of the 2D CNN, pixel-based compartment slices are predicted and in a post-processing step combined to a 3D volume (Figure 22 bottom). False positives are further removed by thresholding and applying a 1D Gaussian filter along the z-axis.

The 3D CNN outputs a scoring matrix, which is either converted to particle coordinates by clustering, cluster size filtering and centroid fitting in the case of macromolecule localizations (ribosomes and FAS), or voxel-based clusters by thresholding and cluster size filtering for membranes, NPCs and cytoskeletal elements. In a post-processing step, predictions can be integrated and optimized with the contextual information (e.g., provided by the 2D CNN, Figure 22 bottom). Particle coordinate lists can be intersected with compartment masks (e.g. ribosomes with the cytosol), clusters in contact with organelles selected (e.g., NPC predictions with the nucleus), or particles colocalized in proximity to specific organelles (e.g., mitochondrion-bound ribosomes). In addition, predictions can be evaluated based on previous (ground truth) annotations if they are provided (s. chapter 5.1.4.3 performance analysis).

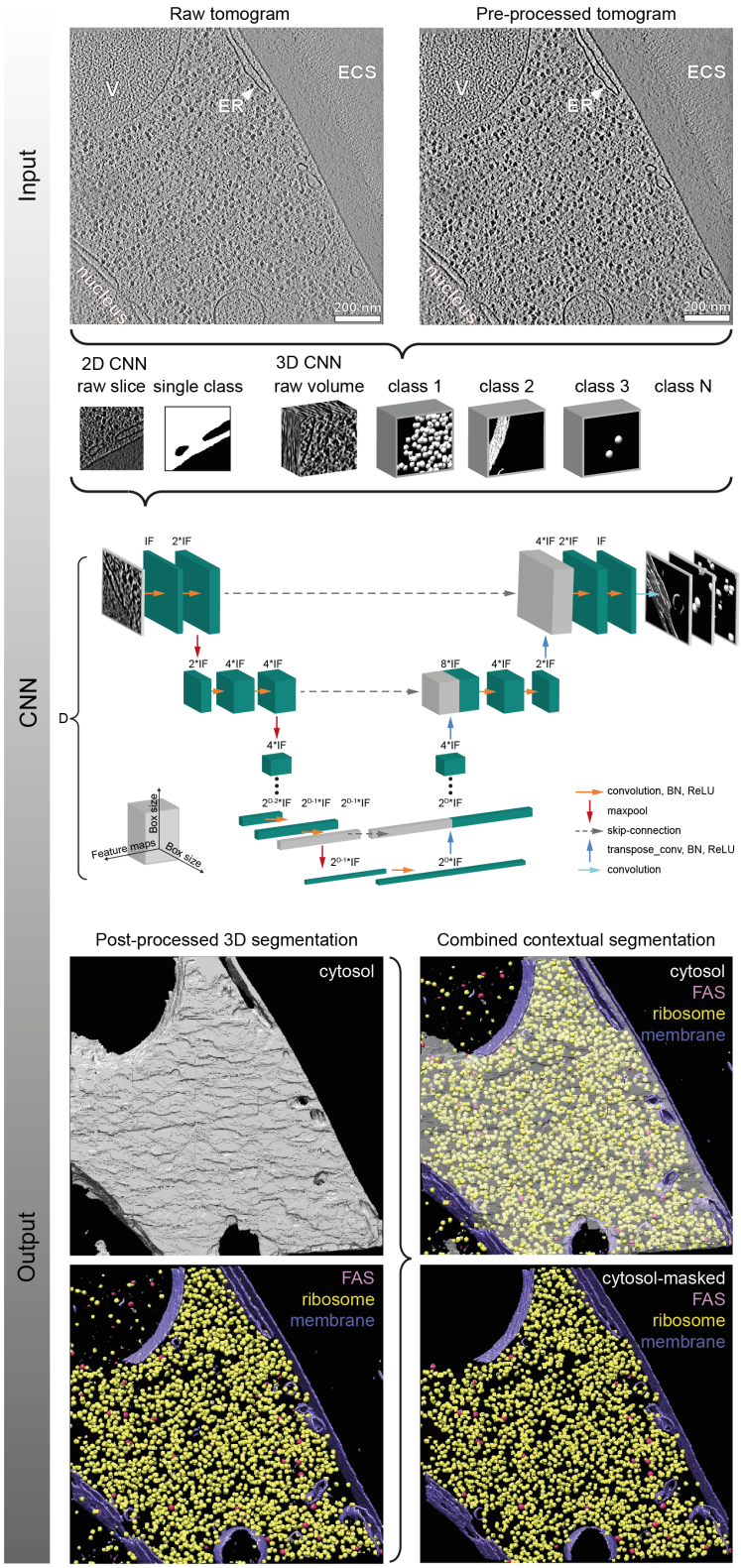
Input
CNN
Output
Raw tomogram
Pre-processed tomogram
V
ER
ECS
nucleus
200 nm
2D CNN
raw slice
single class
3D CNN
raw volume
class 1
class 2
class 3
class N
IF
2*IF
4*IF
8*IF
D
Feature maps
Box size
convolution, BN, ReLU
maxpool
skip-connection
transpose_conv, BN, ReLU
convolution
Post-processed 3D segmentation
Combined contextual segmentation
cytosol
FAS
ribosome
membrane
cytosol-masked

Figure 22: DeePiCt workflow. Raw tomography data can be input as a stack of 2D slices for compartment segmentations or 3D volumes for particle picking. Pre-processing by filtering to match the amplitude spectrum of a high contrast tomogram can be applied (top right). Together with binary masks for the features to be learned, the data is employed in a deep-learning network based on the U-net architecture (middle, Ronneberger et al. 2015). The user can specify initial features (IF), depth (D), batch normalization (BN) and dropout. Trained networks can directly be applied to unseen tomograms. Post-processing of predictions provides 3D segmentations of for example the cytosol in the case of a 2D CNN and FAS and ribosome coordinates, as well as membrane annotations from 3D CNNs (bottom left). The outputs from the different networks can be combined providing contextual information of for example all cytosolic ribosomes (bottom, right). Figure adapted from De Teresa and Goetz et al., 2021, joint manuscript.

5.1.4.3 DeePiCt performance analysis

The performance of DeePiCt networks trained in VPP data was first analyzed within the VPP domain. For this, 10 *S. pombe* VPP tomograms from the ground truth data set were used to train DeePiCt CNNs with specific hyperparameters D and IF. 2D CNNs were employed for cytosol and organelles (D = 5, IF = 16), and 3D networks for FAS, ribosomes and membranes (D = 2, IF = 16, 4 and 4, respectively). For the performance analysis within the same (VPP) domain, cross validations were carried out by training in eight tomograms and leaving two out for testing.

As CNNs are considered classifiers, their performance was evaluated by the quality of their predictions in comparison to the ground truth annotations. Therefore, precision and recall were calculated. Precision is a measure of specificity which describes how correctly the network recalls voxel or coordinates and thus classifies true negatives (TN) and true positives (TP). Recall defines how sensitive the network is. In detail, it measures how much of the positively classified data (P), which can include false negatives (FN), are detected as true positive. For each DeePiCt prediction a precision recall curve (PRC) was calculated using the following assumptions:

$$Precision = \frac{TP}{TP + FP} \tag{4}$$

$$Recall = \frac{TP}{P} = \frac{TP}{TP + FN} \tag{5}$$

Figure 23 shows an example precision recall curve (PRC) produced with the scikit-learn python package (Pedregosa et al. 2011) illustrating the area under the PRC (auPRC). The auPRC is a commonly used performance score for classifiers and does not require thresholding. In general, the higher an auPRC value, the better a classifier performs with a theoretical maximum score of 1. In practice, a network's performance is of high quality if the auPRC is between 1 and a baseline. This threshold is defined by the amount of true positive observations within the complete dataset.

In the case of the compartment segmentation pipeline, two 2D CNNs were trained with binary masks for either cytosol or all organelles combined. The average auPRC for cytosol and organelle predictions was 0.969 and 0.893, respectively. This means that in many cases the voxels of these compartments were precisely recovered. The baseline for cytosol and organelles in the ground truth data is 0.340 and 0.113, respectively. This reflects the fact that these compartments occupy a large volume fraction of the ground truth data.

3D networks were also evaluated based on the auPRC. In the case of particle localization, the precision and recall of coordinates within a user-definable radius (known or evaluated size of a particle, e. g., 10 voxel) was determined. VPP 3D networks for ribosomes and FAS localization, resulted in cross validation average auPRCs of 0.579 and 0.234, respectively. While the value for ribosomes means that DeePiCt precisely recalls many of the ground truth ribosomes, the average auPRC of the FAS network is rather low. However, this CNN still performs better than TM and is less time consuming than manual detection. Thus, this 3D CNN can be used for particle localization and subsequent subtomogram analysis but currently should not be used to predict trends in FAS numbers within cryo-electron tomograms. In general, for particle picking the baseline is close to zero due to the smaller number of labeled voxels in comparison to the complete ground truth.

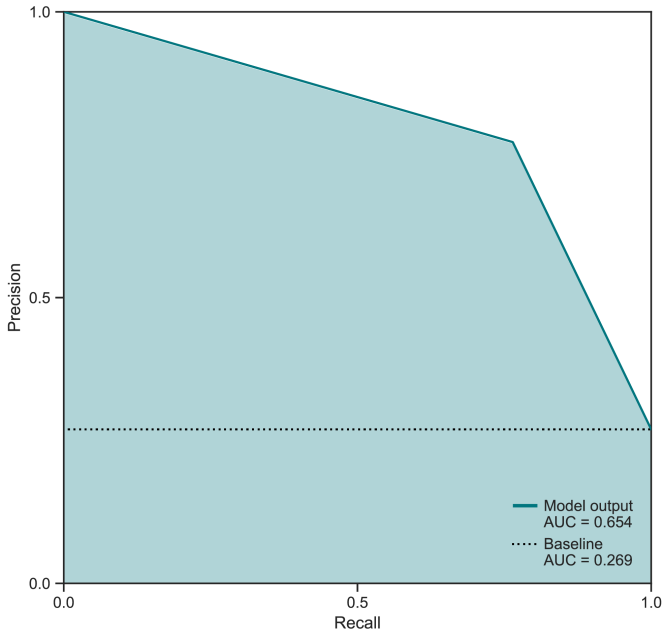

Figure 23: Performance analysis for cytosol segmentations predicted by a DeePiCt 2D CNN. An example precision recall curve (PRC) is plotted for five *S. pombe* tomograms (DEF, 1 h ED) in which cytosol volumes were predicted by a DeePiCt 2D CNN trained in 10 ground truth VPP tomograms. The area under the PRC (auPRC) is highlighted in mint blue.

These results highlight that DeePiCt reliably detects structures in cryo-electron tomograms. Its performance speed is also high in comparison to manual annotations and traditional approaches such as TM which in the case of FAS completely failed. Utilizing the EMBL high performance cluster configurations and hardware (Nvidia GPUs), TM required more than 5 h per tomogram (4x binned with dimensions of 928 x 960 x 500 voxel or 1,024 x 1,440 x 500 voxel and a resulting voxel size of 13.5 Å or 13.7 Å for data acquired with K2 and K3 cameras, respectively) with a search of 1,944 Euler angle combinations (Hrabe et al. 2012). Visual inspection and segmentations took several hours per tomogram depending on the cellular complexity and data quality. In comparison, the above described DeePiCt networks required several hours for training, but once this was accomplished, they could readily be applied to unseen tomograms. Predictions were obtained in only around 2 min for cytosol segmentations and around 30 min for ribosome localizations for the same tomogram dimensions as described above.

5.1.4.4 Domain adaptation of DeePiCt for ribosome localization

The reliable and fast performance of trained DeePiCt networks within the VPP domain opens the possibility of applying these CNNs to any cryo-electron tomogram. Leveraging pre-trained networks eliminates the need to generate more training annotations for new data. This facilitates data mining in large tomography datasets that were and will be acquired with the automated and streamlined cryo-sample preparation and data collection pipelines described above. Here, I applied trained VPP CNNs to *S. pombe* tomograms with different acquisition parameters (DEF), nutritional state (energy depletion, ED) and to another yeast species, namely *S. cerevisiae*.

First, learning transfer between VPP and DEF domains was tested for ribosomes. The 3D CNN trained in VPP was applied to the 10 DEF *S. pombe* tomograms from the ground truth data set and the network's average performance was 0.596 auPRC (Figure 24). In addition, the applicability to different nutritional states was tested in five fully expert-annotated DEF tomograms of *S. pombe* after 1h of energy depletion (ED). The resulting average auPRC was 0.688 (Figure 24, Supplementary Table S6). Applying this network also to another yeast species was evaluated on three fully expert-annotated *S. cerevisiae* DEF tomograms for each normal nutrient state and 1 h ED. In both cases, the VPP 3D CNN for ribosomes performed well with average auPRCs of 0.828 and 0.708, respectively (Figure 24, Supplementary Tables S9 and S11).

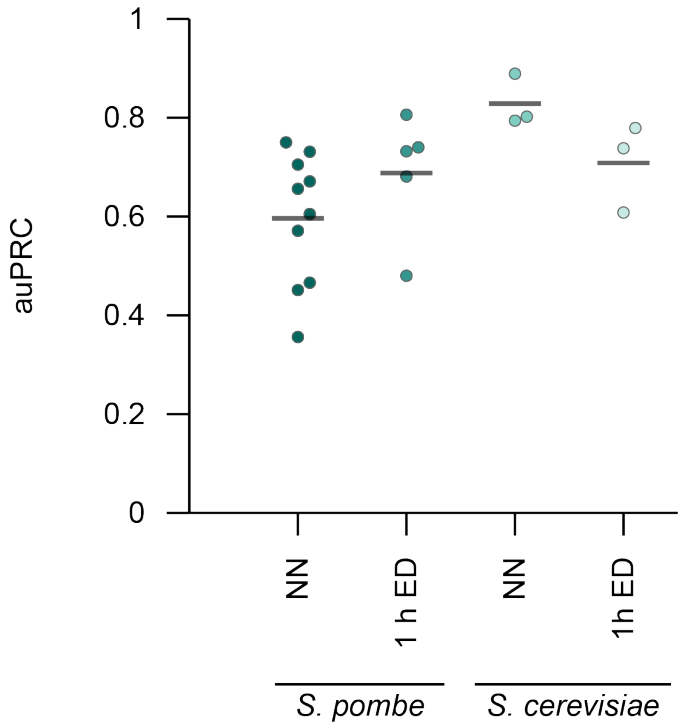

Figure 24: Performance analysis for ribosomes predicted by a DeePiCt 3D CNN trained in VPP and applied to DEF. In comparison to ground truth annotations in defocus data for 10 *S. pombe* normal nutrient (NN) state, five *S. pombe* 1 h energy depletion (ED), three *S. cerevisiae* NN and three *S. cerevisiae* 1 h ED tomograms, the network resulted in average auPRCs of 0.596, 0.688, 0.828 and 0.708, respectively. Average values are indicated by grey horizontal lines.

5.1.4.5 Structural analysis of different DeePiCt-predicted particle populations in the unperturbed *S. pombe* cytosol

The establishment of high performing DeePiCt networks renders this method a valuable tool for pattern recognition in cryo-ET and in particular for macromolecular structural analysis in the cellular context. The trained VPP 2D and 3D CNNs were thus applied to the 10 DEF tomograms of *S. pombe* in normal nutrient conditions, particles structurally analyzed in RELION and compared to the ground truth annotations. An example tomogram and its assembled 3D segmentation provided by DeePiCt is shown in Figure 25. It readily visualizes the crowded *S. pombe* cytosol occupied by different ribosome species and the fatty acid synthase. In agreement with the performance analysis, the visual output is comparable to the ground truth annotations (Figure 26). The obtained DeePiCt-predicted particle lists were further

used for subtomogram averaging and 3D classifications in RELION to dissect different subpopulations.

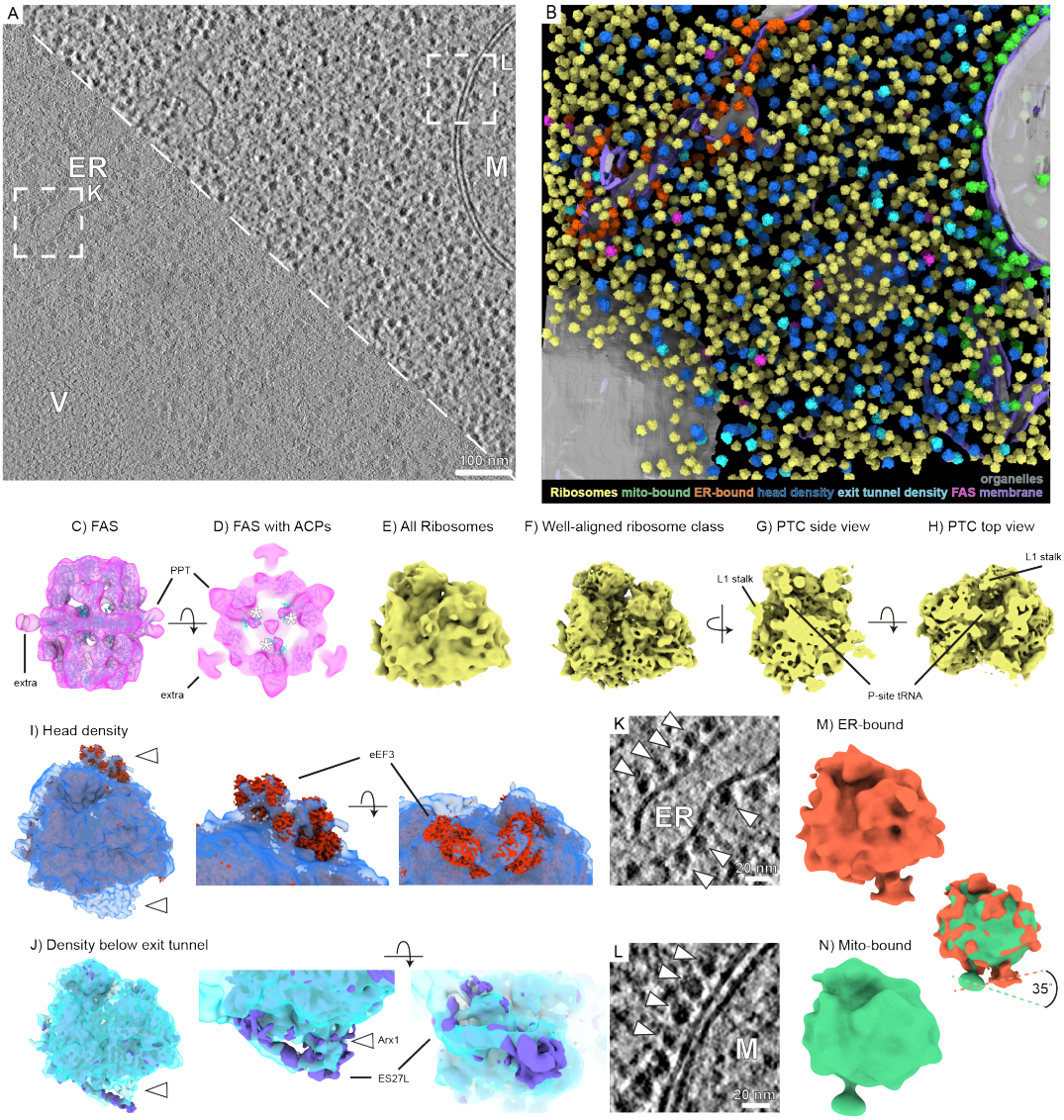

Figure 25: DeePiCt predicts particle populations in their cellular context. A) 2D slice of a raw *S. pombe* DEF tomogram (bottom left triangle) and after amplitude spectrum-matching (top right triangle). Ribosomes in the crowded cytosol (abundant dark objects) and organelles such as a vacuole (V), a mitochondrion (M, mito) and ER (highlighted dashed box K) are observable. Different z-slices of the highlighted areas (dashed boxes) are depicted in K and L. B) The predicted 3D segmentations from DeePiCt networks trained in VPP data mine organelles (grey), membranes (purple), FAS (pink) and ribosomes (yellow). Ribosomes were further analyzed by 3D classifications (focused on head (dark blue) and exit tunnel densities (cyan)) or by integrating the contextual information provided by the organelle segmentations (mito-bound ribosomes (green) and ER-bound (orange)). C-N) Subtomogram averages from predictions in all 10 DEF ground truth tomograms. C) The 3D-refined FAS density (pink) from 108 particles resembles the typical barrel-like shape and matches the published *S. cerevisiae* structure (cyan, PDB 2uv8 (Leibundgut et al. 2007)). Per half dome, along the equatorial plane of the α-wheel, three densities fitting the phosphopantetheine transferase (PPT) and three extra, unassigned densities can be observed. D) Cross-section through the half dome reveals three densities close to the α-wheel which fit acyl carrier proteins (ACPs, white asterisks). E) Subtomogram average of all 26,866 cytosolic ribosomes (yellow). F) Subclass of 5,815 cytosolic ribosomes detected in 3D classifications and refined to 9.4 Å in M. G-H) Cross-sections through the average in F show the peptidyl transferase center (PTC) with a P-site tRNA and the L1 stalk facing the E-site. I) Subset of 3,348 ribosomes (dark blue) classified for an additional density close to the head of the 40S subunit and with extra density at the exit tunnel (white arrowheads). The eukaryotic elongation factor eEF3 (red, EMDB 12062 (Ranjan et al. 2021)) could be assigned to the additional head density. J) Classification for the extra density below the exit tunnel recovered 1,503 cytosolic ribosomes (cyan). The *S. cerevisiae* ribosome with ES27L in a particular configuration fits the extra density (left, purple, EMDB 1667 (Becker et al. 2009), PDB 3izd (Armache et al. 2010)). The remaining density right below the exit tunnel (white arrowhead) fits different factors with a MetAP-like fold such as Arx1 (purple, EMD-3151 (Greber et al. 2016)). K-L) Different z-slices of the areas highlighted in A with ribosomes (white arrowheads) decorating ER and a mitochondrion (M). M) Density of 249 ribosomes bound to the ER membrane via a linker. N) Subtomogram average of 519 mitochondria-bound ribosomes with a connecting density to the membrane. Both sub-classes interact with the respective organelle membranes at different angles with an offset of around 35°. Figure adapted from De Teresa and Goetz et al., 2021, joint manuscript.

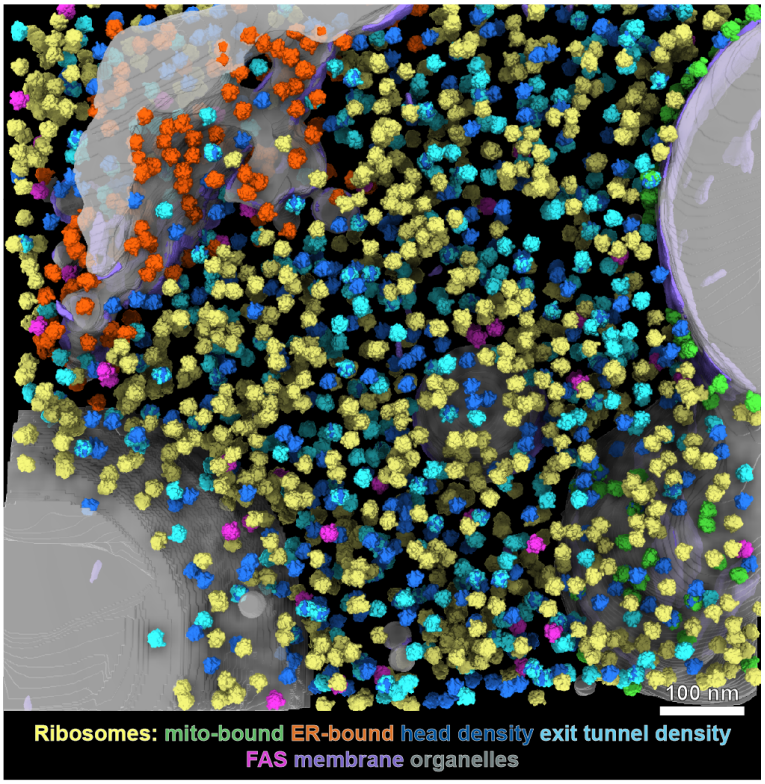

Figure 26: Ground truth annotations of the defocus tomogram depicted in Figure 25. Comprehensive annotations for organelles (grey), FAS (pink), ribosomes (yellow) with subsets displaying extra densities close to the 40S head (dark blue) and the ribosomal exit tunnel (cyan) as well as mitochondria-bound (green) and ER-bound (orange) particles. Membranes (purple) were predicted by DeePiCt. Data jointly produced with Irene De Teresa.

For FAS, 108 particles were localized which is less than the 366 instances in the defocus ground truth annotations. Nevertheless, a subtomogram average at a resolution of 28 Å (with applied D_3-symmetry) resembled the heterododecameric ($\alpha 6 \beta 6$), 2.6-megadalton type I FAS complex with the particular barrel-like shape (Figure 25 C). As neither *S. pombe* and not any cryo-FIB lamella-derived cryo-ET FAS subtomogram averages are publicly available, the density was compared to published X-ray crystallography or single particle cryo-EM structures of other yeast species. The fact that it matches well with the published FAS structures of *S. cerevisiae* (Figure 25 C and D, PDB 2uv8, (Leibundgut et al. 2007)), *P. pastoris* (EMDB 12139, (Snowden et al. 2021)), and the defocus and VPP ground truth subtomogram averages (Figure 27), confirmed its structural integrity. At the equatorial plane along the α-wheel, three additional densities were observable. These could be assigned to the phosphopantetheine transferase (PPT), which acts as activation domain. Three additional densities could not be ascribed based on published structures. Inside each half dome, the three densities are located close to the α-wheel and to the ketosynthase (KS) domain (Figure 25 D). They fit acyl carrier proteins (ACPs), which shuttle the growing acyl chain to each catalytic site. The ACP's location within each half dome or absence of its density due to potential flexibility and substrate-shuttling dynamics have been associated with the activity of the whole FAS complex (Gipson et al. 2010, Jenni et al. 2007, Kastritis et al. 2017, Leibundgut et al. 2007, Singh et al. 2020). The particular localization of the ACPs that was observed here in the FAS subtomogram average derived from lamellae prepared within exponentially growing *S. pombe* cells was also resolvable in the ground truth DEF data, but not in VPP subtomogram averages. This is likely due to the previously observed hampering of high-resolution features in cryo-ET acquisitions with the VPP and thus fine structural details such as ACPs could not be resolved.

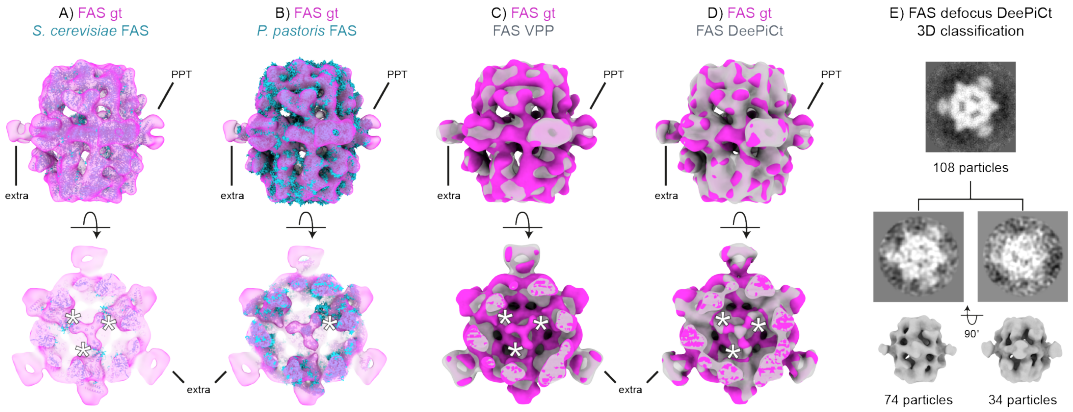

Figure 27: Comparison of FAS subtomogram averages from DEF ground truth and DeePiCt-predicted 3D classifications. A-B) The FAS ground truth (gt) subtomogram average fits the published structures of *S. cerevisiae* and *P. pastoris* (cyan, PDB 2uv8 and EMDB 12139) with ACPs close to the α-wheel (bottom, white asterisks). C-D) The FAS gt density also matches well the VPP and DeePiCt derived subtomogram averages. ACPs could not be resolved in the VPP data (D bottom, white asterisks). E) 3D classification of DeePiCt-predicted FAS in defocus-only tomograms. 2D slices after classification for 25 iterations without applied symmetry and 3D subtomogram averages of the refined classes with applied D_3 symmetry, are depicted. Figure adapted from De Teresa and Goetz et al., 2021, joint manuscript.

In the case of ribosomes, a total of 26,866 cytosolic ribosomes were localized by DeePiCt, matching the range of 25,901 ribosomes from the defocus ground truth annotations and in agreement with the performance analysis. The resulting subtomogram averages for the DEF and DeePiCt datasets, both at a resolution of 11 Å after M refinements, confirmed overall structural integrity of the eukaryotic ribosome (Figure 25 E and 28). Sub-nanometer resolution densities (5,815 particles at 9.4 Å for DeePiCt and 10,970 particles at 9.3 Å for DEF ground truth) were obtained for well-aligned classes recovered via 3D classifications (Figure 25 F, Figures 20 and 29). Here, the peptidyl transferase center (PTC) was clearly occupied by a P-site tRNA and the L1 stalk observed facing the E-site (Figure 25 G, H, Figure 28). The tRNA was not resolvable in the VPP dataset. Furthermore, hierarchical 3D classifications of ribosomes from defocus-only data (both DeePiCt predictions and ground truth annotations cf. Figures 20 and 29) sort out more than half of the particles into poorly defined classes, even when initial alignments were optimized in M (Tegunov et al. 2021). Moreover, a 60S large ribosomal subunit class could not be detected. Thus, VPP data seemed to be more suited for hierarchical 3D

classification due to the improved image contrast of the raw data. However, the observed density differences within the PTC show that defocus-only subtomograms provide higher-resolution information elucidating finer structural details.

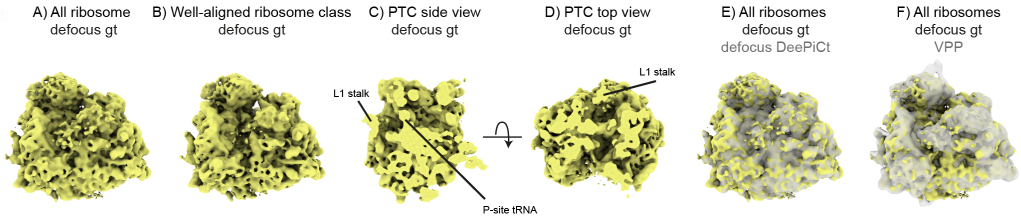

Figure 28: Comparison of ribosome subtomogram averages. A) Subtomogram average of all 25,901 ribosomal particles annotated in the defocus ground truth (gt) data set. B) A well-aligned class detected through 3D classifications could be refined in M to 9.3 Å resolution. C-D) Cross-sections through B reveal the peptidyl transferase center (PTC) occupied by P-site tRNA and the L1 stalk facing the E-site. E-F) The subtomogram average of all DEF gt ribosomes matches the DEF DeePiCt (grey, E) and VPP densities (grey, F). Figure adapted from De Teresa and Goetz et al., 2021, joint manuscript.

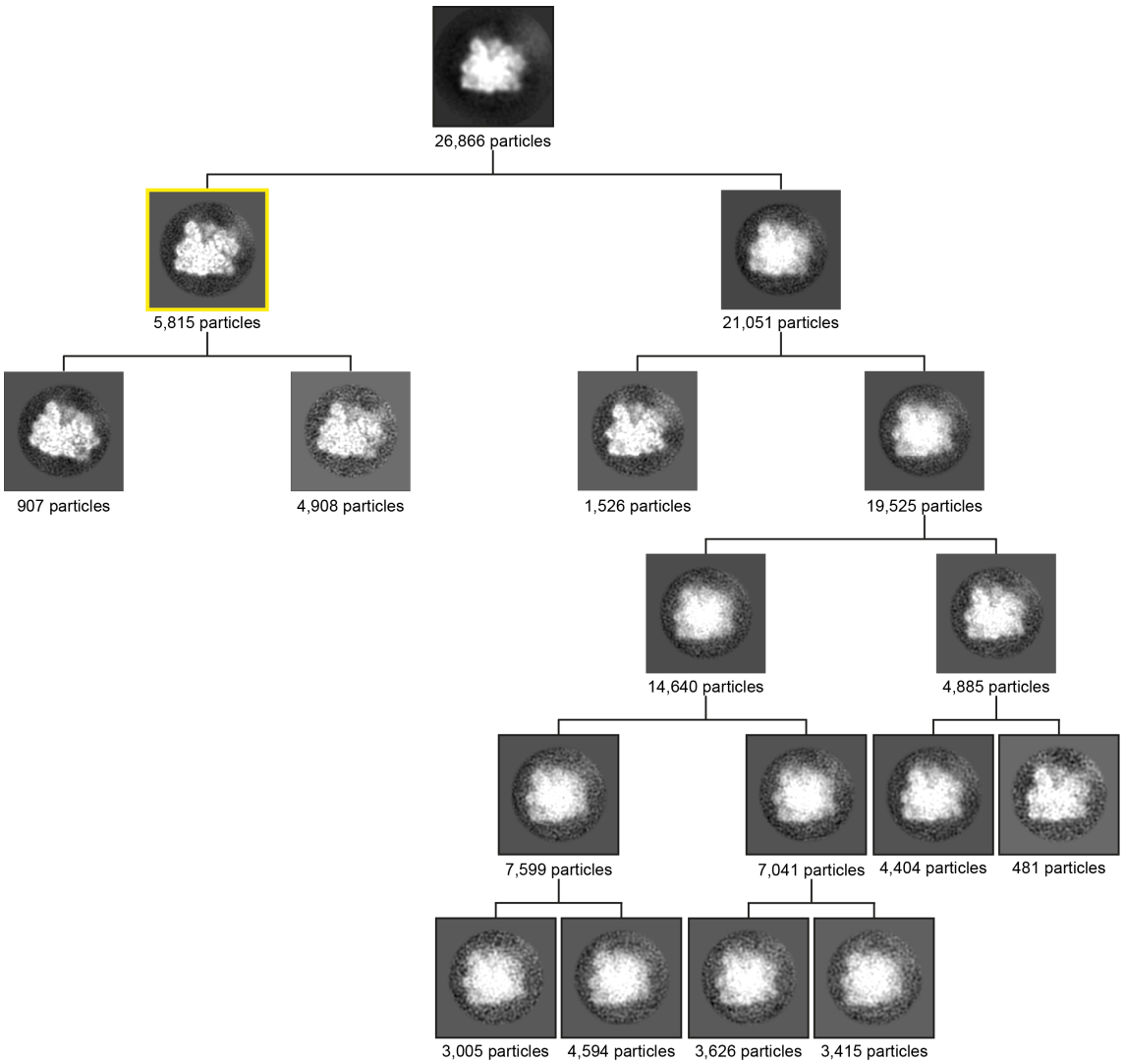

Figure 29: Hierarchical 3D classifications of ribosomes detected by DeePict in DEF. Starting from 26,866 M-refined particles, ribosomes were clustered into two classes at each step (indicated by branching points). A well-aligned class was extracted (yellow box) which could be refined to a resolution of 9.4 Å in M. More than 70 % of the particles ended up in poorly defined classes (right branch). For each class 3D averages of iteration 25 are displayed as 2D slices. Figure adapted from De Teresa and Goetz et al., 2021, joint manuscript.

In order to gain deeper insights into ribosome subpopulations within the *S. pombe* cytosol, 3D classifications of all DeePiCt-predicted ribosomes focused on the head region of the small subunit were performed. 3,348 ribosomes with extra densities at this location, as well as at the ribosomal exit tunnel, which was not included in the mask, were classified and refined to a resolution of 15 Å (Figure 25 I). Similar subtomogram averages were obtained from VPP and DEF ground truth annotations

(3,482 and 3,601 particles at 12 Å and 21 Å, respectively, Figure 30). In the defocus data, P- and E-site tRNAs, as well as the L1 stalk facing towards the E-site were clearly resolvable (Figure 30). Due to the lack of published *S. pombe* ribosome structures, the average was compared to the *S. cerevisiae* ribosome with the bound eukaryotic elongation factor eEF3 (EMDB 12062) which fits well into the extra head density (CC 0.8972, Figure 25 I, Figure 30). Its function is to facilitate binding of a new tRNA to the A-site via the aminoacyl-tRNA–eEF1A–GTP complex during translation (Andersen et al. 2006, Ranjan et al. 2021).

The extra density observed at the exit tunnel could not readily be assigned owing to the fact that many factors bind to this site. Focused 3D classifications at this location within all cytosolic DeePiCt-derived ribosomes recovered a subset of 1,503 particles with the additional exit tunnel density refined to 16 Å (Figure 25 J). A similar class was detected in defocus and VPP ground truth data (3,349 and 5,755 particles refined to 11 Å and 20 Å, respectively, Figure 31). The flexible 60S rRNA expansion segment in its exit configuration fits well into a part of the extra density (Figure 25 J). This orientation of ES27L has an implied function in translation fidelity. It is connected to the remaining density at the point where the growing nascent peptide chain exits the ribosome. Different factors are known to be recruited by ES27L and to bind the ribosome at the exit tunnel. The remaining density fits a domain with a MetAP-like fold, such as for example the methionine aminopeptidase (MetAP (Fujii et al. 2018)) and a domain of the N-terminal acetyltransferase A (NatA (Knorr et al. 2019)), which both co-translationally modify the nascent peptide chain. In addition, the *S. cerevisiae* nuclear export factor Arx1 which is supposed to be released in the cytosol upon maturation of the large subunit and its human homologue the translation regulator Ebp1, which was found to be bound to fully assembled 80S ribosomes, match the density below the exit tunnel (Figure 31, (Greber et al. 2016, Kowalinski et al. 2007, Wild et al. 2020)).

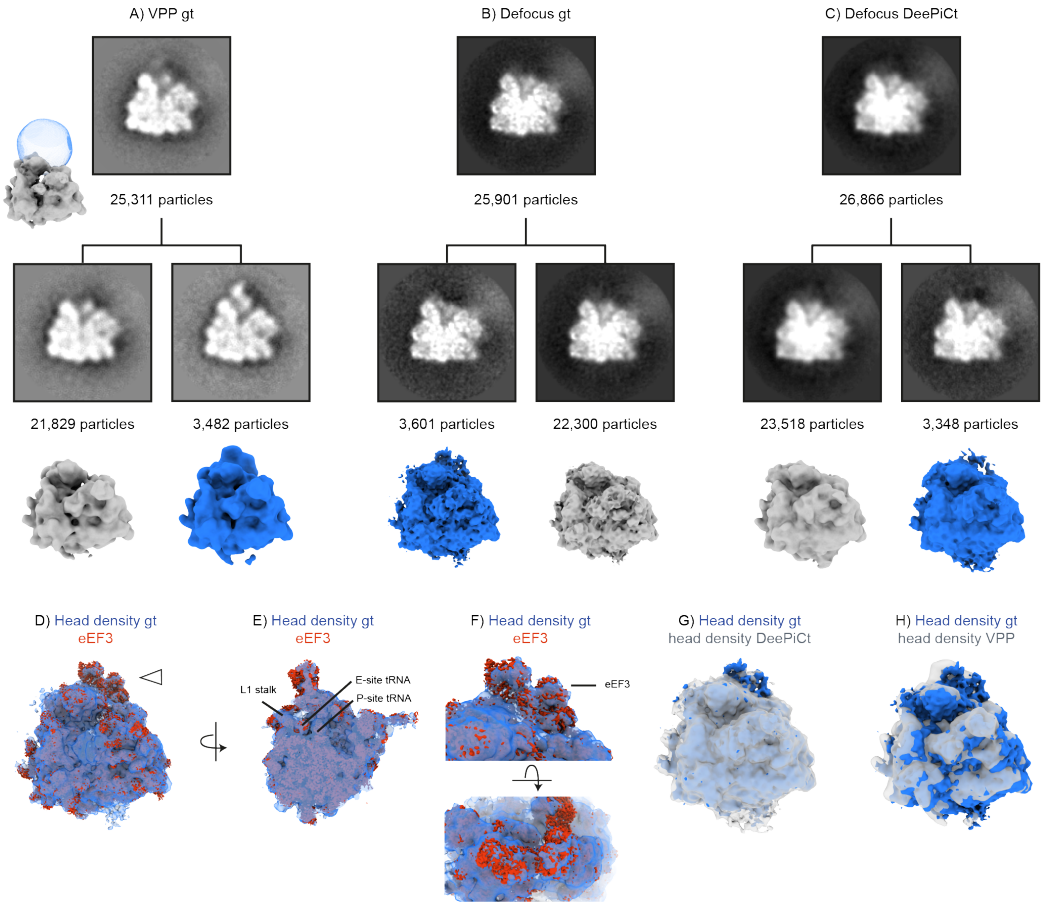

Figure 30: Focused 3D classification of an extra density close to the head of the 40S small subunit and subtomogram average comparison between datasets. A-C) 3D classifications of VPP ground truth (gt), DEF gt and DeePiCt-predicted cytosolic ribosomes focused on a density close to the 40S head. The used classification mask (blue sphere) is displayed in A. In the case of VPP gt data in A the extra head density can already be observed on the level of the 2D slice of the class average after iteration 25. D) Overlay of the subtomogram average from DEF gt data with the published *S. cerevisiae* eEF3-bound (white arrowhead) ribosome (red, EMDB 12062 (Ranjan et al. 2021)). E) Cross-section through D revealing the PTC occupied by E- and P-site tRNAs as well as the L1 stalk facing the E-site. F) Top views of eEF3 fitting the extra head density. G) and H) Overlays of DEF gt with DeePiCt-predicted and VPP densities (grey), respectively. Figure adapted from De Teresa and Goetz et al., 2021, joint manuscript.

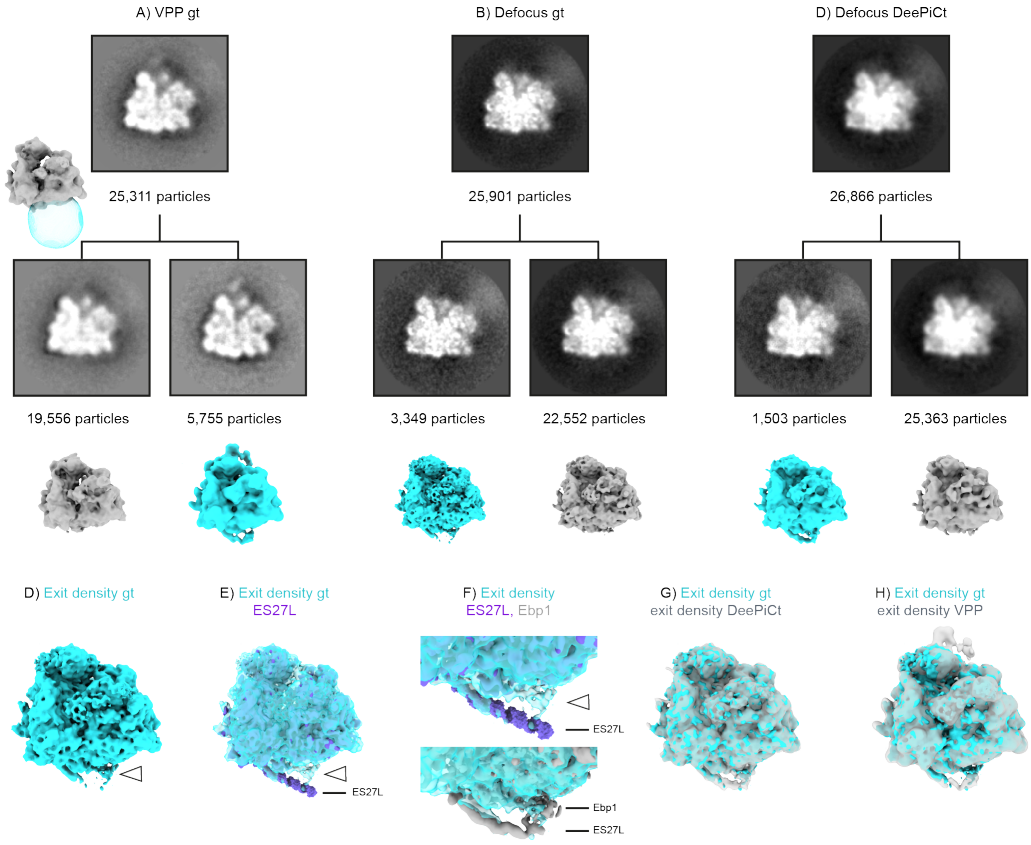

Figure 31: Focused 3D classification at the ribosomal exit tunnel and subtomogram average comparison between datasets. A-C) Hierarchical 3D classifications of VPP ground truth (gt), DEF gt and DeePiCt-predicted cytosolic ribosomes focused on an additional exit tunnel density. The used classification mask (cyan sphere) is displayed in A. 2D slices of 3D class averages after iteration 25 are depicted and the 3D-refined final averages (below). D) Subtomogram average of the DEF gt ribosome with extra exit tunnel density (white arrowhead). E) The ribosomal expansion segment ES27L (purple, PDB 3izd) fits well into a part of the additional density connecting the remaining density (white arrowhead) to the exit tunnel. F) Zoom into the exit tunnel area in E with the human Ebp1-bound ribosome (grey, EMDB 1068) fitted into the map. G) and H) The DEF gt subtomogram average matches well with the DeePiCt-derived and VPP gt densities (grey). Figure adapted from De Teresa and Goetz et al., 2021, joint manuscript.

5.1.4.6 Contextual DeePiCt predictions reveal ribosome-organelle interactions

Ribosomes bound to specific organelles, such as the ER, have been structurally described and enable co-translational insertion of nascent peptide chains into their destined compartments via specialized transporters (Pfeffer et al. 2015, Mahamid et al. 2016, Gold et al. 2017). For instance, ribosomes were previously detected to be attached to *in vitro*-purified mitochondria membranes (Gold et al. 2017). However, their in-cell configurations remain to be explored. As the segmentation and localization of macromolecules in the vicinity of specific organelles is quite tedious with traditional pattern recognition techniques, DeePiCt was employed to investigate its potential of gaining new biological insights. By synergizing compartment segmentation and particle picking networks, ribosomes were detected and analyzed based on their proximity to the ER and mitochondria. Ribosomes decorating specific organelles could already be observed in the raw 2D tomographic slices (Figure 25 K, L). Particles were picked within 25 nm distance to the respective organelle segmentations which were manually selected from the CNN predictions. 3D classifications of each organelle-related subset distinguished two classes: one with and one without a clear membrane density. This was also observed for defocus and VPP ground truth annotations (Figure 32). The recovery of classes without clear membrane density is likely due to the fact that the yeast cytosol is so crowded that ribosomes end up in random orientations in the close vicinity of ER and mitochondria. It can potentially also be emphasized by incorrect organelle and particle predictions.

In the case of the ER subset, 249 ribosomes from six tomograms revealed a connecting density from the exit tunnel to the organelle's membrane at a resolution of 34 Å (Figure 25 K, M). This average matches published structures (Becker et al. 2009, Gold et al. 2017, Mahamid et al. 2016) and was also found in defocus and VPP ground truth datasets (118 and 466 particles at 36 Å and 31 Å, respectively, Figure 32). It likely connects the ribosome to the translocon, which channels proteins into the ER or facilitates lateral insertion of membrane proteins. However, the direct interaction could not be resolved in the VPP subtomogram average despite the larger number of ER-bound particles. This is likely due to the VPP which hampers the fine, high-resolution features in cryo-electron tomograms.

Mitochondria-bound ribosomes (359 particles from three tomograms refined to 34 Å) were found to interact with the membrane at a different angle than at the ER (angular offset of around 35°, Figure 25 L, N). A connecting density originating from below the large subunit close to the interface with the small subunit could be detected in DEF (DeePiCt and ground truth) but not in the VPP dataset (Figure 33). It likely originates from a factor that connects the ribosome to the translocase of the outer membrane (TOM) complex for co-translational nascent peptide insertion (Avendano-Monsalve et al. 2020).

The findings for ribosomes bound to ER and mitochondria highlight the potential of using DeePiCt to explore particles in their cellular context. The high-throughput and sufficient performance render it a valuable tool to explore further datasets.

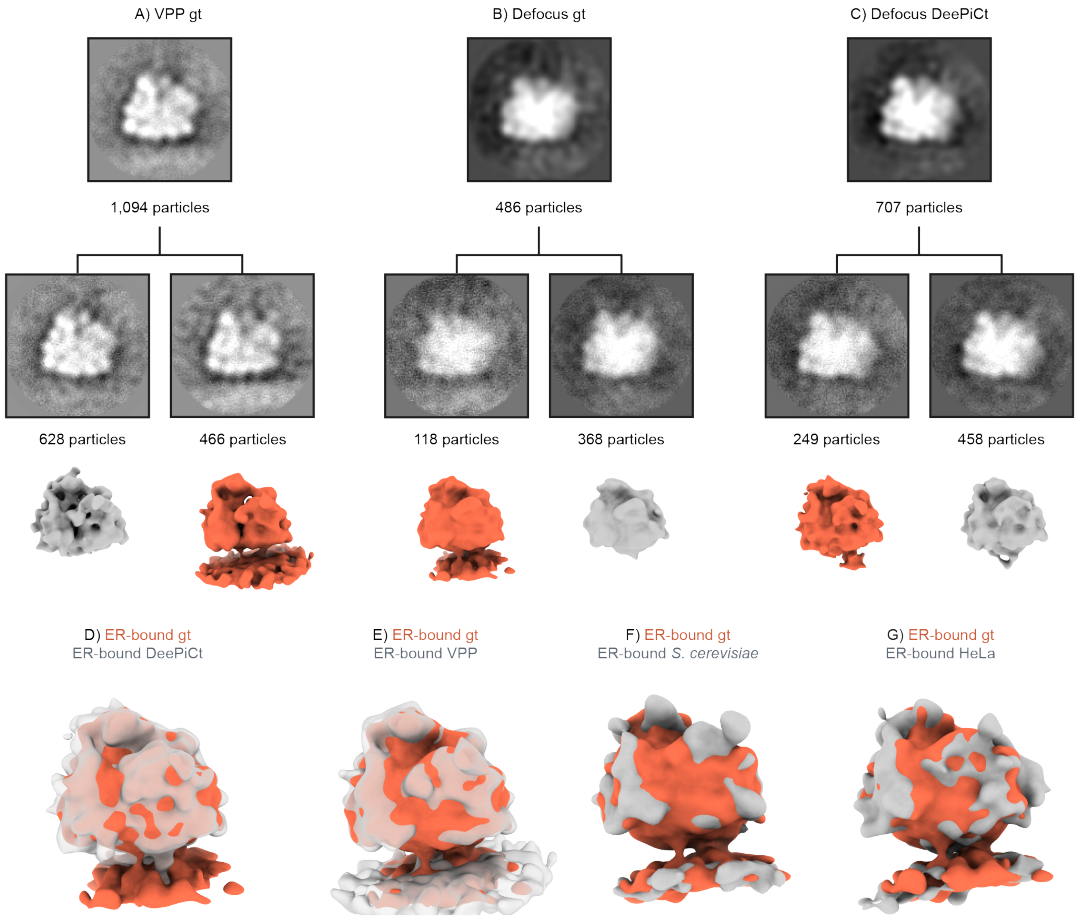

Figure 32: 3D classification of ER-bound ribosomes and subtomogram average comparison between datasets. A-C) Focused 3D classifications of ribosome subpopulations within 25 nm distance to the ER in VPP ground truth (gt), DEF gt and DEF DeePiCt datasets, respectively. The spherical mask positioned at the peptide exit tunnel indicated in Figure 31 A was used for focused classification. 2D slices of 3D class averages after iteration 25 (top) and the 3D-refined final averages (below) are depicted at similar thresholds revealing in all cases a class with and one without (partial) membrane density. D) and E) Subtomogram average of the DEF gt ribosome bound to the ER membrane (orange) overlaid with the DeePiCt-predicted and VPP densities (grey), respectively. F) and G) The density also fits well with published ER-bound *S. cerevisiae* (EMDB 3764) and HeLa (EMDB 8056) ribosomes (both grey), respectively. Figure adapted from De Teresa and Goetz et al., 2021, joint manuscript.

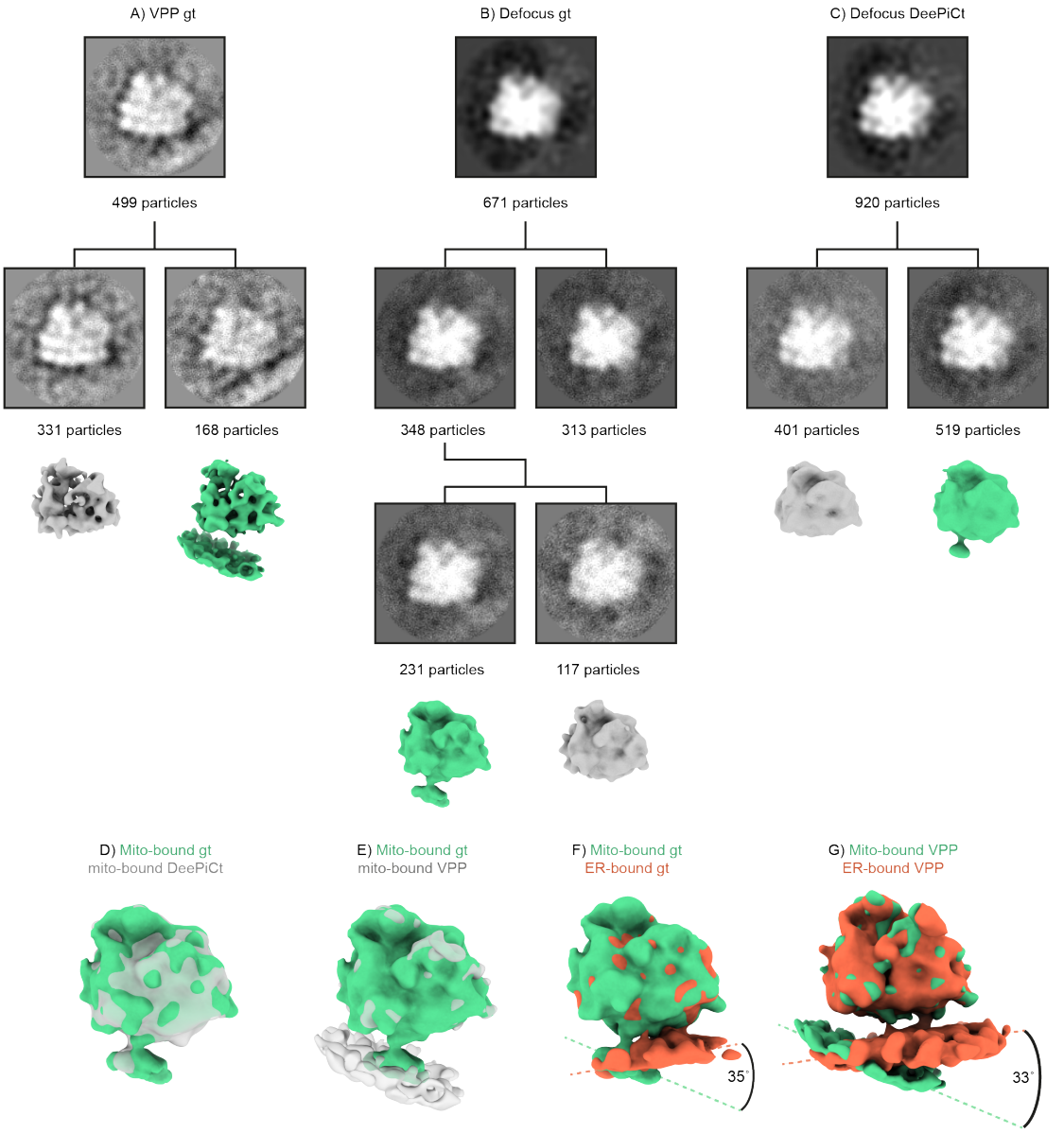

Figure 33: 3D classification of mitochondria-bound ribosomes and subtomogram average comparison between datasets and the ER-bound density. A-C) Hierarchical 3D classifications of all ribosome subsets found within 25 nm distance to ground truth annotations of mitochondria in VPP ground truth (gt), DEF gt and DEF DeePiCt datasets, respectively. The spherical mask positioned at the peptide exit tunnel indicated in Figure 31 A was used for focused classification. 2D slices of 3D class averages after iteration 25 (top) and the 3D-refined final averages (below) are depicted revealing in all cases a class with and one without membrane density. D) and E) Subtomogram average of the DEF gt ribosome bound to the mitochondrion membrane (green) matches the DeePiCt and VPP densities (grey), respectively. F) and G) Overlays between mitochondria-bound (green) and ER bound (orange) DEF gt and VPP subtomogram averages. The structural analysis reveals different interaction surfaces of the ribosome with ER and mitochondria with an angular offset of 33-35°. Figure adapted from De Teresa and Goetz et al., 2021, joint manuscript.

5.2 Nutrient-dependent reorganization of the yeast cytosol

The results described in chapter 5.1 render in-cell cryo-electron tomography a higher-throughput method. Sample preparation was optimized, cryo-FIB milling automated with SerialFIB and tomography data acquisition streamlined in SerialEM. The developed DeePiCt pipeline further allowed for fast and reliable annotation of the generated large datasets.

These tools enabled me to explore molecular crowding inside native, cryo-preserved yeast cells. As mentioned above, the yeast cytosol transitions upon energy depletion from a liquid- to a solid-like state with an expected change in global and local macromolecule distributions. The cytosolic reorganization upon nutritional stress was therefore analyzed in wild-type *S. cerevisiae* and *S. pombe*. Over 370 tomograms were collected visualizing the reshaped yeast cytosol upon nutrient scarcity. Cells were fully deprived of energy for different time windows using synthetic complete medium lacking sugars, supplemented with the glycolysis inhibitor 2-deoxy-D-glucose and the respiratory chain inhibitor Antimycin A (cf. methods chapter 4). This treatment has been shown to lead to an immediate arrest of cell cycle and metabolism similar to a dormant state achieved by long periods of starvation (Munder et al. 2016). In addition, *S. pombe* cells were glucose-depleted for four days in order to compare this more natural type of nutrient limitation with the severe response to energy depletion. As a control, more than 200 tomograms were collected from exponentially growing cells in normal nutrient (NN) conditions. The acquired and reconstructed data sets are summarized in Table 2 (acquisition parameters in Supplementary Table S2). In the following sections I will compare the different nutritional states and the observed changes, first on the level of organelle morphologies, followed by characterization of diverse cytosolic assemblies, and finally, on the fine detail of conformations of protein complexes in cryo-electron tomograms.

Table 2: Cryo-electron tomography summary of yeast cells grown in varying nutrient conditions. Further details including acquisition parameters are described in Supplementary Table S2.

Sample	# Sessions	# Tomograms
S. pombe NN	6	138
S. pombe 1 h ED	4	117
S. pombe 3.5 h ED	2	76
S. pombe 17 h ED	1	34
S. pombe 4 d glucose depletion	1	31
S. cerevisiae NN	3	64
S. cerevisiae 1 h ED	2	62
S. cerevisiae 6 h ED	2	56
SUM	21	578

5.2.1 Cryo-electron tomography of the yeast cytosol in normal nutrient state

Tomograms of cryo-FIB-milled lamellae revealed the crowded nature of the yeast cytosol under normal nutrient conditions (*S. cerevisiae* Figure 34 and *S. pombe* Figures 18 and 25). Mitochondria were elongated and displayed ATP synthases decorating their cristae. This is in line with tubular mitochondria networks that have been detected in light microscopy studies (Jakobs et al. 2020). *S. cerevisiae* cells usually contain around two medium-sized and *S. pombe* several smaller, spherically shaped vacuoles (Li and Kane 2009, Zhou 2004). Structured filaments that could be observed are microtubules and actin filaments, which together with septins in the case of *S. pombe*, constitute the cytoskeleton. Macromolecules such as ribosomes or the fatty acid synthase could also be detected by eye. These complexes were evenly distributed in NN conditions, as confirmed by automated picking allowing for subsequent quantitative characterization.

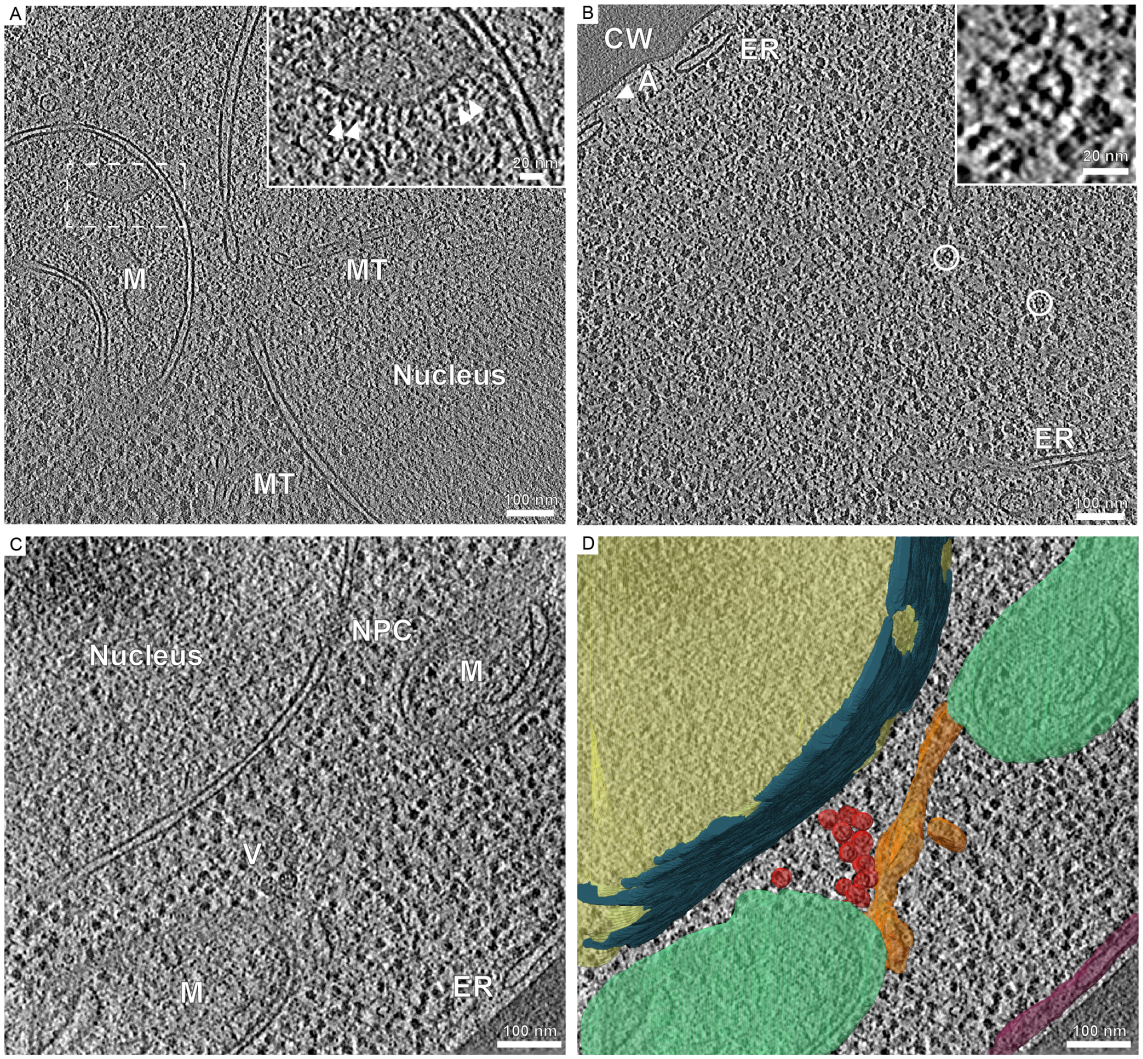

Figure 34: Cellular landscapes of exponentially growing *S. cerevisiae* cells. A) 2D slice of a VPP tomogram depicting the cytosol and an elongated mitochondrion (M). The inset shows the highlighted area (dashed box) with the mitochondrion's cristae decorated by ATP synthases (white arrowheads). Inside the nucleus and within its periphery microtubules (MT) are observable. B) The tomographic slice acquired with a VPP visualizes the crowded cytosol with ribosomes (abundant dark shapes) and FAS (white circles) with a typical barrel-like shape (inset). ER can be observed close to the cell wall (CW) where an actin filament (A) is located close to the plasma membrane. C-D) Defocus tomogram Gaussian low-pass filtered (sigma = 3) to enhance image contrast for manual segmentations in D. The nucleus (yellow) surrounded by the nuclear envelope (petrol) is connected to the cytosol via nuclear pore complexes (NPCs). The cytosol contains elongated mitochondria (M, green), vesicle (V, red) in close proximity to a tubular compartment (likely Golgi apparatus, orange) and the ER (purple) close to the cell wall. Segmentations visualized in 3D.

5.2.2 Nutritional stress induces changes in organelle morphologies and lattice formation on *S. pombe* mitochondria surfaces

Morphological changes of mitochondria could be observed in cryo-electron tomograms of both yeast strains upon different periods of energy depletion and four days of glucose depletion. Under normal nutrient conditions, these dynamic organelles are tubular (cf. Figures 18 A and 34, (Jakobs et al. 2020)). Here, in tomograms of nutritionally stressed yeast cells, they appeared smaller with more spherical shapes and contained ATP synthases decorating cristae membranes (Figure 35). Mitochondria fissioning in *S. pombe* upon glucose starvation has also previously been shown in light microscopy experiments and electron tomography at room temperature (Liu et al. 2019, Zheng et al. 2019). Here, mitochondrion fission could directly be observed in cryo-electron tomograms but on the tomogram level no clear structure was identified at their neck (Figure 35 D). Furthermore, energy-depleted *S. pombe* cells exhibited an additional lattice on the mitochondrion outer membrane (MOM) (Figure 35 A-D). These macromolecular assemblies could be observed in 18-24 % of the acquired *S. pombe* tomograms depending on the duration of energy depletion (Table 3). The structural signature is reminiscent of cryo-EM maps of Dnm1 assemblies (Francy et al. 2017, Ingerman et al. 2005, Mears et al. 2011). This GTPase is a dynamin-related protein and has been shown to be required for mitochondria division. It can bind to the outer membrane, where it self-assembles which is supposed to drive membrane constriction upon GTP hydrolysis (Mears et al. 2011). Further segmentation and subtomogram averaging of the surface lattice will likely identify the components of this energy-depletion induced structure. Dnm1 assemblies might be arrested in this membrane bound state due to the lack of energy which is required for GTP hydrolysis and subsequent membrane fission.

Another organelle changing its morphology upon nutritional stress is the lipid droplet (LD). LDs are metabolic compartments confined by a monolayer serving multiple functions such as storage of TAGs among others (Mahamid et al. 2019, Rogers et al. 2021). In normal nutrient conditions, LDs have a spherical shape. Upon energy depletion, they showed altered morphologies (Figure 36 A-F). Some were engulfed by vacuoles, others connected to the nuclear envelope or displayed deformations. In several cases, peripheral crystalline layers were visible which are caused by lipid phase transition. This happens when TAGs are broken down by lipases to mobilize

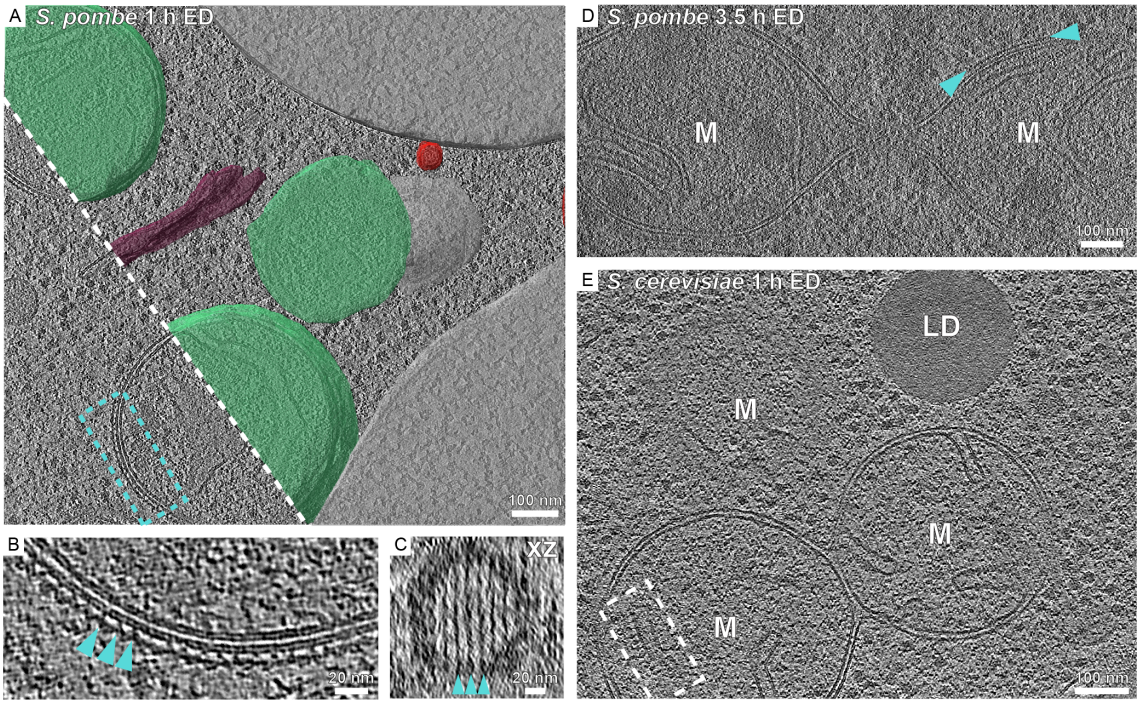

Figure 35: Mitochondria morphologies upon nutritional stress revealed by cryo-ET. A-C) Spherically shaped mitochondria (M, green) were observed in 2D tomographic slices of *S. pombe* upon ED. 3D segmentations of ER (purple), vesicle (red) and vacuoles (grey) are displayed. B) A surface lattice in direct connection (cyan arrowheads) to the mitochondria outer membrane (MOM) could be observed in this zoom of the highlighted area in A (cyan, dashed box). C) Top (xz) view of the lattice in B revealed regular interspacing of this structure (cyan arrowheads). D) Mitochondrion (M) division was directly observed in *S. pombe* by cryo-ET after 3.5 h ED. A MOM-lattice was located close to the fission point (cyan arrowheads). E) Fractionation of mitochondria (M) was also detected in *S. cerevisiae* after 1 h ED. The highlighted area (dashed box) showed ATP synthases decorating mitochondrion cristae. Tomographic xy slices are displayed unless marked otherwise.

fatty acids as energy source (Figure 36 A, B, D, (Mahamid et al. 2019, Rogers et al. 2021)). However, the changes in LD morphology may also in part be attributed to the highly heterogeneous and dynamic character of this organelle (Zhang et al. 2017).

LDs were also observed in connection to vacuoles. In *S. pombe* these organelles were fractionated by monolayers of FAS. Vacuole fractionation can also be caused by hyperosmotic stress. As this leads to a reduction in cytosolic volume, the fractionation of vacuoles into smaller vesicles was suggested to maintain osmotic pressure in the

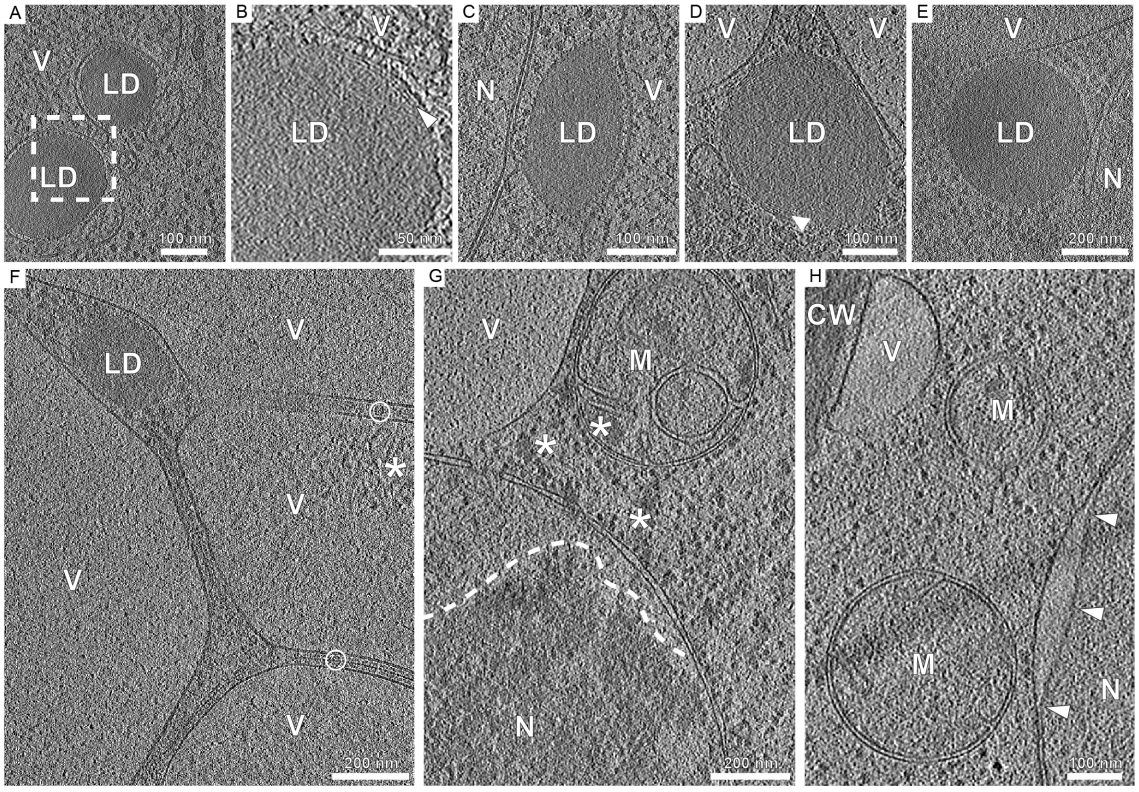

Figure 36: Cryo-ET revealed nutrient-stress induced alterations of organelle morphologies. A-F) Changes in LD morphologies could be observed in 2D tomographic slices of yeast cells upon nutrient scarcity. A) In *S. pombe* after 1 h ED, lipid droplets (LD) were invaginated by membrane-bound compartments which are likely vacuoles based on their texture (V). B) Zoom into the highlighted region in A (dashed box) revealed crystalline layers at the outer part of the lipid droplet (white arrowhead). C) Another LD in proximity of the nucleus (N) was in contact with the nuclear envelope and a vacuole. D) An LD close to vacuoles displayed peripheral crystalline layers (white arrowhead) in *S. pombe* after 17 h ED. E) In *S. cerevisiae* after 1 h ED, an LD is still spherical and located in proximity to a vacuole and the nucleus. F) In *S. pombe* after 3.5 h ED, an LD is squeezed between vacuoles which are fractionated by FAS monolayer arrays (white circles). Reflections (asterisk) are caused by interference of the electron beam with crystalline ice which was not properly vitrified inside the vacuoles. G) The same sample as in F displays dense, unstructured areas (white dashed line and asterisks) in the nucleus, cytosol and inside a mitochondrion (M). H) After 4 days of glucose depletion, *S. pombe* cells revealed altered nuclear envelope volumes (highlighted with white arrowheads), spherical mitochondria and deformed vacuoles close to the cell wall (CW).

cytosol and keep protein concentrations at an isotonic level (Bone et al. 1998, Li and Kane 2009). Thus, the observed morphological adaptation of vacuoles likely also has a functional role in the nutritional stress-response.

Furthermore, at later time points of ED (>3.5 h) dense, unstructured clusters could be observed in nucleus, cytosol and organelles (Figure 36 G). These areas could contain condensed amorphous or aggregated biomolecules. They are likely caused by phase transitions to either cope with the stress in a reversible manner or displaying a malfunctional thermodynamic end state due to the prolonged energy depletion.

A particular nuclear envelope alteration was observed in *S. pombe* after 4 days of glucose depletion (Figure 36 H). Here, the distance between the two membranes was enlarged which might indicate changes in nuclear envelope tension that could also have functional implications on nuclear-cytosolic transport (Zimmerli et al. 2021).

5.2.3 Nutritional stress induces a variety of structured supramolecular assemblies

Cryo-electron tomography revealed that the cellular interior of wild-type yeast cells reorganized upon energy depletion. In cryo-electron tomograms of 1 h energy-depleted (ED) yeast, both unstructured, identified by the presence of ribosome-excluded areas, as well as a large variety of highly-structured meso-scale assemblies could be observed (Table 3, Figure 37). Depending on the type and duration of nutrient stress in 18-45 % of the stochastically acquired tomograms, at least five different classes of macromolecular assemblies were visually distinguishable in the cytosol and nucleus of *S. pombe* and *S. cerevisiae* cells (Table 3). Likewise, supramolecular structures formed and occupied large cytosolic areas upon four days of glucose starvation in *S. pombe* (Figure 37 F).

The structural signatures and dimensions of the observed assemblies were distinct from known cytoskeletal filaments (cf. Figure 34). The architectures were for example constituted by filaments traversing through the cytosol displaying elongated, or hollow structures with a pitch, and clusters resembling lattice formations or rhomboid grids. These assemblies occupied on average 5 % of the cytosolic volume after 1 h ED (Figure 38). At later time points (3.5 h and 17 h for *S. pombe* and 6 h for *S. cerevisiae* identified as relevant time points by light microscopy movies described in chapter 5.6.1) the assemblies seemed to qualitatively occupy even larger fractions of the cellular space (Figure 37 D, E). These observations of highly structured assemblies confirm previous findings by light microscopy studies (Narayanaswamy et

al. 2009, Noree et al. 2019a) revealing that certain protein complexes colocalize or condense upon nutrient stress also in unlabeled, wild-type yeast cells.

Table 3: Quantification of nutrient-dependent supramolecular assemblies in cryo-electron tomograms. Total number of tomograms acquired on stochastically selected positions (# Tomo) and instances in which cytosolic and nuclear filaments, lattices on the mitochondrion (mito) outer membrane and FAS assemblies were observed.

Sample	**# Tomo**	**# Filaments**	**# Cytosolic filaments**	**# Nuclear filaments**	**Tomo with filaments [%]**	**# Mito lattice**	**Tomo with mito lattice [%]**	**# FAS assemblies**	**Tomo with FAS assemblies [%]**
S. pombe 1 h ED	117	39	36	3	33	26	22	43	37
S. pombe 3.5 h ED	76	26	25	1	34	18	24	53	70
S. pombe 17 h ED	34	12	11	1	35	6	18	9	26
S. pombe 4 d glucose depletion	31	14	13	1	45	0	0	0	0
S. cerevisiae 1 h ED	62	14	11	3	23	0	0	10	16
S. cerevisiae 6 h ED	56	10	7	3	18	0	0	8	14

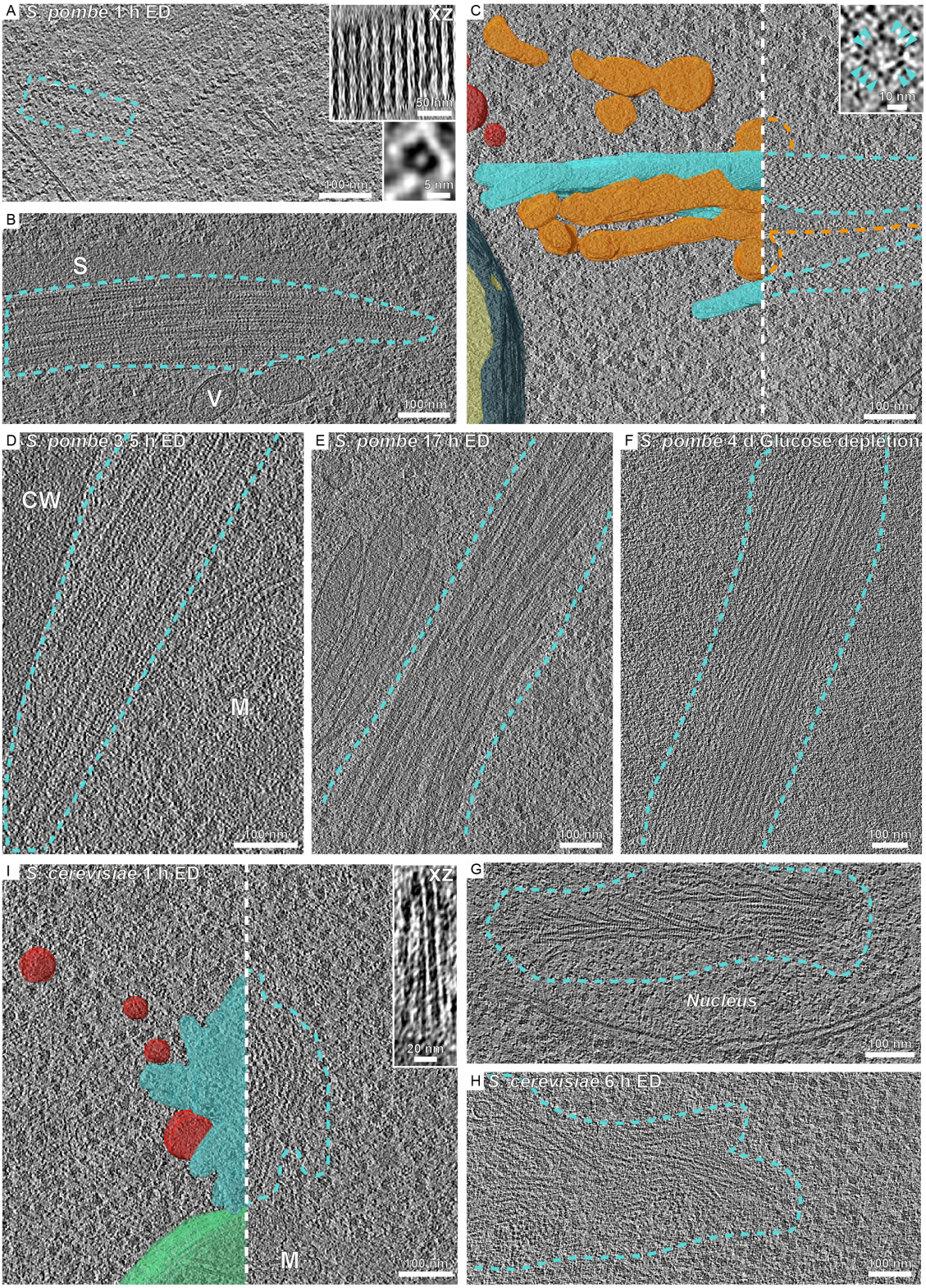
A S. pombe 1 h ED
XZ
50 nm
5 nm
100 nm
B
S
V
100 nm
C
10 nm
100 nm
D S. pombe 3.5 h ED
CW
M
100 nm
E S. pombe 17 h ED
100 nm
F S. pombe 4 d Glucose depletion
100 nm
I S. cerevisiae 1 h ED
XZ
20 nm
M
100 nm
G
Nucleus
100 nm
H S. cerevisiae 6 h ED
100 nm

Figure 37: Examples of nutritional stress-induced macromolecular assemblies revealed by cryo-ET. A-C) In 2D tomographic slices of *S. pombe* after 1 h ED, assemblies with different polymeric architectures could be observed. The structures had characteristics of A) filaments displaying elongated, hollow structures with a pitch of around 30 nm (insets), B) large lattice formations close to a division septum (S) and vesicles (V) or C) rhomboid grids with 10 subunits (inset, cyan arrowheads). D-F) Macromolecular assemblies were also observed at later time points of ED and upon 4 d of glucose depletion (F). They seemed to occupy larger fractions of the cellular volume over time. I-H) Likewise, nutrient stress-induced macromolecular assemblies were revealed in *S. cerevisiae* tomograms. Elongated polymers in both cytosol (I, inset) and nucleus (G) were observed upon 1 h ED. The assemblies seemed to occupy larger volume fractions after 6 h ED (H). Tomographic xy slices are displayed unless marked otherwise. Manual 3D segmentations of organelles are colored for membrane-bound compartments in orange, nucleus in yellow, nuclear envelope in petrol, vesicles in red, mitochondrion (M) in green and ED assemblies are highlighted in cyan.

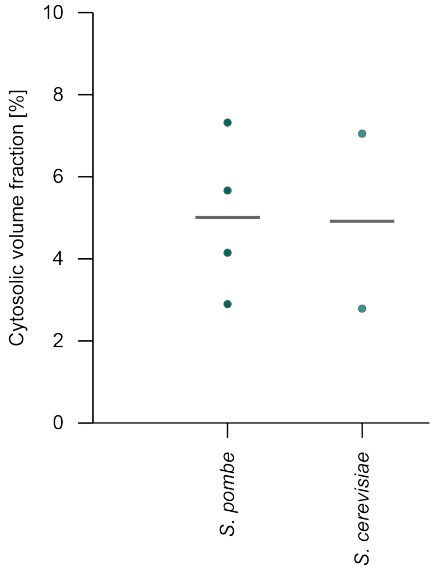

Figure 38: Cytosolic volume fractions occupied by filaments observed after 1 h ED. Cytosol (excluding organelles) and filament volumes were determined by manual segmentations. Cytosolic volume fractions were calculated with the assumption that the combined cytosol and filament volumes correspond to 100 %. The mean is indicated by a horizontal line.

5.2.4 FAS forms assemblies upon energy depletion in a species-dependent manner

The fungal type I fatty acid synthase (FAS) exhibited rearrangement upon energy depletion in yeast tomograms. This observation confirms previous reports by light microscopy movies that show the formation of FAS foci in *S. cerevisiae* upon glucose depletion (Suresh et al. 2015). Under normal nutrient conditions, this multienzyme complex is evenly distributed within the yeast cytosol (cf. Figures 18 A, 25 B, 34). Due to the clear structural signature of FAS, co-localization of individual particles was readily detectable in the cytosol of energy-depleted, unlabeled wild-type *S. cerevisiae* and *S. pombe* cells (Figure 39). In *S. pombe*, FAS assembled into ordered, monolayer arrays which appear separated by membrane-bound compartments (Figure 39 A-D). The overall meso-scale arrangement did not change over time; however, from 1 h to 3.5 h ED, the arrays per tomogram increased (from 37 % to 70 % of tomograms) and then became less frequent at 17 h of energy depletion (observed in 26 % of tomograms, cf. Table 3).

Compared to the membrane-bound FAS monolayers in *S. pombe*, energy-depleted *S. cerevisiae* showed co-localization of FAS, without the presence of membranes in the vicinity and qualitatively occupied more space over time (Figure 39 E, F). In *S. cerevisiae*, the seemingly unorganized meso-scale assemblies contained fully assembled FAS complexes. These assemblies could be observed in 16 % and 14 % of the stochastically collected tomograms after 1 h and 6 h of energy depletion, respectively.

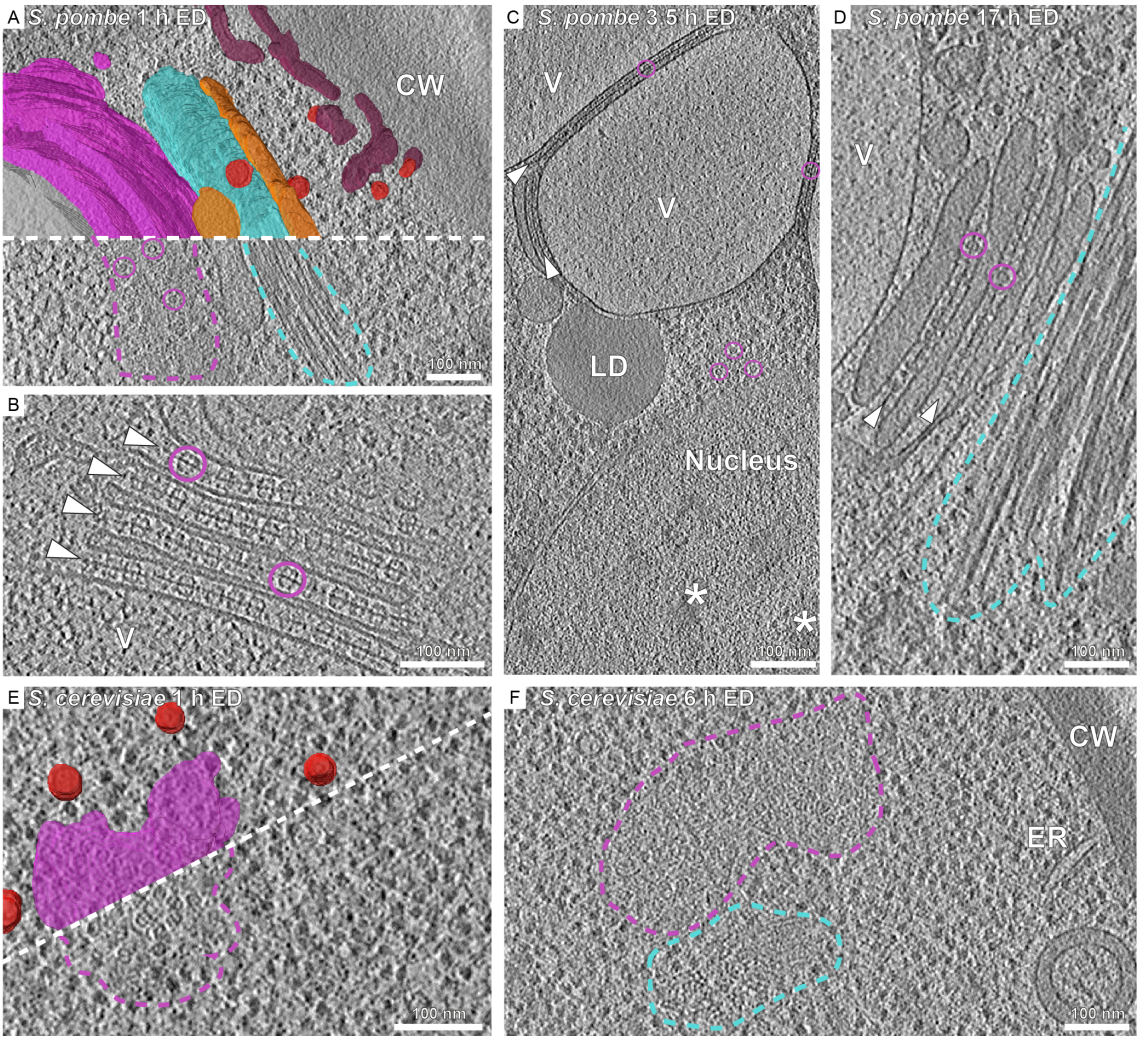

Figure 39: Fatty acid synthases form species-dependent assemblies in the energy-depleted yeast cytosol. A-D) 2D tomographic slices of *S. pombe* upon ED revealed monolayers of FAS identified based on the structural signature of this barrel-shaped complex (examples highlighted with pink circles). The arrays were layered between membrane stacks (indicated by white arrowheads) and connected to vacuoles (grey, V) or other organelles (data not shown). A) After 1 h ED, 3D segmentations showed the colocalization of FAS assemblies (pink, single ones highlighted by circles) with other membrane-bound compartments (orange) and ED-filaments (cyan). In addition, vesicles (red) and ER (purple) close to the cell wall (CW) occupied the cytosol. B) FAS complexes were arranged like beads on a string. C) After 3.5 h ED, FAS monolayers fractionate vacuoles, which are also connected to a deformed lipid droplet (LD), or connect to the nucleus where high density, unstructured areas were observable (asterisks). D) Upon 17 h ED, FAS arrays are still observable between membrane stacks (white arrowheads) and in proximity to an ED-filament assembly (highlighted in cyan). E) In *S. cerevisiae*, FAS complexes colocalize in seemingly random orientations (purple) within the cytosol after 1 h ED. Vesicles are displayed in red. F) After 6 h ED FAS assemblies were concentrated in larger areas of the cytosol. An ED-filament assembly could be observed in the vicinity (cyan dashed line).

5.3 Quantification of molecular concentrations hints at yeast species-dependent changes in crowding upon energy depletion

As described above, cryo-electron tomograms depicting the yeast cytosol were collected under varying nutrient conditions (cf. Table 2). These visualized ribosomes occupying the cytosol in which energy depletion-induced concentration changes were not qualitatively observable. However, for FAS nutrient-dependent localization including the formation of highly structured assemblies was detected (cf. Figure 39). In order to estimate nutrient-dependent changes in crowding on a molecular level, I assessed a) global changes in crowding in terms of cytosolic ribosome concentrations as an approximation, and b) variations in the distribution of individual protein species forming nutrient-dependent local assemblies or condensates with FAS as a model complex. For this purpose, I determined molecular concentrations of ribosomes and FAS from ground truth annotations in cryo-electron tomograms. I first calculated cytosolic volumes from manual cytosol segmentations (cf. Figures 34, 38, 35, 39) in five tomograms of *S. pombe* 1 h ED and three tomograms of *S. cerevisiae* for each NN and 1 h ED (Supplementary Tables S6-S11). In these defocus-only datasets, I localized ribosome and FAS particles by first visual inspection of template matching (TM) results in the case of ribosomes, followed by subsequent iterative manual annotations based on their structural signatures for both particle species. For *S. pombe* NN, the comprehensive ground truth annotations described in chapter 5.1.4 were used (20 tomograms comprised of 10 VPP and 10 defocus-only datasets, cf. Supplementary Tables S4-S5). This enabled the calculation of ribosome and FAS numbers per physical, cytosolic volume. To expand the data and analyze later time points of ED, I used DeePiCt predictions for ribosomes and cytosol in defocus-only tomograms based on the CNNs described in chapter 5.1.4 (cf. Supplementary Tables S6-S13).

The calculated ribosome concentrations for yeast grown in normal nutrient conditions are within the range of published values from MS and EM/cryo-ET studies (Table 4). However, FAS concentrations determined in cryo-electron tomograms were underestimated in comparison to MS studies. This is likely due to the lower abundance and hollow structural signature in comparison to ribosomes which make it more difficult to detect FAS in the noisy images.

Also, only fully assembled complexes could be detected while unassembled proteins can still be identified in proteomic studies.

Table 4: Molecular concentrations of ribosomes and FAS in exponentially growing yeast cells. Values labeled "present work" were calculated for ground truth annotations from cryo-electron tomograms and scaled to particles/cell assuming a 30 % cytosolic volume fraction (Wu and Pollard 2005) of total cell volumes of around 150 µm^3 for *S. pombe* (Mitchison 1957, Nurse 1975) and 54 µm^3 for *S. cerevisiae* (Jorgensen et al. 2002, Powell et al. 2003, Tyson et al. 1979). Mass spectrometry (MS (Marguerat et al. 2012 (1), Von der Haar 2008 (2), Warner 1999 (3), Carpy et al. 2014 (4), Lu et al. 2007 (5)), room temperature EM (Maclean 1965 (6), Yamaguchi et al. 2011 (7)) and cryo-EM data (Delarue et al. 2018 (8)) were directly derived from the indicated publications.

Sample	**Present work [ribo/ µm^3]**	**Present work [ribo/cell]**	**MS [ribo/cell]**	**EM [ribo/cell]**	**Cryo-ET [ribo/ µm^3]**	**Present work [FAS/ µm^3]**	**Present work [FAS/cell]**	**MS [FAS/cell]**
S. pombe	14,918 ± 2,149	∼6.7 * 10^5	∼1.5 * 10^5 (1)	∼2.5-7.3 * 10^5 (6)	-	363 ± 255	∼1.6 * 10^4	5.8-23.2 * 10^4 (1, 4)
S. cerevisiae	18,385 ± 1,720	∼3.0 * 10^5	∼1.9-2 * 10^5 (2, 3)	∼2.2 * 10^5 (7)	∼14,000 (8)	690 ± 84	∼1.1 * 10^4	1.2-6.8 * 10^4 (5)

In Figure 40, a slight trend to increased ribosome concentrations was observable in *S. pombe* upon 1 h ED in the ground truth annotations (20 tomograms for NN and 5 for ED). Ribosome concentrations increased by 9 % from average 14,918 ± 2,149 to 16,285 ± 3,005 particles/µm^3 ($p = 0.125$ one-tailed t-test assuming equal variances according to F-statistics). Molecular concentrations from DeePiCt predictions showed an effective decrease by 4 %, 13 % and 15 % for 1 h, 3.5 h and 17 h ED in comparison to NN, respectively. The observed change between NN and ED became significant after 3.5 h ED ($p = 0.002$ one-tailed t-test assuming equal variances according to F-statistics). The differences in molecular concentrations after 1 h ED determined from ground truth and DeePiCt annotations are likely caused by imperfect predictions of cytosol segmentations and ribosome coordinates, as the utilized CNNs were trained only on normal nutrient state tomograms.

For *S. cerevisiae*, a two-fold increase in ribosome concentrations upon energy depletion has previously been reported for room temperature electron tomograms (Marini et al. 2020). In Figure 40, 1 h energy-depleted *S. cerevisiae* revealed increased ribosome concentrations by an average of 16.7 % from 18,385 ± 1720 to 21,456 ± 1272 ribosomes/µm^3 in ground truth annotations of each three NN and 1 h ED

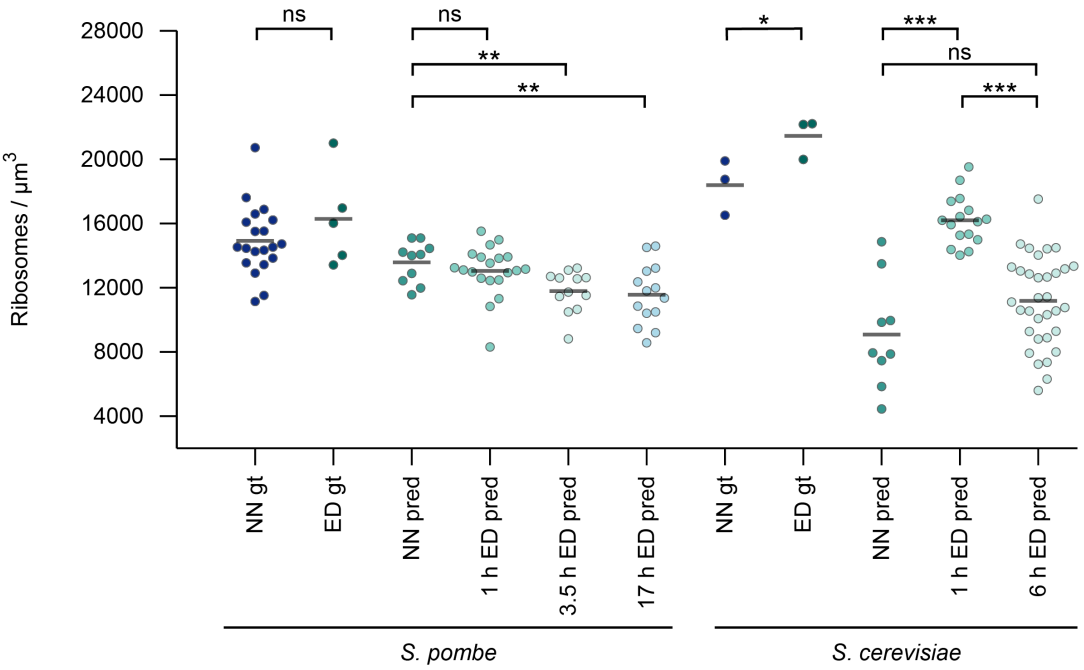

Figure 40: Cytosolic ribosome concentrations in *S. pombe* and *S. cerevisiae* in normal nutrient (NN) state and upon ED. Particle numbers and cytosolic volumes determined in cryo-electron tomograms with ground truth annotations (gt) and DeePiCt predictions (pred). In *S. pombe*, ribosome concentrations decreased over time and were significant after 3.5 h and 17 h ED. *S. cerevisiae* ribosome concentrations increased significantly from normal nutrient state (NN) to 1 h ED in both ground truth and DeePiCt predictions. A decrease could be observed at 6h ED. The mean of each dataset is marked by a grey horizontal line. Black horizontal lines on top indicate non-significant (ns, $p>0.05$) and significant differences between datasets with * ($p<0.05$), ** ($p<0.01$), *** ($p<0.001$).

cryo-electron tomograms. DeePiCt ribosome predictions with an average auPRC of 0.828 and 0.708 for each of the three NN and 1 h ED tomograms (cf. chapter 5.1.4) resulted in average ribosome concentrations of 9,080 ± 3,383 to 16,197 ± 1,548 particles/µm^3 in nine NN and 16 ED tomograms. This corresponds to a 78,4 % increase from NN to 1 h ED (Figure 40). The increased ribosome concentration upon 1 h ED for both ground truth annotations and DeePiCt predictions is significant with p-values of 0.034 and <0.001, respectively (one-tailed t-tests assuming equal variances according to F-statistics). The different increase upon 1 h ED in ground truth and DeePiCt-derived ribosome concentrations likely stems from imperfect predictions of both cytosol segmentations and ribosome localizations in

S. cerevisiae as the networks were trained in *S. pombe* tomograms. In addition, the ground truth annotations represent only three tomograms for each condition while the predictions were derived from nine NN and 16 ED tomograms. Furthermore, DeePiCt predictions in 33 *S. cerevisiae* tomograms after 6 h ED showed average ribosome concentrations of 10,805 ± 3,376 particles/µm^3 (Figure 40). This increase of 21 % from normal nutrient state is not significant ($p = 0.057$ one-tailed t-test assuming the variances are unequal according to F-statistics), but the decrease from 1 h ED is pronounced ($p<0.001$ one-tailed t-test assuming equal variances according to F-statistics). Thus, molecular crowding approximated by ribosomes significantly increased upon 1 h ED and decreased after 6 h ED in *S. cerevisiae*.

In general, DeePiCt predictions underestimated ribosome concentrations (Figure 40). This is likely due to both undetected ribosomes and overestimated cytosol predictions. Although the mean auPRCs for the limited number of comprehensively annotated tomograms showed satisfactory results in direct comparison to the ground truth annotations, the predictions were not perfect and the performances varied between individual tomograms (cf. Figure 24). For example, nuclear volumes containing pre-ribosomal particles were often detected as false positives, leading to misrepresentation of the cytosolic volume (data not shown). In addition, the observed changes in organelle morphology likely also influence the CNNs performance in ED, as the training was conducted in NN tomograms. Furthermore, the statistical evaluation for some conditions has to be considered with caution, as they reflect only a limited number of datasets.

Local variations in the distribution of individual macromolecules were estimated using ground truth annotations of FAS. For different tomography acquisition parameters, the cytosolic concentrations of FAS in *S. pombe* NN varied between 510 ± 265 to 215 ± 136 particles/µm^3 for VPP and defocus-only tomograms, respectively. The improved image contrast in VPP tomograms facilitated particle detection in the case of FAS and thus higher concentration estimates were obtained. As ED FAS particles were localized solely in DEF tomograms, molecular concentrations were only compared to this acquisition type.

Increased local molecular concentrations upon energy depletion were observed for FAS in both *S. cerevisiae* and *S. pombe* (Figure 41). The particles were concen-

trated in differently organized assemblies depending on the yeast species (cf. Figure 39). In addition, FAS could still be observed in the cytosol of nutritionally stressed yeast cells. In *S. pombe* cytosolic FAS concentrations slightly increased from average 215 ± 136 to 253 ± 99 particles/µm^3. However, upon 1 h ED, most particles were sequestered into monolayered FAS assemblies. Their volumes were manually segmented (cf. Figure 39). In these ED compartments, local molecular concentration increased by more than 200-fold to 43,423 ± 7,727 particles/µm^3.

In *S. cerevisiae*, cytosolic FAS concentrations increased more than 2-fold upon energy depletion from average 690 ± 84 to 1464 ± 617 particles/µm^3. A single annotated ED assembly revealed FAS concentration of almost 250-fold to 170,332 particles/µm^3 (Figure 41).

The determined molecular concentrations for both ribosomes and FAS clearly hint at a) global changes in molecular crowding and b) local variations in particle distributions upon energy depletion in both *S. cerevisiae* and *S. pombe*. The overall change in molecular crowding approximated by ribosome concentrations likely affects other biomolecules, especially their effective concentrations, and could drive phase separation. Together with the condensation of individual particle species such as the observed FAS assemblies, this likely influences the global biophysical properties of the whole cell.

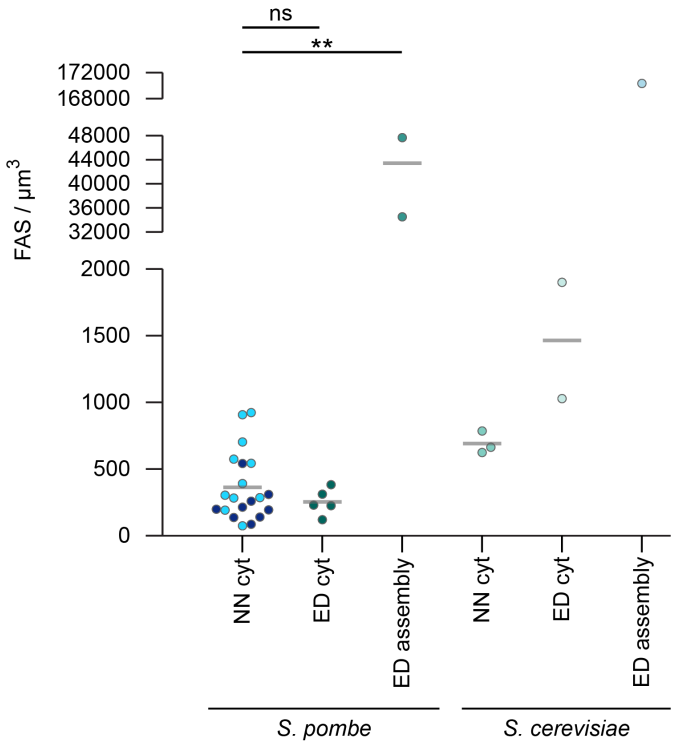

Figure 41: FAS concentrations in *S. pombe* and *S. cerevisiae* in normal nutrient (NN) state and upon 1 h energy depletion (ED). Particle numbers and cellular volumes determined in cryo-electron tomograms with ground truth annotations in the cytosol (cyt) or within ED-induced assemblies. In *S. pombe* NN VPP tomograms (bright blue), more FAS were detected on average and thus higher concentrations obtained than in defocus-only tomograms (dark blue). Cytosolic FAS concentrations increased from NN (dark blue) upon 1 h ED without significance, but the particles were significantly concentrated in ED assemblies. *S. cerevisiae* FAS concentrations increased in both cytosol and ED assemblies upon 1 h ED. The mean of each dataset is marked by a grey horizontal line. Black horizontal lines on top indicate non-significant (ns, $p>0.05$) and significant differences between datasets with * ($p<0.05$), ** ($p<0.01$), *** ($p<0.001$).

5.4 Nutrient-dependent structural variations of ribosomes

In addition to the above-described nutrient-dependent changes in local molecular concentrations of ribosomes, their translational activity was also found to be altered during nutrient starvation in previous studies (Arribere et al. 2011, Ashe et al. 2000, Brengues et al. 2005). To explore this on a structural level, I generated 3D reconstructions of yeast 80S ribosomes, visualizing translational states under normal nutrient (NN) conditions and 1 h of energy depletion (ED). For this purpose, I used the particles detected in defocus-only cryo-electron tomograms described in chapters 5.1.4 and 5.3 which were localized by a combination of template matching and manual detection for ground truth annotations, and extended by DeePiCt predictions (cf. Supplementary Tables S4-S11). For *S. pombe* NN, I utilized these annotations of 25,901 ribosomes from 10 tomograms and for ED 46,120 ribosomes from 20 tomograms. In *S. cerevisiae* 22,986 ribosomes were detected in nine NN tomograms and 54,398 ribosomes in 16 ED tomograms. Subtomograms were reconstructed in Warp (Tegunov and Cramer 2019), classified and aligned in RELION (Zivanov et al. 2018), and refined in M (Tegunov et al. 2021) to obtain 3D averages (Figure 42).

Structural comparisons between the nutritional states showed overall resemblance with the published *S. cerevisiae* ribosome structure and subtomogram average (PDB 6tnu (Buschauer et al. 2020), EMDB 4372 (Delarue et al. 2018)). A large number of fully assembled ribosomes (s. particle numbers above) was detected for both *S. cerevisiae* and *S. pombe* upon 1 h ED. This confirmed conformational similarity and structural integrity between the different densities (Figure 43 A). From 3D classifications, well-aligned classes were obtained, which could be refined in M to resolutions of 11.1-8.4 Å (Figure 42 and 43 B). The lower resolution obtained for the *S. cerevisiae* NN average is potentially caused by the smaller number of ribosomes that were used for structural analysis, as well as a different cryo-ET acquisition scheme with 3° tilt increments (cf. Supplementary Table S2). However, the reconstructions from all four datasets exhibited slightly lower resolutions for the 40S small ribosomal subunit (SSU) which may hint at ratcheting movements potentially connected to translational activity (Zhang et al. 2009). Further 3D classifications did not separate an LSU class in any of the datasets. In addition, a large fraction of particles could not be properly aligned (Figures 44-46). This is in line with the previous

observations described above and is likely due to the low contrast in defocus data (cf. chapter 5.1.4, Figure 20).

In order to gain deeper insights into ribosome subpopulations, focused classifications close to the head of the SSU and at the ribosomal exit tunnel were performed, as additional densities had been detected for *S. pombe* NN (described in chapter 5.1.4). An additional density connected to the head of the SSU was resolved in a subset (2,314 particles) of *S. cerevisiae* NN ribosomes and fitted eEF3 well (Figure 43 F, 47-49 A). However, it could not be observed in any of the ED states. The eEF3 facilitates binding of a new tRNA to the A-site via the aminoacyl-tRNA–eEF1A–GTP complex (Andersen et al. 2006, Ranjan et al. 2021). It is crucial during translation elongation, and thus its absence likely hints at a non-translating, nutritionally arrested ribosome state. A sub-class with an additional density at the ribosomal exit tunnel was detected in all datasets (Figures 43 D, 47-49 B). It could accommodate the ribosomal RNA expansion segment ES27L in its particular exit configuration, leaving an extra density right below the exit tunnel empty (EMDB 1667 (Becker et al. 2009), PDB 3izd (Armache et al. 2010)). The unassigned density could fit several factors with a MetAP-like fold including Arx1 (EMDB 3151 (Greber et al. 2016), Figure 43 D, G).

Independent of the nutritional state, all well-aligned classes depicted at lower intensity thresholds showed additional densities at positions typical for neighboring ribosomes within polysomes (Figure 43 H). As a comparison, previous polysome profiling experiments for *S. cerevisiae* showed polysome disassembly within 10 min of ED (Nuske et al. 2018). This was also reported upon glucose depletion, but in this case polysomes were detected again after 60 min of withdrawal. A restart of translation to synthesize proteins required for the stress response was suggested for the polysome reformation (Arribere et al. 2011). Here, the observation of a polysome fraction in the ED ribosome datasets may represent a similar restart of translation as part of the stress adaptation. However, this observation of polysomes is contradicted by an overall open head conformation of the 1 h ED ribosome averages which is connected to a non-translating, trapped state (Figure 43 C, E).

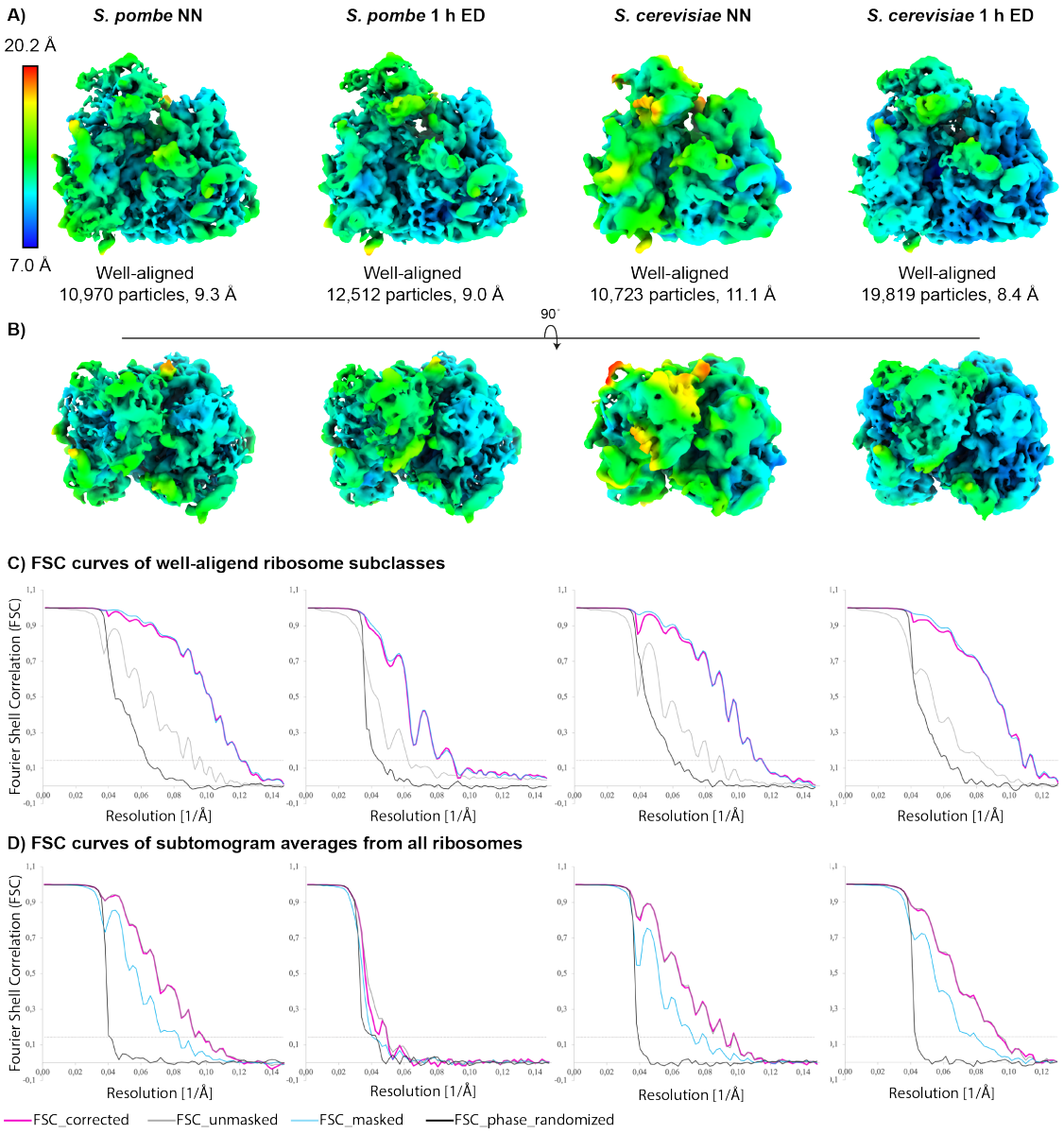

Figure 42: Resolutions of yeast 80S ribosomes at different nutritional states. A) Local resolution maps of well-aligned ribosome classes. B) Top views of the averages depicted in A. C) Fourier shell correlation (FSC) curves of well-aligned ribosome sub-classes refined in M. D) FSC curves of 3D reconstructions from all ribosomes at each of the analyzed nutritional states and refined in RELION. FSC threshold of 0.143 indicated as dotted line in C and D (Rosenthal and Henderson 2003).

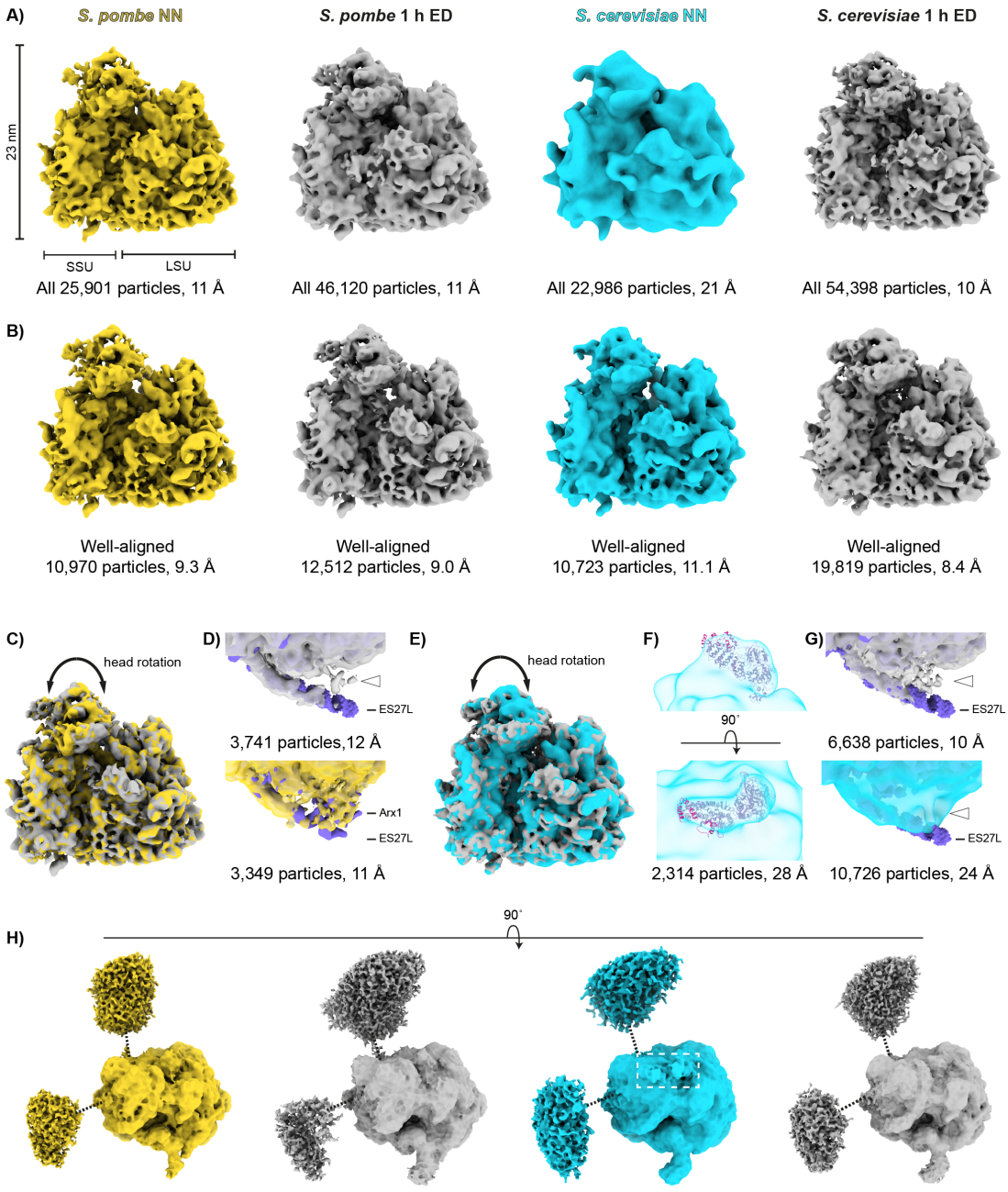
A)
S. pombe NN
S. pombe 1 h ED
S. cerevisiae NN
S. cerevisiae 1 h ED
23 nm
SSU
LSU
All 25,901 particles, 11 Å
All 46,120 particles, 11 Å
All 22,986 particles, 21 Å
All 54,398 particles, 10 Å
B)
Well-aligned
10,970 particles, 9.3 Å
Well-aligned
12,512 particles, 9.0 Å
Well-aligned
10,723 particles, 11.1 Å
Well-aligned
19,819 particles, 8.4 Å
C)
head rotation
D)
ES27L
3,741 particles,12 Å
Arx1
ES27L
3,349 particles, 11 Å
E)
head rotation
F)
90˚
2,314 particles, 28 Å
G)
ES27L
6,638 particles, 10 Å
ES27L
10,726 particles, 24 Å
H)
90˚

Figure 43: Nutrient-dependent structural states of the yeast 80S ribosome elucidated by cryo-electron tomography. A) Subtomogram averages of all cytosolic ribosomes retrieved from tomograms with ground truth annotations and DeePiCt predictions. The 3D reconstructions of *S. pombe* NN (yellow), 1 h ED (grey), *S. cerevisiae* NN (cyan) and 1 h ED (grey) resemble the overall ribosome structure with large and small subunits (LSU and SSU). B) Sub-classes of well-aligned cytosolic ribosomes detected in 3D classifications and refined in M. C) Comparisons between *S. pombe* NN and 1 h ED ribosomes showed a head rotation with a closed conformation towards the PTC in the case of nutrient scarcity (grey). D) 3D classifications focused on the exit tunnel recovered a sub-class for *S. pombe* 1 h ED (top) fitting the *S. cerevisiae* ribosome with ES27L in an exit configuration (purple, EMDB 1667 (Becker et al. 2009), PDB 3izd (Armache et al. 2010), CC 0.7905). A similar subset was detected in *S. pombe* NN ribosomes and the remaining density right below the exit tunnel (white arrowhead) fits different factors with a MetAP-like fold such as Arx1 (bottom purple, EMDB 3151 (Greber et al. 2016), CC 0.8777). E) Comparisons between *S. cerevisiae* NN and 1 h ED ribosomes showed a head rotation with a more closed conformation towards the PTC in the case of nutrient scarcity (grey). F) Sub-class of *S. cerevisiae* NN ribosomes classified for an additional density close to the head of the 40S subunit (highlighted dashed white box below in H). The eukaryotic elongation factor eEF3 (pink, EMD-12062 (Ranjan et al. 2021), CC 0.8481) could be assigned to the additional head density. G) Classification of *S. cerevisiae* ribosomes for an extra density below the exit tunnel recovered similar sub-classes as for *S. pombe* depicted in E. The *S. cerevisiae* ribosome with ES27L in a particular configuration fits the extra density (left, purple, EMDB 1667 (Becker et al. 2009), PDB 3izd (Armache et al. 2010), CC 0.7673). The remaining density right below the exit tunnel (white arrowhead) fits different factors with a MetAP-like fold. H) Rotation by 90° and lowering the intensity threshold recovered density of neighboring ribosomes for all four maps in B. Black dotted lines indicate potential mRNA paths.

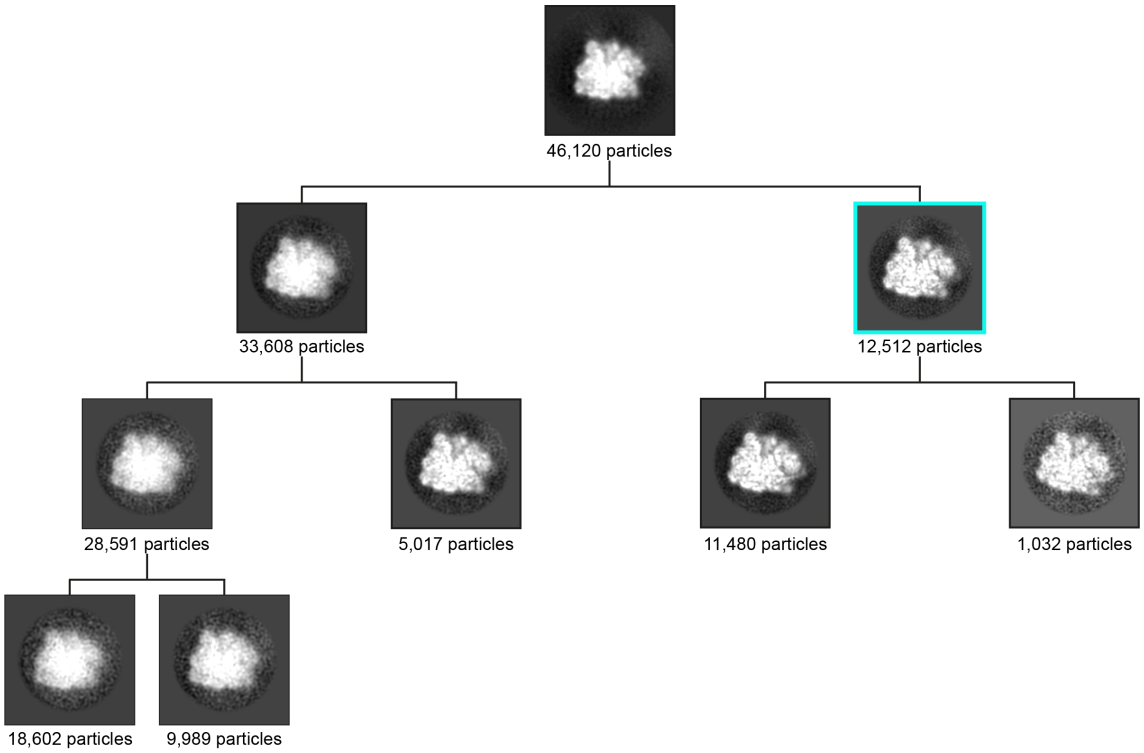

Figure 44: Hierarchical 3D classifications of *S. pombe* 1 h ED ribosomes. Starting from 46,120 M-refined particles, ribosomes were clustered into two classes at each step (indicated by branching points). A well-aligned class was extracted (cyan box) and refined to a resolution of 9.0 Å in M. More than half of the particles ended up in poorly defined classes (left branch). For each class, 3D averages of iteration 25 are displayed as 2D slices.

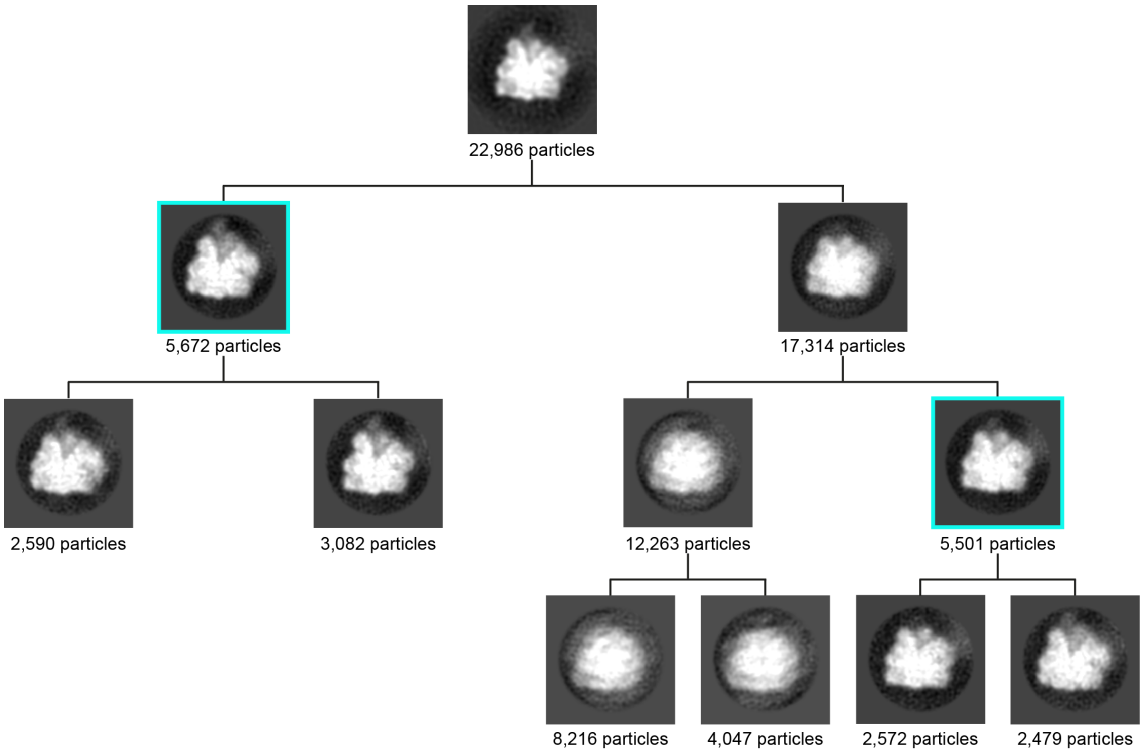

Figure 45: Hierarchical 3D classifications of *S. cerevisiae* NN ribosomes. Starting from 22,986 M-refined particles, ribosomes were clustered into two classes at each step (indicated by branching points). A well-aligned class was extracted (cyan boxes) and refined to a resolution of 11.1 Å in M. More than half of the particles ended up in poorly defined classes. For each class, 3D averages of iteration 25 are displayed as 2D slices.

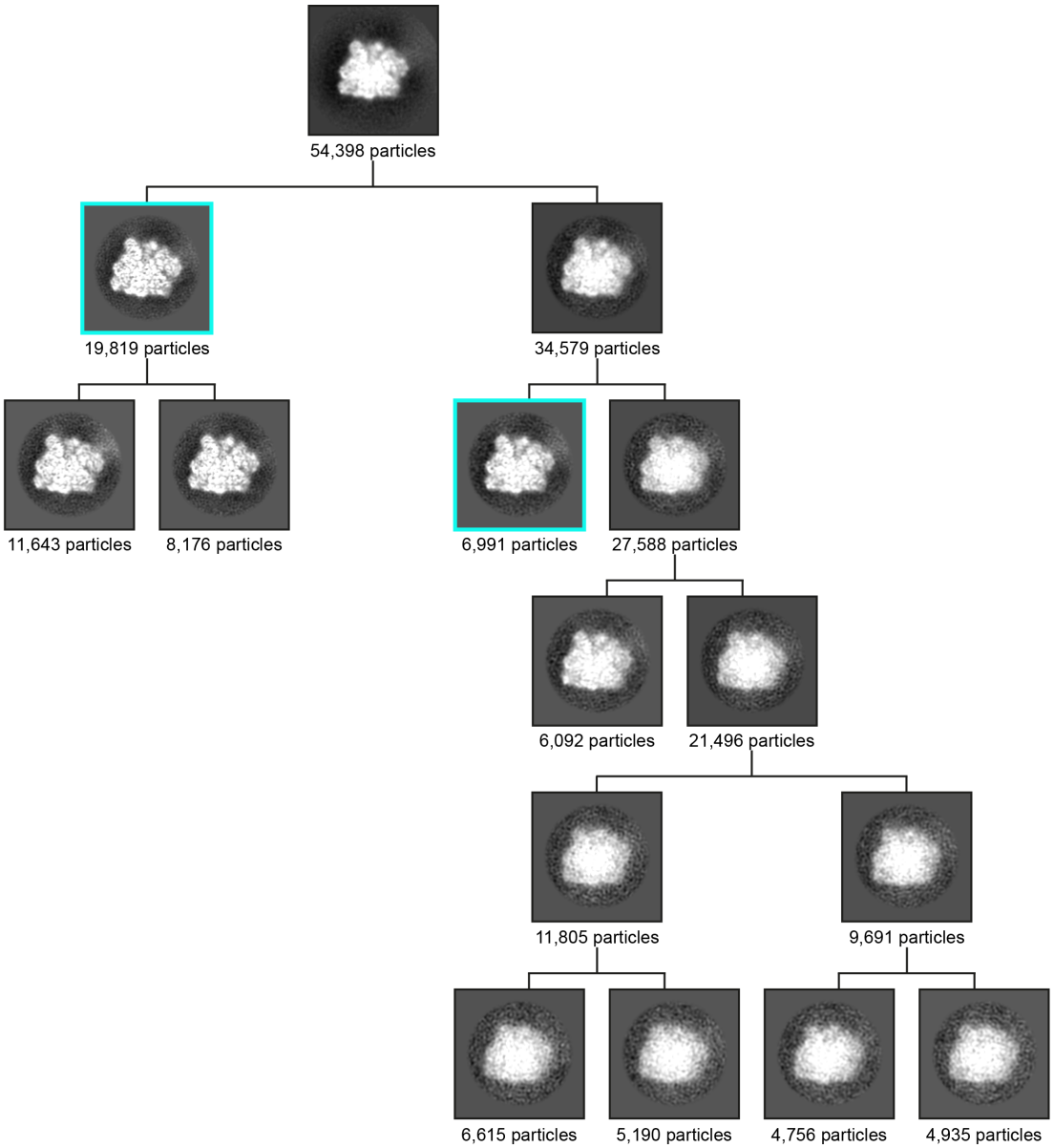

Figure 46: Hierarchical 3D classifications of *S. cerevisiae* 1 h ED ribosomes. Starting from 54,398 M-refined particles, ribosomes were clustered into two classes at each step (indicated by branching points). A well-aligned class was extracted (cyan boxes) and refined to a resolution of 8.4 Å in M. More than half of the particles ended up in poorly defined classes (right branch). For each class, 3D averages of iteration 25 are displayed as 2D slices.

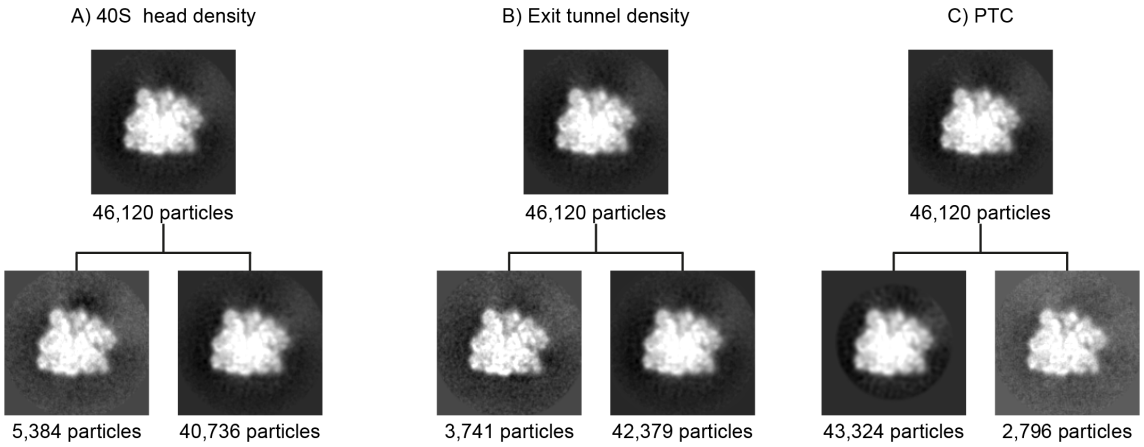

Figure 47: Focused 3D classifications of *S. pombe* 1 h ED cytosolic ribosomes. A) No density close to the 40S head could be observed. The spherical mask indicated in Figure 30 A was used for focused classification. B) A subset of 3,741 ribosomes fitting ES27L with an unassigned density below the exit tunnel was detected. The spherical mask indicated in Figure 31 A was used for focused classification. C) Two classes with distinct PTC densities were obtained.

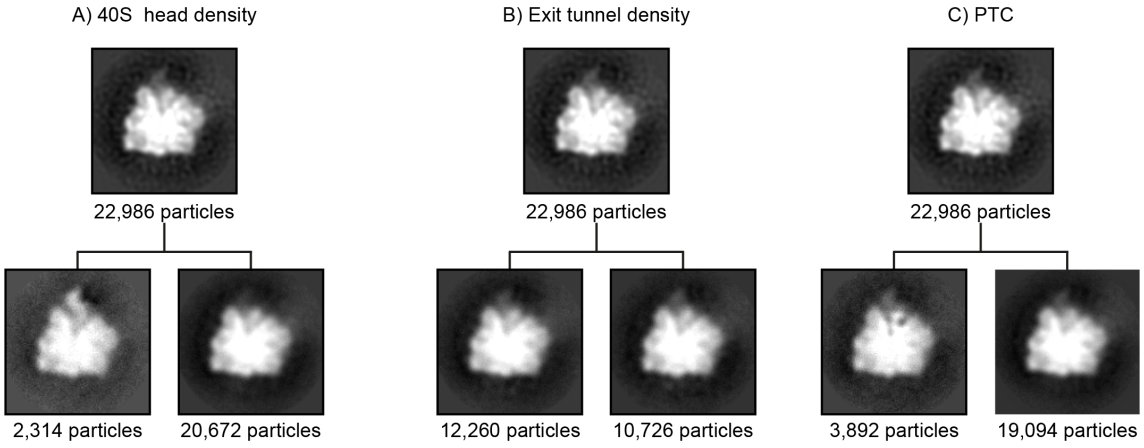

Figure 48: Focused 3D classifications of *S. cerevisiae* NN ribosomes. A) A density close to the 40S head could be observed in 2,314 ribosomes, which were refined in M to 28 Å. The spherical mask indicated in Figure 30 A was used for focused classification. B) A subset of 10,726 ribosomes fitting ES27L with an unassigned density below the exit tunnel was detected. The spherical mask indicated in Figure 31 A was used for focused classification. C) Two classes with distinct PTC densities were obtained.

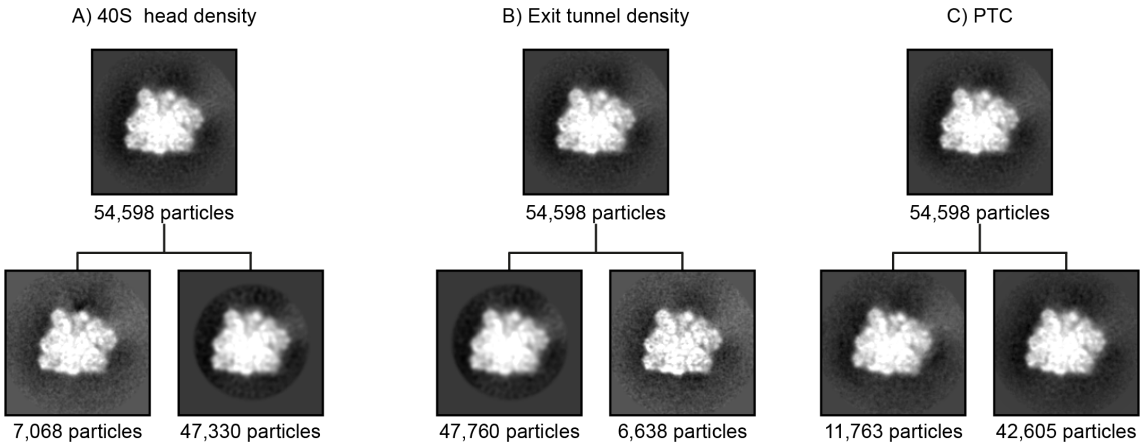

Figure 49: Focused 3D classifications of *S. cerevisiae* 1 h ED ribosomes. A) No density close to the 40S head could be observed. The spherical mask indicated in Figure 30 A was used for focused classification. B) A subset of 6,638 ribosomes fitting ES27L with an unassigned density below the exit tunnel was detected. The spherical mask indicated in Figure 31 A was used for focused classification. C) Two classes with distinct PTC densities were obtained.

To elucidate the translation activity of the individual nutritional states of the ribosome on a structural level, detailed characterization of the peptidyl-transferase center (PTC) was performed (Figures 47-49 C, 50). Focused 3D classifications of all cytosolic ribosomes separated two classes with distinct PTC occupancies in the four datasets.

In the case of *S. pombe* NN, one class contained 32.5 % of the particles with a prominent P-site tRNA and an aminoacyl-tRNA density at the PTC entry site (Figure 50 A). A second class, which clustered 67.5 % of the ribosomes, revealed A- and P-site tRNAs, as well as an additional density at the E-site which did not fit an E-site tRNA but could accommodate the eukaryotic initiation factor 5a (eIF5a). The two observed classes containing P-site tRNAs confirmed active translation expected for exponentially growing yeast cells.

For *S. cerevisiae* NN, despite the lower resolutions, also two distinct PTC classes of ribosomes could be identified (Figure 50 C). Class 1 was reconstructed from 16.9 % of the ribosomes and had no tRNA in the PTC, but an extra density at the E-site fitting eIF5a. This ribosome fraction is not actively translating. However, the majority of particles clustered into class 2 (83.1 %) and contained a prominent P-site tRNA as well as an aa-tRNA at the PTC entry site which confirmed active translation.

Upon 1 h ED, the *S. pombe* PTC contained no tRNAs, which confirmed a non-active state upon nutritional scarcity (Figure 50 B). An extra density at the tRNA entry site could be detected in all ribosomes, which was further analyzed. Class 1 clustered most particles (93.9 %). Here, the eukaryotic release factor 1 (eRF1, (Brown et al. 2015)) could be fitted, which recognizes STOP codons in the A-site and initiates nascent chain release and ribosome recycling (Schuller and Green 2018). In the second, much smaller class (6.1 % of ribosomes), a larger additional density was observed which could fit the eukaryotic elongation factor 2 (eEF2, (Spahn et al. 2004)). This factor is mainly known to facilitate translocation of mRNA and peptidyl-tRNA during translation elongation, but has also been detected in inactive ribosomes (Liu and Qian 2016). On a structural level, it was identified previously together with the SERPINE mRNA binding protein 1 (SREPB1) which binds at the mRNA entrance site of non-translating ribosomes with a vacant PTC (Brown et

al. 2018). At the resolution of 14 Å for the here reported ribosome class, SREPB1 could not be recognized. Also, other factors like the ATP-dependent factor RNase L inhibitor 1 (Rli1 corresponding to human ABCE1) that is required for subunit splitting and recycling after translation termination (Heuer et al. 2017, Van den Elzen et al. 2014), bind the 40S subunit at a similar site as eEF2 and thus higher resolution averages would be required to unambiguously identify the extra density.

Moreover, in both *S. pombe* 1 h ED classes, an extra density in the PTC's E-site did not resemble a tRNA or the proposed hibernation factors Stm1 and Lso2. Structural comparison with the NN map (Figure 50 A, class 2) and published ribosome structures bound to translation factors suggested eIF5a as a potential candidate for this additional density. Initially identified as initiation factor, eIF5a binds to the E-site and conducts important functions during all steps of translation as it enhances the peptidyl-transfer reaction during elongation and peptidyl-tRNA hydrolysis during termination (Schmidt et al. 2016, Schuller et al. 2017). It belongs to the top 50 highest expressing genes in *S. cerevisiae* and *S. pombe*, with levels equivalent to that of ribosomes (Kulak et al. 2014, Von der Haar 2008). In addition to its high abundance, eIF5a binds tightly to 80S ribosomes (approximate dissociation constant of 9 nM (Rossi et al. 2016)), suggesting that it could theoretically interact with all ribosomes that contain an empty E-site, potentially enabling mutual protection from stress-induced degradation together with the other factors bound to the PTC entry site. Thus, the discovered energy-depleted stationary ribosome in an eIF5a-bound state might represent a novel mechanism for translational arrest, which still maintains polysomal arrangements (cf. Figure 43 H).

S. cerevisiae subjected to 1 h ED revealed ribosomes clustered into a class containing 21.6 % of all particles with a P-site tRNA and an extra E-site density fitting eIF5a (Figure 50 D). This subtomogram average hints at a fraction of ribosomes that is still actively translating despite the harsh nutritional stress that the cells were subjected to. It could hint at an adaptation mechanism previously observed in polysome profiling experiments, wherein polysomes were found to reform after 1 h of glucose depletion (Arribere et al. 2011). Nevertheless, most of the ribosomes (78.4 %) contained an empty PTC except for an E-site density matching eIF5a and an additional density at the tRNA entry site which could fit eRF1. This confirmed the expected non-active ribosome state upon energy depletion.

The subtomogram analysis of lamella-derived, cellular ribosomes thus provided functional insights on translation in connection with the energy state of yeast cells. All *S. pombe* NN ribosome classes contained P-site tRNAs which confirmed active translation. However, a ribosome class with a vacant PTC was identified in *S. cerevisiae* NN which revealed the variety of translational activity in exponentially growing yeast cells. Polysome formation could be observed in all datasets including the energy-depleted states. Yet, both *S. cerevisiae* and *S. pombe* ED ribosomes revealed vacant PTCs lacking tRNA densities and the overall open conformation suggested no active translation. This was further confirmed by the lack of a class with an extra density fitting eEF3. However, for *S. cerevisiae* ED, a class encompassing 21.6 % of all ribosomes still contained a P-site tRNA, which could hint at low levels of translation after 1 h ED.

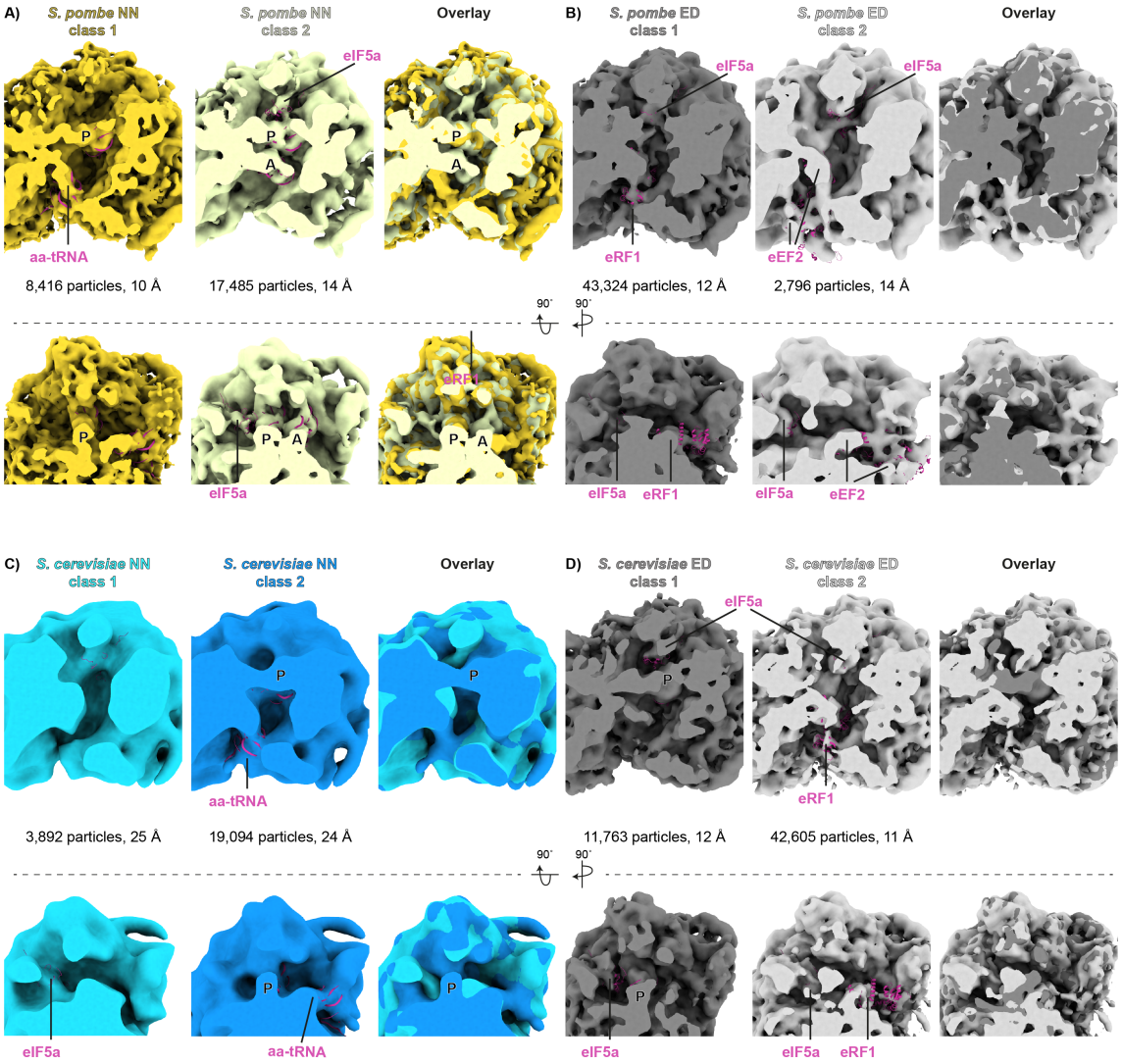

Figure 50: Nutrient-dependent PTC occupancies in yeast 80S ribosomes. 3D classifications focused on the PTC revealed two classes per dataset. Cross-sections from different views are presented to demonstrate the fitting of translation factors. A) *S. pombe* NN ribosomes contained a P-site tRNA and either an aminoacyl (aa-) tRNA (class 1, PDB 5lzs (Shao et al. 2016)) or an A-site tRNA, as well as an extra density at the E-site which could fit eIF5a (class 2, PDB 5gak (Schmidt et al. 2016)). B) *S. pombe* ED ribosomes revealed an empty PTC with an E-site density fitting eIF5a (PDB 5gak (Schmidt et al. 2016)) and PTC entry site densities which could accommodate eRF1 (PDB 3jah, class 1) or eEF2 (PDB 4v4b, class 2). C) Class 1 of *S. pombe* NN ribosomes had an empty PTC, except for an extra density at the E-site which could fit eIF5a (class 1, PDB 5gak (Schmidt et al. 2016)). Class 2 revealed a P-site tRNA and a density at the PTC entry site that could fit an aa-tRNA (PDB 5lzs, (Shao et al. 2016)). D) *S. cerevisiae* ED ribosomes contained either a P-site tRNA (class 1) or revealed an empty PTC (class 2). In both classes a density at the E-site which could fit eIF5a was observable (PDB 5gak (Schmidt et al. 2016)). Class 2 had an additional density at the tRNA entry site which could fit eRF1 (PDB 3jah).

5.5 Nutrient- and species-dependent structural differences of FAS

As described in chapter 5.2.4, cytosolic FAS assemblies were observed in cryo-electron tomograms of energy-depleted *S. pombe* and *S. cerevisiae* and varied significantly in terms of subcellular localization. The membrane association of FAS in *S. pombe* suggested potential conformational changes resulting in an altered 3D structure in comparison to the normal nutrient state and to the *S. cerevisiae* complex. Due to the clear structural signature of FAS, I determined particle coordinates manually in defocus-only cryo-electron tomograms of either exponentially growing or 1 h energy-depleted cryo-FIB-milled *S. pombe* and *S. cerevisiae* cells (cf. chapters 5.1.4 and 5.3, Supplementary Tables S5-S11). For *S. pombe* NN, I utilized these annotations of 366 FAS from 10 tomograms and for ED 3,993 FAS from 16 tomograms. In *S. cerevisiae* 310 FAS were detected in three NN tomograms and 346 FAS in an ED assembly of one tomogram. Subtomograms were reconstructed in Warp (Tegunov and Cramer 2019), classified and aligned in RELION (Zivanov et al. 2018), and refined in M (Tegunov et al. 2021) to obtain 3D averages (Figures 51, 52).

The overall conformation of all four maps matched the barrel-like shape of the published crystal structure of purified *S. cerevisiae* FAS (Figure 52 top row, PDB 2uv8, cyan (Leibundgut et al. 2007)). The dodecameric ($\alpha 6 \beta 6$), 2.6 megadalton, fungal FAS I complex consists of two half domes, each comprised of three FAS1/β subunits, connected via a central wheel constituted by six Fas2/α subunits. The phosphopantetheinyl transferase (PPT) domain was clearly visible in all four subtomogram averages at the C-terminus of Fas2/α. This domain is required to activate FAS by attaching CoA to the acyl carrier protein (ACP) (Leibundgut et al. 2007). Furthermore, an extra density on the level of the α-wheel connected to the N-terminus of Fas2/α was detected in all four datasets. It was more pronounced in *S. pombe*, and could not be assigned by fitting published structures.

In energy-depleted *S. pombe*, FAS organized into highly ordered monolayer arrays between stacked membrane compartments (cf. Figure 39). The subtomogram average of these complexes complements this architecture as two adjacent membrane densities on top and below the barrel-shaped structure could clearly be resolved (Figure 52 A). The thickness of the membrane was 4 nm corresponding to a phospholipid bilayer. Three densities on top of each half dome connected the barrel

structure to the membrane, probably anchoring the complex at this site. These densities were not detected in the normal nutrient state FAS and their composition could not be identified based on published structures (Figure 52 B). Connecting densities to neighboring FAS complexes could also not be resolved by the center-focused 3D alignments, even when D_3 symmetry was applied. This could hint at flexibility or disorder of a potential linker which could establish the highly ordered arrangement of FAS into monolayers upon energy depletion.

Compared to the membrane-bound FAS monolayers in *S. pombe*, energy-depleted *S. cerevisiae* showed co-localization of FAS in foci that lack long range order (cf. Figure 39). The seemingly unorganized meso-scale assemblies, which appeared to grow over time, contained fully assembled FAS complexes, which match the NN structure (Figure 52 C, D). Neither extra densities nor adjacent membranes were observed.

Structural comparison between the two nutritional states of *S. pombe* FAS further revealed that the acyl transferase domain (ATD) of FAS1/β appeared rotated (Figure 52 B, inset). This may have a functional implication on the enzymatic activity of the whole complex during energy depletion. Therefore, the localization of the acyl carrier protein, which shuttles the growing acyl chain to each catalytic site and is thus connected to the activity state of FAS, was analyzed in all four datasets. In both *S. pombe* and *S. cerevisiae*, three densities fitting acyl carrier proteins (ACPs) could be observed at the top of each half dome in energy-depleted FAS (Figure 52 lower panel, middle). In contrast to this observation, NN FAS contained three densities located at the FAS2/α subunits in close proximity to the ketosynthase (KS) domain. They could fit ACPs of *S. cerevisiae* (PDB 2uv8) and *P. pastoris* (EMDB 12139), providing new insights on the structural configuration of FAS in different nutritional states (Figure 52 F, H, bottom (Gipson et al. 2010, Leibundgut et al. 2007, Singh et al. 2020)). Here, in-cell fatty acid synthase complexes within lamellae prepared from exponentially growing and 1 h energy-depleted yeast cells revealed nutrient-dependent ACP localizations. This data lay the foundation for future work on the connection between the different ACP locations and the activity of the multi-enzyme complex.

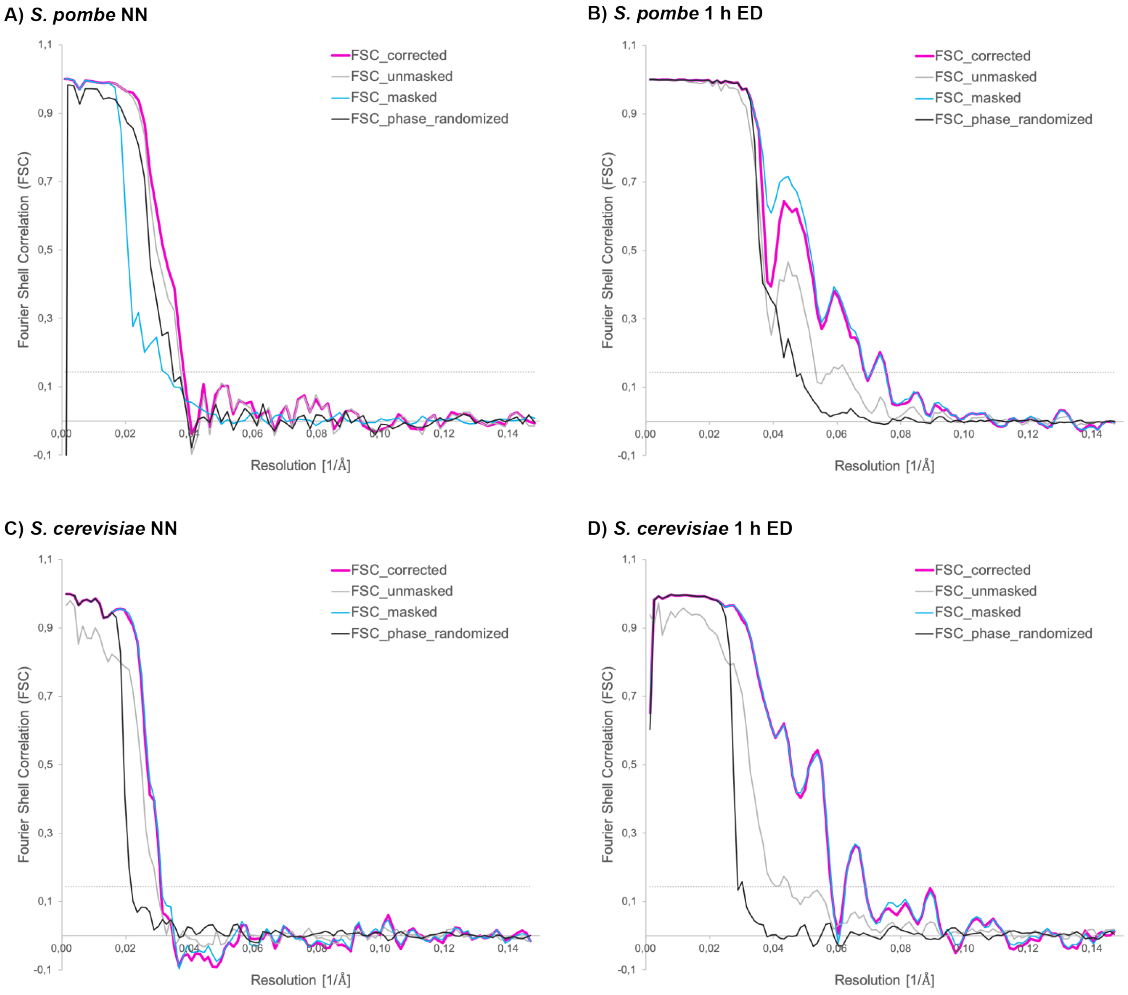

Figure 51: FSC curves of FAS subtomogram averages from *S. pombe* and *S. cerevisiae*. A-D) Fourier shell correlation (FSC) curves of 3D reconstructions from well-aligned FAS classes at each of the analyzed nutritional states and refined in RELION. FSC threshold of 0.143 indicated as dotted line in A-D (Rosenthal and Henderson 2003).

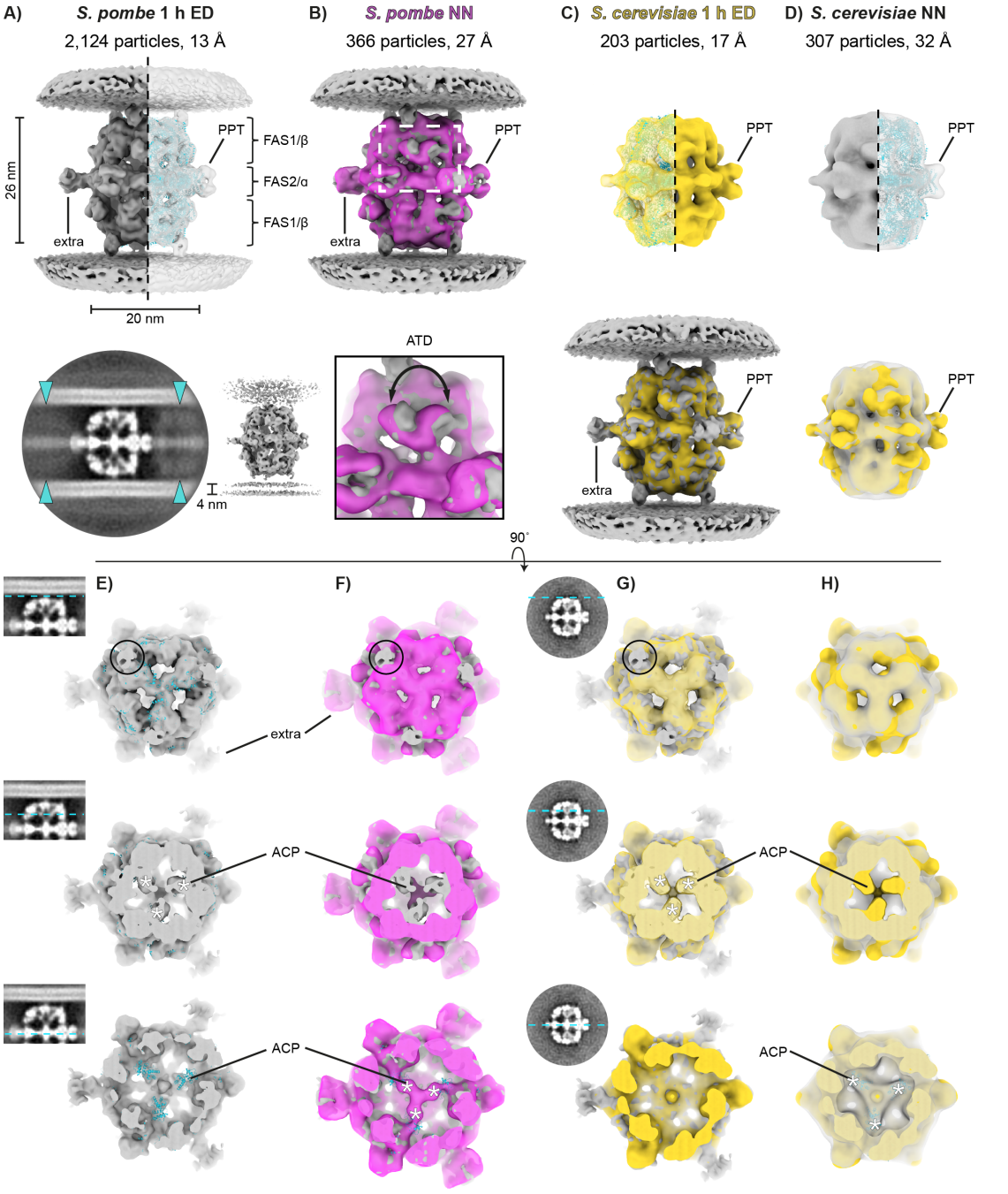
A) S. pombe 1 h ED
2,124 particles, 13 Å
B) S. pombe NN
366 particles, 27 Å
C) S. cerevisiae 1 h ED
203 particles, 17 Å
D) S. cerevisiae NN
307 particles, 32 Å
PPT
FAS1/β
FAS2/α
FAS1/β
26 nm
extra
20 nm
4 nm
ATD
90°
E)
F)
G)
H)
ACP

Figure 52: Nutrient-dependent structural variation of FAS in *S. pombe* and *S. cerevisiae*. A) Averaging of 3D-classified, well-aligned particle classes for each of the four datasets refined with applied D_3 symmetry resulted in 3D reconstructions of FAS with isotropic angular distribution. The complexes resembled the published *S. cerevisiae* structure (PDB 2uv8, cyan) comprised of two half domes separated by a central α wheel. The phosphopantetheinyl transferase (PPT) domain was resolved at the C-terminus of Fas2/α and an extra density linked to the α wheel could not be assigned. A) *S. pombe* 1 h ED FAS particles were picked within monolayer arrays and the resulting complex was positioned between two lipid membranes. On the top and bottom, three connections to the adjacent membranes were visible. Neighboring FAS complexes were detectable on a 2D slice through the *S. pombe* 1 h ED subtomogram average (bottom left, cyan triangles) but no connecting density was resolved. The membrane had a thickness of 4 nm, typical for a phospholipid bilayer (bottom right). B) The overlay of *S. pombe* FAS from normal nutrient conditions (NN, pink) with 1 h ED (grey) revealed that the extra equatorial density was also observed in the control state, but the connecting densities and the adjacent membranes were missing. Zoom into the upper half dome (white dashed box) revealed a rotation of the ETD domain between the two nutritional states (bottom inset). C) For *S. cerevisiae* 1 h ED, the PPT could be resolved, but in comparison to the *S. pombe* 1 h ED map (grey, below) the extra, unassigned densities were not observed. D) FAS subtomogram average from exponentially growing *S. cerevisiae* cells matched the published structure (PDB 2uv8, cyan) and the 1 h ED map (grey, below). E) Rotating the complexes by 90° and cutting through the densities from the top at different levels revealed the D_3 symmetry of the complex with three connecting densities for *S. pombe* 1 h ED (grey in E and G, example highlighted with a black circle). ACPs were located at the top of each half dome after 1 h ED (E and G) and close to the α wheel in control FAS (F and H) independent of the yeast species. The ACP location in normal nutrient yeast cells agreed with the published structure (PDB 2uv8, cyan).

5.6 Dynamics of stress-induced reorganization of the yeast cytosol

In order to assess whether the different architectures of nutrient-dependent cytosolic restructuring in *S. cerevisiae* and *S. pombe* were accompanied by species-specific assembly dynamics, fluorescence microscopy movies were recorded of endogenously tagged FAS-mCherry constructs, as model. In addition, fluorescence recovery after photobleaching (FRAP) was employed to investigate the biophysical state of the observed ED-triggered assemblies. The cells were further treated with different stresses and changes in cytosolic pH were analyzed to investigate the drivers of cytosolic solidification. The following experiments were supported by Ievgeniia Zagoriy and performed and analyzed together with Willram Scholz, a master student intern who I supervised.

5.6.1 The fatty acid synthase reveals species-dependent assembly dynamics upon energy depletion

Fluorescence microscopy movies elucidated that in less than one hour, FAS localized in hollow, spherical shapes within the *S. pombe* cytosol, reaching the highest number of assemblies at around 3.5 h (Figure 53 A, B top). At later time points, the assemblies dissolved. In contrast, FAS foci formed slower in *S. cerevisiae* reaching a plateau of two to three assemblies per cell at around 6 h of ED (Figure 53 A, B bottom). FAS localized into globular punctae distinct from FAS arrangements detected in *S. pombe*. Thus, in agreement with the cryo-electron tomography observations (cf. chapter 5.2.4), energy depletion led to time- and species-specific FAS condensate formation. In general, fluorescence intensities first increased within the first hours of treatment and decreased at later time points (cf. Supplementary Table S3 and Supplementary Figure S1). This could hint at protein degradation upon prolonged nutrient stress, as cells in the glucose control sample continued dividing and therefore also reached a stationary state after around 8 h.

In order to assess whether these assemblies displayed liquid- or solid-like properties, the mobility of FAS within the yeast cytosol was measured by fluorescence recovery after photobleaching (FRAP). As the foci are small (< 0.8 µm) or dispersed, and the bleaching area is restricted by the point spread function of the microscope, a mix of cytosolic and FAS foci were bleached and analyzed. Under normal nutrient conditions, FAS freely diffused within the cytosol displaying fast FRAP with a half

time of around 1-3 s (Figure 53 C, D, Table 5). In the case of *S. pombe*, FAS dynamics slowed down immediately after energy depletion and the signal could not fully recover (immobile fraction of around 90 %, Table 5). Recoveries decelerated even more after 3 h of ED suggesting a solidified state, whereas at around 8 h, FAS seemed to become slightly more dynamic (Figure 53 C, D top panels), in agreement with the dissolution of condensates in light microscopy movies and less frequent observations in cryo-electron tomograms (cf. Table 3). As the overall fluorescence intensity decreased in time-lapse movies, FAS-mCherry was potentially degraded at later time points of ED. For *S. cerevisiae*, FRAP of FAS assemblies was investigated in glucose control and after 6 h of ED when cells consistently contained large foci. Here, dynamics also slowed down drastically and the signal could not be fully recovered (Table 5). Also, the immobilized fraction increased from initial 45 % (glucose control) to 93 % (> 300 min ED).

These FRAP results showed a clear decrease in FAS mobility upon energy depletion. This suggests a change in the cellular biophysical properties, which could either reflect the overall solidification of the cytosol or, in addition, direct interactions within the assemblies leading to a more gel-like state. The observed increase in mobility in *S. pombe* cells at later time points could further indicate an adaptation to the prolonged stress or potentially also degradation.

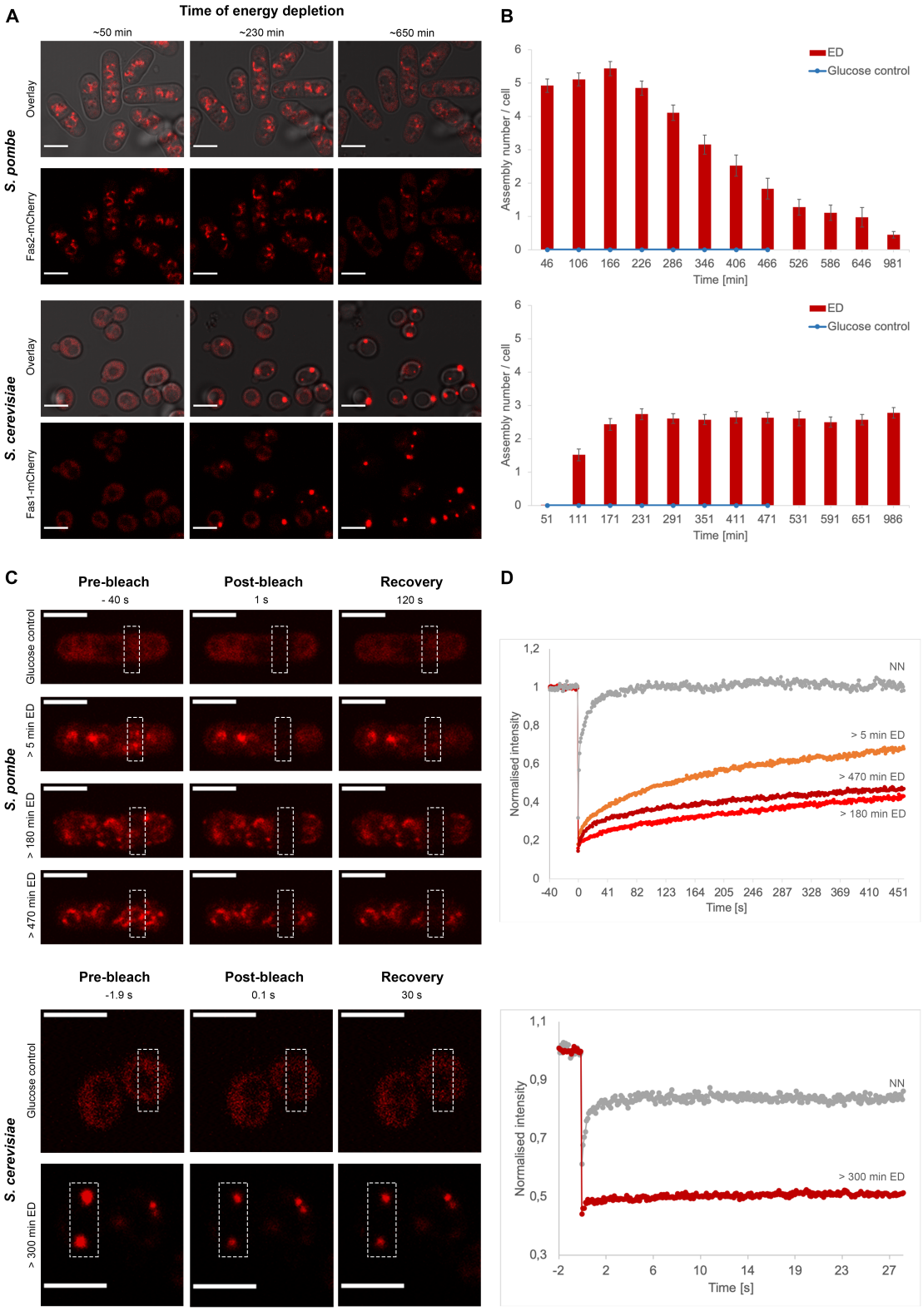
A
Time of energy depletion
~50 min
~230 min
~650 min
S. pombe
Overlay
Fas2-mCherry
S. cerevisiae
Overlay
Fas1-mCherry
B
ED
Glucose control
Assembly number / cell
Time [min]
46 106 166 226 286 346 406 466 526 586 646 981
51 111 171 231 291 351 411 471 531 591 651 986
C
Pre-bleach
Post-bleach
Recovery
- 40 s
1 s
120 s
Glucose control
> 5 min ED
> 180 min ED
> 470 min ED
-1.9 s
0.1 s
30 s
> 300 min ED
D
Normalised intensity
Time [s]
NN
> 5 min ED
> 470 min ED
> 180 min ED
> 300 min ED

Figure 53: Dynamics of fatty acid synthase complexes upon energy depletion. A) In *S. pombe*, FAS immediately co-localized upon energy depletion into spherical assemblies (top panel). In contrast, *S. cerevisiae* FAS assembled over longer time scales into spherical foci (bottom panel). B) Quantification of assembly counts per cell revealed species-dependent differences in assembly dynamics. For yeast cells grown in glucose control medium, no foci were observed (cf. glucose control in C. After more than 8 h, control samples could no longer be analyzed as they were over-grown. C) Example images of FRAP experiments in Fas2-mCherry expressing *S. pombe* (top panel) and Fas1-mCherry expressing *S. cerevisiae* (bottom panel) under varying nutritional conditions. D) FRAP curves revealed that recovery drastically slowed down upon energy depletion in both yeast strains (cf. Table 5). All images display individual z-slices and scale bars of 5 µm. *S. pombe* data produced jointly with Willram Scholz.

Table 5: Fitting parameters of FAS-mCherry FRAP curves. Due to their small size, a cytosolic area larger than individual FAS condensates was bleached. Recovery curves were fitted with either a one-step (glucose control) or two-step exponential model (ED), accounting for the two populations of cytosolic and condensed proteins upon nutrient stress. The resulting half times and immobilized fractions (I_{imm}) are displayed for normalized intensities (cf. Methods 4). For *S. pombe* five replicates per time point were normalized to background and whole cell intensities for each condition. 21 *S. cerevisiae* replicates of individual cells in each > 300 min ED and control conditions were double-normalized to intensities of the background and a reference fluorescence signal in another cell within the field of view. *S. pombe* data produced jointly with Willram Scholz.

Species	**Condition**	$\mathbf{I_0}$	$\mathbf{I_1}$ **(1)**	$\mathbf{I_1}$ **(2)**	$\mathbf{t_{1/2}}$ **(1)** [s]	$\mathbf{t_{1/2}}$ **(2)** [s]	$\mathbf{I_{imm}}$ **(1)**	$\mathbf{I_{imm}}$ **(2)**
S. pombe	Gluc. control	0.66	0.35	-	13.27	-	0.00	-
	> 10 min ED	0.23	0.10	0.39	15.16	158.67	0.87	0.56
	> 180 min ED	0.18	0.06	0.39	19.33	485.53	0.93	0.58
	> 470 min ED	0.18	0.11	0.23	9.85	209.33	0.86	0.75
S. cerevisiae	Gluc. control	0.64	0.20	-	3.94	-	0.45	-
	> 300 min ED	0.44	0.04	0.02	1.18	38.25	0.93	0.98

5.6.2 Fatty acid synthase assembly formation is stress type-dependent

FAS sequestration has previously been observed in light microscopy experiments of *S. cerevisiae* after four days of glucose depletion (Suresh et al. 2015). The above described findings for energy-depleted yeast thus opened the question whether the more physiological stress of glucose depletion, which yeast cells likely encounter in their natural habitats, also leads to FAS assembly formation in *S. pombe*. To investigate this, *S. cerevisiae* cells were treated first with minimal medium lacking glucose to reproduce the results by Suresh et al. 2015. This confirmed that similar FAS foci formed, but on different time scales than upon ED (Figure 54 A, cf. Figure 53 A lower panel). In addition, staining by the pH-sensitive dye CDCFDA showed a shift from acidic vacuoles to lower pH in the cytosol over several days of glucose depletion. In comparison, in *S. pombe* glucose depletion conditions induced a different cell shape and increased FAS signal close to the nucleus after two days of treatment (Figure 54 B, cf. Figure 53 A top panel). This less elongated cell shape could also be observed in TEM overviews of lamellae prepared from 4-day glucose-depleted *S. pombe* cells (data not shown). Morphologically, FAS assemblies were different from the observed ED arrays, but likely still surrounded vacuoles which also changed their cellular distribution as observed in TEM overviews (data not shown). The energy state of the cell has been suggested to mediate cytosolic pH. Monitoring cellular acidification, CDCFDA initially stained vacuoles and enabled the tracking of their morphological changes during one day of glucose depletion. At later time points, no fluorescence signal could be detected which was either caused by the fact that the stain could not enter the cells upon glucose depletion or the dye could not be hydrolyzed by endogenous enzymes to produce fluorescence.

Molecular crowding has been implied to induce phase separation (Kuznetsova et al. 2014, Petrovska et al. 2014). Increased ribosome concentrations, which serve as an approximation for cellular crowdedness, were observed for *S. cerevisiae* upon 1 h ED, while no significant change was detected for *S. pombe* (cf. chapter 5.3). However, colocalization and local increase in FAS concentrations was observed in both species. Hyper-osmotic stress was applied ectopically to induce crowding in FAS-mCherry tagged yeast. For *S. pombe*, this treatment showed condensation of FAS and redistribution at time scales different from energy depletion (Figure 54 C). In *S. cerevisiae* FAS condensation could not be observed upon osmotic stress in the

time scales of ED-induced assembly formation (data not shown). Thus, molecular crowding could induce similar FAS assemblies as in energy depleted *S. pombe* cells and therefore is a potential driver of cytosolic condensation, ultimately leading to a more solid state.

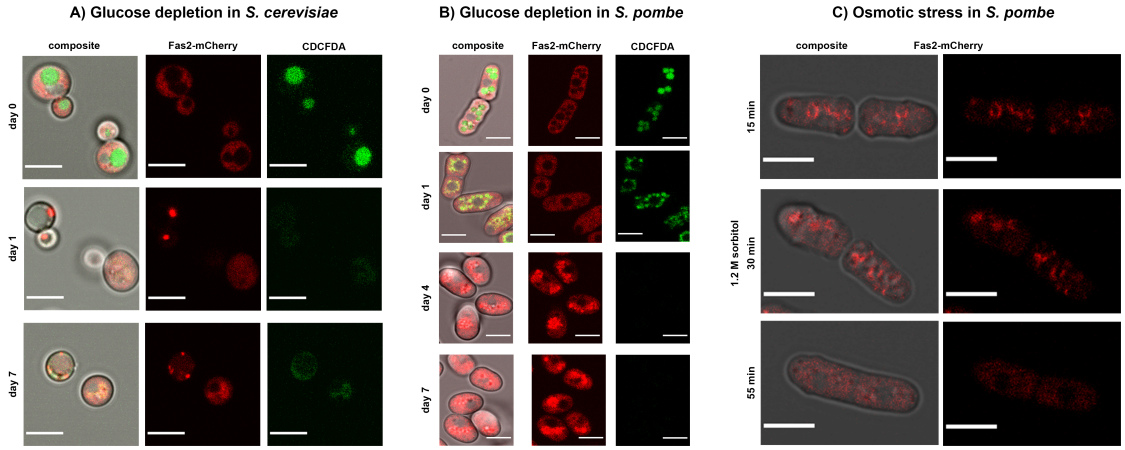

Figure 54: FAS assembly formation varied depending on strain and stress type. A) Glucose depletion over several days induced FAS foci formation and acidification (CDCFDA staining in green) of the *S. cerevisiae* cytosol. B) Vacuole morphology and FAS assembly in glucose-depleted *S. pombe* was distinct from energy-depleted cells. Here, CDCFDA could either not enter the cells upon glucose depletion beyond day 1 or it could not be hydrolyzed by endogenous enzymes to show fluorescence. C) Hyper-osmotic stress induced in *S. pombe* upon treatment with 1.2 M sorbitol in glucose-containing medium caused FAS co-localization similar to energy depletion, but on different time scales. All images display individual, central z-slices with scale bars of 5 µm. Glucose depletion data produced jointly with Willram Scholz.

5.6.3 Cytosolic acidification depends on the type of nutritional stress

Energy depletion was shown to induce cytosolic acidification in yeast (Munder et al. 2016). As a change in cellular pH alters protein surface charges, it thereby might drive protein oligomerization and thus cytosolic solidification. To investigate nutrient stress-dependent cytosolic acidification, light microscopy movies of wild-type yeast cells treated with different starvation media were recorded. Changes in cellular pH were observed with the pH-sensitive dye CDCFDA and membrane morphology alterations detected with the lipophilic membrane stain FM4-64. The cytosolic pH changed similarly upon energy and glucose depletion in *S. cerevisiae* and revealed cytosolic acidification (Figure 55 A). For *S. pombe* different scenarios

were observed. Here, glucose depletion did not induce a decrease in cytosolic pH, but rather a change in vacuole morphology resembling the fractionation previously described upon hyperosmotic stress (Figure 55 B, (Bone et al. 1998)). Oversaturation of the CDCFDA signal upon acidification did not allow for a quantitative analysis of this change.

In addition, the internalization of plasma membrane proteins and lipids and their subsequent hydrolysis was found to provide energy during nutrient scarcity (Lang et al. 2014). The FM4-64 signal showed that endocytosis still happened in both yeast species upon glucose depletion but not during energy depletion.

Future experiments including induction of direct cytosolic acidification with acidic medium and treatment with a protonophore permeabilizing the membranes for strains with fluorescently-tagged proteins, identified in the oligomeric assemblies, will help to disentangle the influence of these factors on the large-scale self-assemblies observed in cryo-electron tomograms.

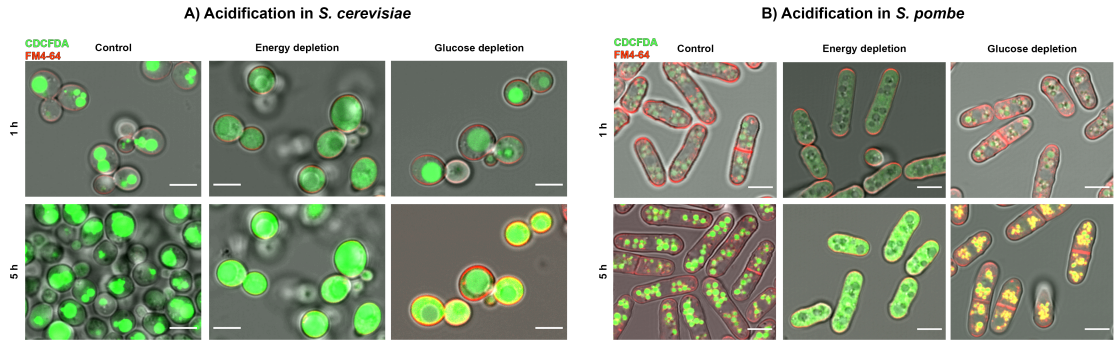

Figure 55: Cellular acidification upon nutritional stress. A) In *S. cerevisiae* CDCFDA (green) stained acidic environments. In normal nutrient conditions (control), it highlighted vacuoles and upon energy depletion, as well as after 5 h of glucose depletion, the yeast cytosol. The non-specific membrane dye FM4-64 (red) visualized the plasma membrane and endocytic vesicles. B) In *S. pombe* vacuoles were acidic in control and glucose-depleted cells, whereas cytosolic acidification could only be observed after 5 h of energy depletion. All images display individual, central z-slices with scale bars of 5 µm. Data produced jointly with Willram Scholz.

6 Discussion

In this thesis, I presented the development of automated cryo-sample preparation and data collection workflows, as well as data mining software, which enabled me to collect and analyze large cryo-ET datasets. I utilized these advances to investigate nutrient-dependent reorganization of the yeast cytosol. In the following, I will first discuss the obtained results for automating the cryo-ET workflow, challenges that still reside and opportunities that these new tools enable. Then, I will highlight the gained biological insights on cytosolic organization and local variations in molecular crowding and structural variations in specific macromolecular species. Finally, I will address open questions for future studies.

6.1 Sample optimization for in-cell structural biology

Cryo-electron tomography of cellular samples enables the direct visualization of macromolecules in their native environments. In order to obtain high quality and large tomography datasets, specimen need to first be optimized (cf. Figure 8). Cells have to be properly vitrified in order to preserve their delicate, internal structures in a frozen-hydrated state. The localization of individual mammalian cells or an agglomerate of smaller cells, such as yeast, in the center of a grid square is required for subsequent cryo-FIB milling. Optimized grids contain several such positions and thus increase throughput by providing a sufficient number of potential lamella preparation sites. Using parallel blotting from the back side of a grid, implemented in the Leica grid plunger, resulted in even distribution of vitrified yeast cells on TEM grids. The concentration of cells grown in suspension, which are directly applied to grids prior to vitrification, further influences the cell density and therefore the number of cells from which a lamella is created. This subsequently impacts the number of areas that can be imaged by cryo-ET. In comparison, lamellae prepared from mammalian cells usually contain cellular material from only 1-2 cells and therefore their positioning requires optimization with for example micro-patterning techniques (Toro-Nahuelpan et al. 2020). For single-particle cryo-EM, tools are already available that deposit small volumes of protein solutions in a controlled manner directly onto grids prior to vitrification (Dandey et al. 2020, Ravelli et al. 2020). Although these instruments have yet to be tested for cellular samples, further development will likely facilitate optimal positioning of cells and save resources by application of multiple conditions or cell-types on a single grid.

In addition, sample stability plays an important role in the subsequent steps of sample thinning by cryo-FIB milling and targeting of intracellular structures via cryo-CLEM. First of all, gentle handling of the fragile, plunge-frozen grids and minimizing the number of transfers between instruments is required to reduce mechanical damage or sample loss. Unifying designs for sample holders (Kuba et al. 2020), combining several imaging modalities in a single instrument (Bieber et al. 2021, Gorelick et al. 2019), and optimizing transfer and loading stations (Tacke et al. 2021) will likely improve cryo-sample throughput in the future.

Grid types (mesh and hole spacings) and substrate properties also need to be considered for optimal sample stability. Matching heat expansion coefficients between grid and support materials decrease internal stresses and differential compression (Russo and Passmore 2016b, Thorne 2020). Also, vitreous buffer surrounding cellular samples can bear tension (Naydenova et al. 2020). The introduction of micro-expansion joints post vitrification relieves such sample strains and prevents lamella bending (Wolff et al. 2019). This renders the sample more stable during lamella milling and subsequent cryo-ET imaging.

6.2 Establishment of high-throughput cryo-FIB milling workflows

Cryo-samples need to be thinned in order to elucidate the underlying structures of cellular landscapes by cryo-ET. Creating around 200 nm thin, cellular slices by cryo-FIB milling is a manual process which requires a high level of expertise, is tedious and time-consuming (Schaffer et al. 2015, Schaffer et al. 2017, Villa et al. 2013). Therefore, the development of automated procedures has facilitated high-throughput lamella generation for cryo-ET (Buckley et al. 2020, Kuba et al. 2020, Zachs et al. 2020). The here presented SerialFIB software (Klumpe, Fung and Goetz et al. 2021) also automates such on-grid lamella preparations with a success rate of 91.5 % for rough milling and 83.1 % for fine milling tested on six different cell types (cf. Table 1). Although manual operations by expert users likely achieve success rates of up to 100 %, as milling can simply be stopped before the lamella gets damaged, automated workflows reliably and reproducibly achieve high-quality lamellae from optimized samples. This is especially beneficial for unexperienced users. For this purpose, SerialFIB entails an easy-to-use GUI and established milling protocols for several use-cases which represent a valuable resource. Furthermore, the microscope

does not require supervision while milling and therefore this time is saved for the user.

In addition, the modularity of SerialFIB enables targeted lamella milling utilizing prior localization by 3D correlative light microscopy, cryo-FIB SEM volume imaging and custom milling procedures, e. g. for lamella lift-out workflows (Mahamid et al. 2015, Schaffer et al. 2019), as well as additional modules that will likely be developed for new use-cases in the future owing to the scripting interface of SerialFIB.

The current major bottleneck to achieve higher throughput for lamella preparations is dictated by a) the slow ablation rates of Ga^+ ions that will likely be improved by plasma FIB instruments (Burnett et al. 2016), and b) the number of samples that can be loaded into a cryo-FIB instrument and therefore processed to generate lamellae during one session. A solution to this challenge requires cryo-FIB microscopes with better vacuum and integrated cryo-traps resulting in lower amorphous ice condensation rates on the sample (Tacke et al. 2021), improved cooling systems that will allow longer and overnight operations, and sample storage devices to sequentially mill lamellae on more than the currently possible two grids without the need to transfer samples in or out of the microscope.

Furthermore, SerialFIB is applicable to cryo-CLEM approaches to generate lamellae in a site-specific manner. Here, lipid droplets were targeted in HeLa cells in four sessions corresponding to four grids and 15 lamellae sites. 14 lamellae were successfully fine-milled, while one was lost during empirical optimization of milling parameters. Sample deformations were observed on grid squares with thin vitreous ice, regardless of whether cellular material was present (cf. Figure 14). Although sample deformations compromise correlation accuracy, the targeted lipid droplets were maintained in seven out of 10 lamellae created on three $TiSiO_2$ grids whereas none of the four lamellae created on one $AuSiO_2$ support contained the aimed feature. This was validated by a comparison between lipid droplet signal in different cryo-FLM slices and the structural signature in TEM overview of the cellular slices. Cryo-ET also produced high-quality tomograms from lamellae prepared with SerialFIB, which confirmed the usability of the automation software for cryo-CLEM workflows and the potential usage of lipid droplets as intracellular fiducials for cryo-ET (Klein et al. 2021, Okolo et al. 2021, Scher et al. 2021). This also opens

the possibility, in combination with super-resolution techniques (Moser et al. 2019, Moser et al. 2021), to target even smaller objects relative to LDs acting as internal reference points. Thus, it will likely facilitate correlation of other cellular features, such as biomolecular condensates in yeast cells, in the future.

SerialFIB also enabled automated acquisition of cryo-FIB SEM volumes of two mammalian cell types (i. e., HeLa and Sum159) revealing nanoscale information of organelle (i. e., lipid droplets and nuclei) sizes, localization and distributions. Subsequent lamella preparation below the FIB-micromachined and SEM-imaged area, followed by cryo-ET acquisition confirmed the feasibility to collect high-quality tomograms with this approach. The cellular context together with on-the-fly segmentations, which might become available in the future, can thus guide lamella preparations in the vicinity of specific cellular structures at higher precision.

The correlation of cryo-FLM and cryo-FIB SEM volumes of HeLa cells with stained lipid droplets and fiducial beads was demonstrated using SerialFIB's cryo-FIB SEM volume imaging modality. Affine transformations between centroids of lipid droplets and fiducial beads in both imaging modalities resulted in an average residual error of 386 nm which is within the current resolution limit of around 400 nm for cryo-confocal light microscopy (Arnold et al. 2016, Van Driel et al. 2009). The error might also stem from imperfect FIB slicing, which influences the centroid fitting of lipid droplet and bead segmentations in the cryo-FIB SEM volume. However, the observation of local point clusters with similarly behaving residual vectors (data not shown) may allow the refinement of local correlations with lipid droplets taking internal sample deformations into account. 3D correlations utilizing the here demonstrated combined cryo-FLM and cryo-FIB SEM volume imaging will likely also enable targeting in larger high-pressure frozen volumes for lift-out approaches.

In summary, the method developments for cryo-FIB workflows presented in this thesis enable automated, high-throughput generation of lamellae with high quality for subsequent cryo-ET. SerialFIB facilitates cryo-FIB-milling of cellular samples for users with different levels of expertise and thereby streamlines cryo-sample preparations. Furthermore, this software represents a modular platform for diverse cryo-preparations including cryo-FIB SEM volume imaging and trench milling for lift-out approaches. Especially its scriptable and open-source interface will serve the in-cell

structural biology community for future developments of more advanced cryo-FIB procedures.

6.3 Automated in-cell cryo-electron tomography acquisition

For this study, more than 140 lamellae were generated using automated, high-throughput on-grid cryo-FIB milling in SerialFIB, as well as manual operations. Imaging the biological information contained in these cellular slices by cryo-ET was automated with the help of Wim Hagen and Felix Weis using SerialEM (cf. Figure 16, (Mastronarde 2005, Mastronarde 2018, Weis and Hagen 2020)) and resulted in over 500 tomograms of yeast cells under varying nutritional conditions. Newly developed features in SerialEM (version 3.8 (Mastronarde 2018)) include the tilt series controller which enables abortion of tilt series acquisition in user-definable cases. For instance, when tracking is off, the signal recorded by the camera is too dim at high tilts or when obstacles such as crystalline ice or bulk cellular material at the edge of a lamella obstruct the field of view. This implementation saves time and thus increases tomography throughput. Further software tools support TEM data collection with SerialEM and utilize virtual maps on which target sites are selected and set-up while the microscope is already acquiring tomograms on previously defined positions (Schorb et al. 2019). Furthermore, the development of new acquisition schemes that circumvent the trade-off between field of view and resolution, and allow the acquisition of tomographic data across the complete lamella at high resolutions, are currently being developed to increase the biological information that can be obtained from a single lamella (Peck et al. 2021).

6.4 DeePiCt automates data mining to explore macromolecules in their cellular context

With optimized high-throughput cryo-sample generation and acquisition of high-quality tomograms described above, data mining in cryo-electron tomograms becomes the major challenge of the cryo-ET workflow. Traditional methods such as template matching (Hrabe et al. 2012) are computationally expensive, require careful manual inspection, do not detect all target structures, which is likely due to the crowdedness of the cytosol, and are only amenable to particles which show good contrast in inherently low signal-to-noise tomograms (cf. Figure 17). CNN-based tools for pattern recognition in cryo-electron tomograms, once trained, enable fast and

reliable detection of many different structural features (Chen et al. 2017, Moebel et al. 2021). The here presented DeePiCt workflow is based on the U-net architecture (Ronneberger et al. 2015) and entails 2D CNNs for compartment segmentation which provide functional context to the output of 3D CNNs for cellular structure annotations, as well as particle localizations. The development of this software required first the generation of ground truth, expert annotations for training and evaluation in real cryo-ET data which are not yet publicly available. Therefore, cellular compartments, including organelles and cytosol, membranes, ribosomes and FAS were fully segmented and localized in 20 high-quality cryo-electron tomograms depicting cellular landscapes of exponentially growing wild-type *S. pombe*. The annotated ribosome and FAS particles resulted in subtomogram averages providing valuable structural insights into *S. pombe* enzyme complexes inside exponentially-growing cells which are not yet publicly available.

Moreover, the ground truth data set consists of 10 tomograms acquired with a Volta potential phase plate and 10 tomograms acquired with defocus only (DEF). This enabled the training of networks with 10 VPP tomograms, which were applied to individual datasets of different acquisition parameters, and precision and recall were evaluated (cf. chapter 5.1.4).

The DeePiCt 2D CNN readily discriminates cellular compartments with average auPRCs of 0.969 for cytosol and 0.893 for organelles in the VPP domain. The resulting segmentations can be used to mask certain cellular areas to improve particle localizations by either removing false positives or by the detection of specific structures in their cellular context, such as ribosomes close to organelles (e.g., ER and mitochondria). The successful discrimination of cytosol and organelles further opens the possibility to train DeePiCt networks which segment and classify specific organelle types and structured ED filaments or condensates with newly generated ground truth data in the future.

For DeePiCt particle predictions in the VPP domain, the auPRC values for ribosomes and FAS calculated by cross validation of 0.579 and 0.234, respectively, were rated adequate and was further confirmed by subtomogram averaging (cf. Figure 18). For the ground truth construction, DeePiCt outperformed TM as the software recovered more ribosomes and also FAS particles for which the traditional method

completely failed (cf. Figure 17). In the future, detailed method comparisons with the newly developed 3D CNN-based DeepFinder will be performed to analyze DeePiCt's performance in more detail (Moebel et al. 2021).

For this thesis, I utilized DeePiCt to further detect ribosomes in both *S. pombe* and *S. cerevisiae* under normal nutrient and energy depletion conditions in DEF tomograms. The predictions showed satisfactory performances and added a substantial number of particles to the individual datasets (cf. Figure 24, Supplementary tables S4-S13). This enabled subtomogram averaging of ribosomes to high-resolutions at which structural and functional insights on nutrient-dependent ribosome configurations were revealed (cf. Figures 25, 50). While the performance was sufficient for improving subtomogram averaging by increasing particle numbers, DeePiCt predictions are not yet suited to calculate absolute particle numbers in the cytosolic volume. This was especially apparent for *S. cerevisiae* NN where the combination of cytosol and ribosome predictions resulted in less than half of the ground truth ribosome concentration. Although this is sufficient to detect general trends, it is not enough to provide quantitative data on global molecular crowding with ribosomes as an approximation. As the utilized DeePiCt network was trained on VPP *S. pombe* data, retraining with comprehensive annotations for *S. cerevisiae* under specific nutrient conditions might improve the method's performance in the future.

Moreover, DeePiCt networks trained in the here discussed *S. pombe* VPP dataset can be directly applied to other species as demonstrated for *S. cerevisiae*, various experimental conditions (cf. chapter 5.4), and even unseen tomograms of other organisms such as HeLa cells (data not shown), and objectively predict macromolecules in their cellular context. These results lay the ground for automated particle detection and subtomogram averaging in other large cryo-ET datasets in the future. Thus, the presented real cryo-ET ground truth together with pre-trained and ready-to-use CNNs represent a major contribution to the cryo-ET community for both method development and immediate segmentation tasks. Users can easily apply trained models to unseen tomograms, which takes only minutes. The flexibility of the DeePiCt workflow design further allows users to tailor the network's architecture to their needs dictated by the structures to be trained which will likely take several hours depending on the data size and cluster configurations.

DeePiCt also harbors a major advantage in comparison to other particle picking procedures, which is the cellular context provided by the 2D CNNs. This was demonstrated for ribosomes in close proximity to mitochondria and ER. Subtomogram averaging and 3D classifications revealed for both ribosome classes connecting densities to the adjacent membrane (cf. Figure 25). Interestingly, the ribosomes were oriented differently with an angular offset of around 35° facing the membrane. This highlights the fact that DeePiCt can predict particles in their cellular context providing new biological insights.

Taken together, the presented results emphasize the potential of deep-learning methods such as DeePiCt. A community effort to provide trained CNNs on imaging data from different modalities has already started and will likely enable faster and higher throughput data segmentation in a multitude of organisms in the future (ModelZoo, (Koh 2021)). Also, further development of unsupervised methods for cryo-ET will enable mapping of many more structural features than the ones shown here (Gubins et al. 2019, Martinez-Sanchez et al. 2020, Zeng et al. 2021). Harnessing the valuable information deposited in protein structure data bases and the ground-breaking protein structure predictions of AlphaFold2 (Jumper et al. 2021) may accelerate these developments and help to generate holistic cell models at high resolutions within the cellular context provided by large scale cryo-ET datasets.

6.5 Nutrient stress induces morphological changes of specific organelles with implications for the metabolic state of yeast cells

By employing cryo-electron tomography, utilizing the improved cryo-sample preparation workflows described above, I showed that energy and glucose depletion induced large scale structural rearrangement of the yeast cytosol in unlabeled, wild-type strains. Upon nutritional stress, yeast cells displayed a variety of organelles changing their morphologies, including mitochondria and lipid droplets. In addition, unstructured high-density assemblies were observed upon prolonged starvation conditions which could represent aggregates. Also, the nuclear envelope was expanded upon four days of glucose depletion in *S. pombe*. Despite these observations of altered cellular ultrastructures, continuity of the membranes and overall compartment integrity, especially of mitochondria, were observed in all cryo-electron tomograms of energy-depleted yeast. This showed that the cells can cope and adapt to the

harsh nutrient stress without inducing cell death, or apoptosis, which would lead to mitochondria outer membrane rupture and leakage (Ader et al. 2019). However, the unstructured, high density assemblies observed at later time points of energy depletion could represent amorphous protein aggregates which hint at a shift towards non-reversible, solid phases. This could indicate that prolonged nutrient starvation ultimately leads to cell death as observed in many protein aggregation diseases (Bauerlein et al. 2017, Patel et al. 2015, Shin and Brangwynne 2017).

Mitochondria fissioned and adopted a more spherical shape in both investigated yeast species confirming previous studies (Bagamery et al. 2020, Liu et al. 2019, Zheng et al. 2019). These organelles are the energy producing factories of the cell and provide ATP for many cellular processes under normal nutrient conditions. Thus, the observed morphological changes might be attributable to the low energy state of the cells. The inhibition of the Cytochrome C reductase and therefore of the respiratory chain via Antimycin A stops ATP generation upstream of the ATP synthase which likely explains the observation of seemingly intact dimers decorating cristae in *S. cerevisiae* (cf. Figure 35 E).

Furthermore, in *S. pombe* an additional layer on the surface of the mitochondrion's outer membrane was detected (cf. Figure 35). Its structural signature resembled cryo-EM maps of Dnm1 polymers, constituted by this self-assembling dynamin-related GTPase which is implied to facilitate mitochondria fission (Francy et al. 2017, Ingerman et al. 2005, Mears et al. 2011). However, this structure was not captured by tomography directly at the neck of dividing mitochondria where it was suggested to fulfill its function. Thus, the assembly displays another energy depletion-induced supramolecular architecture which might indicate a trapped state of Dnm1 due to the lack of energy. Segmentation and subsequent subtomogram averaging will confirm the identity of the structure and, depending on the resolution, reveal its functional state based on catalytic site occupancy.

In addition, lipid droplets were observed with altered morphologies upon nutrient deprivation. As these organelles store and provide energy, they are highly relevant for the metabolism and their morphologies inform on the energy state of yeast cells. LDs are usually spherical to reduce surface tension via a minimal contact area between the aqueous cytosol and the lipid interior (M'barek et al. 2017).

Here, energy-depletion induced deformation of these organelles in several instances and showed connections to vacuoles hinting at a potential utilization of the stored lipids to provide the cells with energy (cf. Figure 36). Also, peripheral crystalline layers of sterol esters caused by a phase transition via lipases that free fatty acids from the stored TAGs were observed in accordance with other studies (Mahamid et al. 2019, Rogers et al. 2021). The free fatty acids could then be subjected to beta-oxidation in order to provide energy to the cells (Weber et al. 2020). As no double membrane-bound compartments which correspond to autophagosomes were observed in cryo-electron tomograms, utilizing free fatty acids could respresent a potential adaptation mechanism to survive energy depletion and compensate for a lack of macro autophagy (Lang et al. 2014). However, it has to be considered that individual cells often display an inherent variety of lipid droplet morphologies and in the scope of this thesis no comprehensive analysis of all observed LDs was performed. Also complementing metabolomics studies might reveal changes in the lipidome of energy-depleted yeast cells. Nevertheless, the examples of LD morphological changes together with the observed FAS condensates, which will be discussed in detail below, hint at nutrient-dependent changes in the lipid metabolism of yeast cells.

6.6 Cryo-ET unveils nutrient-dependent supramolecular assemblies in the cytosol

A number of distinct supramolecular assemblies were observed in cryo-electron tomograms of the *S. cerevisiae* and *S. pombe* cytosol and nucleus. Their structural features were different from known cytoskeletal filaments, as observed in exponentially growing yeast cells. The assemblies occupied a large fraction of the cytosolic volume (around 5 %, cf. Figures 37, 38) and seemed to grow over time, which was indicated by qualitative observations in tomograms collected at later time points. This suggested that within one hour of energy depletion, despite previously being reported to result in cytosolic solidification (Joyner et al. 2016, Munder et al. 2016), condensation of structured assemblies did not yet reach a steady state, but rather continued to evolve over longer periods of time. The accompanied excluded volume effect has been suggested to drive polymerization in addition to attractive protein-surface interactions (Banani et al. 2017, Hyman et al. 2014, Walter and Brooks 1995). Segmenting these polymeric structures either manually or by training a dedicated DeePiCt 2D network will allow a quantitative analysis in all acquired

tomograms. This unique data set will then be utilized for meso-scale modelling to understand how the global changes in molecular organization lead to polymerization and ultimately establish cytosolic solidification as a strategy for survival (Minton 2019).

In accordance with previous light microscopy findings (Narayanaswamy et al. 2009, Park and Horton 2019, Petrovska et al. 2014, Prouteau and Loewith 2018), the components of these higher-order biomolecular assemblies are likely protein complexes, which may self-assemble upon energy depletion or require nucleic acids and/or metabolites to do so. Specific macromolecules are concentrated and possibly condensed within individual meso-scale architectures. Many metabolism-related enzymes have been shown to reversibly form polymers (Park and Horton 2019, Prouteau and Loewith 2018, Stoddard et al. 2020) and are interesting candidates for identifying the filament-forming components. However, it is unclear whether their formation represents an example of liquid-liquid demixing, as most of the so far described phase-separated condensates are comprised of intrinsically disordered proteins (Banani et al. 2017, Shin and Brangwynne 2017, Pak et al. 2016) and only some were observed to be highly structured assemblies (reviewed in Goetz and Mahamid 2020). Therefore segmentation and subsequent subtomogram averaging will be combined with mass-spectrometry approaches to unambiguously identify the components of the detected supramolecular architectures. This integrated approach may further decipher whether conformational changes, post-translational modification, accessibility of catalytic sites and ligand binding, as well as specific interaction surfaces drive self-assembly. The structural analysis in combination with light microscopy movies of the identified molecular species will further inform on their physical phase and dynamics which may also enable an understanding of potential molecular condensation and growth pathways.

6.7 Cytosolic ribosome concentrations inform on global, species -dependent changes in molecular crowding upon energy depletion

Molecular crowding was hypothesized to increase upon nutrient stress, based on the observed energy-depletion induced reduction in cell volume (Joyner et al. 2016, Marini et al. 2020, Munder et al. 2016) and the expectation that the yeast proteome does not significantly change in 1 h of treatment. The here presented quantitative

analysis of molecular crowding in cryo-electron tomograms which directly depict native molecular landscapes was performed via evaluation of the concentration of ribosomes as an approximation for global changes in molecular crowding. The ribosomes themselves are also likely to have a major contribution to crowding due to their large size and high abundance. Ribosome concentrations calculated with this approach were within the reported range of other studies for exponentially growing yeast cells (cf. Table 4).

In *S. pombe* a non-significant increase in ribosome concentrations, which was not reflected by DeePiCt predictions, was observed within 1 h of ED. Vacuoles have been observed to fission and this morphology change was suggested to compensate for the reduction of cellular volume in context of hyperosmotic stress, while keeping cytosolic concentrations isotonic (Bone et al. 1998). Thus, *S. pombe* cells likely already adapt to the energy depletion-induced changes in macromolecule concentrations within 1 h of treatment. For the later time points, DeePict predictions suggested a decrease in cytosolic ribosome concentrations which could indicate disassembly of the protein complex and potentially degradation. However, these observations for ribosome concentrations will have to be confirmed by light microscopy and mass spectrometry experiments.

In agreement with the expectations, for *S. cerevisiae* a significant average increase of 16.7 % in ribosome concentrations (based on ground truth annotations) was observed upon 1 h energy depletion. This could stem not only from the previously observed cell size reduction but also the expansion of vacuoles which further reduces the available cytosolic volume. For *S. cerevisiae*, molecular concentrations changed during prolonged stress (6 h ED) upon which ribosomes were still more concentrated than in normal nutrient conditions but less crowded than upon 1 h ED.

Taken together, these findings suggest that energy-depletion induces significant changes in global molecular crowding, approximated by ribosome concentrations, in *S. cerevisiae*. As the molecular concentrations seem to be dynamic, indicated by a dependence on the duration of stress, cells likely adapt in a time-dependent manner potentially also with different strategies to cope with the energy deprivation. In addition, the observed changes in ribosome concentrations, which due to their high abundance and large size exclude a significant fraction of the cytosolic volume,

likely influence other molecular species. Thereby, they might influence their effective concentrations and biophysical properties via phase separation or polymerization.

6.8 Energy-depleted yeast reveal non-translating stationary state ribosomes

The development of high-throughput cryo-ET sample preparation and particle picking workflows enabled the generation of large cryo-ET datasets of nutrient-dependent ribosomes. In addition to the gained information on particle concentrations and distributions inside cells, subsequent subtomogram averaging further informed on the nutrient-dependent functional states of yeast ribosomes. Comparisons between normal nutrient state and 1 h energy depletion confirmed overall structural similarity between *S. pombe* and *S. cerevisiae* maps and published *S. cerevisiae* structures (cf. Figure 43, (Buschauer et al. 2020, Delarue et al. 2018)). The achievement of sub-nanometer resolutions for well-aligned classes allowed the analysis of the ribosome interactome (cf. Figure 50). In normal nutrient conditions, ribosomes were identified in a translating state based on PTC occupancies with P-site tRNAs, as well as additional densities fitting various translation factors including eIF5a, eEF3 and eEF2. Also, ribosome sub-classes showed the expansion segment ES27L in an exit configuration connecting an extra density to the ribosomal exit tunnel.

Upon 1 h of energy depletion, fully assembled ribosomes were detected with vacant PTCs (cf. Figure 50). Additional densities were observed at the E-site likely fitting eIF5a and at the PTC entry site matching eRF1 or eEF2. Also, a sub-class with an additional density close to the head of the 40S subunit fitting eEF3 was not detectable. This suggested a stationary non-translating ribosome state as the cells are lacking energy to synthesize new proteins. Nevertheless, the observed complete 80S structures represent a large pool of functional complexes which are ready to be recycled and re-start translation once energy is supplied again. Furthermore, the assembly of ribosomes in polysomes was observed in all four datasets (cf. Figure 43 H). Coordinate-based distance analysis between neighboring ribosomes could be further performed in the future to identify polysomes and to quantify the fraction of ribosomes that form these assemblies in the different nutritional states and species. In combination with the identified functional states, this will likely inform further on translational activity of ribosomes inside yeast cells.

While a clear distinction between occupied and empty PTCs was observed for normal nutrient and energy-depleted *S. pombe* ribosomes, *S. cerevisiae* ribosomes revealed a mix of translational states in both nutrient conditions (cf. Figure 50). Despite the applied harsh nutritional stress, a class containing 21.6 % of all detected *S. cerevisiae* ribosomes revealed a P-site tRNA occupying the PTC and could hint at ongoing translation activity and thus protein synthesis. The newly produced proteins are likely relevant for the stress response and this observation is in accordance with previous polysome profiling experiments indicating reversible translation inhibition upon glucose depletion (Arribere et al. 2011). The structural analysis and classifications of PTC occupancies at later time points of ED may also inform on dynamic ribosome conformations. This will complement the observed changes in ribosome crowding which can be combined with proteome profiling experiments to inform on abundance changes and potential degradation upon prolonged starvation.

6.9 Energy depletion-induced FAS assemblies are condensates with species-dependent organization and structural variation

Cryo-electron tomography and light microscopy movies revealed that FAS complexes were evenly distributed under normal nutrient conditions and colocalized in species-dependent 3D assemblies upon energy depletion (cf. Figures 39 and 53). Overall, cytosolic FAS concentrations in exponentially growing cells were underestimated in comparison to mass spectrometry methods (cf. Table 4). This is likely caused by the fact that this enzyme complex is rather difficult to detect in cryo-electron tomograms due to its hollow structure. More particles were identified by boosting image contrast in tomograms acquired with a VPP. In addition, only fully assembled complexes can be localized with this method, while mass spectrometry approaches also detect individual peptides of non-assembled proteins.

In addition to the observed FAS foci upon 1 h of energy-depletion, individual complexes were still detected randomly distributed in the cytosol at similar concentrations as in normal nutrient conditions for *S. pombe* and increased particle numbers per cytosolic volume in *S. cerevisiae* tomograms (cf. Figure 41). This complements the findings for ribosome concentrations and therefore emphasizes species-dependent global changes in crowding upon 1 h of energy depletion.

Moreover, the instances of FAS foci observed in tomograms at different time points of ED match the species-dependent assembly dynamics of fluorescently-tagged FAS in light microscopy movies (cf. Table 3 and Figure 53). This is expected as the fluorescence data was used to select time points of interest for tomography acquisition upon prolonged energy depletion.

Inside the condensates, FAS concentrations were drastically increased and the fully assembled complexes clearly separated from the surrounding cytosol (cf. Figures 39 and 41). In the case of *S. pombe*, FAS arranged in monolayer arrays connected to adjacent membranes. In these almost crystalline architectures, FAS was concentrated more than 200-fold which likely indicates a space-efficient way to store this important enzyme complex in its functional, folded state. The seemingly unorganized condensates observed in *S. cerevisiae*, also contained fully assembled complexes with an increase in local concentrations of almost 250-fold for a single annotated tomogram. In both cases fluorescence recoveries after photobleaching (FRAP) were reduced in the condensed state which could not be disentangled from the overall cytosolic solidification due to the small foci size (cf. Figure 53). Together with the increase in local concentration, FAS assemblies represent an example of nutrient-dependent demixing and a phase transition towards a more solid state. The fact that in *S. pombe* faster recoveries were observed in FRAP experiments at later time points further highlights that the stress response is a dynamic, time-dependent process and a steady state is not reached in 1 h of energy depletion.

Structural analysis of individual FAS complexes by subtomogram averaging further revealed nutrient-dependent conformations indicating different functional states (cf. Figure 52). Normal nutrient state FAS complexes showed overall structural similarity and matched published X-ray structures of *S. cerevisiae* FAS (Leibundgut et al. 2007). The ACPs fitted a density localized close to the α-wheel which implied an active state in which this protein shuttles the growing acyl chain to the individual catalytic sites of the multi-enzyme complex in order to synthetize long chain fatty acids. Furthermore, it might also indicate a kinetically controlled step in the fatty acid synthesis in which the otherwise dynamic protein resides most of the time in this specific position and is thus captured by cryo-ET.

Upon 1 h of energy depletion, the densities fitting ACPs were detected at the top of each half dome suggesting a stalled, hibernating state of the otherwise intact complex. This is in line with previous observations where fluorescently-tagged FAS foci formed after 4 d of glucose depletion in *S. cerevisiae* and contained functional complexes (Suresh et al. 2015).

In *S. pombe*, additional densities connecting to the adjacent, in many cases vacuolar, membranes were observed and could not be assigned based on published structures. However, they likely represent proteins anchoring the complex in the membrane and thus contribute to the formation of the highly organized assemblies. As no additional linkers between individual FAS complexes were detected by subtomogram averaging, they either do not exist or are unstructured and flexible. Similar to other studies of structured condensates, future analysis of packaging densities together with molecular dynamic simulations will likely inform on the biophysical state of FAS assemblies to complement the light microscopy experiments (Dai et al. 2018, Oltrogge et al. 2020, Rosenzweig et al. 2017). Interestingly, on the micron scale of light microscopy experiments with hyperosmotic stress, which induces intracellular molecular crowding (Abuhattum et al. 2018), *S. pombe* FAS assembled into similar foci but dissolved in less than 1 h in comparison to energy depletion (cf. Figures 53 and 54). As the oligomerization of several metabolic enzymes has been connected to specific functions, in addition to their storage and protection (Park and Horton 2019, Prouteau et al. 2017, Prouteau and Loewith 2018), FAS foci might also serve another stress-induced purpose. Further metabolomic experiments of energy-depleted yeast together with cross-linking mass spectrometry to identify the unassigned densities, will likely complement and further inform on the functional states of FAS.

6.10 Deciphering the mechanisms driving liquid- to solid-like state transition and cytosolic polymerization

Cytosolic solidification upon energy depletion was suggested to be driven by an overall increase in molecular crowding and/or polymerization of macromolecules establishing interaction networks that provide mechanical stability (Abuhattum et al. 2018, Joyner et al. 2016, Munder et al. 2016). The determined ribosome concentrations in cryo-electron tomograms of yeast cells in different nutrient states suggested species-dependent changes in global molecular crowding. Using this valuable

quantitative information on crowders inside cells in combination with the observed supramolecular assemblies occupying a large fraction of the cellular volume will enable coarse grain modeling to obtain a more holistic understanding of subcellular organization. This will likely elucidate whether the excluded volume effect is sufficient to drive phase transition to a solid-like state in energy-depleted cells (Minton 2019).

The structural elucidation of individual assemblies at different time points readily visualized intermediate formation states (cf. Figure 39). In addition, light microscopy movies displaying changes in cytosolic pH upon energy and glucose depletion revealed similar cytosolic acidification in *S. cerevisiae*, but different scenarios for *S. pombe*. Here, glucose depletion did not induce a decrease in cytosolic pH, but rather a change in vacuole morphology (cf. Figure 54). Also, applying osmotic stress to ectopically induce crowding showed condensation of FAS at time scales different from energy depletion for *S. pombe* but no foci formation for *S. cerevisiae* (cf. Figure 54 C). While crowding can increase the number of encounters between individual proteins, a change in pH influences protein surface charges and thus the "stickiness" of surface patches which likely increases interactions (Levy et al. 2012). Thus, complementary light microscopy experiments using yeast strains with fluorescently-tagged proteins identified in the oligomeric assemblies and applying active cytosolic acidification will disentangle the influence of these factors on the large-scale self-assembly. By combining the findings on changes in pH and crowding affecting condensation similar to ED, molecular dynamics simulations can be employed to investigate how in addition to global excluded volume effects changes in conformation and surface charges influence condensate or molecular assembly and growth pathways.

7 Conclusions

In this thesis, I explored the potential to harness in-cell cryo-ET to quantitatively and structurally investigate intracellular crowding and revealed the nutrient-dependent organization of the wild-type yeast cytosol. This required method developments and resulted in the following conclusions:

- The co-developed modular platform SerialFIB enables and facilitates high-throughput cryo-FIB preparations. This software was benchmarked with six different cell types for on-grid high-quality lamella generation. Furthermore, SerialFIB encompasses modules for cryo-CLEM-guided lamella preparation, cryo-FIB SEM volume imaging and trench milling for lift-out procedures and bears the potential to implement other, more advanced approaches in the future.

- Data mining workflows utilizing Deep-Learning algorithms were co-developed to overcome limitations of traditional template matching methods. The established software DeePiCt synergizes particle localization and compartment segmentations in cryo-electron tomograms. It is applicable to data acquired with different acquisition parameters. This revealed particle populations in the cellular context of the *S. pombe* cytosol. In detail, ribosomes bound to mitochondria were structurally analyzed and showed a particular orientation facing the membrane, which was different from ER-associated ribosomes.

- Automated cryo-ET acquisition on lamellae micromachined from yeast cells under varying nutritional conditions resulted in >500 cryo-electron tomograms reavealing the underlying structural architectures. These data provide a great opportunity to quantitatively characterize structural reorganization inside cells in response to environmental strains.

- Upon energy depletion morphological changes of organelles and the formation of large-scale supramolecular assemblies were observed in the cytosol and nucleus of *S. cerevisiae* and *S. pombe*. These results confirm previously debated observations by genome-wide light microscopy screens with tagged proteins (Narayanaswamy et al. 2009, Noree et al. 2019a), and open the possibility to derive a mechanistic understanding of large-scale molecular assemblies in response to stress.

- Significant global changes in molecular crowding were detected upon energy-depletion in the *S. cerevisiae* cytosol, but not in *S. pombe*, approximated by ribosome concentrations. These results suggest divergent mechanisms of stress response and adaptation.

- Nutrient stress led to structural variations of the ribosome, that while fully assembled into an 80S complex and engaged in polysomes, exhibited a vacant PTC. This hints at a stationary, non-active state which potentially represents a protective mechanism of yeast cells to survive in energy-scarce environments.

- Energy-depletion induced condensation of FAS. These assemblies revealed high local concentrations of fully assembled complexes, species-dependent dynamics and organization into higher-order structures. In both characterized yeast species, nutrient stress led to a particular structural reconfiguration of the individual FAS complexes with ACPs located at the top of each half dome indicating a potential hibernating state.

- Light microscopy experiments confirmed previously described acidification of the cytosol upon energy depletion (Joyner et al. 2016, Munder et al. 2016). A similar reduction in cytosolic pH was observed upon glucose depletion in *S. cerevisiae*, but not in *S. pombe* where a change in vacuole morphology was detected. To investigate the influence of molecular crowding on FAS condensation, hyperosmotic stress was ectopically applied and revealed assemblies in *S. pombe* at time scales different from ED, but no foci formation in *S. cerevisiae*. These results hint at different strategies of the two yeast species to adapt to environmental perturbations.

In the future, the here presented data across scales will be essential to model global cytosolic solidification and local molecular condensation of the observed oligomers in order to gain a more holistic understanding of the molecular details governing phase transitions inside cells.

8 Contributions

SerialFIB, the modular platform for cryo-FIB workflows, was jointly developed and data produced with Sven Klumpe and Herman Fung. *E. huxleyi* samples were kindly provided by Zohar Eyal and Assaf Gal. Sum159 and HeLa cell samples were kindly prepared by Ievgeniia Zagoriy and Wioleta Dudka.

DeePiCt, the deep-learning based software for particle localization and cellular compartment segmentation was jointly developed and data produced with Irene de Teresa and Alexander Mattausch.

Matteo Allegretti and Christian Zimmerli provided defocus-only tomography data for *S. cerevisiae* NN. Christian Zimmerli also annotated NPC data utilized to train DeePiCt networks (data not shown).

Tobias Walter inspected TM results for *S. pombe* and *S. cerevisiae* 1 h ED tomograms.

Ievgeniia Zagoriy cloned the *S. pombe* FAS-mCherry construct and supported confocal microscopy experiments. Confocal microscopy and FRAP experiments were jointly performed and analyzed with Willram Scholz.

9 Acknowledgements

I would like to acknowledge and thank everyone who has accompanied, supported and motivated me throughout this journey.

First of all, I would like to express my deep appreciation and gratitude to Julia Mahamid for giving me the opportunity to perform my PhD in her research group at EMBL, Heidelberg. Receiving all the valuable advice and support, I am sincerely grateful for having her as supervisor and mentor. Her knowledge and passion for science are truly inspirational.

I also want to acknowledge and thank my defence committee members Prof. Dr. Michael Knop, Dr. Judith Zaugg, Prof. Dr. Irmgard Sinning and Dr. Stefan Pfeffer, as well as my thesis advisory member Sara Cuylen-Häring, for their guidance, precious advice and support.

In addition, I am thankful for the support from EMBL, especially Wim Hagen and Felix Weiss for ensuring that all microscopes are running smoothly, as well as Thomas Hoffmann for taking care of the IT and Aliaksandr Halavatyi for his support with FRAP measurements.

Furthermore, I would like to express my gratitude to Sven Klumpe, Herman Fung and Jürgen Plitzko for the great collaboration that made SerialFIB possible. Thank you to the Dream Team for making all the hard work so much fun, especially the countless virtual coffee breaks and late-night sessions.

I would also like to acknowledge and thank Irene De Teresa, Alexander Mattausch, Frosina Stojanovska and Judith Zaugg for their collaboration and contributions that enabled DeePiCt.

Moreover, I thank the group of Simon Alberti at the TU Dresden, especially Titus Franzmann and Anne Esslinger for their collaboration, showing me how to energy deplete yeast and for the exciting scientific discussions.

In addition, I would like to thank the group of Martin Beck, in particular Christian Zimmerli, Matteo Allegretti and Beata Turonova for the scientific discussions, sharing experience and giving valuable advice.

I am very grateful for all members of the Mahamid group who create such a pleasant working environment. Especially, Ievgeniia Zagoriy for teaching me how to culture yeast and being so supportive about any kind of wet lab experiments. Special thanks to Herman for being such an awesome person, to Edo for the scientific discussions, virtual cooking sessions and fun runs, and to Mauricio for his exciting stories and non-scientific advice. I also want to thank Marie for joining the yeast team and kindly reading this thesis, as well as Xiaojie and Wioleta for being such admirable women. I would like to thank my students Alex, Willram and Tobi for their contributions to this project.

The past four years would have been a lot less fun without the great friends I made at and through EMBL. I want to especially thank Carolita, Erica, Kristina, Ivan, Bianca, Gabi, Michael, Emmanuelle, Mathias, Julian, Jakob, Max, Raj, Virginia and Vero for the joyful times we spent together. Thank you Natalie and Chris for all the wine, deep conversations and for being my lockdown weekend highlights; Mariana, for sharing rooms, laughing fits and showing me that it is always worth fighting for your goals.

Thank you also to all my friends who keep me grounded. A special shout out from Heidi to the Heidelberg Lacrosse team. You will always be my happy place. I am especially grateful for the precious conversations, runs or longboard tours with Isa, Thruni, Cori and Caro.

Finally, I want to thank my mum, Cori, Antje and Alpi for their unconditional love and support.

10 Appendix

10.1 Supplementary Tables

Supplementary Tables 1-3 are part of the methods section (cf. chapter 4).

Table S4: Ribosome ground truth construction in 20 *S. pombe* tomograms. Data produced jointly with Irene De Teresa.

VPP	Tomo	Step 1 # TM	Step 1 # true positive TM	Step 2 DeePiCt # TM unde-tected Ribo	Step 2 DeePiCt # true positive TM un-detected Ribo	Step 3 # manual	Total	Clean
TRUE	1.4	2000	1662	1980	1912	394	3968	2450
TRUE	1.5	2000	1371	2170	1855	415	3641	2342
TRUE	1.6	2000	1377	1450	1342	563	3282	3373
TRUE	1.21	2000	1260	2242	1699	481	3440	2429
TRUE	1.24	2000	1262	3061	2092	681	4035	2967
FALSE	1.26	2000	533	359	122	621	1276	838
FALSE	1.27	2000	881	969	699	1037	2617	1673
FALSE	1.28	2000	718	1125	307	5280	6305	5305
FALSE	1.29	2000	713	1346	905	2177	3795	2897
FALSE	1.30	2000	682	1132	541	2247	3470	2783
FALSE	1.34	3000	770	932	380	3015	4165	3783
FALSE	1.37	3000	590	710	242	1414	2246	1646
FALSE	1.41	3000	537	1657	694	1908	3139	2813
FALSE	1.43	3000	1263	872	513	1742	3518	1815
FALSE	1.45	3000	358	762	235	2239	2832	2348
TRUE	2.3	3000	1391	3296	2648	517	4556	3571
TRUE	2.4	3000	981	1302	1039	238	2258	1336
TRUE	2.5	3000	495	775	558	131	1184	617
TRUE	2.18	3000	1066	2268	1747	668	3481	2744
TRUE	3.27	3000	1243	2280	2115	421	3779	3482

Table S5: FAS ground truth construction in 20 *S. pombe* tomograms. Data produced jointly with Irene De Teresa.

VPP	Tomo	Step 1 # manual	Step 2 DeePiCt # undetected FAS	Step 2 DeePiCt # true positive undetected FAS	Step 3 # manual	Total	Clean
TRUE	1.4	86	96	14	2	102	102
TRUE	1.5	50	37	15	16	81	81
TRUE	1.6	-	166	34	32	66	66
TRUE	1.21	45	32	8	6	59	59
TRUE	1.24	84	61	18	10	112	112
FALSE	1.26	9	2	2	5	16	16
FALSE	1.27	27	47	22	7	56	56
FALSE	1.28	29	191	41	6	76	76
FALSE	1.29	27	42	12	3	42	42
FALSE	1.30	38	53	17	9	64	64
FALSE	1.34	19	90	11	7	37	37
FALSE	1.37	7	66	10	5	22	22
FALSE	1.41	8	224	9	1	18	18
FALSE	1.43	9	44	3	5	17	17
FALSE	1.45	5	188	8	5	18	18
TRUE	2.3	22	44	20	11	53	47
TRUE	2.4	17	7	1	52	70	70
TRUE	2.5	6	11	2	19	27	27
TRUE	2.18	34	69	14	16	64	60
TRUE	3.27	-	54	34	30	64	64

Table S6: *S. pombe* 1 h ED Ribosome and FAS particle picking results. Tomograms were collected with defocus only. For manual picking, up to three rounds were performed using EMAN2 (Tang et al. 2007). # total corresponds to the ribosome particles used for subtomogram averaging. FAS particles were only detected manually and sorted depending on their location in ED assemblies (# ED) or the cytosol (# cyt). Highlighted rows (cyan) correspond to ground truth (gt) data.

Tomo	**Ribosome**						**FAS**		
	# TM cleaned	**# manual**	**# DeePiCt total**	**# DeePiCt undetected**	**auPRC**	**# total**	**# manual**	**# ED**	**# cyt**
1	1,020	-	2,001	1,309	-	2,329	-	-	-
2	1,010	-	1,407	782	-	1,792	-	-	-
3	-	-	-	-	-	-	233	233	0
4	907	2,133	2,230	522	0.81	3,040	22	0	22
5	1,147	1,514	2,475	1,068	0.74	2,661	647	584	63
6	894	-	3,006	2,398	-	3,292	-	-	-
7	557	-	1,596	1,252	-	1,809	-	-	-
9	-	-	-	-	-	-	348	348	0
10	669	-	1,655	1,168	-	1,200	-	-	-
11	494	1,398	1,699	726	0.48	1,892	32	0	32
12	-	-	-	-	-	-	132	132	-
13	934	-	2,372	1,860	-	2,794	-	-	-
14	615	-	995	665	-	1,280	-	-	-
15	790	2,530	2,319	709	0.68	3,320	82	28	54
16	-	-	-	-	-	-	274	274	0
17	652	-	1,593	1,146	-	1,798	-	-	-
18	708	-	1,624	1,113	-	1,789	-	-	-
19	752	-	3,174	2,689	-	3,441	-	-	-
20	910	-	2,093	1,488	-	2,398	-	-	-
21	763	-	1,448	936	-	1,699	-	-	-
22	-	-	-	-	-	-	194	194	-
23	970	1,539	2,180	650	0.73	2,509	93	93	37
26	761	-	2,395	1,832	-	2,593	-	-	-
28	-	-	-	-	-	-	162	162	-
29	819	-	1,766	1,217	-	2,036	-	-	-
30	665	-	2,255	1,783	-	2,448	-	-	-
31	-	-	-	-	-	-	46	46	-
32	-	-	-	-	-	-	225	225	-
33	-	-	-	-	-	-	203	203	-
35	-	-	-	-	-	-	390	390	-
37	-	-	-	-	-	-	261	261	-
43	-	-	-	-	-	-	428	428	-
45	-	-	-	-	-	-	392	392	-
Average	802	1,823	2,014	1,266	0.69	2,306	231	222	26
STD	170	488	541	591	0.12	660	164	162	25
Total	16,037	9,114	40,283	25,313	-	46,120	4,164	3,993	208

Table S7: *S. pombe* 1 h ED cytosolic volumes and particle concentrations. Volumes determined from manual ground truth (gt) segmentations, DeePiCt predictions (pred). ED-induced FAS assemblies and filaments were also manually segmented. Highlighted rows are ground truth (gt) data.

Tomo	Cellular volumes					Particle concentrations			
	cytosol gt [µm³]	cytosol pred [µm³]	FAS ED [µm³]	Fil ED [µm³]	Fraction Fil ED [%]	gt ribo [part/ µm³]	pred ribo [part/ µm³]	FAS cyt [part/ µm³]	FAS ED [part/ µm³]
1	-	0.153	-	-	-	-	13,065	-	-
2	-	0.130	-	-	-	-	10,835	-	-
3	-	0.031	-	-	-	-	-	-	-
4	0.184	0.179	-	0.005	0.029	16,965	12,444	120	-
5	0.165	0.198	0.012	0.013	0.073	13,419	12,481	382	48,100
6	-	0.213	-	-	-	-	14,101	-	-
7	-	0.122	-	-	-	-	13,105	-	-
9	-	0.096	-	-	-	-	-	-	-
10	-	0.126	-	-	-	-	13,159	-	-
11	0.103	0.135	-	-	-	14,021	12,591	311	-
12	-	0.129	-	-	-	-	-	-	-
13	-	0.171	-	-	-	-	13,902	-	-
14	-	0.120	-	-	-	-	8,310	-	-
15	0.240	0.158	0.001	0.014	0.057	21,002	14,670	225	34,504
16	-	0.008	-	-	-	-	-	-	-
17	-	0.106	-	-	-	-	14,985	-	-
18	-	0.105	-	-	-	-	15,517	-	-
19	-	0.235	-	-	-	-	13,529	-	-
20	-	0.158	-	-	-	-	13,244	-	-
21	-	0.128	-	-	-	-	11,318	-	-
22	-	0.153	-	-	-	-	-	-	-
23	0.162	0.157	0.001	0.007	0.041	16,020	13,919	229	47,665
26	-	0.184	-	-	-	-	12,983	-	-
28	-	0.177	-	-	-	-	-	-	-
29	-	0.137	-	-	-	-	12,937	-	-
30	-	0.163	-	-	-	-	13,833	-	-
Average	0.17	0.14	0.00	0.01	0.05	16,285	13,046	253	43,423
STD	0.05	0.05	0.01	0.00	0.02	3,005	1,577	99	7,727

Table S8: *S. pombe* long ED cytosolic volumes and ribosome concentrations. Volumes and particles determined from DeePiCt predictions (pred).

Tomo	*S. pombe* 3.5 h ED			Tomo	*S. pombe* 17 h ED		
	Ribosome # DeePiCt total	Cellular volumes cytosol pred [µm³]	particle concentrations pred ribo [part/µm³]		Ribosome # DeePiCt total	Cellular volumes cytosol pred [µm³]	particle concentrations pred ribo [part/µm³]
1	3,725	0.30	12,607	1	929	0.09	10,492
2	4,256	0.40	10,653	20	1,434	0.17	8,568
5	2,757	0.31	8,814	21	2,098	0.17	11,990
6	3,908	0.31	12,702	22	2,846	0.20	14,509
9	4,966	0.40	12,554	23	1,701	0.14	11,801
11	2,783	0.22	12,626	25	1,431	0.13	10,852
12	2,584	0.22	11,526	26	3,086	0.24	13,031
14	4,142	0.35	11,728	47	2,222	0.21	10,410
15	4,506	0.34	13,094	48	1,053	0.11	9,199
16	4,004	0.30	13,221	61	2,314	0.20	11,356
17	3,603	0.34	10,494	73	1991	0.16	12,361
18	3,863	0.34	11,454	76	3,249	0.25	13,221
-	-	-	-	86	1,431	0.15	9,460
-	-	-	-	87	2,892	0.20	14,590
Average	3,758	0.32	11,789	**Average**	2,048	0.17	11,560
STD	730	0.06	1,299	**STD**	758	0.05	1,873
Total	45,097	-	-	**Total**	28,677	-	-

Table S9: *S. cerevisiae* NN Ribosome and FAS particle picking results. Tomograms were collected with defocus only by Matteo Allegretti (Allegretti et al. 2020). For manual picking, up to three rounds were performed using EMAN2 (Tang et al. 2007). # total corresponds to the ribosome particles used for subtomogram averaging. FAS particles were detected manually. Highlighted rows are ground truth (gt) data.

Tomo	Ribosome						FAS
	# TM cleaned	# manual	# DeePiCt total	# DeePiCt undetected	auPRC	# total	# manual
24	-	-	1,855	-	-	1,855	-
32	-	-	1,472	-	-	1,472	-
37	893	1,820	1,480	248	0.89	2,713	85
50	-	-	1,188	-	-	1,188	-
54	982	1,434	1,160	235	0.80	2,416	97
154	-	-	1,689	-	-	1,689	-
215	-	-	3,338	-	-	3,338	-
289	994	2,063	2,259	506	0.79	3,057	128
295	-	-	3,569	-	-	3,569	-
Average	956	1,772	2,001	330	0.83	2,366	103
STD	55	317	891	153	0.05	859	22
Total	2,869	5,317	18,010	989	-	22,986	310

Table S10: *S. cerevisiae* NN cytosolic volumes and particle concentrations. Volumes determined from manual ground truth segmentations (gt, highlighted rows) and DeePiCt predictions (pred).

Tomo	Cellular volumes		particle concentrations		
	cytosol gt [µm^3]	cytosol pred [µm^3]	gt ribo [part/ µm^3]	pred ribo [part/ µm^3]	FAS [part/ µm^3]
24	-	0.24	-	7,869	-
32	-	0.20	-	7,458	-
37	0.14	0.25	19,895	5,846	623
50	-	0.15	-	7,941	-
54	0.15	0.26	16,513	4,448	663
154	-	0.17	-	9,955	-
215	-	0.22	-	14,863	-
289	0.16	0.23	18,747	9,848	785
295	-	0.26	-	13,488	-
Average	0.15	0.22	18,385	9,080	690
STD	0.01	0.04	1,720	3,383	84

Table S11: *S. cerevisiae* 1 h ED Ribosome and FAS particle picking results. Tomograms (Tomo) were collected with defocus only. For manual picking, up to three rounds were performed using EMAN2 (Tang et al., 2007). # total corresponds to the ribosome particles used for subtomogram averaging. FAS particles were only detected manually and sorted depending on their location in ED assemblies (# ED) or the cytosol (# cyt). Highlighted rows correspond to ground truth (gt) data.

Tomo	Ribosome						FAS		
	# TM cleaned	# manual	# DeePiCt total	# DeePiCt undetected	auPRC	# total	# manual	# ED	# cyt
1	632	-	2,826	2,334	-	2,966	-	-	-
4	876	-	3,312	2,623	-	3,499	-	-	-
5	876	-	3,051	2,426	-	3,302	-	-	-
7	774	-	3,028	2,445	-	3,219	-	-	-
10	534	-	2,943	2,504	-	3,038	-	-	-
12	943	-	4,805	4,146	-	5,089	-	-	-
13	665	-	1,635	1,178	-	1,843	-	-	-
15	760	-	3,420	2,892	-	3,652	-	-	-
17	858	2,229	2,505	587	0.74	3,674	264	0	264
21	788	-	2,742	2,203	-	2,991	-	-	-
22	1,051	-	2,942	2,106	-	3,157	-	-	-
23	750	-	2,981	2,432	-	3,182	-	-	-
25	738	1,693	2,291	659	0.61	3,090	125	0	125
28	777	4,316	4,226	921	0.78	6,014	443	346	97
32	826	-	2,469	1,850	-	2,676	-	-	-
36	573	-	2,737	2,433	-	3,006	-	-	-
Average	776	2,746	2,995	2,109	0.71	3,400	277	115	162
STD	134	1,386	735	910	0.09	955	159	200	89
Total	12,421	8,238	47,913	33,739	-	54,398	832	346	486

Table S12: *S. cerevisiae* 1 h ED cytoplasmic volumes and particle concentrations. Volumes determined from manual ground truth segmentations (gt, highlighted rows) and DeePiCt predictions (pred). ED-induced FAS assemblies and filaments (Fil ED) were also manually segmented.

Tomo	Cellular volumes					Particle concentrations			
	cytosol gt [µm³]	cytosol pred [µm³]	FAS ED [µm³]	Fil ED [µm³]	Fraction Fil ED [%]	gt ribo [part/ µm³]	pred ribo [part/ µm³]	FAS cyt [part/ µm³]	FAS ED [part/ µm³]
1	-	0.197	-	-	-	-	14,379	-	-
4	-	0.208	-	-	-	-	15,928	-	-
5	-	0.199	-	-	-	-	15,333	-	-
7	-	0.187	-	-	-	-	16,201	-	-
10	-	0.207	-	-	-	-	14,249	-	-
12	-	0.257	-	-	-	-	18,692	-	-
13	-	0.109	-	-	-	-	14,986	-	-
15	-	0.212	-	-	-	-	16,112	-	-
17	0.140	0.149	-	0.004	0.028	22,214	16,823	1,900	-
21	-	0.180	-	-	-	-	15,267	-	-
22	-	0.168	-	-	-	-	17,554	-	-
23	-	0.171	-	-	-	-	17,382	-	-
25	0.120	0.141	-	0.009	0.070	19,988	16,267	1,028	-
28	0.230	0.216	0.002	-	-	22,166	19,523	-	170,332
32	-	0.150	-	-	-	-	16,428	-	-
36	-	0.195	-	-	-	-	14,025	-	-
Average	0.163	0.184	-	0.007	0.049	21,456	16,197	1,464	-
STD	0.059	0.036	-	0.004	0.030	1,272	1,548	617	-

Table S13: *S. cerevisiae* 6 h ED cytosolic volumes and ribosome concentrations.Volumes and particles determined from DeePiCt predictions (pred).

Tomo	**Ribosome # DeePiCt total**	**Cellular volumes cytosol pred [µm³]**	**particle concentrations pred ribo [part/µm³]**
1	3,745	0.30	12,621
2	3,476	0.39	8,805
3	4,496	0.34	13,173
6	2,752	0.30	9,291
9	3,532	0.33	10,547
11	4,160	0.31	13,286
15	5,651	0.43	13,045
19	2,797	0.30	9,274
21	6,448	0.46	14,032
22	6,684	0.45	14,720
23	6,391	0.48	13,343
28	4,711	0.47	10,078
29	2,537	0.45	5,598
34	3,648	0.46	7,922
35	5,504	0.38	14,421
36	2,604	0.41	6,309
37	4,231	0.38	11,108
39	6,123	0.48	12,665
41	4,907	0.38	12,905
45	3,506	0.44	7,998
46	4,038	0.35	11,428
47	2,243	0.31	7,353
49	3,523	0.34	10,316
52	3,982	0.37	10,765
54	4,085	0.32	12,855
55	4,789	0.27	17,520
56	5,743	0.40	14,457
57	3,789	0.26	14,489
58	4,330	0.41	10,603
59	2,667	0.37	7,237
62	4,965	0.44	11,373
64	3,187	0.36	8,883
67	3,463	0.33	10,555
Average	4,203	0.38	11,181
STD	1,219	0.06	2,778
Total	138,707	-	-

10.2 List of Abbreviations

ACP ..... acyl carrier protein

API ..... application programming interface

auPRC ..... area under the precision recall curve

CC ..... cross correlation

cryo-CLEM .... cryo-correlative light and electron microscopy

CNN ..... convolutional neural network

Cryo-EM ..... cryo-electron microscopy

Cryo-ET ..... cryo-electron tomography

CTF ..... contrast transfer function

DEF ..... defocus-only

DH ..... dehydratase

ED ..... energy depletion

EMM ..... Edinburgh minimal media

ENR ..... enoyl reductase

ER ..... endoplasmic reticulum

FAS ..... fatty acid synthase

FIB ..... focused ion beam

FLM ..... fluorescence light microscopy

FRAP ..... fluorescence recovery after photobleaching

FSC ..... Fourier shell correlation

gt ..... ground truth

GUI ..... graphical user interface

IDR ..... intrinsically disordered region

KR ..... ketoacyl reductase

KS ..... ketosynthase

LD ..... lipid droplet

LLPS ..... liquid-liquid phase separation

LSU ..... 60S large ribosomal subunit

MIP ..... maximum intensity projection

MOM ..... mitochondrion outer membrane

MPT ..... malonyl/palmitoyl transferase

NN ..... normal nutrient

NPC ..... nuclear pore complex

P ..... positively classified data

PCM ..... pericentriolar matrix

PPT ..... phosphopantetheine transferase

PRC ..... precision recall curve

PTC ..... peptidyl transferase center

PTM ..... post-translational modification

RT ..... room temperature

SIRT ..... simultaneous iterations reconstruction technique

SSU ..... 40S small ribosomal subunit

OD_{600} ..... absorbance (optical density) measured at 600 nm

2-DG 2-Deoxyglucose

Rpm ..... rounds per minute

SEM ..... scanning electron microscope

STD ..... standard deviation

TAG ..... triacyl glyceride

TEM ..... transmission electron microscopy

TM ..... template matching

TN ..... true negative

TP ..... true positive

VPP ..... Volta potential phase plate

WBP ..... weighted back projection

YES ..... yeast extract with supplements

YP(A)D ..... yeast extract-peptone (adenine) dextrose

11 References

Abuhattum S, Kim K, Franzmann TM, Esslinger A, Midtvedt D, et al.. 2018. Intracellular Mass Density Increase Is Accompanying but Not Sufficient for Stiffening and Growth Arrest of Yeast Cells. Front Phys 6

Adachi A, Koizumi M, Ohsumi Y. 2017. Autophagy induction under carbon starvation conditions is negatively regulated by carbon catabolite repression. J Biol Chem 292: 19905-18

Addadi L, Raz S, Weiner S. 2003. Taking advantage of disorder: Amorphous calcium carbonate and its roles in biomineralization. Adv Mater 15: 959-70

Ader NR, Hoffmann PC, Ganeva I, Borgeaud AC, Wang C, et al.. 2019. Molecular and topological reorganizations in mitochondrial architecture interplay during Bax-mediated steps of apoptosis. Elife 8

Afonina ZA, Myasnikov AG, Shirokov VA, Klaholz BP, Spirin AS. 2014. Formation of circular polyribosomes on eukaryotic mRNA without cap-structure and poly(A)-tail: a cryo electron tomography study. Nucleic Acids Res 42: 9461-69

Afonina ZA, Myasnikov AG, Shirokov VA, Klaholz BP, Spirin AS. 2015. Conformation transitions of eukaryotic polyribosomes during multi-round translation. Nucleic Acids Res 43: 618-28

Al-Amoudi A, Studer D, Dubochet J. 2005. Cutting artefacts and cutting process in vitreous sections for cryo-electron microscopy. J Struct Biol 150: 109-21

Albert S, Wietrzynski W, Lee CW, Schaffer M, Beck F, et al.. 2020. Direct visualization of degradation microcompartments at the ER membrane. P Natl Acad Sci USA 117: 1069-80

Alberti S. 2017. The wisdom of crowds: regulating cell function through condensed states of living matter. J Cell Sci 130: 2789-96

Alberti S, Dormann D. 2019. Liquid-Liquid Phase Separation in Disease. Annu Rev Genet 53: 171-94

Alberti S, Gladfelter A, Mittag T. 2019. Considerations and Challenges in Studying Liquid-Liquid Phase Separation and Biomolecular Condensates. Cell 176: 419-34

Allaire J. 2012. RStudio: integrated development environment for R. Boston, MA 770: 165-71

Allegretti M, Zimmerli CE, Rantos V, Wilfling F, Ronchi P, et al.. 2020. In-cell architecture of the nuclear pore and snapshots of its turnover. Nature 586: 796-800

Andersen CB, Becker T, Blau M, Anand M, Halic M, et al.. 2006. Structure of eEF3 and the mechanism of transfer RNA release from the E-site. Nature 443: 663-8

Armache JP, Jarasch A, Anger AM, Villa E, Becker T, et al.. 2010. Cryo-EM structure and rRNA model of a translating eukaryotic 80S ribosome at 5.5-Å resolution. Proc Natl Acad Sci U S A 107: 19748-53

Arnold J, Mahamid J, Lucic V, de Marco A, Fernandez JJ, et al.. 2016. Site-Specific Cryo-focused Ion Beam Sample Preparation Guided by 3D Correlative Microscopy. Biophys J 110: 860-9

Arribere JA, Doudna JA, Gilbert WV. 2011. Reconsidering movement of eukaryotic mRNAs between polysomes and P bodies. Mol Cell 44: 745-58

Ashe MP, De Long SK, Sachs AB. 2000. Glucose depletion rapidly inhibits translation initiation in yeast. Mol Biol Cell 11: 833-48

Avendano-Monsalve MC, Ponce-Rojas JC, Funes S. 2020. From cytosol to mitochondria: the beginning of a protein journey. Biol Chem 401: 645-61

Bagamery LE, Justman QA, Garner EC, Murray AW. 2020. A Putative Bet-Hedging Strategy Buffers Budding Yeast against Environmental Instability. Curr Biol 30: 4563-78 e4

Banani SF, Lee HO, Hyman AA, Rosen MK. 2017. Biomolecular condensates: organizers of cellular biochemistry. Nat Rev Mol Cell Biol 18: 285-98

Banani SF, Rice AM, Peeples WB, Lin Y, Jain S, et al.. 2016. Compositional Control of Phase-Separated Cellular Bodies. Cell 166: 651-63

Banerjee S, Coussens NP, Gallat FX, Sathyanarayanan N, Srikanth J, et al.. 2016. Structure of a heterogeneous, glycosylated, lipid-bound, in vivo-grown protein crystal at atomic resolution from the viviparous cockroach Diploptera punctata. Iucrj 3: 282-93

Bauerlein FJB, Baumeister W. 2021. Towards Visual Proteomics at High Resolution. J Mol Biol 433: 167187

Bauerlein FJB, Saha I, Mishra A, Kalemanov M, Martinez-Sanchez A, et al.. 2017. In Situ Architecture and Cellular Interactions of PolyQ Inclusions. Cell 171: 179-87

Beck M, Baumeister W. 2016. Cryo-Electron Tomography: Can it Reveal the Molecular Sociology of Cells in Atomic Detail? Trends in Cell Biology 26: 825-37

Becker T, Bhushan S, Jarasch A, Armache JP, Funes S, et al.. 2009. Structure of monomeric yeast and mammalian Sec61 complexes interacting with the translating ribosome. Science 326: 1369-73

Bepler T, Kelley K, Noble AJ, Berger B. 2020. Topaz-Denoise: general deep denoising models for cryoEM and cryoET. Nat Commun 11: 5208

Berg S, Kutra D, Kroeger T, Straehle CN, Kausler BX, et al.. 2019. ilastik: interactive machine learning for (bio) image analysis. Nature Methods 16: 1226-32

Bharat TA, Scheres SH. 2016. Resolving macromolecular structures from electron cryo-tomography data using subtomogram averaging in RELION. Nat Protoc 11: 2054-65

Bieber A, Capitanio C, Schiøtz O, Smeets M, Fenzke J, et al.. 2021. Precise 3D-correlative FIB-milling of biological samples using METEOR, an integrated cryo-CLEM imaging system. Microscopy and Microanalysis 27: 3230-32

Boczek EE, Fursch J, Niedermeier ML, Jawerth L, Jahnel M, et al. 2021. HspB8 prevents aberrant phase transitions of FUS by chaperoning its folded RNA-binding domain. Elife 10

Boersma AJ, Zuhorn IS, Poolman B. 2015. A sensor for quantification of macromolecular crowding in living cells. Nat Methods 12: 227-29

Bogovic JA, Hanslovsky P, Wong A, Saalfeld S. 2016. Robust registration of calcium images by learned contrast synthesis. ISBI: 1123-26

Bohm J, Frangakis AS, Hegerl R, Nickell S, Typke D, Baumeister W. 2000. Toward detecting and identifying macromolecules in a cellular context: template matching applied to electron tomograms. Proc Natl Acad Sci U S A 97: 14245-50

Bolte S, Cordelières FP. 2006. A guided tour into subcellular colocalization analysis in light microscopy. Journal of Microscopy 224: 213-32

Bone N, Millar JB, Toda T, Armstrong J. 1998. Regulated vacuole fusion and fission in Schizosaccharomyces pombe: an osmotic response dependent on MAP kinases. Curr Biol 8: 135-44

Brangwynne CP, Tompa P, Pappu RV. 2015. Polymer physics of intracellular phase transitions. Nat Phys 11: 899-904

Brengues M, Teixeira D, Parker R. 2005. Movement of eukaryotic mRNAs between polysomes and cytosolic processing bodies. Science 310: 486-9

Briggs JA. 2013. Structural biology in situ–the potential of subtomogram averaging. Curr Opin Struct Biol 23: 261-7

Brilot AF, Chen JZ, Cheng AC, Pan JH, Harrison SC, et al.. 2012. Beam-induced

motion of vitrified specimen on holey carbon film. Journal of Structural Biology 177: 630-37

Brown A, Baird MR, Yip MC, Murray J, Shao S. 2018. Structures of translationally inactive mammalian ribosomes. Elife 7

Brown A, Shao S, Murray J, Hegde RS, Ramakrishnan V. 2015. Structural basis for stop codon recognition in eukaryotes. Nature 524: 493-96

Buchholz TO, Krull A, Shahidi R, Pigino G, Jekely G, Jug F. 2019. Content-aware image restoration for electron microscopy. Methods Cell Biol 152: 277-89

Buckley G, Gervinskas G, Taveneau C, Venugopal H, Whisstock JC, de Marco A. 2020. Automated cryo-lamella preparation for high-throughput in-situ structural biology. J Struct Biol 210: 107488

Buijsse B, Trompenaars P, Altin V, Danev R, Glaeser RM. 2020. Spectral DQE of the Volta phase plate. Ultramicroscopy 218: 113079

Burnett TL, Kelley R, Winiarski B, Contreras L, Daly M, et al.. 2016. Large volume serial section tomography by Xe Plasma FIB dual beam microscopy. Ultramicroscopy 161: 119-29

Buschauer R, Matsuo Y, Sugiyama T, Chen YH, Alhusaini N, et al.. 2020. The Ccr4-Not complex monitors the translating ribosome for codon optimality. Science 368

Buttgereit F, Brand MD. 1995. A Hierarchy of Atp-Consuming Processes in Mammalian-Cells. Biochem J 312: 163-67

Callebaut W. 2005. The ubiquity of modularity. Modularity: Understanding the development and evolution of natural complex systems. MIT press: 3-28

Campbell K, Westholm J, Kasvandik S, Di Bartolomeoa F, Mormino M, Nielsen J. 2020. Building blocks are synthesized on demand during the yeast cell cycle. P

Natl Acad Sci USA 117: 7575-83

Carpy A, Krug K, Graf S, Koch A, Popic S, et al.. 2014. Absolute proteome and phosphoproteome dynamics during the cell cycle of Schizosaccharomyces pombe (Fission Yeast). Mol Cell Proteomics 13: 1925-36

Castano-Diez D. 2017. The Dynamo package for tomography and subtomogram averaging: components for MATLAB, GPU computing and EC2 Amazon Web Services. Acta Crystallogr D Struct Biol 73: 478-87

Castelli LM, Lui J, Campbell SG, Rowe W, Zeef LAH, et al.. 2011. Glucose depletion inhibits translation initiation via eIF4A loss and subsequent 48S preinitiation complex accumulation, while the pentose phosphate pathway is coordinately upregulated. Molecular Biology of the Cell 22: 3379-93

Chen M, Dai W, Sun SY, Jonasch D, He CY, et al.. 2017. Convolutional neural networks for automated annotation of cellular cryo-electron tomograms. Nat Methods 14: 983-85

Dahlberg PD, Saurabh S, Sartor AM, Wang J, Mitchell PG, et al.. 2020. Cryogenic single-molecule fluorescence annotations for electron tomography reveal in situ organization of key proteins in Caulobacter. Proc Natl Acad Sci U S A 117: 13937-44

Dai W, Chen MY, Myers C, Ludtke SJ, Pettitt BM, et al.. 2018. Visualizing Individual RuBisCO and Its Assembly into Carboxysomes in Marine Cyanobacteria by Cryo-Electron Tomography. Journal of Molecular Biology 430: 4156-67

Dandey VP, Budell WC, Wei H, Bobe D, Maruthi K, et al.. 2020. Time-resolved cryo-EM using Spotiton. Nature Methods 17: 897

Danev R, Buijsse B, Khoshouei M, Plitzko JM, Baumeister W. 2014. Volta potential phase plate for in-focus phase contrast transmission electron microscopy. Proc Natl Acad Sci U S A 111: 15635-40

Danev R, Tegunov D, Baumeister W. 2017. Using the Volta phase plate with defo-

cus for cryo-EM single particle analysis. Elife 6

De Virgilio C. 2012. The essence of yeast quiescence. Fems Microbiol Rev 36: 306-39

De Virgilio C, Simmen U, Hottiger T, Boiler T, Wiemken A. 1990. Heat shock induces enzymes of trehalose metabolism, trehalose accumulation, and thermotolerance in Schizosaccharomyces pombe, even in the presence of cycloheximide. FEBS letters 273: 107-10

De Yoreo JJ, Gilbert PU, Sommerdijk NA, Penn RL, Whitelam S, et al.. 2015. CRYSTAL GROWTH. Crystallization by particle attachment in synthetic, biogenic, and geologic environments. Science 349

Dechant R, Binda M, Lee SS, Pelet S, Winderickx J, Peter M. 2010. Cytosolic pH is a second messenger for glucose and regulates the PKA pathway through V-ATPase. The EMBO journal 29: 2515-26

Delarue M, Brittingham GP, Pfeffer S, Surovtsev IV, Pinglay S, et al.. 2018. mTORC1 Controls Phase Separation and the Biophysical Properties of the cytosol by Tuning Crowding. Cell 174: 338-49 e20

Dubochet J. 1995. High-pressure freezing for cryoelectron microscopy. Trends Cell Biol 5: 366-8

Dubochet J, Adrian M, Chang JJ, Homo JC, Lepault J, et al.. 1988. Cryo-electron microscopy of vitrified specimens. Q Rev Biophys 21: 129-228

Dubochet J, Mcdowall AW. 1981. Vitrification of Pure Water for Electron-Microscopy. J Microsc-Oxford 124: Rp3-Rp4

Earnest TM, Watanabe R, Stone JE, Mahamid J, Baumeister W, et al.. 2017. Challenges of Integrating Stochastic Dynamics and Cryo-Electron Tomograms in Whole-Cell Simulations. J Phys Chem B 121: 3871-81

Ebbinghaus S, Kim SJ, Heyden M, Yu X, Heugen U, et al.. 2007. An extended

dynamical hydration shell around proteins. Proc Natl Acad Sci U S A 104: 20749-52

Ellis RJ. 2001. Macromolecular crowding: obvious but underappreciated. Trends Biochem Sci 26: 597-604

Ellis RJ, Minton AP. 2003. Cell biology - Join the crowd. Nature 425: 27-28

Erdmann PS, Plitzko JM, Baumeister W. 2018. Addressing cellular compartmentalization by in situ cryo-electron tomography. Curr Opin Colloid In 34: 89-99

Faelber K, Dietrich L, Noel JK, Wollweber F, Pfitzner AK, et al.. 2019. Structure and assembly of the mitochondrial membrane remodelling GTPase Mgm1. Nature 571: 429-433

Faoro R, Bassu M, Mejia YX, Stephan T, Dudani N, et al. 2018. Aberration-corrected cryoimmersion light microscopy. Proc Natl Acad Sci U S A 115: 1204-09

Feig M, Yu I, Wang PH, Nawrocki G, Sugita Y. 2017. Crowding in Cellular Environments at an Atomistic Level from Computer Simulations. J Phys Chem B 121: 8009-25

Fernandez JJ, Li S, Bharat TAM, Agard DA. 2018. Cryo-tomography tilt-series alignment with consideration of the beam-induced sample motion. J Struct Biol 202: 200-09

Francy CA, Clinton RW, Frohlich C, Murphy C, Mears JA. 2017. Cryo-EM Studies of Drp1 Reveal Cardiolipin Interactions that Activate the Helical Oligomer. Sci Rep-Uk 7

Franzmann TM, Jahnel M, Pozniakovsky A, Mahamid J, Holehouse AS, et al.. 2018. Phase separation of a yeast prion protein promotes cellular fitness. Science 359

Fuest M, Schaffer M, Nocera GM, Galilea-Kleinsteuber RI, Messling JE, et al.. 2019. In situ Microfluidic Cryofixation for Cryo Focused Ion Beam Milling and

Cryo Electron Tomography. Sci Rep-Uk 9

Fujii K, Susanto TT, Saurabh S, Barna M. 2018. Decoding the Function of Expansion Segments in Ribosomes. Mol Cell 72: 1013

Fukuda Y, Laugks U, Lučić V, Baumeister W, Danev R. 2015. Electron cryotomography of vitrified cells with a Volta phase plate. Journal of structural biology 190: 143-54

Fuller GG, Han T, Freeberg MA, Moresco JJ, Niaki AG, et al.. 2020. RNA promotes phase separation of glycolysis enzymes into yeast G bodies in hypoxia. Elife 9

Fulton AB. 1982. How crowded is the cytosol? Cell 30: 345-7

Futcher B, Latter GI, Monardo P, McLaughlin CS, Garrels JI. 1999. A sampling of the yeast proteome. Mol Cell Biol 19: 7357-68

Galaz-Montoya JG, Flanagan J, Schmid MF, Ludtke SJ. 2015. Single particle tomography in EMAN2. J Struct Biol 190: 279-90

Garcia-Seisdedos H, Empereur-Mot C, Elad N, Levy ED. 2017. Proteins evolve on the edge of supramolecular self-assembly. Nature 548: 244-47

Garenne D, Libchaber A, Noireaux V. 2020. Membrane molecular crowding enhances MreB polymerization to shape synthetic cells from spheres to rods. Proc Natl Acad Sci U S A 117: 1902-09

Gavin AC, Aloy P, Grandi P, Krause R, Boesche M, et al.. 2006. Proteome survey reveals modularity of the yeast cell machinery. Nature 440: 631-36

Gipson P, Mills DJ, Wouts R, Grininger M, Vonck J, Kuhlbrandt W. 2010. Direct structural insight into the substrate-shuttling mechanism of yeast fatty acid synthase by electron cryomicroscopy. Proc Natl Acad Sci U S A 107: 9164-9

Glaeser RM. 2013. Invited review article: Methods for imaging weak-phase ob-

jects in electron microscopy. Rev Sci Instrum 84: 111101

Goetz SK, Mahamid J. 2020. Visualizing Molecular Architectures of Cellular Condensates: Hints of Complex Coacervation Scenarios. Developmental Cell 55: 97-107

Goggin P, Ho EML, Gnaegi H, Searle S, Oreffo ROC, Schneider P. 2020. Development of protocols for the first serial block-face scanning electron microscopy (SBF SEM) studies of bone tissue. Bone 131: 115107

Gold VA, Chroscicki P, Bragoszewski P, Chacinska A. 2017. Visualization of cytosolic ribosomes on the surface of mitochondria by electron cryo-tomography. EMBO Rep 18: 1786-800

Goodsell DS. 2005. cytosol. doi: 10.2210/rcsb_pdb/goodsell-gallery-006

Gorelick S, Buckley G, Gervinskas G, Johnson TK, Handley A, et al.. 2019. PIEscope, integrated cryo-correlative light and FIB/SEM microscopy. Elife 8

Greber BJ, Gerhardy S, Leitner A, Leibundgut M, Salem M, et al.. 2016. Insertion of the Biogenesis Factor Rei1 Probes the Ribosomal Tunnel during 60S Maturation. Cell 164: 91-102

Gruber A, Hornburg D, Antonin M, Krahmer N, Collado J, et al.. 2018. Molecular and structural architecture of polyQ aggregates in yeast. Proc Natl Acad Sci U S A 115: E3446-E53

Gubins I, Schot Gvd, Veltkamp RC, Förster F, Du X, et al.. 2019. Classification in Cryo-Electron Tomograms. SHREC'19 Track

Guillen-Boixet J, Kopach A, Holehouse AS, Wittmann S, Jahnel M, et al.. 2020. RNA-Induced Conformational Switching and Clustering of G3BP Drive Stress Granule Assembly by Condensation. Cell 181: 346-61

Guizar-Sicairos M, Thurman ST, Fienup JR. 2008. Efficient subpixel image registration algorithms. Opt Lett 33: 156-8

Guo Q, Lehmer C, Martinez-Sanchez A, Rudack T, Beck F, et al.. 2018. In Situ Structure of Neuronal C9orf72 Poly-GA Aggregates Reveals Proteasome Recruitment. Cell 172: 696-705

Hagen WJH, Wan W, Briggs JAG. 2017. Implementation of a cryo-electron tomography tilt-scheme optimized for high resolution subtomogram averaging. J Struct Biol 197: 191-98

Halavatyi A, Terjung S. 2017. FRAP and Other Photoperturbation Techniques. Standard and Super-Resolution Bioimaging Data Analysis: A Primer: 99

Harold FM. 2005. Molecules into cells: specifying spatial architecture. Microbiol Mol Biol Rev 69: 544-64

Haubold C, Schiegg M, Kreshuk A, Berg S, Koethe U, Hamprecht FA. 2016. Segmenting and Tracking Multiple Dividing Targets Using ilastik. Adv Anat Embryol Cel 219: 199-229

Heimlicher MB, Bachler M, Liu MH, Ibeneche-Nnewihe C, Florin EL, et al.. 2019. Reversible solidification of fission yeast cytosol after prolonged nutrient starvation. J Cell Sci 132

Heng Y, Jingnan S, Luca C. 2020. TEASER: Fast and Certifiable Point Cloud Registration. IEEE Transactions on Robotics

Heuer A, Gerovac M, Schmidt C, Trowitzsch S, Preis A, et al.. 2017. Structure of the 40S-ABCE1 post-splitting complex in ribosome recycling and translation initiation. Nat Struct Mol Biol 24: 453-60

Himes BA, Zhang P. 2018. emClarity: software for high-resolution cryo-electron tomography and subtomogram averaging. Nat Methods 15: 955-61

Ho B, Baryshnikova A, Brown GW. 2018. Unification of Protein Abundance Datasets Yields a Quantitative Saccharomyces cerevisiae Proteome. Cell Syst 6: 192-205 e3

Hofweber M, Dormann D. 2019. Friend or foe—Post-translational modifications as regulators of phase separation and RNP granule dynamics. J Biol Chem 294: 7137-50

Hohmann S. 2002. Osmotic stress signaling and osmoadaptation in yeasts. Microbiol Mol Biol Rev 66: 300-72

Hrabe T, Chen Y, Pfeffer S, Cuellar LK, Mangold AV, Forster F. 2012. PyTom: a python-based toolbox for localization of macromolecules in cryo-electron tomograms and subtomogram analysis. J Struct Biol 178: 177-88

Huh W-K, Falvo JV, Gerke LC, Carroll AS, Howson RW, et al.. 2003. Global analysis of protein localization in budding yeast. Nature 425: 686-91

Hyman AA, Weber CA, Julicher F. 2014. Liquid-liquid phase separation in biology. Annu Rev Cell Dev Biol 30: 39-58

Ingerman E, Perkins EM, Marino M, Mears JA, McCaffery JM, et al.. 2005. Dnm1 forms spirals that are structurally tailored to fit mitochondria. Journal of Cell Biology 170: 1021-27

Ioffe S, Szegedy C. 2015. Batch normalization: Accelerating deep network training by reducing internal covariate shift. International conference on machine learning: 448-56. PMLR.

Jakobs S, Stephan T, Ilgen P, Bruser C. 2020. Light Microscopy of Mitochondria at the Nanoscale. Annu Rev Biophys 49: 289-308

Jamieson DJ. 1998. Oxidative stress responses of the yeast Saccharomyces cerevisiae. Yeast 14: 1511-27

Jenni S, Leibundgut M, Boehringer D, Frick C, Mikolasek B, Ban N. 2007. Structure of fungal fatty acid synthase and implications for iterative substrate shuttling. Science 316: 254-61

Jiang H, Song C, Chen CC, Xu R, Raines KS, et al.. 2010. Quantitative 3D imaging of whole, unstained cells by using X-ray diffraction microscopy. Proc Natl Acad Sci U S A 107: 11234-9

Johansson P, Mulinacci B, Koestler C, Vollrath R, Oesterhelt D, Grininger M. 2009. Multimeric options for the auto-activation of the Saccharomyces cerevisiae FAS type I megasynthase. Structure 17: 1063-74

Johansson P, Wiltschi B, Kumari P, Kessler B, Vonrhein C, et al.. 2008. Inhibition of the fungal fatty acid synthase type I multienzyme complex. Proc Natl Acad Sci U S A 105: 12803-8

Jona G, Choder M, Gileadi O. 2000. Glucose starvation induces a drastic reduction in the rates of both transcription and degradation of mRNA in yeast. Bba-Gene Struct Expr 1491: 37-48

Joppe M, D'Imprima E, Salustros N, Paithankar KS, Vonck J, et al.. 2020. The resolution revolution in cryoEM requires high-quality sample preparation: a rapid pipeline to a high-resolution map of yeast fatty acid synthase. Iucrj 7: 220-27

Jorgensen P, Nishikawa JL, Breitkreutz BJ, Tyers M. 2002. Systematic identification of pathways that couple cell growth and division in yeast. Science 297: 395-400

Joyner RP, Tang JH, Helenius J, Dultz E, Brune C, et al.. 2016. A glucose-starvation response regulates the diffusion of macromolecules. Elife 5

Jumper J, Evans R, Pritzel A, Green T, Figurnov M, et al.. 2021. Highly accurate protein structure prediction with AlphaFold. Nature 596: 583-89

Jun S, Ro HJ, Bharda A, Kim SI, Jeoung D, Jung HS. 2019. Advances in Cryo-Correlative Light and Electron Microscopy: Applications for Studying Molecular and Cellular Events. Protein J 38: 609-15

Kastritis PL, O'Reilly FJ, Bock T, Li Y, Rogon MZ, et al.. 2017. Capturing protein

communities by structural proteomics in a thermophilic eukaryote. Mol Syst Biol 13: 936

Kelley K, Jaroenlak P, Raczkowski A, Eng E, Bhabha G, et al.. 2021. Waffle Method for optimizing cryo-FIB-milling. Microscopy and Microanalysis 27: 2078-80

Klein S, Wachsmuth-Melm M, Winter SL, Kolovou A, Chlanda P. 2021. Cryo-correlative light and electron microscopy workflow for cryo-focused ion beam milled adherent cells. Method Cell Biol 162: 273-302

Klosinska MM, Crutchfield CA, Bradley PH, Rabinowitz JD, Broach JR. 2011. Yeast cells can access distinct quiescent states. Gene Dev 25: 336-49

Klumpe S, Fung HKH, Goetz SK, Zagoriy I, Hampoelz B, et al.. 2021. A Modular Platform for Streamlining Automated Cryo-FIB Workflows.
bioRxiv: 2021.05.19.444745

Knorr AG, Schmidt C, Tesina P, Berninghausen O, Becker T, et al.. 2019. Ribosome-NatA architecture reveals that rRNA expansion segments coordinate N-terminal acetylation. Nature Structural and Molecular Biology 26: 35

Koc A, Wheeler LJ, Mathews CK, Merrill GF. 2004. Hydroxyurea arrests DNA replication by a mechanism that preserves basal dNTP pools. J Biol Chem 279: 223-30

Koh JY. 2021. ModelZoo. https://modelzoo.co.

Koning RI, Koster AJ, Sharp TH. 2018. Advances in cryo-electron tomography for biology and medicine. Ann Anat 217: 82-96

Kowalinski E, Bange G, Bradatsch B, Hurt E, Wild K, Sinning I. 2007. The crystal structure of Ebp1 reveals a methionine aminopeptidase fold as binding platform for multiple interactions. Febs Letters 581: 4450-54

Kuba J, Mitchels J, Hovorka M, Erdmann P, Berka L, et al.. 2020. Advanced

cryo-tomography workflow developments - correlative microscopy, milling automation and cryo-lift-out. Journal of Microscopy 281: 112-24

Kulak NA, Pichler G, Paron I, Nagaraj N, Mann M. 2014. Minimal, encapsulated proteomic-sample processing applied to copy-number estimation in eukaryotic cells. Nature Methods 11: 319-U00

Kuznetsova IM, Turoverov KK, Uversky VN. 2014. What Macromolecular Crowding Can Do to a Protein. Int J Mol Sci 15: 23090-140

Kuznetsova IM, Zaslavsky BY, Breydo L, Turoverov KK, Uversky VN. 2015. Beyond the excluded volume effects: mechanistic complexity of the crowded milieu. Molecules 20: 1377-409

Lang MJ, Martinez-Marquez JY, Prosser DC, Ganser LR, Buelto D, et al.. 2014. Glucose Starvation Inhibits Autophagy via Vacuolar Hydrolysis and Induces Plasma Membrane Internalization by Down-regulating Recycling. Journal of Biological Chemistry 289: 16736-47

Lasker K, von Diezmann L, Zhou XF, Ahrens DG, Mann TH, et al.. 2020. Selective sequestration of signalling proteins in a membraneless organelle reinforces the spatial regulation of asymmetry in Caulobacter crescentus. Nat Microbiol 5: 418-29

Leibovitch M, Topisirovic I. 2018. Dysregulation of mRNA translation and energy metabolism in cancer. Adv Biol Regul 67: 30-39

Leibundgut M, Jenni S, Frick C, Ban N. 2007. Structural basis for substrate delivery by acyl carrier protein in the yeast fatty acid synthase. Science 316: 288-90

Lennon JT, Jones SE. 2011. Microbial seed banks: the ecological and evolutionary implications of dormancy. Nat Rev Microbiol 9: 119-30

Levy ED, De S, Teichmann SA. 2012. Cellular crowding imposes global constraints on the chemistry and evolution of proteomes. Proc Natl Acad Sci U S A 109: 20461-6

Levy ED, Kowarzyk J, Michnick SW. 2014. High-resolution mapping of protein concentration reveals principles of proteome architecture and adaptation. Cell Rep 7: 1333-40

Li SC, Kane PM. 2009. The yeast lysosome-like vacuole: Endpoint and crossroads. Bba-Mol Cell Res 1793: 650-63

Li XM, Mooney P, Zheng S, Booth CR, Braunfeld MB, et al.. 2013. Electron counting and beam-induced motion correction enable near-atomic-resolution single-particle cryo-EM. Nature Methods 10: 584

Lindqvist LM, Tandoc K, Topisirovic I, Furic L. 2018. Cross-talk between protein synthesis, energy metabolism and autophagy in cancer. Curr Opin Genet Dev 48: 104-11

Liu B, Qian SB. 2016. Characterizing inactive ribosomes in translational profiling. Translation (Austin) 4: e1138018

Liu M, Heimlicher MB, Bachler M, Ibeneche-Nnewihe CC, Florin EL, et al.. 2019. Glucose starvation triggers filamentous septin assemblies in an S. pombe septin-2 deletion mutant. Biol Open 8

Liu YT, Zhang H, Wang H, Tao CL, Bi GQ, Zhou ZH. 2021. Isotropic Reconstruction of Electron Tomograms with Deep Learning. bioRxiv 2021.07.17.452128

Lu P, Vogel C, Wang R, Yao X, Marcotte EM. 2007. Absolute protein expression profiling estimates the relative contributions of transcriptional and translational regulation. Nat Biotechnol 25: 117-24

Lucas BA, Himes BA, Xue L, Grant T, Mahamid J, Grigorieff N. 2021. Locating macromolecular assemblies in cells by 2D template matching with cisTEM. Elife 10

Lynen F. 1980. On the Structure of Fatty-Acid Synthetase of Yeast. Eur J Biochem

112: 431-42

Maclean N. 1965. Ribosome numbers in a fission yeast. Nature 207: 322-3

Madeira PP, Bessa A, Alvares-Ribeiro L, Aires-Barros MR, Reis CA, et al.. 2012. Salt effects on solvent features of coexisting phases in aqueous polymer/polymer two-phase systems. J Chromatogr A 1229: 38-47

Mahamid J, Pfeffer S, Schaffer M, Villa E, Danev R, et al.. 2016. Visualizing the molecular sociology at the HeLa cell nuclear periphery. Science 351: 969-72

Mahamid J, Schampers R, Persoon H, Hyman AA, Baumeister W, Plitzko JM. 2015. A focused ion beam milling and lift-out approach for site-specific preparation of frozen-hydrated lamellas from multicellular organisms. J Struct Biol 192: 262-9

Mahamid J, Tegunov D, Maiser A, Arnold J, Leonhardt H, et al.. 2019. Liquid-crystalline phase transitions in lipid droplets are related to cellular states and specific organelle association. Proc Natl Acad Sci U S A 116: 16866-71

Makarova M, Peter M, Balogh G, Glatz A, MacRae JI, et al.. 2020. Delineating the Rules for Structural Adaptation of Membrane-Associated Proteins to Evolutionary Changes in Membrane Lipidome. Current Biology 30: 367

Marguerat S, Schmidt A, Codlin S, Chen W, Aebersold R, Bahler J. 2012. Quantitative analysis of fission yeast transcriptomes and proteomes in proliferating and quiescent cells. Cell 151: 671-83

Marini G, Nuske E, Leng W, Alberti S, Pigino G. 2020. Reorganization of budding yeast cytosol upon energy depletion. Molecular Biology of the Cell 31: 1232-45

Martinez-Sanchez A, Garcia I, Asano S, Lucic V, Fernandez JJ. 2014. Robust membrane detection based on tensor voting for electron tomography. J Struct Biol 186: 49-61

Martinez-Sanchez A, Kochovski Z, Laugks U, Meyer Zum Alten Borgloh J,

Chakraborty S, et al.. 2020. Template-free detection and classification of membrane-bound complexes in cryo-electron tomograms. Nat Methods 17: 209-16

Mastronarde DN. 2005. Automated electron microscope tomography using robust prediction of specimen movements. Journal of Structural Biology 152: 36-51

Mastronarde DN. 2018. Advanced Data Acquisition From Electron Microscopes With SerialEM. Microscopy and Microanalysis 24: 864-65

Mastronarde DN, Held SR. 2017. Automated tilt series alignment and tomographic reconstruction in IMOD. J Struct Biol 197: 102-13

Mateju D, Franzmann TM, Patel A, Kopach A, Boczek EE, et al. 2017. An aberrant phase transition of stress granules triggered by misfolded protein and prevented by chaperone function. EMBO J 36: 1669-87

Mazzarello P. 1999. A unifying concept: the history of cell theory. Nat Cell Biol 1: E13-5

McGuffee SR, Elcock AH. 2010. Diffusion, crowding and protein stability in a dynamic molecular model of the bacterial cytosol. PLoS Comput Biol 6: e1000694

M'barek K, Ajjaji D, Chorlay A, Vanni S, Foret L, Thiam AR. 2017. ER Membrane Phospholipids and Surface Tension Control Cellular Lipid Droplet Formation. Dev Cell 41: 591-604 e7

Meaden PG, Arneborg N, Guldfeldt LU, Siegumfeldt H, Jakobsen M. 1999. Endocytosis and vacuolar morphology in Saccharomyces cerevisiae are altered in response to ethanol stress or heat shock. Yeast 15: 1211-22

Mears JA, Lackner LL, Fang S, Ingerman E, Nunnari J, Hinshaw JE. 2011. Conformational changes in Dnm1 support a contractile mechanism for mitochondrial fission. Nat Struct Mol Biol 18: 20-6

Mejlvang J, Olsvik H, Svenning S, Bruun JA, Abudu YP, et al.. 2018. Starvation

induces rapid degradation of selective autophagy receptors by endosomal microautophagy. Journal of Cell Biology 217: 3640-55

Minton AP. 2019. The Cumulative Effect of Surface Adsorption and Excluded Volume in 2D and 3D on Protein Fibrillation. Biophysical Journal 117: 1666-73

Mitchison JM. 1957. The growth of single cells. I. Schizosaccharomyces pombe. Exp Cell Res 13: 244-62

Mittasch M, Tran VM, Rios MU, Fritsch AW, Enos SJ, et al.. 2020. Regulated changes in material properties underlie centrosome disassembly during mitotic exit. J Cell Biol 219

Miyagi T, Yamanaka Y, Harada Y, Narumi S, Hayamizu Y, et al.. 2021. An improved macromolecular crowding sensor CRONOS for detection of crowding changes in membrane-less organelles under stressed conditions. Biochem Biophys Res Commun 583: 29-34

Moebel E, Kervrann C. 2020. A Monte Carlo framework for missing wedge restoration and noise removal in cryo-electron tomography. J Struct Biol X 4: 100013

Moebel E, Martinez-Sanchez A, Lamm L, Righetto RD, Wietrzynski W, et al.. 2021. Deep learning improves macromolecule identification in 3D cellular cryo-electron tomograms. Nat Methods 18: 1386-94

Mölder F, Jablonski K, Letcher B, Hall M, Tomkins-Tinch C, et al.. 2021. Sustainable data analysis with Snakemake [version 1; peer review: 1 approved, 1 approved with reservations]. F1000Research 10

Moser F, Prazak V, Mordhorst V, Andrade DM, Baker LA, et al.. 2019. Cryo-SOFI enabling low-dose super-resolution correlative light and electron cryo-microscopy. P Natl Acad Sci USA 116: 4804-09

Moser F, Prazak V, Mordhorst V, Andrade DM, Baker LA, et al.. 2021. Cryo-SOFI enabling low-dose super-resolution correlative light and electron cryo-microscopy

(vol 116, pg 4804, 2019). P Natl Acad Sci USA 118

Mourao MA, Hakim JB, Schnell S. 2014. Connecting the dots: the effects of macromolecular crowding on cell physiology. Biophys J 107: 2761-66

Mudogo CN, Falke S, Brognaro H, Duszenko M, Betzel C. 2020. Protein phase separation and determinants of in cell crystallization. Traffic 21: 220-30

Munder MC, Midtvedt D, Franzmann T, Nuske E, Otto O, et al.. 2016. A pH-driven transition of the cytosol from a fluid- to a solid-like state promotes entry into dormancy. Elife 5

Murakami T, Qamar S, Lin JQ, Schierle GS, Rees E, et al.. 2015. ALS/FTD Mutation-Induced Phase Transition of FUS Liquid Droplets and Reversible Hydrogels into Irreversible Hydrogels Impairs RNP Granule Function. Neuron 88: 678-90

Murphy JP, Stepanova E, Everley RA, Paulo JA, Gygi SP. 2015. Comprehensive Temporal Protein Dynamics during the Diauxic Shift in Saccharomyces cerevisiae. Molecular and Cellular Proteomics 14: 2454-65

Myasnikov A, Zheng S, Bulkley D, Cheng Y, Agard D. 2018. K3-a first look at the new direct electron detection camera from Gatan company. Microscopy and Microanalysis 24: 890-91

Narayanaswamy R, Levy M, Tsechansky M, Stovall GM, O'Connell JD, et al.. 2009. Widespread reorganization of metabolic enzymes into reversible assemblies upon nutrient starvation. Proc Natl Acad Sci U S A 106: 10147-52

Naydenova K, Jia PP, Russo CJ. 2020. Cryo-EM with sub-1 angstrom specimen movement. Science 370: 223

Noda NN, Wang Z, Zhang H. 2020. Liquid–liquid phase separation in autophagy. Journal of Cell Biology 219: e202004062

Noree C, Begovich K, Samilo D, Broyer R, Monfort E, Wilhelm JE. 2019a. A

quantitative screen for metabolic enzyme structures reveals patterns of assembly across the yeast metabolic network. Mol Biol Cell 30: 2721-36

Noree C, Sato BK, Broyer RM, Wilhelm JE. 2010. Identification of novel filament-forming proteins in Saccharomyces cerevisiae and Drosophila melanogaster. J Cell Biol 190: 541-51

Noree C, Sirinonthanawech N, Wilhelm JE. 2019b. Saccharomyces cerevisiae ASN1 and ASN2 are asparagine synthetase paralogs that have diverged in their ability to polymerize in response to nutrient stress. Sci Rep-Uk 9

Nott TJ, Petsalaki E, Farber P, Jervis D, Fussner E, et al.. 2015. Phase Transition of a Disordered Nuage Protein Generates Environmentally Responsive Membraneless Organelles. Mol Cell 57: 936-47

Nurse P. 1975. Genetic-Control of Cell-Size at Cell-Division in Yeast. Nature 256: 547-51

Nuske E, Marini G, Richter D, Leng W, Bogdanova A, et al.. 2020. Filament formation by the translation factor eIF2B regulates protein synthesis in starved cells. Biol Open

O'Reilly FJ, Xue L, Graziadei A, Sinn L, Lenz S, et al.. 2020. In-cell architecture of an actively transcribing-translating expressome. Science 369: 554-57

Oesterhelt D, Bauer H, Lynen F. 1969. Crystallization of a multienzyme complex: fatty acid synthetase from yeast. Proc Natl Acad Sci U S A 63: 1377-82

Okolo CA, Kounatidis I, Groen J, Nahas KL, Balint S, et al.. 2021. Sample preparation strategies for efficient correlation of 3D SIM and soft X-ray tomography data at cryogenic temperatures. Nature Protocols 16: 2851-85

Oltrogge LM, Chaijarasphong T, Chen AW, Bolin ER, Marqusee S, Savage DF. 2020. Multivalent interactions between CsoS2 and Rubisco mediate alpha-carboxysome formation. Nature Structural and Molecular Biology 27: 281-87

Orlova EV, Saibil HR. 2011. Structural analysis of macromolecular assemblies by electron microscopy. Chem Rev 111: 7710-48

Oshidari R, Huang R, Medghalchi M, Elizabeth Y, Ashgriz N, et al.. 2020. DNA repair by Rad52 liquid droplets. Nature communications 11: 1-8

Pak CW, Kosno M, Holehouse AS, Padrick SB, Mittal A, et al.. 2016. Sequence Determinants of Intracellular Phase Separation by Complex Coacervation of a Disordered Protein. Mol Cell 63: 72-85

Park CK, Horton NC. 2019. Structures, functions, and mechanisms of filament forming enzymes: a renaissance of enzyme filamentation. Biophys Rev 11: 927-94

Patel A, Lee HO, Jawerth L, Maharana S, Jahnel M, et al.. 2015. A Liquid-to-Solid Phase Transition of the ALS Protein FUS Accelerated by Disease Mutation. Cell 162: 1066-77

Patel A, Malinovska L, Saha S, Wang J, Alberti S, et al.. 2017. ATP as a biological hydrotrope. Science 356: 753-56

Peck A, Carter SD, Mai H, Chen S, Burt A, Jensen GJ. 2021. Montage electron tomography of vitrified specimens. bioRxiv: 2021.11.02.466666

Pedregosa F, Varoquaux G, Gramfort A, Michel V, Thirion B, et al.. 2011. Scikit-learn: Machine learning in Python. the Journal of machine Learning research 12: 2825-30

Penczek PA. 2010. Image restoration in cryo-electron microscopy. Methods Enzymol 482: 35-72

Persson LB, Ambati VS, Brandman O. 2020. Cellular Control of Viscosity Counters Changes in Temperature and Energy Availability. Cell 183: 1572

Petrovska I, Nuske E, Munder MC, Kulasegaran G, Malinovska L, et al.. 2014.

Filament formation by metabolic enzymes is a specific adaptation to an advanced state of cellular starvation. Elife 3

Pettersen EF, Goddard TD, Huang CC, Couch GS, Greenblatt DM, et al.. 2004. UCSF Chimera–a visualization system for exploratory research and analysis. J Comput Chem 25: 1605-12

Pettersen EF, Goddard TD, Huang CC, Meng EC, Couch GS, et al.. 2021. UCSF ChimeraX: Structure visualization for researchers, educators, and developers. Protein Sci 30: 70-82

Pfeffer S, Burbaum L, Unverdorben P, Pech M, Chen Y, et al.. 2015. Structure of the native Sec61 protein-conducting channel. Nat Commun 6: 8403

Pfeffer, S., and Mahamid, J. (2018). Unravelling molecular complexity in structural cell biology. Curr Opin Struct Biol 52, 111-118

Plitzko JM, Rigort A, Leis A. 2009. Correlative cryo-light microscopy and cryo-electron tomography: from cellular territories to molecular landscapes. Curr Opin Biotech 20: 83-89

Pocker Y. 2000. Water in enzyme reactions: biophysical aspects of hydration-dehydration processes. Cell Mol Life Sci 57: 1008-17

Powell CD, Quain DE, Smart KA. 2003. Chitin scar breaks in aged Saccharomyces cerevisiae. Microbiology (Reading) 149: 3129-37

Prouteau M, Desfosses A, Sieben C, Bourgoint C, Lydia Mozaffari N, et al.. 2017. TORC1 organized in inhibited domains (TOROIDs) regulate TORC1 activity. Nature 550: 265-69

Prouteau M, Loewith R. 2018. Regulation of Cellular Metabolism through Phase Separation of Enzymes. Biomolecules 8

R Core Team. 2013. R: A language and environment for statistical computing.

Raff JW. 2019. Phase Separation and the Centrosome: A Fait Accompli Trends Cell Biol 29: 612-22

Ranjan N, Pochopien AA, Chih-Chien Wu C, Beckert B, Blanchet S, et al.. 2021. Yeast translation elongation factor eEF3 promotes late stages of tRNA translocation. EMBO J 40: e106449

Ravelli RBG, Nijpels FJT, Henderikx RJM, Weissenberger G, Thewessem S, et al.. 2020. Cryo-EM structures from sub-nl volumes using pin-printing and jet vitrification. Nature Communications 11

Richards A, Gow NAR, Veses V. 2012. Identification of vacuole defects in fungi. J Microbiol Meth 91: 155-63

Rickgauer JP, Grigorieff N, Denk W. 2017. Single-protein detection in crowded molecular environments in cryo-EM images. Elife 6

Ridler T, Calvard S. 1978. Picture thresholding using an iterative selection method. IEEE trans syst Man Cybern 8: 630-32

Rigort A, Bauerlein FJ, Villa E, Eibauer M, Laugks T, et al.. 2012. Focused ion beam micromachining of eukaryotic cells for cryoelectron tomography. Proc Natl Acad Sci U S A 109: 4449-54

Rigort A, Plitzko JM. 2015. Cryo-focused-ion-beam applications in structural biology. Arch Biochem Biophys 581: 122-30

Rogers S, Gui L, Kovalenko A, Reetz E, Nicastro D, Henne WM. 2021. Liquid-crystalline lipid phase transitions in lipid droplets selectively remodel the LD proteome. bioRxiv: 2021.08.30.458229

Ronneberger O, Fischer P, Brox T. Cham, 2015. U-net: Convolutional networks for biomedical image segmentation. International Conference on Medical image computing and computer-assisted intervention: 234-41. Springer International Pub-

lishing.

Rosenthal PB, Henderson R. 2003. Optimal determination of particle orientation, absolute hand, and contrast loss in single-particle electron cryomicroscopy. J Mol Biol 333: 721-45

Rosenzweig ESF, Xu B, Cuellar LK, Martinez-Sanchez A, Schaffer M, et al.. 2017. The Eukaryotic CO2-Concentrating Organelle Is Liquid-like and Exhibits Dynamic Reorganization. Cell 171: 148-62

Rossi D, Barbosa NM, Galvao FC, Boldrin PEG, Hershey JWB, et al.. 2016. Evidence for a Negative Cooperativity between eIF5A and eEF2 on Binding to the Ribosome. Plos One 11

Russo CJ, Passmore LA. 2016a. Progress towards an optimal specimen support for electron cryomicroscopy. Curr Opin Struct Biol 37: 81-9

Russo CJ, Passmore LA. 2016b. Ultrastable gold substrates: Properties of a support for high-resolution electron cryomicroscopy of biological specimens. Journal of Structural Biology 193: 33-44

Sanchez-Garcia R, Segura J, Maluenda D, Carazo JM, Sorzano COS. 2018. Deep Consensus, a deep learning-based approach for particle pruning in cryo-electron microscopy. Iucrj 5: 854-65

Schaffer M, Engel BD, Laugks T, Mahamid J, Plitzko JM, Baumeister W. 2015. Cryo-focused Ion Beam Sample Preparation for Imaging Vitreous Cells by Cryo-electron Tomography. Bio Protoc 5

Schaffer M, Mahamid J, Engel BD, Laugks T, Baumeister W, Plitzko JM. 2017. Optimized cryo-focused ion beam sample preparation aimed at in situ structural studies of membrane proteins. J Struct Biol 197: 73-82

Schaffer M, Pfeffer S, Mahamid J, Kleindiek S, Laugks T, et al.. 2019. A cryo-FIB lift-out technique enables molecular-resolution cryo-ET within native Caenorhabdi-

tis elegans tissue. Nature Methods 16: 757-62

Scher N, Rechav K, Paul-Gilloteaux P, Avinoam O. 2021. In situ fiducial markers for 3D correlative cryo-fluorescence and FIB-SEM imaging. Iscience 24

Schindelin J, Arganda-Carreras I, Frise E, Kaynig V, Longair M, et al.. 2012. Fiji: an open-source platform for biological-image analysis. Nat Methods 9: 676-82

Schmidt C, Becker T, Heuer A, Braunger K, Shanmuganathan V, et al.. 2016. Structure of the hypusinylated eukaryotic translation factor eIF-5A bound to the ribosome. Nucleic Acids Res 44: 1944-51

Schorb M, Gaechter L, Avinoam O, Sieckmann F, Clarke M, et al.. 2017. New hardware and workflows for semi-automated correlative cryo-fluorescence and cryo-electron microscopy/tomography. Journal of Structural Biology 197: 83-93

Schorb M, Haberbosch I, Hagen WJH, Schwab Y, Mastronarde DN. 2019. Software tools for automated transmission electron microscopy. Nat Methods 16: 471-77

Schuller AP, Green R. 2018. Roadblocks and resolutions in eukaryotic translation. Nat Rev Mol Cell Biol 19: 526-41

Schuller AP, Wu CCC, Dever TE, Buskirk AR, Green R. 2017. eIF5A Functions Globally in Translation Elongation and Termination. Mol Cell 66: 194

Schwartz O, Axelrod JJ, Campbell SL, Turnbaugh C, Glaeser RM, Muller H. 2019. Laser phase plate for transmission electron microscopy. Nature Methods 16: 1016

Serrano R. 1977. Energy-Requirements for Maltose Transport in Yeast. Eur J Biochem 80: 97-102

Shao S, Murray J, Brown A, Taunton J, Ramakrishnan V, Hegde RS. 2016. Decoding Mammalian Ribosome-mRNA States by Translational GTPase Complexes. Cell 167: 1229-40 e15

Sharp KA. 2015. Analysis of the size dependence of macromolecular crowding shows that smaller is better. P Natl Acad Sci USA 112: 7990-95

Shaw PJ. 2006. Comparison of widefield/deconvolution and confocal microscopy for three-dimensional imaging. Handbook of biological confocal microscopy: 453-67. Springer

Shen QJ, Kassim H, Huang Y, Li H, Zhang J, et al. 2016. Filamentation of Metabolic Enzymes in Saccharomyces cerevisiae. J Genet Genomics 43: 393-404

Shin Y, Brangwynne CP. 2017. Liquid phase condensation in cell physiology and disease. Science 357

Singh K, Graf B, Linden A, Sautner V, Urlaub H, et al.. 2020. Discovery of a Regulatory Subunit of the Yeast Fatty Acid Synthase. Cell 180: 1130-43 e20

Smith AE, Zhou LZ, Gorensek AH, Senske M, Pielak GJ. 2016. In-cell thermodynamics and a new role for protein surfaces. Proc Natl Acad Sci U S A 113: 1725-30

Snowden JS, Alzahrani J, Sherry L, Stacey M, Rowlands DJ, et al.. 2021. Structural insight into Pichia pastoris fatty acid synthase. Sci Rep 11: 9773

Sorzano COS, Thevenaz P, Unse M. 2005. Elastic registration of biological images using vector-spline regularization. IEEE Transactions on Biomedical Engineering 52: 652-63

Spahn CM, Gomez-Lorenzo MG, Grassucci RA, Jorgensen R, Andersen GR, et al.. 2004. Domain movements of elongation factor eEF2 and the eukaryotic 80S ribosome facilitate tRNA translocation. EMBO J 23: 1008-19

Spehner D, Steyer AM, Bertinetti L, Orlov I, Benoit L, et al.. 2020. Cryo-FIB-SEM as a promising tool for localizing proteins in 3D. J Struct Biol 211: 107528

Srivastava N, Hinton G, Krizhevsky A, Sutskever I, Salakhutdinov R. 2014. Dropout:

a simple way to prevent neural networks from overfitting. The journal of machine learning research 15: 1929-58

Stalling D, Westerhoff M, Hege H-C. 2005. Amira: A highly interactive system for visual data analysis. The visualization handbook 38: 749-67

Stoddard PR, Lynch EM, Farrell DP, Dosey AM, DiMaio F, et al.. 2020. Polymerization in the actin ATPase clan regulates hexokinase activity in yeast. Science 367: 1039-42

Stoops JK, Kolodziej SJ, Schroeter JP, Bretaudiere JP, Wakil SJ. 1992. Structure-function relationships of the yeast fatty acid synthase: negative-stain, cryo-electron microscopy, and image analysis studies of the end views of the structure. Proc Natl Acad Sci U S A 89: 6585-9

Suresh HG, da Silveira Dos Santos AX, Kukulski W, Tyedmers J, Riezman H, et al.. 2015. Prolonged starvation drives reversible sequestration of lipid biosynthetic enzymes and organelle reorganization in Saccharomyces cerevisiae. Mol Biol Cell 26: 1601-15

Tacke S, Erdmann P, Wang Z, Klumpe S, Grange M, et al.. 2021. A streamlined workflow for automated cryo focused ion beam milling. J Struct Biol: 107743

Takaine M, Ueno M, Kitamura K, Imamura H, Yoshida S. 2019. Reliable imaging of ATP in living budding and fission yeast. J Cell Sci 132

Tang G, Peng L, Baldwin PR, Mann DS, Jiang W, et al.. 2007. EMAN2: an extensible image processing suite for electron microscopy. J Struct Biol 157: 38-46

Tang L. 2019. Liquid phase separation. Nat Methods 16: 18

Tarafder AK, von Kugelgen A, Mellul AJ, Schulze U, Aarts DGAL, Bharat TAM. 2020. Phage liquid crystalline droplets form occlusive sheaths that encapsulate and protect infectious rod-shaped bacteria. P Natl Acad Sci USA 117: 4724-31

Tegunov D, Cramer P. 2019. Real-time cryo-electron microscopy data preprocessing with Warp. Nat Methods 16: 1146-52

Tegunov D, Xue L, Dienemann C, Cramer P, Mahamid J. 2021. Multi-particle cryo-EM refinement with M visualizes ribosome-antibiotic complex at 3.5 A in cells. Nat Methods 18: 186-93

Theilet FX, Binolfi A, Bekei B, Martorana A, Goldfarb D, Selenko P. 2017. Structural disorder of monomeric alpha-synuclein persists in mammalian cells. Eur Biophys J Biophy 46: S396-S96

Theillet FX, Binolfi A, Frembgen-Kesner T, Hingorani K, Sarkar M, et al.. 2014. Physicochemical Properties of Cells and Their Effects on Intrinsically Disordered Proteins (IDPs). Chem Rev 114: 6661-714

Thorne RE. 2020. Hypothesis for a mechanism of beam-induced motion in cryo-electron microscopy. Iucrj 7: 416-21

Toone WM, Jones N. 2004. Stress responses in S. pombe In The molecular biology of Schizosaccharomyces pombe, pp. 57-72: Springer

Toro-Nahuelpan M, Zagoriy I, Senger F, Blanchoin L, Thery M, Mahamid J. 2020. Tailoring cryo-electron microscopy grids by photo-micropatterning for in-cell structural studies. Nat Methods 17: 50-54

Traut TW. 1994. Physiological Concentrations of Purines and Pyrimidines. Mol Cell Biochem 140: 1-22

Tuijtel MW, Koster AJ, Jakobs S, Faas FGA, Sharp TH. 2019. Correlative cryo super-resolution light and electron microscopy on mammalian cells using fluorescent proteins. Sci Rep-Uk 9

Turk M, Baumeister W. 2020. The promise and the challenges of cryo-electron tomography. FEBS Lett 594: 3243-61

Turonova B, Hagen WJH, Obr M, Mosalaganti S, Beugelink JW, et al.. 2020. Benchmarking tomographic acquisition schemes for high-resolution structural biology. Nature Communications 11

Turonova B, Schur FKM, Wan W, Briggs JAG. 2017. Efficient 3D-CTF correction for cryo-electron tomography using NovaCTF improves subtomogram averaging resolution to 3.4A. J Struct Biol 199: 187-95

Tyson CB, Lord PG, Wheals AE. 1979. Dependency of size of Saccharomyces cerevisiae cells on growth rate. J Bacteriol 138: 92-8

Van den Elzen AM, Schuller A, Green R, Seraphin B. 2014. Dom34-Hbs1 mediated dissociation of inactive 80S ribosomes promotes restart of translation after stress. EMBO J 33: 265-76

Van Driel LF, Valentijn JA, Valentijn KM, Koning RI, Koster AJ. 2009. Tools for correlative cryo-fluorescence microscopy and cryo-electron tomography applied to whole mitochondria in human endothelial cells. Eur J Cell Biol 88: 669-84

Van Rossum G. 2020. The Python Library Reference, release 3.8. 2. Python Software Foundation 16

Van Rossum G, Drake FL. 2011. The python language reference manual. Network Theory Ltd.

Villa E, Schaffer M, Plitzko JM, Baumeister W. 2013. Opening windows into the cell: focused-ion-beam milling for cryo-electron tomography. Curr Opin Struct Biol 23: 771-7

Von Bulow S, Siggel M, Linke M, Hummer G. 2019. Dynamic cluster formation determines viscosity and diffusion in dense protein solutions. Proc Natl Acad Sci U S A 116: 9843-52

Von der Haar T. 2008. A quantitative estimation of the global translational activity in logarithmically growing yeast cells. Bmc Syst Biol 2 Wagner T, Merino

F, Stabrin M, Moriya T, Antoni C, et al.. 2019. SPHIRE-crYOLO is a fast and accurate fully automated particle picker for cryo-EM. Commun Biol 2: 218

Walter H, Brooks DE. 1995. Phase separation in cytosol, due to macromolecular crowding, is the basis for microcompartmentation. FEBS Lett 361: 135-9

Warner JR. 1999. The economics of ribosome biosynthesis in yeast. Trends Biochem Sci 24: 437-40

Weber CA, Sekar K, Tang JH, Warmer P, Sauer U, Weis K. 2020. beta-Oxidation and autophagy are critical energy providers during acute glucose depletion in Saccharomyces cerevisiae. P Natl Acad Sci USA 117: 12239-48

Weis F, Hagen WJH. 2020. Combining high throughput and high quality for cryo-electron microscopy data collection. Acta Crystallogr D Struct Biol 76: 724-28

Wells JN, Buschauer R, Mackens-Kiani T, Best K, Kratzat H, et al.. 2020. Structure and function of yeast Lso2 and human CCDC124 bound to hibernating ribosomes. Plos Biol 18

Wheeler JR, Matheny T, Jain S, Abrisch R, Parker R. 2016. Distinct stages in stress granule assembly and disassembly. Elife 5

Wild K, Aleksic M, Lapouge K, Juaire KD, Flemming D, et al.. 2020. MetAP-like Ebp1 occupies the human ribosomal tunnel exit and recruits flexible rRNA expansion segments. Nature Communications 11

Wilfling F, Lee CW, Erdmann PS, Zheng YM, Sherpa D, et al.. 2020. A Selective Autophagy Pathway for Phase-Separated Endocytic Protein Deposits. Molecular Cell 80

Winderickx J, Holsbeeks I, Lagatie O, Giots F, Thevelein J, de Winde H. 2003. From feast to famine; adaptation to nutrient availability in yeast. Yeast Stress Responses, ed. S Hohmann, WH Mager: 305-86. Springer Berlin Heidelberg

Wolff G, Limpens RWAL, Zheng S, Snijder EJ, Agard DA, et al.. 2019. Mind the gap: Micro-expansion joints drastically decrease the bending of FIB-milled cryo-lamellae. J Struct Biol 208: 107389

Woodruff JB, Ferreira Gomes B, Widlund PO, Mahamid J, Honigmann A, Hyman AA. 2017. The Centrosome Is a Selective Condensate that Nucleates Microtubules by Concentrating Tubulin. Cell 169: 1066-77

Wu JQ, Pollard TD. 2005. Counting cytokinesis proteins globally and locally in fission yeast. Science 310: 310-14

Yamaguchi M, Namiki Y, Okada H, Mori Y, Furukawa H, et al.. 2011. Structome of Saccharomyces cerevisiae determined by freeze-substitution and serial ultrathin-sectioning electron microscopy. J Electron Microsc (Tokyo) 60: 321-35

Yasuda S, Tsuchiya H, Kaiho A, Guo Q, Ikeuchi K, et al.. 2020. Stress- and ubiquitylation-dependent phase separation of the proteasome. Nature 578: 296-300

Yu HY, Lu S, Gasior K, Singh D, Vazquez-Sanchez S, et al.. 2021. HSP70 chaperones RNA-free TDP-43 into anisotropic intranuclear liquid spherical shells. Science 371: 585

Yu I, Mori T, Ando T, Harada R, Jung J, et al.. 2016. Biomolecular interactions modulate macromolecular structure and dynamics in atomistic model of a bacterial cytosol. Elife 5

Zachs T, Schertel A, Medeiros J, Weiss GL, Hugener J, et al.. 2020. Fully automated, sequential focused ion beam milling for cryo-electron tomography. Elife 9: e52286

Zeng X, Kahng A, Xue L, Mahamid J, Chang Y-W, Xu M. 2021. DISCA: high-throughput cryo-ET structural pattern mining by deep unsupervised clustering. bioRxiv: 2021.05.16.444381

Zhang J, Lan Y, Sanyal S. 2017. Modulation of Lipid Droplet Metabolism-A Poten-

tial Target for Therapeutic Intervention in Flaviviridae Infections. Front Microbiol 8: 2286

Zhang W, Dunkle JA, Cate JH. 2009. Structures of the ribosome in intermediate states of ratcheting. Science 325: 1014-7

Zhang X, Mahamid J. 2020. Addressing the challenge of in situ structural studies of ribonucleoprotein granules in light of emerging opportunities. Curr Opin Struct Biol 65: 1-10

Zheng F, Jia B, Dong F, Liu L, Rasul F, et al.. 2019. Glucose starvation induces mitochondrial fragmentation depending on the dynamin GTPase Dnm1/Drp1 in fission yeast. J Biol Chem 294: 17725-34

Zhou HX. 2004. Loops, linkages, rings, catenanes, cages, and crowders: entropy-based strategies for stabilizing proteins. Acc Chem Res 37: 123-30

Zhou Y, Kastritis PL, Dougherty SE, Bouvette J, Hsu ALL, et al.. 2020. Structural impact of K63 ubiquitin on yeast translocating ribosomes under oxidative stress. P Natl Acad Sci USA 117: 22157-66

Zimmerli CE, Allegretti M, Rantos V, Goetz SK, Obarska-Kosinska A, et al.. 2021. Nuclear pores dilate and constrict in cellulo. Science: eabd9776

Zimmerman SB, Trach SO. 1991. Estimation of macromolecule concentrations and excluded volume effects for the cytosol of Escherichia coli. J Mol Biol 222: 599-620

Zivanov J, Nakane T, Forsberg BO, Kimanius D, Hagen WJ, et al.. 2018. New tools for automated high-resolution cryo-EM structure determination in RELION-3. Elife 7

Zuiderveld K. 1994. Contrast limited adaptive histogram equalization. Graphics gems IV: 474-85